



**Separation and Recovery of a Complexing Agent in the  
Production of Lithium Hexfluorophosphate**

**by**

**Nadine Moodley**

**BSc. Eng.**

**Submitted in fulfilment of the academic requirements of**

**Master of Science**

**in**

**Chemical Engineering**

**College of Agriculture, Engineering and Science**

**University of KwaZulu-Natal**

**February 2019**

**Supervisors: Prof D Ramjugernath, Prof P Naidoo, Dr WM Nelson  
and Dr K Wagener**

## PREFACE

The research contained in this thesis was completed by the candidate while based in the Discipline of Chemical Engineering, School of Engineering of the College of Agriculture, Engineering and Science, University of KwaZulu-Natal, Howard College, South Africa.

The contents of this work have not been submitted in any form to another university and, except where the work of others is acknowledged in the text, the results reported are due to investigations by the candidate.

As the candidate's Supervisor I agree/do not agree to the submission of this thesis.



---

Prof D Ramjugernath

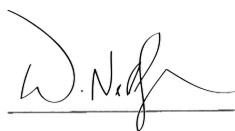
Date: 07/03/2019



---

Prof P Naidoo

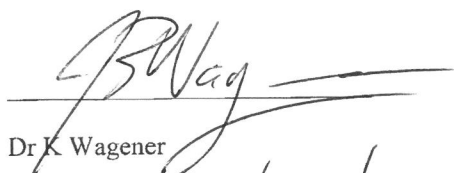
Date: 07/03/2019



---

Dr WM Nelson

Date: 2019/03/06



---

Dr K Wagener

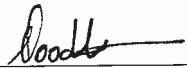
Date:

2019/03/06

## DECLARATION: PLAGIARISM

I, Nadine Moodley, declare that:

1. The research reported in this thesis, except where otherwise indicated, is my original research.
2. This thesis has not been submitted for any degree or examination at any other university.
3. This thesis does not contain other persons' data, pictures, graphs or other information, unless specifically acknowledged as being sourced from other persons.
4. This thesis does not contain other persons' writing, unless specifically acknowledged as being sourced from other researchers. Where other written sources have been quoted, then:
  - a. Their words have been re-written but the general information attributed to them has been referenced
  - b. Where their exact words have been used, then their writing has been placed inside quotation marks, and referenced.
5. This thesis does not contain text, graphics or tables copied and pasted from the Internet, unless specifically acknowledged, and the source being detailed in the thesis and in the References sections.



---

Signed: Nadine Moodley

Date: February 2019

## ACKNOWLEDGMENTS

I would like to acknowledge and thank the following people:

The DST/NRF South African Research Chairs Initiative (SARChI), the Nuclear Energy Corporation of South Africa (NECSA) and the Thermodynamics Research Unit (TRU) for the support of this research.

Dr Kobus Wagener for granting permission to present the information and flow sheets regarding the PF<sub>5</sub> production process.

My supervisors Prof Deresh Ramjugernath, Prof Prathieka Naidoo and Dr Wayne Michael Nelson for their guidance and for imparting their extensive knowledge.

My colleagues and research staff in the Thermodynamics Research Unit and the department: Ayanda Khanyile, Sivanna Naicker, Sanjay Deeraj and Sikhumbuzo Sithole for their assistance with the lab equipment and procedures.

My parents, grandparents and friends for their constant prayers, motivation and support.

And God for providing me with the strength, motivation and determination to persevere.

## ABSTRACT

A novel process for the production of lithium hexafluorophosphate ( $\text{LiPF}_6$ ) has been developed by NECSA (Nuclear Energy Corporation of South Africa). The starting materials include hexafluorophosphoric acid ( $\text{HPF}_6$ ) aqueous solution and a complexing agent, pyridine. This study focused on the separation and recovery of the waste material from this production process (pyridine, ethanol, water and nitrogen), with high recovery rates and final mole purities for each component such that they can be recycled and reused in the process. Two separation schemes were investigated. Process A treats the waste stream firstly via a flash vessel to remove the nitrogen, then a conventional distillation column to separate the pyridine from the mixture followed by an extractive distillation column to separate the ethanol from water. The solvent chosen for extractive distillation was ethylene glycol. Process B follows the same scheme as process A for the nitrogen and pyridine separation; however it uses a pervaporation membrane modular setup, incorporating a polyvinylalcohol membrane in a spiral wound configuration, to separate ethanol from water as opposed to the use of the extractive distillation column in process A. Modifications were made to each process where an additional flash vessel was used to further purify the nitrogen stream. The Aspen Plus® process simulator was used to design the proposed separation schemes. The design and development of separation processes rely on accurate vapour liquid equilibrium (VLE) data. The ethanol/pyridine (40 kPa, 100 kPa, 313.15 K) and water/pyridine (40 kPa, 333.15 K) phase data were measured since the VLE data found in literature for these systems were inconsistent. A modified recirculating VLE still was used to measure the phase equilibrium data with sample analysis performed using a Shimadzu GC-2014. The measured data was regressed using various thermodynamic models in Aspen Plus®. The model that best suited the components of interest was the Peng-Robinson equation of state incorporating the Mathias Copeman alpha function with the Wong-Sandler mixing rules and the NRTL activity coefficient model (PR-MC-WS-NRTL). The binary parameters obtained with the use of this model was then incorporated into the Aspen Plus® computer software where it was used to simulate the proposed process schemes. The purpose of this is to provide a more accurate representation of the industrial process. A sensitivity analysis on the proposed process schemes was performed in order to obtain the optimal solution. The economic analysis showed that while process A met the specified purity and recovery of 99.9 mol %, it had a high total annual cost (approximately R46 million) due to the large amount of solvent required for extractive distillation. Process B had a significantly lower total annual cost (approximately R32 million). However, this is due to the area restriction imposed on the membrane (960 m<sup>2</sup>) due to the pyridine loss and slow separation process as the water composition decreased. The ethanol-rich stream (retentate) leaving the membrane unit contained a water content of 0.21 mol %; had this stream been

dehydrated to a water content of 0.01 mol % (similar to the purity obtained with extractive distillation), the total membrane area would have increased to a value of 2000 m<sup>2</sup>. The area required for the membrane then becomes practically and economically unfeasible. Furthermore, increasing the membrane area, increases the flow rate of the recycle stream (permeate) thereby decreasing the allowable recovery and purity of the core component, pyridine. Thus, process B does not meet the purity and recovery specifications for pyridine and ethanol. If it is attempted to achieve the ethanol purity specification, the membrane process becomes impractical due to the large membrane area required and the recovery and purity of the core component pyridine decreases. Furthermore, the additional flash vessel used in this process significantly increases the total annual cost (R4 million) and does not improve the product purities. Process A meets the required purity and recovery specifications for all components and is practically feasible. The additional flash vessel used in this process recovers a further 6.18 kg/hr of ethanol whilst slightly increasing the total annual cost (R0.14 million) and hence is the optimal solution.

# TABLE OF CONTENTS

	<u>Page</u>
Preface.....	i
Declaration: Plagiarism.....	ii
Acknowledgements.....	iii
Abstract.....	iv
Table of Contents.....	vi
List of Tables.....	ix
List of Figures.....	xiii
Nomenclature.....	xviii
Chapter 1: Introduction.....	1
1.1 Project Background.....	2
1.2 Thesis Outline.....	12
Chapter 2: Theoretical Background.....	13
2.1 Phase Equilibrium Data Available in Literature.....	14
2.2 Residue Curve Map.....	18
2.3 Extractive Distillation.....	21
2.4 Pervaporation.....	22
2.4.1 Selection of Membrane (Pervaporation) Material.....	23
2.4.2 Membrane Design.....	23
2.4.3 Selection of Membrane (Pervaporation) Module.....	24
Chapter 3: Theoretical Modelling.....	27
3.1 Analyses of VLE Data.....	27
3.2 Thermodynamic Models used in this study.....	28
3.2.1 Peng-Robinson Cubic Equation of State.....	29
3.2.2 Mathias Copeman Alpha Function.....	30
3.2.3 Mixing rules: Wong-Sandler.....	30
3.2.4 Activity Coefficient Models.....	32
3.3 Vapour Liquid Equilibrium Prediction.....	35
3.3.1 Predictive Soave Redlich Kwong (PSRK).....	35
3.4 Data Regression.....	36
Chapter 4: Experimental Equipment and Procedure.....	37
4.1 Low Pressure VLE Equipment.....	37

4.2 Experimental Method .....	40
4.2.1 Preparation .....	40
4.2.2 Temperature and Pressure Calibration .....	40
4.2.3 Gas Chromatograph Thermal Conductivity Detector Calibration .....	43
4.2.4 Isobaric Operation.....	44
4.2.5 Isothermal Operation.....	45
Chapter 5: Results and Discussion: Experimental VLE Data and Modelling.....	46
5.1 Chemical Characterisation .....	46
5.2 Vapour Pressure Measurement .....	47
5.3 Phase Equilibrium Measurements and Modelling .....	51
5.3.1 Test System: Ethanol (1) + Cyclohexane (4) .....	53
5.3.2 New Binary Phase Equilibrium Data .....	55
5.4 Comparison of Model Parameters .....	81
Chapter 6: Process Design and Costing .....	85
6.1 Design Methodology.....	85
Process A.....	89
Process B.....	92
6.2 Process Optimisation .....	93
6.2.1 Flash Vessels.....	93
6.3.2 Distillation Columns .....	95
Conventional Distillation Column (C-01).....	96
Extractive Distillation Column (C-02).....	99
Solvent Recovery Distillation Column (C-03).....	101
6.3 Membrane Design.....	102
6.4 Simulation Results .....	105
6.5 Comparison of the Design Proposed by NECSA and this study .....	109
6.6 Cost Evaluation.....	110
Chapter 7: Conclusion.....	116
Chapter 8: Recommendations .....	119
References .....	120
Appendix A: Membrane Design .....	126
Appendix B: Detailed Costing Procedure .....	129
B.1: Capital Investment Cost of Membrane and Module .....	129



B.2: Operating Costs.....	129
B.3: Inter-stage Heat Exchangers .....	131
Appendix C: Gas Chromatograph Calibration Charts .....	132
C.1 Test System: Ethanol (1) + Cyclohexane (4) System .....	132
C.2 Ethanol (1) + Pyridine (3) System .....	134
C.3 Water (2) + Pyridine (3) System .....	136
Appendix D: Experimental Uncertainty Calculation .....	138
D.1 Temperature and Pressure Uncertainty .....	139
D.2 Phase Composition Uncertainty .....	139
Appendix E: Sensitivity Analysis Plots .....	141
E.1 Process 1FE (1 flash, extractive distillation): .....	141
Solvent Recovery Column (C-03).....	141
E.2 Process 2FE (2 flash, extractive distillation): .....	142
Conventional Distillation Column (C-01).....	142
Extractive Distillation Column (C-02).....	143
Solvent Recovery Column (C-03).....	145
E.3 Process 1FM (1 flash, membranes) .....	146
Conventional Distillation Column (C-01).....	146
E.4 Process 2FM (2 flash, membranes) .....	147
Conventional Distillation Column (C-01).....	147

## LIST OF TABLES

Table 1.1: Stream results for the PF <sub>5</sub> production process proposed by NECSA.....	5
Table 1.2: Stream results for the waste treatment process proposed by NECSA .....	10
Table 2.1: Boiling points and azeotropic compositions for the system ethanol (1) + water (2) + pyridine (3) generated on Aspen Plus® at 80 kPa. ....	18
Table 3.1: Significance of $k_{ij}$ binary interaction parameter .....	31
Table 3.2: Suitable guideline for $\alpha_{ij}$ parameter.....	34
Table 4.1: Operating conditions for the Shimadzu GC- 2014.....	43
Table 5.1: Chemical characterisation at 293.15 K .....	46
Table 5.2: Combined expanded uncertainties for temperature and pressure.....	47
Table 5.3: Comparison of experimental vapour pressure data for cyclohexane to literature sources .....	48
Table 5.4: Comparison of the experimental vapour pressure data for ethanol to literature sources. ....	49
Table 5.5: Comparison of the experimental vapour pressure data for pyridine to literature sources. ....	50
Table 5.6: Average absolute deviation (AAD) and average absolute relative deviation (AARD) for the experimental vapour pressures using the reference sources. ....	51
Table 5.7: Uncertainties observed in temperature and pressure for the systems of interest .....	51
Table 5.8: Uncertainties observed in composition for the systems of interest.....	52
Table 5.9: Combined expanded uncertainties for temperature, pressure and mole compositions for the VLE binary systems, averaged over all data points for each system .....	52
Table 5.10: Regressed MC parameters (PR-MC-EoS) .....	55
Table 5.11: Deviations in the experimental vapour pressure data from modelled data using the PR EoS with the MC alpha function.....	56

Table 5.12: Comparison of the experimental VLE data to modelled data for the isobaric ethanol (1) + pyridine (3) system at 40 kPa.....	65
Table 5.13: Comparison of the experimental VLE data to modelled data for the ethanol (1) + pyridine (3) system at 100 kPa.....	66
Table 5.14: Comparison of the experimental VLE data to modelled data for the ethanol (1) + pyridine (3) system at 313.15 K.....	67
Table 5.15: Data regression deviations for the isobaric ethanol (1) + pyridine (3) binary system. ....	68
Table 5.16: Data regression deviations for the isothermal ethanol (1) + pyridine (3) binary system. ....	69
Table 5.17: Model parameters regressed for the ethanol (1) + pyridine (3) binary system .....	69
Table 5.18: Azeotropic data for the water (2) + pyridine (3) system.....	75
Table 5.19: Comparison of the experimental VLE data to modelled data for the water (2) + pyridine (3) system at 40 kPa.....	76
Table 5.20: Comparison of the experimental VLE data to modelled data for the water (2) + pyridine (3) system at 333.15 K.....	77
Table 5.21: Data regression deviations for the isobaric water (2) + pyridine (3) binary system	78
Table 5.22: Data regression deviations for the isothermal water (2) + pyridine (3) binary system. ....	79
Table 5.23: Model parameters regressed for the water (2) + pyridine (3) binary system .....	80
Table 5.24: Data regression deviations for the systems studied averaged over all points. ....	84
Table 6.1: Stream results for process 1FE (1-flash extractive) .....	87
Table 6.2: Stream results for process 2FE (2-flash extractive) .....	88
Table 6.3: Stream results for process 1FM (1-flash membrane).....	91
Table 6.4: Stream results for process 2FM (2-flash membrane).....	91
Table 6.5: Component Murphree Efficiencies .....	95

Table 6.6: Critical properties of components .....	96
Table 6.7: Variation of feed stage (FS) location and reflux ratio (RR) to meet desired distillate specifications for column C-01 (process A: 1 flash extractive) .....	97
Table 6.8: Extractive distillation column specifications for each case for column C-02 (process A: 1 flash extractive) .....	100
Table 6.9: Membrane and module specifications .....	103
Table 6.10: First row results of module configuration .....	104
Table 6.11: Distillation column specifications for process A (2FE & 1FE) .....	105
Table 6.12: Distillation column specifications for process B (2FM & 1FM) .....	105
Table 6.13: Flash vessel specifications .....	106
Table 6.14: Final stream compositions and purities for process A: .....	107
Table 6.15: Final stream compositions and purities for process B .....	109
Table 6.16: Capital and operating cost summary .....	111
Table 6.17: Purity and flow rate of relevant streams .....	114
Table A.1: Coefficients for the Antoine equation: .....	128
Table A.2: Coefficients for the Van Laar equation: .....	128
Table B.1: Literature cost of membrane and module .....	129
Table B.2: Utility costs .....	129
Table B.3: Conversion of currencies to rands .....	130
Table B.4: Chemical Engineering Plant Cost Index .....	130
Table B.5: Enthalpy of vaporisation and heat capacities .....	131
Table B.6: Enthalpy of vaporisation and heat capacities from Aspen Plus® .....	131
Table E.1: Variation of feed stage location with reflux ratio .....	141
Table E.2: Variation of feed stage location with reflux ratio .....	142

Table E.3: Extractive distillation column specifications for each case.....	144
Table E.4: Variation of feed stage location with reflux ratio.....	145
Table E.5: Variation of feed stage location with reflux ratio.....	146
Table E.6: Variation of feed stage location with reflux ratio.....	147

## LIST OF FIGURES

Figure 1.1: PF <sub>5</sub> production process as proposed by NECSA .....	4
Figure 1.2: Waste treatment process as proposed by NECSA .....	9
Figure 2.1: Literature data available for ethanol (1) + pyridine (3) system .....	16
Figure 2.2: Some of the literature data available for the water (2) + pyridine (3) system .....	17
Figure 2.3: Residue curve map generated on Aspen Plus® using the NRTL activity coefficient model with azeotropes (mole fractions) at 80 kPa .....	19
Figure 2.4: Residue curve map generated on Aspen Plus® using the NRTL activity coefficient model with stream compositions and azeotropes (mole fractions) at 80 kPa .....	20
Figure 2.5: Schematic of the pervaporation process .....	23
Figure 4.1: Schematic diagram of the VLE recirculating still .....	38
Figure 4.2: Temperature calibration for the VLE still .....	41
Figure 4.3: Uncertainty in temperature calibration for the VLE still .....	42
Figure 4.4: Pressure calibration for the VLE still .....	42
Figure 4.5: Uncertainty in pressure calibration for the VLE still .....	43
Figure 5.1: Vapour pressure data for cyclohexane .....	48
Figure 5.2: Vapour pressure data for ethanol .....	49
Figure 5.3: Vapour pressure data for pyridine .....	50
Figure 5.4: Isobaric VLE data for the ethanol (1) + cyclohexane (4) system at 40 kPa .....	53
Figure 5.5: Isobaric x-y data for the ethanol (1) + cyclohexane (4) system at 40 kPa .....	53
Figure 5.6: Isothermal VLE data for the ethanol (1) + cyclohexane (4) system at 313.15 K .....	54
Figure 5.7: Isothermal x-y data for the ethanol (1) + cyclohexane (4) system at 313.15 K .....	54
Figure 5.8: Isobaric VLE data for the ethanol (1) + pyridine (3) system at 40 kPa. Comparison of experimental data to literature and predicted data .....	56

Figure 5.9: Isobaric x-y data for the ethanol (1) + pyridine (3) system at 40 kPa. Comparison of experimental data to literature and predicted data .....	57
Figure 5.10: Isobaric VLE data for the ethanol (1) + pyridine (3) system at 100 kPa. Comparison of experimental data to literature and predicted data .....	57
Figure 5.11: Isobaric x-y data for the ethanol (1) + pyridine (3) system at 100 kPa. Comparison of experimental data to literature and predicted data .....	58
Figure 5.12: Isothermal VLE data for the ethanol (1) + pyridine (3) system at 313.15 K. Comparison of experimental data to literature and predicted data.....	59
Figure 5.13: Isothermal x-y data for the ethanol (1) + pyridine (3) system at 313.15 K. Comparison of experimental data to literature and predicted data .....	59
Figure 5.14: Isobaric VLE data for the ethanol (1) + pyridine (3) system at 40 kPa. Comparison of experimental data to modelled data .....	60
Figure 5.15: Isobaric x-y data for the ethanol (1) + pyridine (3) system at 40 kPa. Comparison of experimental data to modelled data.....	61
Figure 5.16: Isobaric VLE data for the ethanol (1) + pyridine (3) system at 100 kPa. Comparison of experimental data to modelled data .....	61
Figure 5.17: Isobaric x-y data for the ethanol (1) + pyridine (3) system at 100 kPa. Comparison of experimental data to modelled data .....	62
Figure 5.18: Isothermal VLE data for the ethanol (1) + pyridine (3) system at 313.15 K. Comparison of experimental data to modelled data.....	63
Figure 5.19: Isothermal x-y data for the ethanol (1) + pyridine (3) system at 313.15 K. Comparison of experimental data to modelled data .....	63
Figure 5.20: Isobaric VLE data for the water (2) + pyridine (3) system at 40 kPa. Comparison of experimental data to literature and predicted data .....	70
Figure 5.21: Isobaric x-y data for the water (2) + pyridine (3) system at 40 kPa. Comparison of experimental data to literature and predicted data .....	70
Figure 5.22: Isothermal VLE data for the water (2) + pyridine (3) system at 333.15 K. Comparison of experimental data to literature and predicted data .....	71

Figure 5.23: Isothermal x-y data for the water (2) + pyridine (3) system at 333.15 K. Comparison of experimental data to literature and predicted data .....	72
Figure 5.24: Isobaric VLE data for the water (2) + pyridine (3) system at 40 kPa. Comparison of experimental data to modelled data.....	72
Figure 5.25: Isobaric x-y data for the water (2) + pyridine (3) system at 40 kPa. Comparison of experimental data to modelled data.....	73
Figure 5.26: Isothermal VLE data for the water (2) + pyridine (3) system at 333.15 K. Comparison of experimental data to modelled data .....	73
Figure 5.27: Isothermal x-y data for the water (2) + pyridine (3) system at 333.15 K Comparison of experimental data to modelled data .....	74
Figure 5.28: Isothermal VLE data for the ethanol (1) + pyridine (3) system. Comparison of literature data to modelled data using the Dortmund Data Bank and Aspen Plus® .....	81
Figure 5.29: Isothermal VLE data for the water (2) + pyridine (3) system. Comparison of literature data to modelled data using the Dortmund Data Bank and Aspen Plus®.....	82
Figure 5.30: Isothermal x-y data for the water (2) + pyridine (3) system. Comparison of literature data to modelled data using the Dortmund Data Bank and Aspen Plus®.....	83
Figure 6.1: Process A .....	86
Figure 6.2: Process B .....	90
Figure 6.3: Influence of pressure on the nitrogen mole purity, nitrogen recovery and ethanol mass flow rate in the vapour outlet for F-01 (1-flash process) .....	93
Figure 6.4: Influence of pressure on the nitrogen mole purity, nitrogen recovery and ethanol mass flow rate in the vapour outlet for F-01 (2-flash process) .....	94
Figure 6.5: Influence of pressure on the nitrogen mole purity, nitrogen recovery and ethanol mass flow rate in the vapour outlet for F-02 (2-flash process) .....	94
Figure 6.6: Influence of the number of stages on TAC for column C-01, process A: 1 flash extractive.....	98
Figure 6.7: Influence of the feed stage on the total annual cost at 75 stages for column C-01, process A: 1 flash extractive .....	98



Figure 6.8: Influence of number of stages on reboiler heat duty for column C-02, process A: 1 flash extractive .....	99
Figure 6.9: Effect of solvent to feed ratio on RHD for case 5 for column C-02, process A: 1 flash extractive.....	100
Figure 6.10: Total annual cost for the different cases in column C-02, process A, 1 flash extractive. ....	101
Figure A.1: Permeation flux of ethanol as a function of ethanol feed concentration.....	127
Figure A.2: Permeation flux of water as a function of ethanol feed concentration.....	128
Figure C.1: GC calibration for the ethanol (1) + cyclohexane (4) system in the more dilute regions of ethanol. Representation of the relationship between the number of moles vs the peak area.	132
Figure C.2: GC calibration for ethanol (1) + cyclohexane (4) system in the more dilute regions of ethanol. Deviations in composition using a second order polynomial.....	132
Figure C.3: GC calibration for the ethanol (1) + cyclohexane (4) system in the more concentrated regions of ethanol. Representation of the relationship between the number of moles vs the peak area. ....	133
Figure C.4: GC calibration for the ethanol (1) + cyclohexane (4) system in the more concentrated regions of ethanol. Deviations in composition using a second order polynomial.....	133
Figure C.5: GC calibration for the ethanol (1) + pyridine (3) system in the more dilute regions of ethanol. Representation of the relationship between the number of moles vs the peak area. ...	134
Figure C.6: GC calibration for the ethanol (1) + pyridine (3) system in the more dilute regions of ethanol. Deviations in composition using a second order polynomial.....	134
Figure C.7: GC calibration for the ethanol (1) + pyridine (3) system in the more concentrated regions of ethanol. Representation of the relationship between the number of moles vs the peak area. ....	135
Figure C.8: GC calibration for the ethanol (1) + pyridine (3) system in the more concentrated regions of ethanol. Deviations in composition using a second order polynomial.....	135
Figure C.9: GC calibration for the water (2) + pyridine (3) system in the more dilute regions of water. Representation of the relationship between the number of moles vs the peak area. ....	136

Figure C.10: GC calibration for the water (2) + pyridine (3) system in the more dilute regions of water. Deviations in composition using a second order polynomial.....	136
Figure C.11: GC calibration for the water (2) + pyridine (3) system in the more concentrated regions of water. Representation of the relationship between the number of moles vs the peak area.....	137
Figure C.12: GC calibration for the water (2) + pyridine (3) system in the more concentrated regions of water. Deviations in composition using a second order polynomial.....	137
Figure E.1: Influence of number of stages on the total annual cost .....	141
Figure E.2: Influence of feed entry stage on the total annual cost at 32 stages .....	141
Figure E.3: Influence of number of stages on the total annual cost .....	142
Figure E.4: Influence of feed entry stage on total annual cost at 73 stages .....	142
Figure E.5: Influence of number of stages on reboiler heat duty .....	143
Figure E.6: Influence of solvent to feed ratio on reboiler heat duty for case 6.....	143
Figure E.7: Total annual cost for the different cases in the extractive distillation column .....	144
Figure E.8: Influence of number of stages on the total annual cost .....	145
Figure E.9: Influence of feed entry stage on total annual cost at 33 stages .....	145
Figure E.10: Influence of number of stages on the total annual cost .....	146
Figure E.11: Influence of feed entry stage on the total annual cost at 65 stages .....	146
Figure E.12: Influence of number of stages on the total annual cost .....	147
Figure E.13: Influence on feed entry stage on the total annual cost at 63 stages.....	147

## NOMENCLATURE

### Symbol

$a$	Intermolecular attraction force parameter in PR EoS
$A$	Integrated peak area from GC (m <sup>2</sup> )
$A^E$	Excess Helmholtz free energy (kJ/mol)
$A_k$	Differential area of element k in membrane (m <sup>2</sup> )
$A_{12}, A_{21}$	Van Laar equation constants
$A, B, C$	Antoine equation constants
$a_{ij}, b_{ij}, c_{ij}, d_{ij}, e_{ij}, f_{ij}$	NRTL parameters from Aspen Plus®
$b$	Molecular size parameter in EoS, half width interval in type B evaluation
$c$	Composition (kmol/h)
$C$	Mathias Copeman parameter
$C_f$	Annual fixed cost
$C_p$	Heat capacity (kJ/kmol.h)
$C_v$	Process variable cost
$f$	Fugacity (kPa)
$f_c$	Fixed capital investment
$F$	Response factor from GC
$F_F$	Feed flow rate to membrane (kmol/h)
$F_P$	Permeate flow rate from membrane (kmol/h)
$G$	Gas
$G^E$	Excess Gibbs free energy (kJ/mol)
$G_{ij}, G_{ji}$	Parameter in the NRTL model (kJ/mol)
$\Delta h_{vap}$	Enthalpy of vapourisation (kJ/kmol)

$i_m$	Minimum acceptable rate of return
$i_r$	Fixed capital recovery rate
J	Normalised permeation flux (kmol/m <sup>2</sup> .h.kPa)
k	Coverage factor
$k_{ij}, l_{ij}$	Binary interaction parameter for the Wong-Sandler mixing rule
L	Liquid
m	Mass (kg)
n	Number of moles (mol)
$N_p$	Number of points
P	Pressure (kPa), permeate (kmol/h)
$p^o$	Vapour pressure on feed side of membrane (kPa)
$p''$	Vapour pressure on permeate side of membrane (kPa)
Q	Duty (kW), permeation flux (kmol/h.m <sup>2</sup> )
$Q_C$	Condenser duty (kW)
$Q_R$	Reboiler duty (kW)
$Q_{tot}$	Total permeation flux (kmol/h.m <sup>2</sup> )
R	Universal gas constant (J/mol.K), retentate (kmol/h)
S	Solid
T	Temperature (K)
$T_R$	Reduced temperature (K)
TRUE	True value of the property
u	Uncertainty
$u_C$	Combined standard uncertainty
$U_C$	Combined expanded uncertainty
V	Vapour, volume (m <sup>3</sup> )

$V^l$	Saturated liquid molar volume (m <sup>3</sup> /mol)
$v$	Molar volume (m <sup>3</sup> /mol) in PR EoS
$w$	Weight fraction
$x$	Liquid phase mole fraction
$y$	Vapour phase mole fraction

### Greek Symbols

$\alpha$	Scaling factor in the PR EoS, non-randomness interaction parameter in the NRTL model
$\alpha_i$ (T)	Alpha function in cubic equation of state
$\tau_{ij}, \tau_{ji}$	Parameter in the NRTL model
$\gamma$	Activity Coefficient
$\sigma$	Standard deviation for type A evaluation
$\phi$	Fugacity coefficient
$\Phi$	Ratio of fugacity coefficient and Poynting correction factor
$\omega$	Acentric factor

### Subscript

bal	Mass balance
c	Critical property
calc	Calculated
cali	Calibrated
exp	Experimental
fluct	Fluctuation
i, j	Component identification
ij	Interaction between molecular species i and j

lit	Literature
rep	Repeatability
std	Standard

### **Superscripts**

sat	Property evaluated at the saturation pressure
o	Standard state
l	Liquid
v	Vapour
^	Mixture
E	Excess

### **Abbreviations**

AAD	Absolute Average Deviation
AARD	Absolute Average Relative Deviation
DDB	Dortmund Data Bank
DSV	Design/Spec Vary
EoS	Equation of State
FS	Feed Stage
GC	Gas Chromatograph
MC	Mathias Copeman
NoS	Number of Stages
NIST	National Institute of Standards and Technology
NRTL	Non-Random-Two-Liquid
PR	Peng-Robinson
PSRK	Predictive-Soave-Redlich-Kwong

PVA	Polyvinyl alcohol
RCM	Residue Curve Map
RHD	Reboiler Heat Duty
RMSE	Root Mean Square Error
RR	Reflux Ratio
RSS	Root Sum Squares
S/F	Solvent to Feed ratio
TAC	Total Annual Cost
TCD	Thermal Conductivity Detector
VLE	Vapour Liquid Equilibrium
WS	Wong-Sandler
UNIFAC	Universal Functional Group Activity Coefficient Model
UNIQUAC	Universal Quasi-Chemical Activity Coefficient Model

## CHAPTER 1: INTRODUCTION

Fossil fuels such as coal, oil and gas are predominantly the main energy sources citizens rely upon, however these fuels will eventually be depleted or become uneconomical (Renewable Energy, 2017). Furthermore, there is sufficient literature about the negative impact on continuing use of fossil fuels which contribute to global warming and polluting of the environment. Therefore, alternative energy sources, such as renewable wind and solar energy are becoming increasingly valuable since they do not emit any greenhouse gases and can be regenerated for an indefinite period of time (Renewable Energy, 2017). The disadvantages in its use however is its inconsistent/unreliable supply (solar power is only available during daylight), hence an effective storage device is essential.

Lithium-ion batteries can provide a reliable rechargeable storage technology. Of the different lithium salts that can be used as a component of the electrolyte, only lithium hexafluorophosphate ( $\text{LiPF}_6$ ) is employed in industry (Daniel, 2008). This  $\text{LiPF}_6$  is synthesised using phosphorus pentafluoride gas ( $\text{PF}_5$ ) as a starting material. However, during industrial synthesis of  $\text{PF}_5$ , hydrogen fluoride (HF), a contamination is produced (Lekgoathi, et al., 2015). This HF is corrosive to the battery components and reacts with the electrolyte causing it to decompose (Lekgoathi, et al., 2015). There is therefore a need to synthesise uncontaminated  $\text{PF}_5$ .

The Nuclear Energy Corporation of South Africa (NECSA) developed and patented a novel process in 2015 for the production of  $\text{PF}_5$ , using hexafluorophosphoric acid ( $\text{HPF}_6$ ) and a complexing agent pyridine, as starting materials. This process produces uncontaminated  $\text{PF}_5$  gas which is used as a precursor to the synthesis of  $\text{LiPF}_6$ . Currently NECSA is investigating alternative complexing agents due to the toxic nature of pyridine. Additionally, the extraction and treatment of the waste material (pyridine, ethanol, water and nitrogen) from the patented process requires investigation. It is important to recycle these components to prevent wastage of materials that could potentially be useful thereby reducing the consumption of fresh raw materials, energy usage and cost.

The aim of this study was the design and economic evaluation of a separation scheme to recover pyridine, ethanol and nitrogen with high recovery rates and final mole purities such that they can be recycled and reused in the  $\text{PF}_5$  production process. The objectives of this study were to:

- Study phase equilibrium data for the binary (ethanol/pyridine, water/pyridine and ethanol/water) and ternary (ethanol/water/pyridine) combinations of interest in order to determine the optimal thermodynamic model and parameters to theoretically design the process required.



- Investigate typical separation methods for the components of interest to gain an understanding on the current processes used and to determine whether a cheaper and more efficient alternative can be found.
- Propose a separation scheme to recover and recycle pyridine, ethanol and nitrogen with high recovery rates and final mole purities such that they can be recycled and reused in the  $\text{PF}_5$  production process.

Process simulation tools are able to represent (based on the information and thermodynamic models inherent in the package) the behaviour of a chemical process and are very useful to determine the validity of the design from an energetic and economic point of view. The Aspen Plus® process simulator was used to design the proposed separation schemes. The design and development of separation processes rely on accurate vapour liquid equilibrium (VLE) data. Therefore, the first step in this study was to perform VLE experiments to acquire the binary ethanol/pyridine and water/pyridine phase data since the VLE data found in literature for these systems were inconsistent. A modified recirculating VLE still was used to measure the phase equilibrium data with sample analysis performed using a Shimadzu GC-2014. The isothermal and isobaric binary VLE data measurements were undertaken for pyridine + ethanol at 313.15 K; 100 kPa and 40 kPa respectively. The isothermal and isobaric VLE data measurements for pyridine + water was performed at 333.15 K and 40 kPa respectively. The measured data was regressed on Aspen Plus® using various thermodynamic models to obtain the binary parameters required for process design. With the use of these parameters, two process schemes were designed and a sensitivity analysis performed in order to obtain the optimal solution. There-after, an economic analysis was performed to compare the processes and determine its feasibility.

### 1.1 Project Background

The current industrial process for  $\text{LiPF}_6$  involves reacting  $\text{PF}_5$  and  $\text{LiF}$  (dry method) in the presence of anhydrous hydrofluoric acid (Nakajima and Groult, 2011). The  $\text{PF}_5$  gas normally used in this reaction is produced from fluorine gas, which is contaminated with impurities such as  $\text{N}_2$ ,  $\text{SF}_4$ ,  $\text{COF}_2$  and  $\text{HF}$ . Contamination with  $\text{HF}$  results in the corrosion of the battery components and consequently distillation is required to purify the  $\text{PF}_5$  gas. However, distillation is an additional and expensive step in the process (Lekgoathi, et al., 2015). The production process as proposed by NECSA differs from the current method in that it involves cationic exchange and emanates from the idea of Willmann, et al. (1999) where it is believed that the direct synthesis of  $\text{LiPF}_6$  is possible when the hydrogen ion in the pyridinium hexafluorophosphate ( $\text{C}_5\text{H}_5\text{NHPF}_6$ ) is exchanged with the lithium ion, forming  $\text{C}_5\text{H}_5\text{NLiPF}_6$ . According to Lekgoathi, et al. (2015), this direct route for  $\text{LiPF}_6$  synthesis is not viable since the  $\text{C}_5\text{H}_5\text{NLiPF}_6$  compound is stable, hence the separation of  $\text{LiPF}_6$  from pyridine is not possible. However, the same technique used to synthesise

the LiPF<sub>6</sub>–pyridine complex can be utilised to synthesise the less electronegative alkali metal hexafluorophosphate NaPF<sub>6</sub>. This compound forms less stable complexes than the LiPF<sub>6</sub>–pyridine complex and can therefore be used as a PF<sub>5</sub> generator by thermal decomposition as shown in equation 1.1.



This process is illustrated in Figure 1.1. The PF<sub>5</sub> gas produced is used as a precursor to the synthesis of LiPF<sub>6</sub>. The stream compositions and conditions are presented in Table 1.1. The waste streams that require purification and recycling from Figure 1.1 are streams 5 (pyridine to pervaporation), 12 (liquid to pervaporation system) and 25 (wet N<sub>2</sub> to gas membranes). These streams are highlighted in red in Figure 1.1 and highlighted in bold in Table 1.1.

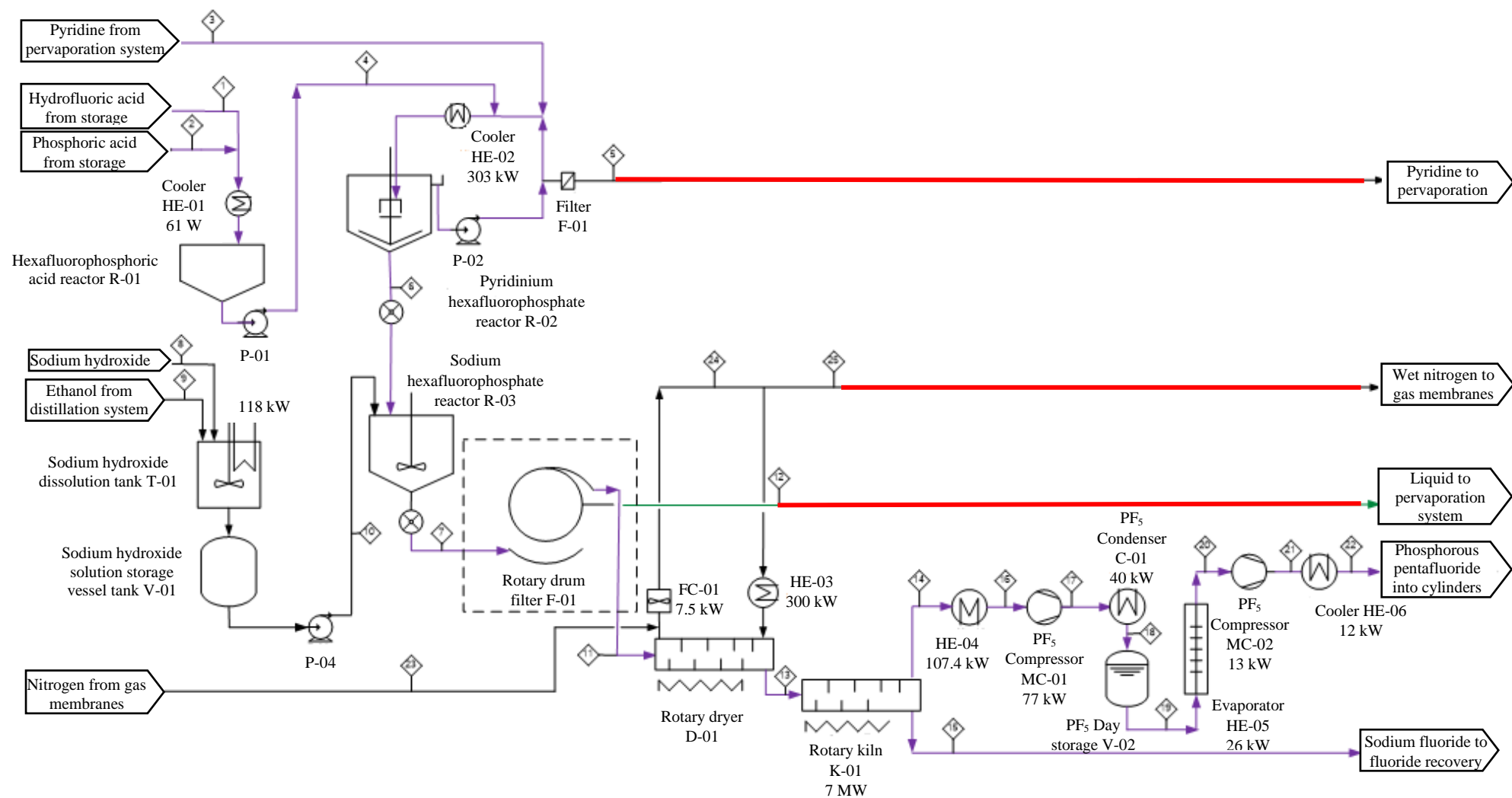


Figure 1.1: PF<sub>5</sub> production process (NECSA, 2017)

Table 1.1: Stream results for the PF<sub>5</sub> production process proposed by NECSA

Stream Number			1	2	3	4	5	6	7	8	9	10
Component	Phase	Unit										
Hydrofluoric acid	L	kg/hr	1190.8									
Phosphoric acid	L	kg/hr		972.2								
Hexafluorophosphoric acid	L	kg/hr				1666.7						
Water	L	kg/hr		171.6	2.7	171.6	<b>886.0</b>	296.0	474.6			
Water	V	kg/hr										
Pyridine	L	kg/hr			1832.9		<b>785.7</b>	262.2	1047.2			
Pyridine	V	kg/hr										
Pyridinium hexafluorophosphate	S	kg/hr						2233.0				
Sodium hydroxide	S	kg/hr								397.0		397.0
Ethanol	L	kg/hr			38.8		<b>16.3</b>	5.4	19414.6		19420.0	19420.0
Ethanol	V	kg/hr										
Sodium hexafluorophosphate	S	kg/hr							1666.7			
Sodium fluoride	S	kg/hr										
Phosphorus pentafluoride	G	kg/hr										
Phosphorus pentafluoride	L	kg/hr										
Nitrogen	G	kg/hr										
Total		kg/hr	1191	1144	1874	1838	<b>1688</b>	2797	22603	397	19420	19817
Temperature		K	298.15	298.15	298.15	303.15	<b>303.15</b>	303.15	298.15	298.15	298.15	298.15
Pressure		kPa	100	100	100	100	<b>100</b>	100	100	100	100	100

Stream Number			11	12	13	14	15	16	17	18	19	20
Component	Phase	Unit										
Hydrofluoric acid	L	kg/hr										
Phosphoric acid	L	kg/hr										
Hexafluorophosphoric acid	L	kg/hr										
Water	L	kg/hr	8.4	<b>467.1</b>								
Water	V	kg/hr										
Pyridine	L	kg/hr	15.9	<b>1030.5</b>								
Pyridine	V	kg/hr										
Pyridinium hexafluorophosphate	S	kg/hr										
Sodium hydroxide	S	kg/hr										
Ethanol	L	kg/hr	309.1	<b>19110.9</b>								
Ethanol	V	kg/hr										
Sodium hexafluorophosphate	S	kg/hr	1667.0		1667.0							
Sodium fluoride	S	kg/hr					575.6					
Phosphorus pentafluoride	G	kg/hr				1250.0		1250.0	1250.0			1250.0
Phosphorus pentafluoride	L	kg/hr								1250.0	1250.0	
Nitrogen	G	kg/hr										
Total		kg/hr	2000	<b>20609</b>	1667	1250	576	1250	1250	1250	1250	1250
Temperature		K	298.15	<b>298.15</b>	311.15	673.15	673.15	303.15	313.15	253.15	253.15	278.15
Pressure		kPa	100	<b>100</b>	100	100	100	100	2000	2000	2000	2000

Stream Number			21	22	23	24	25
Component	Phase	Unit					
Hydrofluoric acid	L	kg/hr					
Phosphoric acid	L	kg/hr					
Hexafluorophosphoric acid	L	kg/hr					
Water	L	kg/hr					
Water	V	kg/hr			0.6		<b>7.6</b>
Pyridine	L	kg/hr					
Pyridine	V	kg/hr					<b>16.7</b>
Pyridinium hexafluorophosphate	S	kg/hr					
Sodium hydroxide	S	kg/hr					
Ethanol	L	kg/hr					
Ethanol	V	kg/hr					<b>309.1</b>
Sodium hexafluorophosphate	S	kg/hr					
Sodium fluoride	S	kg/hr					
Phosphorus pentafluoride	G	kg/hr	1250.0	1250.0			
Phosphorus pentafluoride	L	kg/hr					
Nitrogen	G	kg/hr			9524.0	9804.0	<b>9524.0</b>
Total		kg/hr	1250	1250	9525	9804	<b>9857</b>
Temperature		K	313.15	303.15	298.15	313.15	<b>313.15</b>
Pressure		kPa	2860	2860	100	100	<b>100</b>

Figure 1.2 presents the process scheme proposed by NECSA to treat waste streams 5, 12 and 25. It is important to note that this separation scheme has not been designed but merely suggested. Figure 1.2 comprises the following process streams:

Stream 5: Pyridine from Reactor R-02

Stream 12: Liquid from Rotary Filter

Stream 23: Nitrogen gas to dryer D-01

Stream 25: Nitrogen Gas from Rotary Drum D-01

Stream 27: Liquid from Condenser C-03

Stream 28: Feed to Gas Membrane System GM-101

Stream 29: Vapour from Gas Membrane System GM-101 (Ethanol + Pyridine)

Stream 30: Vapour from Gas Membrane System GM-101 (Nitrogen + Water)

Stream 31: Nitrogen gas to atmosphere

Stream 32: Liquid from Pervaporation Feed Tank T-09

Stream 34: Vapour from Pervaporation System PV-101

Stream 36: Feed to Distillation System DC-101

Stream 37: Feed to Ethanol Storage Tank T-12

Stream 38: Feed to Pyridine Storage Tank T-13

Stream 25 (comprising nitrogen, ethanol, water and pyridine) is first fed to a compressor (MC-03) to set the required temperature and pressure and there-after to a condenser (C-03) to separate some of the ethanol, water and pyridine from nitrogen. Stream 28 from C-03 is then fed to a gas permeation unit (GM-01) where only nitrogen and water leave in the permeate (stream 30). This stream is sent to a temperature swing absorption dryer (AD-01) to remove the water from nitrogen. Make-up nitrogen gas is then mixed with stream 23 from AD-01 and sent for use in the PF<sub>5</sub> production process. Streams 5, 12 and 27 (comprising ethanol, water and pyridine) are mixed and sent to a pervaporation unit (PV-01) to remove the water from the mixture. Stream 34 from PV-01 is then mixed with stream 29 from GM-01 and sent to a distillation column (DC-01) where ethanol is obtained in stream 37 and pyridine achieved in stream 38. These streams are then sent for use in the PF<sub>5</sub> production process.

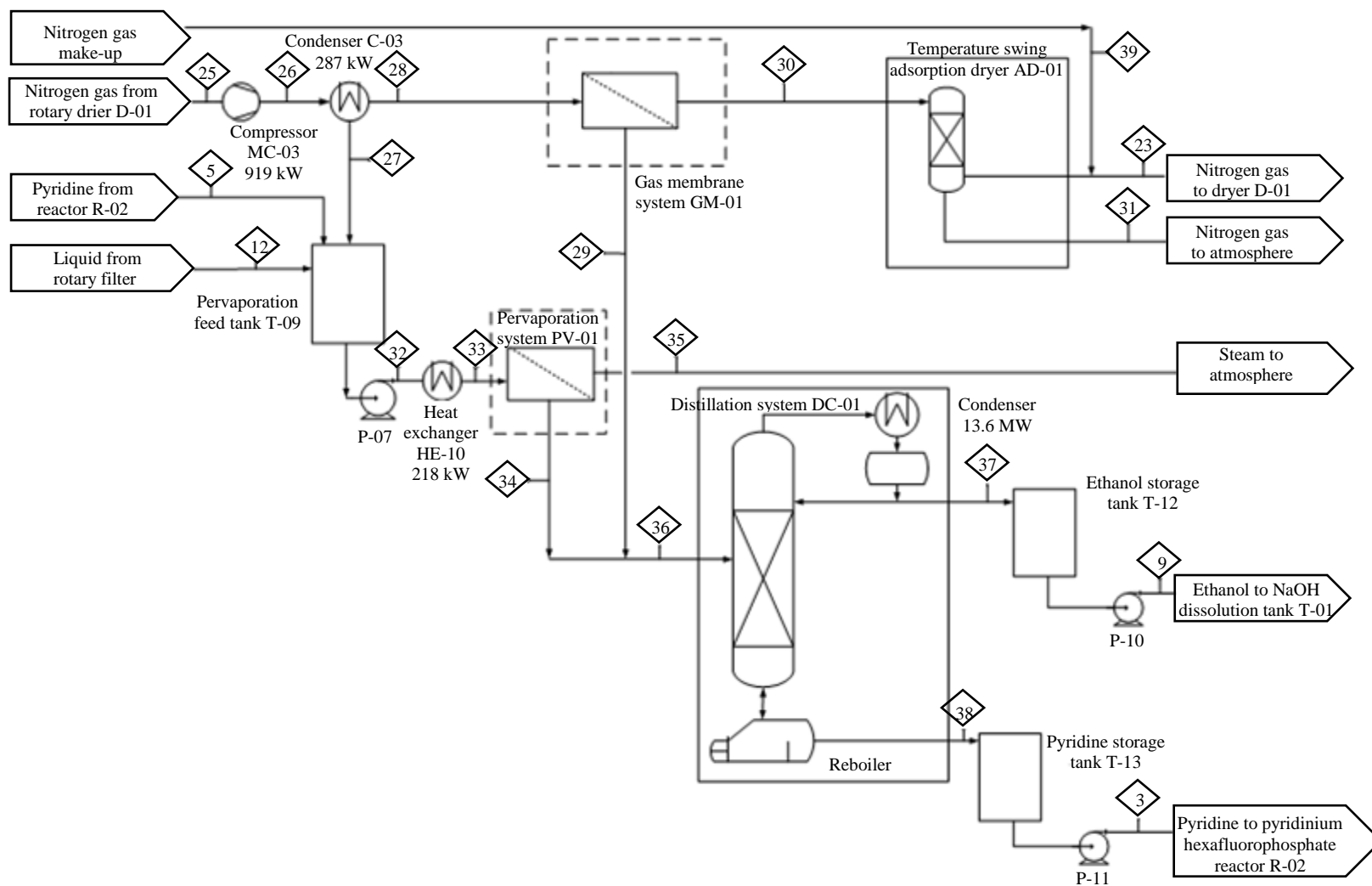


Figure 1.2: Waste treatment process (NECSA, 2017)



Table 1.2 presents the stream composition and conditions for the waste treatment process proposed by NECSA. This process was not designed but merely suggested. The values presented in the table comprise predominantly of assumptions and estimations.

Table 1.2: Stream results for the waste treatment process proposed by NECSA

Stream Number			26	27	28	29	30	31	32	33	34	35
Component	Phase	Unit										
Water	L	kg/hr		6.0					1359.1			
Water	V	kg/hr	7.6		1.5		1.5	0.9		1359.1	2.7	1356.4
Pyridine	L	kg/hr		10.2					1826.5			
Pyridine	V	kg/hr	16.7		6.5	6.5				1826.5	1826.5	
Ethanol	L	kg/hr		298.9					19409.8			
Ethanol	V	kg/hr	309.1		10.2	10.2				19409.8	19409.8	
Sodium fluoride	S	kg/hr										
Nitrogen	G	kg/hr	9524.0		9524.0		9524.0	476.2				
Total		kg/hr	9857	315	9542	17	9526	477	22595	22595	21239	1356
Temperature		K	353.15	280.15	280.15	293.15	293.15	343.15	298.15	393.15	373.15	303.15
Pressure		kPa	4000	4000	4000	4000	600	100	100	100	100	500

Stream Number			36	37	38	39
Component	Phase	Unit				
Water	L	kg/hr		0	2.7	
Water	V	kg/hr	2.7			
Pyridine	L	kg/hr			1832.9	
Pyridine	V	kg/hr	1832.9			
Ethanol	L	kg/hr		19381.2	38.9	
Ethanol	V	kg/hr	19420.0			
Sodium fluoride	S	kg/hr				
Nitrogen	G	kg/hr				476.2
Total		kg/hr	21256	19381	1875	476
Temperature		K	303.15	351.15	373.15	298.15
Pressure		kPa	100	100	100	100

In this study, it was intended to preliminary design NECSA's proposal presented in Figure 1.2 however, this could not be done. In order to design a membrane, experimental permeation flux data for the system of components needs to be available. After extensive research, no data for both the nitrogen/ethanol/water/pyridine system (fed to the gas permeation unit) and the ethanol/water/pyridine system (fed to the pervaporation unit) were found in literature; hence the membrane design presented in Figure 1.2 could not be performed.

Furthermore, physically measuring the permeation flux data was not in the scope of this project since the focus of the thermodynamics research group is phase equilibrium measurements and simulation design; hence the equipment required for measurements were not available. Therefore, alternative separation schemes for the waste treatment process were developed and designed in this work.

## **1.2 Thesis Outline**

The thesis has been compiled in 8 chapters. Chapter 1 provides a brief background to the process and presents the aims and objectives. Chapter 2 describes the separation technologies available and the phase behaviour of the systems studied. Chapter 3 presents a brief review of the thermodynamic principles for low pressure VLE data correlation and analysis. Chapter 4 focuses on the description of the low pressure VLE recirculating still and the experimental procedure followed in this study. Chapter 5 presents and analyses the experimental results via a comparison to literature data, predicted data and modelled data. Chapter 6 describes the process design and costing for both processes. The conclusion is presented in chapter 7 followed by the recommendations in chapter 8.

## CHAPTER 2: THEORETICAL BACKGROUND

This chapter describes the separation technologies available and the phase behaviour of the systems studied. A mixture of four components (nitrogen, ethanol, water and pyridine) required separation and recovery. Nitrogen can be easily removed with the use of a flash vessel, condenser, etc. A typical separation method for the ethanol (1) + water (2) + pyridine (3) system is distillation. However, there exist two homogenous binary azeotropes in this mixture, one between ethanol and water and the other between water and pyridine. Azeotropic mixtures cannot be easily separated by conventional distillation and hence require enhanced separation techniques. Some of the separation methods available in literature to break the ethanol/water azeotrope include:

- Heterogeneous azeotropic distillation: utilises a solvent with an intermediate boiling point, such as cyclohexane, to form new azeotropes in the mixture, generating two liquid phases allowing the separation of ethanol from water. Although this process is widely used, it has poor stability and a high energy consumption (Bastidas, et al., 2010).
- Adsorption on molecular sieves: operates on the difference in molecular size of components to be separated, defined types of chemical species are retained on its surface. Water molecules are adsorbed in a selective way allowing ethanol separation (Bastidas, et al., 2010). However, the net flow rate of the anhydrous ethanol produced is lower than that achieved in the distillation-based operations and the total energy consumption is increased due to the high ethanol recycle required and energy necessary for the regeneration cycle (Bastidas, et al., 2010).
- Extractive distillation: utilises a solvent with a high boiling point, such as ethylene glycol, to alter the relative volatility, allowing the separation of components. A second column is required to recover and recycle the solvent. When compared to azeotropic distillation and adsorption on molecular sieves, it has a lower energy consumption and capital cost (Bastidas, et al., 2010).
- Pervaporation: “Mixtures are separated on the basis of physical or chemical attributes, such as molecular size, charge, or solubility” (Kujawski, 2000). Pervaporation transport is driven by a pressure gradient across the membrane, and therefore operates independently from the vapour liquid equilibrium, avoiding the issue of the ethanol/water azeotrope. The addition of a third component is not required thereby reducing the energy consumption and operating costs associated with solvent recovery. However, this process produces a low flux and has a high membrane replacement cost (Kujawski, 2000).

The separation methods available in literature to break the water/pyridine azeotrope include:

- Liquid-liquid extraction: “compounds are separated based on their relative solubilities in two immiscible liquids” (Kumar, et al., 2010). An organic solvent is introduced into the mixture, separating the organic phase and aqueous phase. Pyridine is transferred from the aqueous phase to the organic phase. The aqueous phase and organic phase are then separated, thereafter pyridine is separated from the organic phase. The organic solvent is then recovered and recycled (Kumar, et al., 2010). Organic solvents generally employed to break the water/pyridine azeotrope include benzene, methylene chloride, chloroform, xylene, nitrobenzene, caustic soda (Crew & Schafer, 1993), environmentally non-hazardous alkyl acetate and pressurised carbon dioxide (Kumar, et al., 2010).
- Azeotropic distillation: a typical solvent used for the water/pyridine azeotrope is toluene (Wu & Chien, 2009). Benzene is also commonly used as a solvent for this system. However, benzene is a hazardous component associated with high costs (Kumar, et al., 2011).
- Extractive distillation: typical examples of effective agents are: isophorone, sulfolane and a caustic solution (Kumar, et al., 2011).
- Pervaporation: a hydrophilic cross-linked poly (vinyl alcohol) membrane withdraws the water from the organic stream by attracting the polar water molecules in the solution (Cheng, et al., 2010). Further examples include a polyethylene membrane to extract the pyridine and a cellophane membrane to extract the water (Kujawski, 2000).

Hybrid systems (pervaporation, extraction, etc. in combination with distillation) have also been employed and show promising results, in some cases: reduces costs, energy requirements and loss of chemical.

## 2.1 Phase Equilibrium Data Available in Literature

The design and development of separation processes rely on accurate vapour liquid equilibrium (VLE) data. Therefore, the phase equilibrium data available in literature (NIST, DDB, internet searches) up until the year 2014 for the systems of interest were collected and comprise the following:

- 3 isothermal P-x data sets exist for the ethanol (1) + pyridine (3) system from 2 sources:
  - At temperatures between 338.15 K and 348.15 K and pressures between 18.2 kPa and 88.7 kPa (Findlay & Copp, 1969)

- At a temperature of 313.15 K and pressures between 6.04 and 17.90 (Warycha, 1977)
- 23 Isothermal P-x-y, isothermal P-x and isobaric T-x-y data sets exist for the water (2) + pyridine (3) system from 13 sources:
  - At a temperature of 353.17 K and pressures between 31.85 kPa and 58.80 kPa (Zawidzki, 1900)
  - At temperatures between 303.13 K and 323.13 K and pressures between 3.60 kPa and 59.11 kPa (Ibl, et al., 1954) & (Ibl, et al., 1956)
  - At a temperature of 342.97 K and pressures between 22.02 kPa and 38.84 kPa (Andon, et al., 1957)
  - At temperatures between 300.19 K and 339.37 K and pressures between 11.93 kPa and 60.81 kPa (Woycicka & Kurtyka, 1965)
  - At a temperature of 353.15 K and pressures between 32.23 kPa and 47.73 kPa (Gierycz, 1996)
  - At temperatures between 293.14 K and 303.13 K and pressures between 2.23 kPa and 5.25 kPa (Ewert, 1936)
  - At temperatures between 298.15 K and 318.15 K and pressures between 2.80 kPa and 12.0 kPa (Abe, et al., 1978)
  - At pressures between 15.9 kPa and 101 kPa and temperatures between 322.53 K and 388.43 kPa (Fowler, 1952).
  - At a pressure of 101 kPa and temperatures between 367.52 K and 384.03 kPa (Vriens & Medcalf, 1953)
  - At a pressure of 101.325 kPa and temperatures between 367.62 K and 377.12 kPa (Prausnitz & Targovnik, 1958)
  - At a pressure of 101.3 kPa and temperatures between 367.9 K and 384.3 kPa (Dharmendra Kumar & Rajendran, 1998)
  - At a pressure of 94 kPa and temperatures between 366.05 K and 385.75 kPa (Abu Al-Rub & Datta, 2001)
- Isobaric VLE, SLE and isothermal VLE data for the ethanol (1) + water (2) system are well documented in hundreds of literature sources. Listed are a few: (Pickering, 1893), (Beebe, et al., 1942), (D'Avila & Silva, 1970).
- An extensive search through the open literature showed that no ternary phase equilibria exist for the system ethanol (1) + water (2) + pyridine (3).

Figure 2.1 presents graphical representations of the ethanol (1) + pyridine (3) data found in literature. It can be seen that the literature data is fairly consistent however, there is no vapour composition data available for this system.

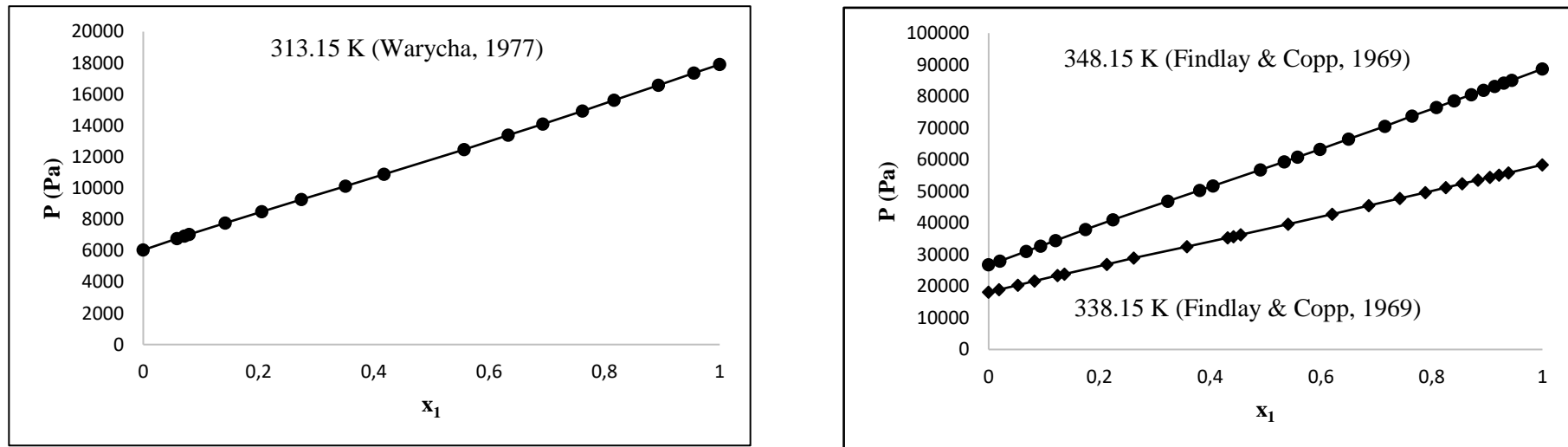


Figure 2.1: Literature data available for ethanol (1) + pyridine (3) system

Figure 2.2 presents graphical representations of the water (2) + pyridine (3) data found in literature. It can be seen that the literature data is inconsistent and would not produce accurate results if used for distillation column design.

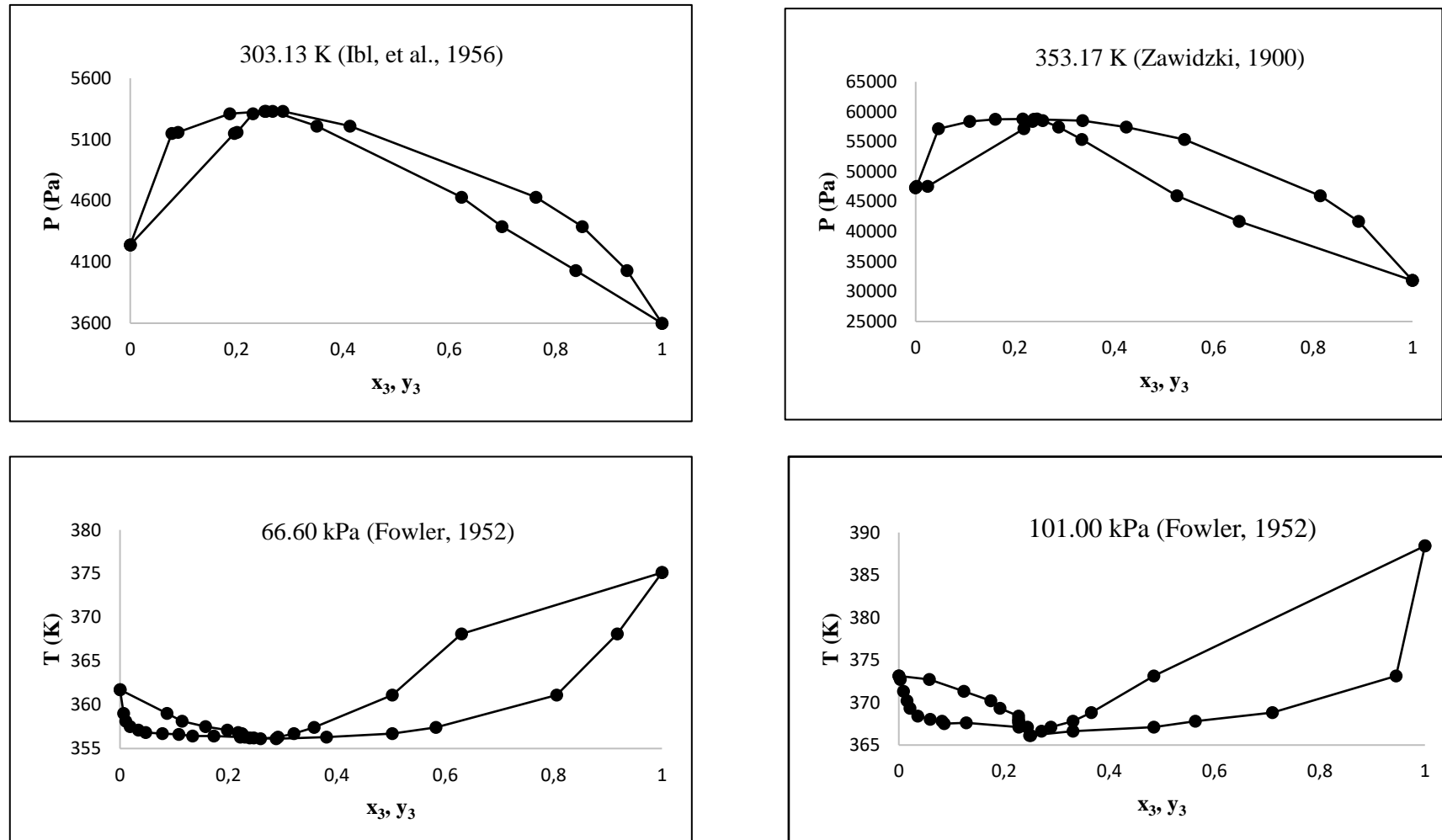


Figure 2.2: Some of the literature data available for the water (2) + pyridine (3) system



## 2.2 Residue Curve Map

A residue curve map (RCM) describes the equilibrium relationships for a ternary mixture. Each curve represents the liquid residue composition with time obtained from a one stage batch distillation. The process designed in this study is continuous (the RCM can also be used to illustrate continuous distillation). Residue curves are used to test the feasibility of separation schemes and therefore are a valuable tool in designing separation schemes for distillation processes. These diagrams are commonly used for studying ternary mixtures which cannot be easily separated by distillation due to azeotropic points.

An extensive literature review indicated that the Non-Random Two Liquid (NRTL) activity coefficient model was the appropriate thermodynamic model for the binary/ternary combinations studied. Hence, the RCM for the ethanol (1) + water (2) + pyridine (3) system was generated on Aspen Plus® using the NRTL activity coefficient model and is displayed in Figure 2.3. This Figure was generated at a series of pressures to study the phase behaviour at various conditions. The RCM presented in Figure 2.3 is at a pressure of 80 kPa. The remaining diagrams display a similar trend with slight differences in temperature and composition.

Table 2.1 presents the boiling points for the system ethanol (1) + water (2) + pyridine (3) with the azeotropic compositions included. In the RCM, the unstable node is referred to the point where all residue curves in a region originate and typically has the lowest boiling point; the stable node refers to the point where all residue curves terminate and has the highest boiling point in the region; lastly, the saddle is the point which residue curves move toward and then away from and consists of intermediate boiling components in the region (Seader, et al., 2011).

Table 2.1: Boiling points and azeotropic compositions for the system ethanol (1) + water (2) + pyridine (3) generated on Aspen Plus® at 80 kPa.

Temperature (K)	Classification	Mole Fraction		
		Ethanol	Water	Pyridine
345.58	Saddle	1	0	0
366.67	Stable Node	0	1	0
380.38	Stable Node	0	0	1
345.44	Unstable Node	0.9012	0.0988	0
360.57	Saddle	0	0.7443	0.2557

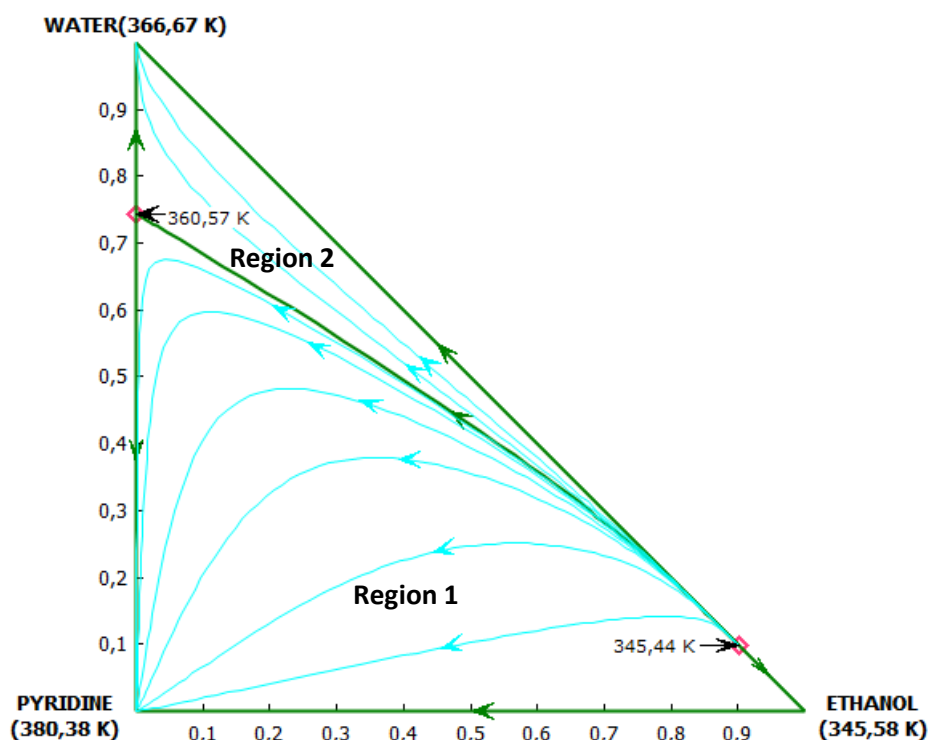


Figure 2.3: Residue curve map generated on Aspen Plus® using the NRTL activity coefficient model with azeotropes (mole fractions) at 80 kPa, (◇) indicates azeotropic compositions.

Each apex in Figure 2.3 represents the pure chemical component, labelled with the pure component boiling temperature at 80 kPa (ethanol: 345.58 K; water: 366.67 K; pyridine: 380.38 K). The RCM shows an arrow on each residue curve. The arrows point from a lower boiling point to a higher boiling point. All residue curves originate from the ethanol/water azeotrope (lowest boiling point, 345.44 K). One of the curves terminates at the other azeotrope (water/pyridine, which has a higher boiling point, 360.57 K) and is a special residue curve, called a distillation boundary (indicated by bold green line) because it divides the ternary diagram into two separate regions. This boundary cannot be crossed or is extremely difficult to cross thus; restricting the possible distillation products. All residue curves in region 1 terminate at the pyridine apex, which has the highest boiling point (380.38 K) for that region. All residue curves in region 2 terminate at the water apex, whose boiling point (366.67 K) is the highest for that region (Seader, et al., 2011).

From the RCM, it can be seen that if a mixture composition point lies in region 1, pure pyridine can be obtained by conventional distillation since the residue curves move toward and terminate at the pyridine apex. The output from the top of the distillation column will result at/near the ethanol/water azeotropic composition. Enhanced distillation processes are then required to break the ethanol/water azeotrope to separate these components.

If a mixture composition point lies in region 2, the process becomes more complex because the pyridine and ethanol apex lie on the other side of the distillation boundary hence the stream cannot be separated by conventional distillation into pure components. Instead the product streams will consist of an ethanol/water mixture at the top of the column and a water/pyridine mixture at the bottom of the column. Enhanced distillation processes will be required to break both azeotropes.

The RCM displayed in Figure 2.4 below includes the stream compositions of interest. Streams 5, 12, 27 and 29 are obtained from the process flow diagram developed by NECSA (Figure 1.2). Stream 36 is the mixed stream (a combination of streams 5, 12, 27 and 29).

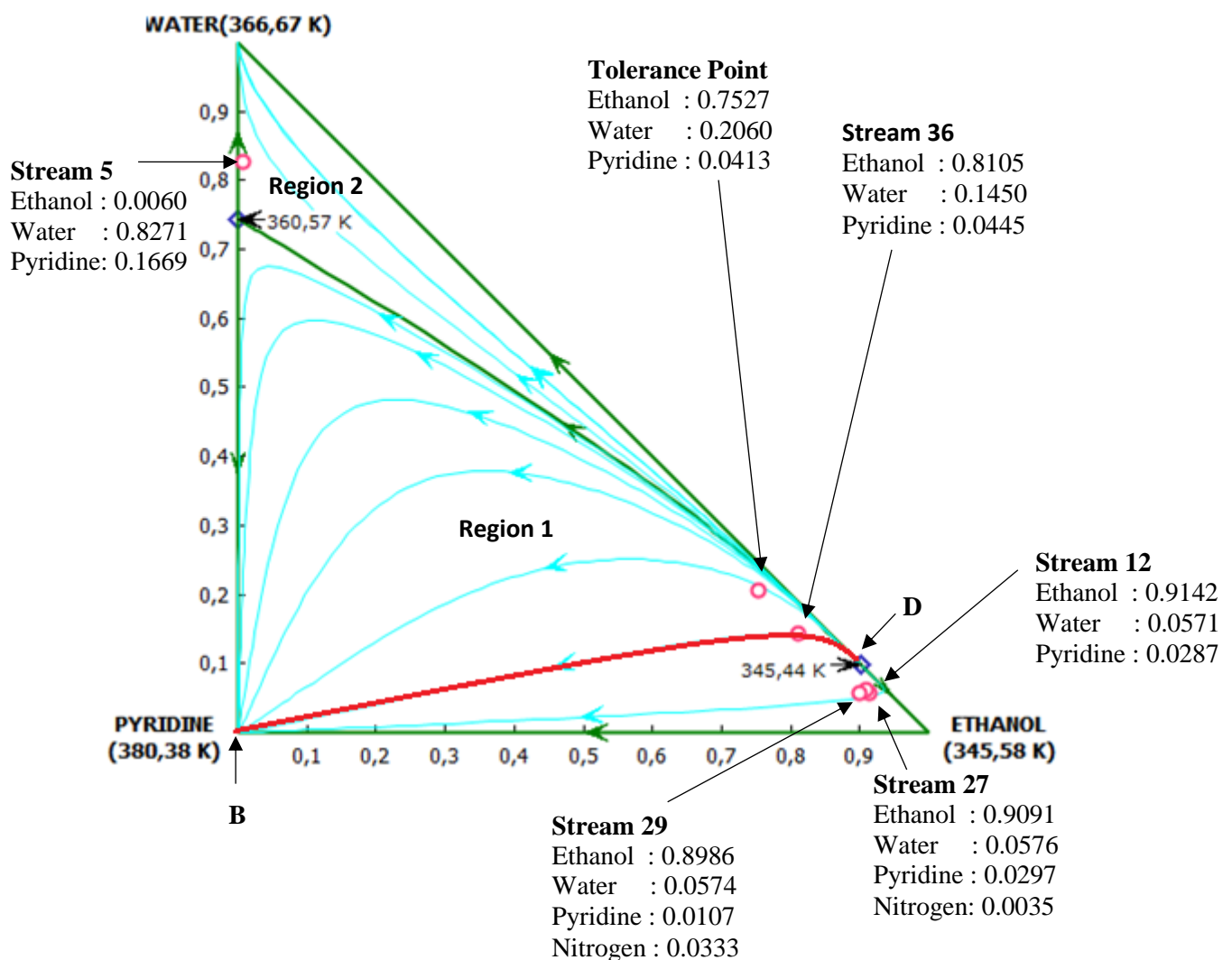


Figure 2.4: Residue curve map generated on Aspen Plus® using the NRTL activity coefficient model with stream compositions and azeotropes (mole fractions) at 80 kPa, (○) indicates stream compositions, (◇) indicates azeotropic compositions.

Since the objective of this project is to separate the waste stream into pure components: pyridine, ethanol and nitrogen, it is therefore necessary to ensure that the combined waste stream (streams 5, 12, 27 & 29 combined to stream 36) has a final composition which still lies in region 1 so that the separation scheme developed will be less complex, costly and energy intensive as opposed to the separation scheme required if the final composition lies in region 2. The tolerance point as shown in Figure 2.4 indicates the composition with the maximum allowable water concentration to remain in region 1 so as to obtain a high pyridine mole purity after distillation.

If more water is added to stream 36, its composition will be altered and its location on the diagram will move. This new location is called the tolerance point. It was found that a mass addition of 540 kg/hr of water to stream 36 will still enable good separation to meet the objectives. However, as the water content is increased above this composition, a high pyridine mole purity is still possible but the recovery decreases resulting in a loss of pyridine. This is not acceptable since the complexing agent is the most vital component in this study. If a larger amount of water is added to stream 36 such that it is shifted into region 2, the separation of pyridine via conventional methods is not possible due to the azeotrope it forms with water. Therefore, an enhanced distillation process such as extractive distillation, azeotropic distillation, pervaporation, etc. is required to obtain pure pyridine which would increase costs and complicate the design process.

From Figure 2.4, it can be seen that stream 36 does lie in region 1. Therefore, pure pyridine can be obtained by conventional distillation since the residue curves move toward and terminate at the pyridine apex (output from the bottom of the distillation column represented by point B). The output from the top of the distillation column will result at/near the ethanol/water azeotropic composition (point D). The ethanol/water mixture will then be separated using an enhanced separation technique. Extractive distillation and pervaporation were selected for further investigation since these are common and simple processes, less energy intensive than the alternatives and can handle the feed capacity. These processes are discussed in the sections which follow.

### **2.3 Extractive Distillation**

Extractive distillation utilises a solvent with a high boiling point to alter the relative volatility of the azeotropic mixture, thereby allowing the separation of components. A second column is required to recover and recycle the solvent. It is essential that the most suitable solvent (one which minimises the solvent to feed ratio and liquid load) is selected to economically design the extractive distillation column. The four kinds of solvents used for distillation include solid salt, liquid solvent, the combination of liquid and solid salt, ionic liquid (Lie, et al., 2003).

The advantages of using the solid salt includes good separation ability and low energy consumption due to the lower solvent to feed ratio required (Gil, et al., 2008). However, problems are encountered with the dissolution reuse and transport of salt when used in industrial operation (Lie, et al., 2003). With ionic liquids, insufficient knowledge exists on the optimal properties and their implementation in real process systems (Gutierrez H, 2013). The combination of a salt and liquid solvent allows utilising the advantages of both components such as good separation ability (solid salt) and easy solvent (liquid solvent). Furthermore, the combination produces a greater effect on the relative volatility of the ethanol/water system and the quantity of the solvent to recycle is reduced thereby lowering energy consumption (Gil, et al., 2008). However, solvent may be entrained along with the product and many salts are corrosive to the equipment and tend to decompose at high temperatures (Lie, et al., 2003). The liquid solvent is the most common operation used with the most effective solvents being ethylene glycol and glycerol. Glycerol has a higher selectivity, higher heat of vaporisation, and higher boiling point hence it is able to achieve a high purity product more effectively than ethylene glycol under the same operating conditions, but requires a higher energy consumption and produces higher temperatures at the reboiler which may lead to thermal degradation of the mixture (Gil, et al., 2014). Ethylene glycol was selected as the solvent for further investigation since it is a common and simple process, is less energy intensive than its alternative liquid solvents and ionic liquids and contains no unwanted entrainment (solid salt) into the product or equipment. For the column design and optimisation, simulation results are presented in chapter 6.

## **2.4 Pervaporation**

“Pervaporation involves the separation of liquid mixtures by partial vaporization through a dense non-porous membrane” (Kujawski, 2000). Pervaporation operates independently from the vapour liquid equilibrium, avoiding the issue of the ethanol/water azeotrope. Hence, the addition of a third component is not required thereby reducing the energy consumption and operating costs associated with solvent recovery (Kujawski, 2000). Figure 2.5 presents a schematic representation of a pervaporation unit. A liquid mixture is fed into one side of the membrane. Transportation of the mixture is driven by a pressure gradient across the membrane. The permeate undergoes a phase change and is removed as a vapour while the retentate retains its liquid form. The pressure gradient involves the difference in partial pressure between the liquid feed solution and the permeate vapour (Xu, 2001). The feed mixture is usually at atmospheric pressure, therefore in order to generate a good driving force, a vacuum is drawn on the permeate side and hence requires condensing before recycling or reuse of components.

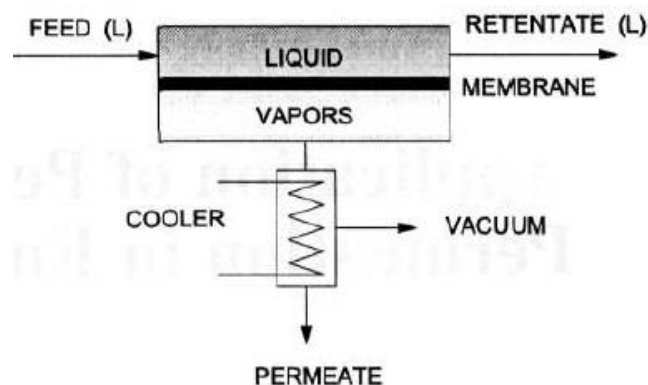


Figure 2.5: Schematic of the pervaporation process (Kujawski, 2000)

### 2.4.1 Selection of Membrane (Pervaporation) Material

The membrane selected depends on the type of application: the components involved and which of those components is required to be separated from the mixture. For the removal of water from organic liquids (ethanol), hydrophilic polymers have to be chosen. Some examples include ionic polymers, polyvinylalcohol (PVA), polyacrylonitrile (PAN) and polyvinylpyrrolidone (PVPD) (Kujawski, 2000). Materials such as silica and zeolite can also be used and may be more effective. In order to design a membrane, the permeation flux must be known, which is obtained from graphs generated from experimentally determined feed and permeate composition data. Physically measuring this data was not in the scope of this project, hence the permeation flux for the ethanol/water system had to be obtained from literature. An extensive search through the open literature showed that the only data available was one which used a PVA membrane (Wijmans & Baker, 1993). Hence the PVA membrane was selected to separate the ethanol/water mixture. There are numerous membrane processes developed with various materials for the ethanol/water system however the permeation flux data is proprietary hence could not be accessed.

The separation scheme specified by NECSA in Figure 1.2 proposed that the waste streams (5, 12 and 27) containing ethanol, water and pyridine be fed into the membrane, where water is removed followed by separation of ethanol and pyridine via conventional distillation. However, this task could not be performed since there exists no permeation flux data for the combination of chemicals (ethanol + pyridine with water) in literature.

### 2.4.2 Membrane Design

In this work, the membrane was designed following the procedure by Wijmans & Baker (1993). The performance of the pervaporation system was calculated using equation (2.1). This required the normalized permeation fluxes ( $J_i$ ) of the membrane and the operating conditions of the

pervaporation process, such as, the feed composition ( $c_i$ ), the feed temperature and the permeate pressure ( $p_i''$ ) to be known.

$$Q_i = J_i (c_i' \gamma_i' p_i^o - p_i'') \quad (2.1)$$

The normalized permeation fluxes were read from graphs of feed and permeate composition data which was determined experimentally. The activity coefficients ( $\gamma_i$ ) were calculated using the Van Laar equations, and the saturated vapour pressure ( $p_i^o$ ) calculated from the Antoine equation. The correlations (shown in Appendix A) were then manipulated to calculate the remaining unknown parameters such as the total permeation flux ( $Q$ ), the partial permeate pressure ( $p_i''$ ) and the partial permeate fluxes ( $Q_i$ ). Once these variables were known, the separation of components could be evaluated for one fixed feed composition. However, it is important to note that the composition of the feed changes if a substantial fraction of the liquid was permeated. Hence, the total membrane area was divided into  $N$  differential elements and the new parameters calculated for each sector as shown in Figure 2.6. A detailed explanation of this procedure is shown in Appendix A.

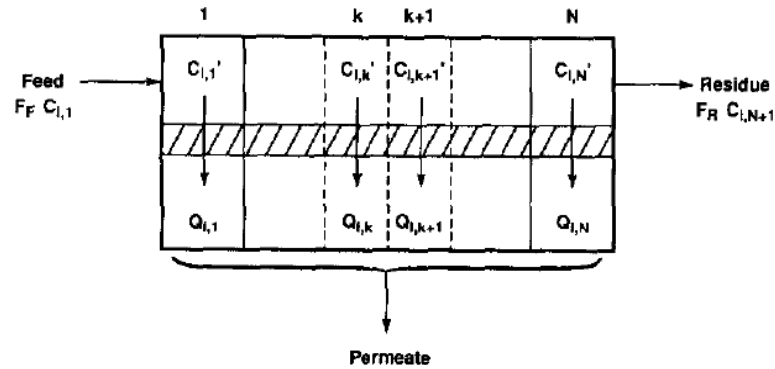


Figure 2.6: Differential elements in pervaporation system under cross flow condition (Wijmans & Baker, 1993)

### 2.4.3 Selection of Membrane (Pervaporation) Module

The membrane area required in industrial operation is in the range of hundreds to thousands square meters. There is therefore a need to economically and efficiently package these large areas into membrane modules (Matteo, 2015). The common module designs include flat configurations such as plate and frame and spiral wound or tubular configurations such as hollow fibre modules (Xu, 2001). The plate and frame modules were the first industrial membrane modules used for pervaporation (Schiffmann, 2014). “Stainless steel plates form the feed channels and compartments which are sealed to the membranes by gaskets. Stainless steel perforated plates and spaces form the permeate channels” (Kujawski, 2000). This module has a low packing density, low efficiency, high pressure drop and a higher cost than its alternatives (Xu, 2001). In the hollow

fibre module, fibres are combined in bundles and sealed at the ends with impermeable material. Feed flows through the fibres and the permeate is removed from the shell. This module has irreversible fouling, easy breakage due to high flexibility of fibres, high temperature drop and increased installation costs (Schiffmann, 2014). Figure 2.7 presents a schematic of the spiral wound module. Membrane envelopes are wound around a perforated central collection tube which is placed inside a tubular pressure vessel. This design is the simplest and most widely used, as it allows for easy cleaning, has a high packing density and is inexpensive. The major problem with this design is the high pressure drop (Xu, 2001). The spiral wound module was selected for further investigation since it is simpler and less expensive than its alternatives.

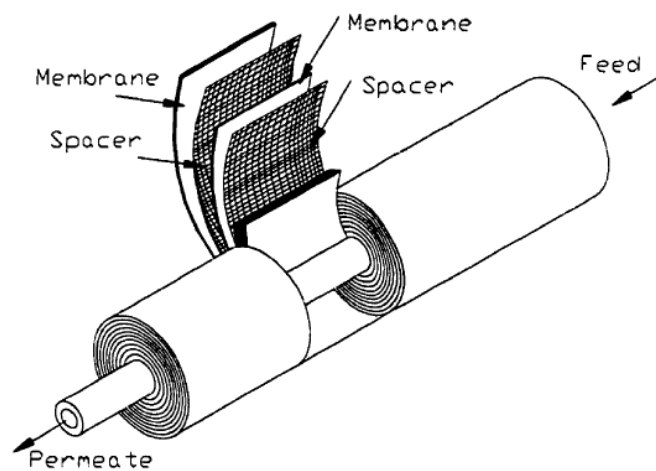


Figure 2.7: Spiral wound module (Xu, 2001)

Figure 2.8 illustrates an example of the module configuration expected. The number of modules in series and parallel depend on the capacity of the flow rate and the membrane and module specifications selected. The total flow rate would be divided by the number of parallel modules and fed in equal amounts to each parallel arrangement as shown in the Figure. The retentate exiting each module becomes the feed to the next module, this is represented by the black lines in the diagram. The permeate exits the bottom of each module and accumulates to a single stream, this is represented by the red lines in the diagram.



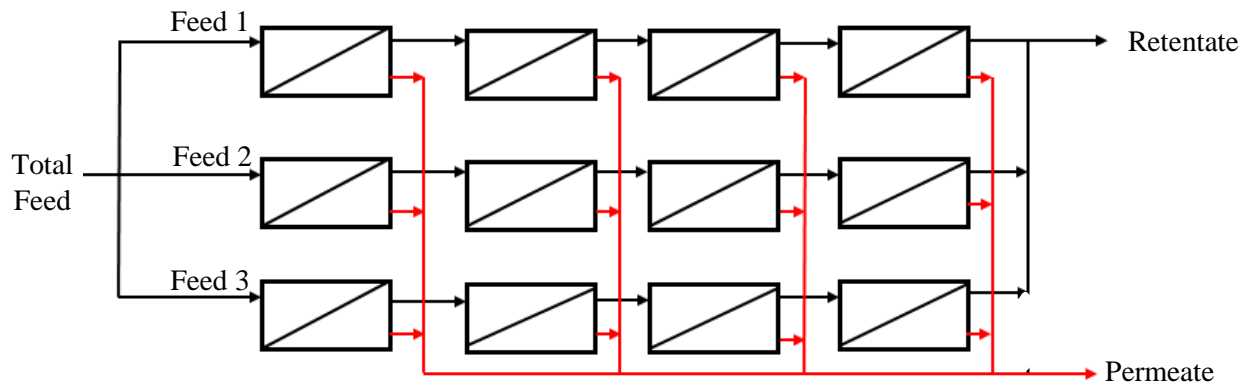


Figure 2.8: Membrane network configuration

Another element of the membrane design are the inter-stage heat exchangers. In a pervaporation process, the latent heat of evaporation of the permeate is drawn from the sensible heat of the feed liquid. Thus, the feed liquid is cooled as it passes through the module. However, a decrease in temperature decreases the driving force and hence slows the separation. Therefore, reheating of the liquid is required and is achieved by placing heat exchangers between modules in a series arrangement (Schiffmann, 2014). A detailed explanation of this procedure is shown in Appendix B.3.

## CHAPTER 3: THEORETICAL MODELLING

The aim of data modelling is to select a thermodynamic model that accurately represents the measured VLE data and is able to extrapolate to conditions beyond the measurement conditions. Such modelling is necessary for the process design and optimisation. This chapter presents a brief review of the thermodynamic principles for low pressure VLE data correlation and analysis.

### 3.1 Analysis of VLE Data

Phase equilibria data can be described from the understanding of a basic principle which becomes valid only when the phases are at equilibrium. This principle is represented by equation 3.1 for a vapour–liquid system.

$$\hat{f}_i^l(T, P, x_i) = \hat{f}_i^v(T, P, y_i) \quad (3.1)$$

The symbols  $\hat{f}_i^l$  and  $\hat{f}_i^v$  represent the fugacities of the liquid and vapour phases, respectively. The fugacities are related to temperature, pressure and composition via the use of the activity coefficient ( $\gamma$ ) and the fugacity coefficient ( $\Phi$ ). This resulted in the development of the following analytical methods to describe the phase equilibria data: the combined method ( $\gamma$ – $\Phi$ ), the direct ( $\Phi$ – $\Phi$ ) method and the modern direct method.

The combined method uses both the activity coefficient and the fugacity coefficient to describe the non-idealities of the liquid and vapour phases respectively according to the following correlation:

$$\hat{f}_i^l = x_i \gamma_i f_i^o = \hat{f}_i^v = y_i \hat{\Phi}_i^v P \quad (3.2)$$

The symbol  $f_i^o$  is the fugacity of pure component  $i$  at standard state and  $\hat{\Phi}_i^v$  is the fugacity coefficient of component  $i$  in the vapour phase. The fugacity coefficient is generated from an equation of state while the activity coefficient is generated from the excess Gibbs energy model. Although the ( $\gamma$ – $\Phi$ ) method allows for accurate analysis of non-ideal mixtures due to the ability of the activity coefficient model to generate large excess Gibbs free energies of mixing (Orbey & Sandler, 1998), this model has significant drawbacks. The details of these disadvantages can be found in the following texts: Raal & Muhlbaier (1998) and Orbey & Sandler (1998).

This resulted in the development of the ( $\Phi$ – $\Phi$ ) method. This method uses the fugacity coefficient to describe the non-idealities in both the vapour and liquid phases as follows:

$$\hat{f}_i^l = x_i \hat{\Phi}_i^l = \hat{f}_i^v = y_i \hat{\Phi}_i^v \quad (3.3)$$

This method had difficulties describing data for complex systems hence the modern direct method was developed. This method uses equation of state (EoS) mixing rules to incorporate activity coefficients (excess free energy models) into the fugacity coefficients of the liquid and vapour phases. The relationship between the EoS and the activity coefficient described by Orbey and Sandler (1998) is represented by equation 3.4:

$$\gamma_i = [\hat{\Phi}_i(T, P, x_i) / \phi_i(T, P)] \quad (3.4)$$

The symbols  $\hat{\Phi}_i(T, P, x_i)$  is the fugacity coefficient of species  $i$  in the mixture, and  $\phi_i(T, P)$  is the pure component fugacity coefficient. Equation 3.5 gives the correlation for the molar excess Gibbs free energy. The combination of equations (3.4) and (3.5) results in the mixture EoS models which are capable of describing high degrees of non-ideality.

$$\frac{G^E}{RT} = \sum x_i \ln \gamma_i \quad (3.5)$$

In an ideal system, the vapour phase is represented by an ideal gas and the liquid phase by an ideal solution. This is accomplished by setting  $\Phi_i$  and  $\gamma_i$  to a value of one.

An extensive search was conducted which showed that the popular models used in literature and simulation packages to regress data for the systems studied are the following activity coefficient models: NRTL, Wilson and UNIQUAC (Universal Quasi-Chemical) along with an ideal vapour phase. However, in this study, an EoS needed to be incorporated due to the high pressure used for one of the units in the separation scheme (*flash vessel at 1930 kPa*). Hence, both the combined method and the modern direct method were used to regress the measured VLE data in this study.

For the derivation of all the equations above, and definitions of fugacity coefficient and activity coefficient, the reader is referred to the following texts Raal and Mühlbauer (1998), Orbey and Sandler (1998), Kontogeorgis & Folas (2009) and Seader, et al.(2011).

### 3.2 Thermodynamic Models used in this study

The thermodynamic models used in describing the liquid and vapour phases will be discussed in this section. The modern direct method was used in conjunction with a configuration of models which included an equation of state, a mixing rule, an alpha function and an activity coefficient model. The direct method comprised of an ideal vapour phase and an activity coefficient model. These models are common and widely used hence only a brief discussion is presented.

The development of the EoS models is described by Seader and Henley (2011) as follows: the simplest EoS is the ideal gas law. This model does not take into account the volume occupied by the molecules and the interaction forces. Hence, alternative EoS models developed attempt to provide a correction for these two factors. The first successful EoS developed for a non-ideal gas was the van der Waals equation. This model proposed that all species have equal reduced molar volumes at the same reduced temperature and reduced pressure. This was used to develop the compressibility factor which accounts for differences in molecular shape. The Redlich Kwong (RK) equation was then developed as an improvement to the van der Waals equation. A modification was made to this equation where a parameter was added (acentric factor,  $\omega$ ) resulting in the Soave-Redlich-Kwong (SRK) equation. This model is simple, accurate and provides a good fit to vapour pressure data thereby improving the ability of the equation to predict liquid phase properties. A modification was made to the RK and SRK models which resulted in the Peng-Robinson (PR) EoS. This model displayed improvements in the critical region and accounted for liquid molar volume. Hence the PR EoS was selected for data regression and is presented in the sections to follow.

### 3.2.1 Peng-Robinson Cubic Equation of State

The popular EoS is reported as:

$$P = \frac{RT}{V-b} - \frac{a_c \alpha}{v(v+b)+b(v-b)} \quad (3.6)$$

$$a_c = 0.45724 \left( \frac{R^2 T_c^2}{P_c} \right) \quad (3.7)$$

$$b = 0.07780 \left( \frac{RT_c}{P_c} \right) \quad (3.8)$$

The parameters  $a$  (temperature dependent) is related to the intermolecular attraction force of molecules and  $b$  (temperature independent) accounts for the molecular size of the molecule. The  $\alpha$  function which was used in equation (3.6) is represented as follows:

$$\alpha = [1 + (0.37464) + 1.54226\omega - 0.2699\omega^2 \times (1 + T_r^{0.5})^2] \quad (3.9)$$

$\omega$  is the acentric factor. The Peng-Robinson EoS is widely used in industry but it has some limitations. Some of which include not accurately predicting data for long chain molecules and predicting saturation pressure for vapour liquid equilibrium data. A detailed review of the shortcomings can be found in the following text Abbott (1979). Due to these drawbacks, the model has been modified to improve upon the predictive capabilities. This will be discussed in the sections to follow.

### 3.2.2 Mathias Copeman Alpha Function

Alpha functions were developed to improve the ability of EoS models in representing the thermodynamic properties of components at various conditions. The original alpha function which was implemented into the Peng-Robinson EoS was developed by Soave (1972). This alpha function however could not predict vapour pressures at low temperatures, including temperatures above the critical point (Twu, et al., 2002). Thus, alternative alpha functions were developed seeking to improve the vapour pressure prediction.

There are numerous correlations available hence in this study, various alpha functions were incorporated into the Peng-Robinson EoS in order to investigate the performance of alpha functions, with the aim of selecting the most suitable function. The Mathias-Copeman (MC) alpha function was used as it produced the best improvement to the vapour pressure fit. The MC alpha function is represented by the following correlation:

$$\alpha_i(T) = \left[ 1 + C_{1,i}(1 - \sqrt{T_{R,i}}) + C_{2,i}(1 - \sqrt{T_{R,i}})^2 + C_{3,i}(1 - \sqrt{T_{R,i}})^3 \right]^2 \quad (3.10)$$

The function parameters are represented by  $C_{1,i}$ ,  $C_{2,i}$  and  $C_{3,i}$ , with  $T_{R,i}$  signifying the reduced temperature of species  $i$ . These parameters are generated through the regression of vapour pressure data.

### 3.2.3 Mixing rules: Wong-Sandler

EoS models were initially developed for pure substances. In order to account for mixtures, these correlations were extended through the use of the mixing and combining rules (Sadus, 2012). Hence, these rules correlate the properties of the pure component to those of the mixture. The standard was the Van der Waals one-fluid mixing rules represented by equations 3.11 and 3.12:

$$a = \sum \sum x_i x_j a_{ij} \quad (3.11)$$

$$b = \sum \sum x_i x_j b_{ij} \quad (3.12)$$

The symbols  $a_{ij}$  and  $b_{ij}$  are evaluated through the use of combining rules, which essentially optimise the agreement between theory and experimental data. The combining rules are correlated as follows:

$$a_{ij} = \sqrt{a_{ii} a_{jj}} (1 - k_{ij}) \quad (3.13)$$

$$b_{ij} = \frac{1}{2}(b_{ii} + b_{jj})(1 - l_{ij}) \quad (3.14)$$

The symbols  $k_{ij}$  and  $l_{ij}$  represent the binary interaction parameters.  $k_{ij}$  is calculated from fitting EoS predictions to experimental VLE data.  $l_{ij}$  is usually set equal to zero (Seader, et al., 2011).

The  $k_{ij}$  parameter has the ability to determine the strength of the intermolecular forces in a mixture as shown in Table 3.1. The closer  $k_{ij}$  is to zero, the better the agreement between experimental and predicted data (Kontogeorgis & Folas, 2009). Non-ideal behaviour is characterised by the azeotropes.

Table 3.1: Significance of  $k_{ij}$  binary interaction parameter

$k_{ji} = 0$	System is ideal exhibiting Raoult's law (forces between like and unlike molecules are equal)
$k_{ji} > 0$	System exhibits a positive deviation from Raoult's law (forces between like molecules are stronger)
$k_{ji} < 0$	System exhibits a negative deviation from Raoult's law (forces between unlike molecules are stronger)

The original form of the Peng-Robinson EoS utilises the Van der Waal one fluid mixing rules. This combination effectively describes phase equilibria data for mixtures of hydrocarbons and hydrocarbons with inorganic gases (Sandler, 1994) but is only useful in mixtures with moderate solution non-ideality. Most industrial chemical mixtures however have a relatively higher degree of non-ideality. Thus, in order to account for this shortcoming, mixing rules that combine EoS models with activity coefficient models were developed.

The first mixing rule (combining EoS models with activity coefficient models) was developed by Huron and Vidal (1979). This was achieved through empirical means, by dictating that the EoS of the mixture at the density of the liquid should behave in the same manner as an activity coefficient model (Orbey & Sandler, 1998). The mixing rule combines the excess Gibbs energy of mixing for an EoS and that of an activity coefficient model as follows:

$$G_y^E(T, P = \infty, x) = G_{EoS}^E(T, P = \infty, x) \quad (3.15)$$

The subscripts EoS and  $\gamma$  refer to an equation of state and activity coefficient model, respectively. The superscript E represents the excess energy.

This mixing rule was partially successful but had significant flaws. It had difficulty describing mixtures that the Van der Waal one fluid mixing rule could effectively describe. Furthermore, it failed to satisfy the composition dependency, which is required for the second virial coefficient. This led to the development of the modified Huron – Vidal second order model (Sandler, 1994). However, this mixing rule also failed due to its inability to satisfy the composition dependency.

These flaws were overcome with the development of the mixing rules by Wong and Sandler (1992) which succeeded where Huron and Vidal (1979) failed. This was achieved through the use of the excess Helmholtz free –energy ( $A^E$ ) at an infinite pressure. The mixing rule parameters are formulated based on the following condition:

$$A_{EoS}^E = A_y^E(T, P = \infty, x_i) = A_y^E(T, \text{low}, P, x_i) = G_y^E(T, \text{low}, P, x_i) \quad (3.16)$$

The resulting mixing rules were then correlated as follows:

$$a_m = RT(Z) \frac{W}{(1-W)} \quad (3.17)$$

$$b_m = \frac{Z}{(1-W)} \quad (3.18)$$

$$Z = \sum \sum x_i x_j \left( b - \frac{a}{RT} \right)_{ij} \quad (3.19)$$

$$W = \sum x_i \frac{a_i}{b_i RT} + \frac{G^{(E)}(x_i)}{\sigma RT} \quad (3.20)$$

The constant  $\sigma$  depends on the equation of state being used and for the Peng-Robinson EoS, this constant is correlated as:

$$\sigma = -1 \frac{1}{\sqrt{2}} \ln(1 + \sqrt{2}) \quad (3.21)$$

The mixing rule uses the following combining rules as restrictions for the EoS parameters  $a$  and  $b$ :

$$\left( b_{ij} - \frac{a_{ij}}{RT} \right) = \frac{1}{2} \left[ \left( \frac{b_{ii} - a_{ii}}{RT} \right) + \left( \frac{b_{jj} - a_{jj}}{RT} \right) \right] (1 - k_{ij}) \quad (3.22)$$

### 3.2.4 Activity Coefficient Models

In order to effectively assess the properties of non-ideal liquid mixtures an activity coefficient model is utilised, which relates the Gibbs excess function to the liquid composition. Presented is a brief description of the activity coefficient models used in this study.

#### The Wilson Activity Coefficient Model

The Wilson activity coefficient model (Wilson, 1964) is based on the concept of local composition, which occurs within a liquid solution. Local compositions are areas in the mixture that differ from the overall mixture composition. It accounts for the non-random molecular orientations in the solution which results from differences in molecular size and intermolecular forces. The Wilson equation has two limitations: the inability to predict immiscibility and not being able depict maximum or minimum activity coefficient - mole fraction relationships (Nelson, 2012).

## The Non-Random Two Liquid (NRTL) Activity Coefficient Model

The NRTL equation (Renon & Prausnitz, 1968) was then developed as an improved local composition model. This equation is capable of predicting both partially miscible and completely miscible systems and is suitable for highly-non-ideal systems. The NRTL equation for the excess Gibbs energy for a binary mixture is:

$$\frac{G^E}{RT} = x_i x_j \left( \frac{\tau_{ji} G_{ji}}{x_i + x_j G_{ji}} + \frac{\tau_{ij} G_{ij}}{x_j + x_i G_{ij}} \right) \quad (3.23)$$

The parameters  $\tau_{ji}$  and  $\tau_{ij}$  are adjustable and ( $G_{ij} = -\sigma\tau_{ij}$ ). The activity coefficient of the model is represented by

$$\ln \gamma_i = x_j^2 \left[ \tau_{ji} \left( \frac{G_{ji}}{x_i + x_j G_{ji}} \right)^2 + \frac{\tau_{ij} G_{ij}}{(x_j + x_i G_{ij})^2} \right] \quad (3.24)$$

While  $\ln \gamma_j$  is obtained through interchanging the subscripts in equation (3.24). In the software package Aspen Plus® V 8.4, which was employed in the regression of all experimental data in this work, the NRTL model is defined as follows:

$$\tau_{ij} = a_{ij} + \frac{b_{ij}}{T} + e_{ij} \ln T + f_{ij} T \quad (3.25)$$

The symbols  $\tau_{ij}$  is the interaction binary parameter and  $a_{ij}$ ,  $b_{ij}$ ,  $e_{ij}$ ,  $f_{ij}$  are obtained through the regression of the experimental data. The parameters  $e_{ij}$ ,  $f_{ij}$  were not used in this work, and as such were assigned a value of zero. The non-randomness parameter is correlated by the following formulae:

$$\alpha_{ij} = c_{ij} + d_{ij}(T - 273.15 \text{ K}) \quad (3.26)$$

The symbol  $d_{ij}$  is set to zero, thus resulting in the reduction of the above correlation into an identity of the form ( $\alpha_{ij} = c_{ij}$ ). The parameter  $c_{ij}$  is selected based on the chemical characteristics of the components which make up the mixture. Suitable guidelines for values of  $\alpha_{ij}$  are shown in Table 3.2. Model parameters obtained from literature and VLE applications using the Dortmund Data Bank are stored in Aspen Plus® for over 1000 component pairs. The fixed parameter  $c_{ij}$  selected in this work was the literature value stored in Aspen Plus® for each binary system (0.3 for ethanol/pyridine and 0.69 for water/pyridine).



Table 3.2: Suitable guideline for  $\alpha_{ij}$  parameter (Seader, et al., 2011)

$\alpha_{ji} = 0.20$	Hydrocarbons and polar, non-associated species
$\alpha_{ji} = 0.30$	Non-polar compounds, except fluorocarbons and paraffins; nonpolar and polar, non-associated species; polar species that exhibit negative deviations from Raoult's law and moderate positive deviations; mixtures of water and polar non-associated species.
$\alpha_{ji} = 0.40$	Saturated hydrocarbons and homolog perfluorocarbons.
$\alpha_{ji} = 0.47$	Alcohols or other strongly self-associated species with nonpolar species.

### The Universal Quasi-Chemical (UNIQUAC) Equation

The UNIQUAC equation (Abrams & Prausnitz, 1975) comprises a combinatorial part and a residual part. The combinatorial part accounts for the variances in sizes and shapes of the molecules. The residual part accounts for the intermolecular forces between the molecules. UNIQUAC utilises local area fraction as the prime concentration variable as opposed to local volume fractions and local mole fractions used for Wilson and NRTL. The disadvantages of this equation are its algebraic complexity and the requirement for pure component structural parameters. These parameters however are available for the components of interest in this work.

### Universal Functional Group Activity Coefficient Model (UNIFAC)

An estimation method was developed since liquid-phase activity coefficients are required for design purposes even when experimental equilibria data are not available. This method is based on functional groups instead of molecules. "For partial molar excess free energies and activity coefficients, size parameters for each functional group and interaction parameters for each pair are required. Size parameters can be calculated from theory. Interaction parameters are back-calculated from existing phase-equilibria data and used with the size parameters to predict properties of mixtures for which data are unavailable" (Seader, et al., 2011). Hence, the group contribution methods rely on available data and functional groups to predict the data that is unavailable. These are available for the systems in this study. Though, there are some combinations for which this information is not available.

The UNIFAC (UNIQUAC Functional-group Activity Coefficients) group-contribution method was first introduced by Fredenslund, Jones, and Prausnitz (1975) and developed further by Fredenslund, Gmehling, and Rasmussen (1977), Gmehling, Rasmussen, and Fredenslund (1982),

and Larsen, Rasmussen, and Fredenslund (1987). The UNIFAC method is based on the UNIQUAC equation, wherein the sum of the volume and area parameters of each functional group in the molecule are used instead of the molecular volume and area parameters.

Gmehling et al. (1982) improved the group-contribution method by the introduction of a modified UNIFAC method referred to as UNIFAC (Dortmund). The combinational part of the original equation was modified due to mixtures having a range of molecular sizes and the temperature dependence was replaced with a three-coefficient equation. Details of these modifications and equations can be found in Seader, et al. (2011). These changes permit reliable predictions of activity coefficients, azeotropic compositions and heats of mixing.

### 3.3 Vapour Liquid Equilibrium Prediction

The VLE data in this work is also compared to estimated data obtained from the Aspen Physical Property System. Aspen Plus® stores physical property parameters for several components in numerous databanks which are developed from the thermodynamic models inherent in the package and data from the Dortmund Databank. These are the parameters retrieved to calculate temperatures, pressures, mole compositions, etc. to generate the phase data required. The predictive models used in this work are PSRK (Predictive Soave Redlich Kwong) and UNIFAC (Universal Functional Group Activity Coefficient Model). Only a brief description is presented. The list of equations and a more detailed explanation can be found in the following texts: Seader, et al (2011) and AspenTech (2015).

#### 3.3.1 Predictive Soave Redlich Kwong (PSRK)

For mixtures of nonpolar and slightly polar compounds, EoS models are useful. Gibbs free-energy activity coefficient models are suitable for liquid subcritical nonpolar and polar compounds. For mixtures that contain both polar compounds and supercritical gases, these methods are not suitable. Hence, theoretically based mixing rules involving the SRK and PR EoS were developed to describe vapour-liquid equilibria for such mixtures. Holderbaum and Gmehling (1991) further developed these models for a range of applications by formulating a group-contribution equation of state called the Predictive Soave Redlich Kwong (PSRK) model, which combines the SRK equation of state with UNIFAC. The pure-component parameter  $a$  shown in equation 3.27 becomes temperature dependent in order to increase the ability of the SRK equation to predict vapour pressure of polar compounds. A mixing rule that includes the UNIFAC model for non-ideal effects was incorporated into the  $a$  parameter to account for mixtures of nonpolar, polar and supercritical components.

$$P = \frac{RT}{v-b} - \frac{a}{v^2+bv} \quad (3.27)$$

### 3.4 Data Regression

The proprietary software from Aspen Technology, Aspen Plus® V 8.4 was utilised for the regression of experimental data and calculation of predicted data. An extensive literature review showed that the popular models used in literature and simulation packages to regress data for the systems studied are the following activity coefficient models: NRTL, Wilson and UNIQUAC along with an ideal vapour phase. However, in this study, an EoS needed to be incorporated due to the high pressure used for one of the units in the separation scheme (*flash vessel at 1930 kPa*). Hence, the following configuration of models was used: Peng-Robinson EoS, with the incorporation of the Mathias–Copeman alpha function, the Wong–Sandler mixing rules and an activity coefficient model (Wilson, NRTL, UNIQUAC).

Furthermore, since the focus of this work was partly VLE measurement and design simulation and costing; it was not the focus to provide too much time to data regression and modelling; the popular and common models which proved adequate in correlating the data were used.

The objective function  $F$  is the sum of the squares of the errors between the calculated and experimental values of one or more equilibrium-related properties. The optimal interaction parameters in the chosen thermodynamic model are those that minimize the objective function. In this study two different objective functions were used. For the ethanol + pyridine literature data, the barker's method shown in equation 3.28 was utilised since only the P-x data was available.

$$\varphi = \sum_{j=1}^{ndata} (P_j - P_j^{calc})^2 \quad (3.28)$$

$P_j$  and  $P_j^{calc}$  represent the experimental and calculated values for the pressure respectively. The ordinary least squares objective function was used for the water + pyridine literature data and in the regression of all the measured VLE data. The objective function is calculated as follows:

$$F = \frac{100}{N} \left[ \sum \left( \frac{P_{exp} - P_{cal}}{P_{exp}} \right)^2 + \sum \left( \frac{y_{exp} - y_{cal}}{y_{exp}} \right)^2 \right] \quad (3.29)$$

$P_{exp}$ ,  $y_{exp}$ ,  $P_{calc}$  and  $y_{calc}$  represent the experimental and calculated values for the pressure and vapour compositions respectively.

## **CHAPTER 4: EXPERIMENTAL EQUIPMENT AND PROCEDURE**

This chapter will focus on the description of the low-pressure vapour liquid equilibrium still and the experimental procedure followed in this study. This includes calibrations, equilibrium cell preparation, the measurement and control of temperature and pressure and analysis of the equilibrium phases. For experimental VLE data that will be used in distillation design, any errors in the measured data would not produce an accurate representation of the real system such as predicting higher or lower product purities and energy demands. Therefore, the equipment used should be correctly calibrated and operated; temperature, pressure and composition measurements must be taken at the point where equilibrium actually occurs and the equilibrium should not be disturbed whilst withdrawing the samples for analysis.

### **4.1 Low Pressure VLE Equipment**

It is important to note that no single apparatus or single technique can measure VLE for all kinds of systems, as the variation in temperatures, pressures and component characteristics (volatility, corrosivity, thermal stability etc.) are too diverse. Thus, there exists a large array of experimental techniques for VLE measurement. This section presents a brief description of the two methods relevant in this study: static method and dynamic method. In the static method, the liquid mixture is charged into the cell and agitated mechanically until equilibrium is reached with the vapour at a fixed temperature. The static cells are usually immersed in a water bath at constant temperature to produce isothermal data. For this method, complete degassing of the system is essential (effective degassing can be very difficult and is the main source of error) since even minor impurities could produce useless results (Bhownath, 2008). The dynamic method, also known as the circulation method, involves the continuous separation of vapour phase from liquid phase under steady state conditions and the recirculation of phases. The still can be operated under isobaric or isothermal conditions. This method was employed to acquire the VLE data since it allows measurements of high accuracy, it is simple, reliable and is typically used for low-pressure VLE (Bhownath, 2008).

The VLE recirculating still of Raal and Mühlbauer (1998), which is based on the designs of Heertjes (1960) and Yerezunis (1964), was used to acquire the binary VLE data. The design of the still has not been changed drastically but some modifications have been undertaken by Joseph, et al (2001), Ndlovu (2005) and Bhownath (2008) which will be discussed in the sections to follow. Figure 4.1 presents a schematic representation of the VLE recirculating still used in this study.

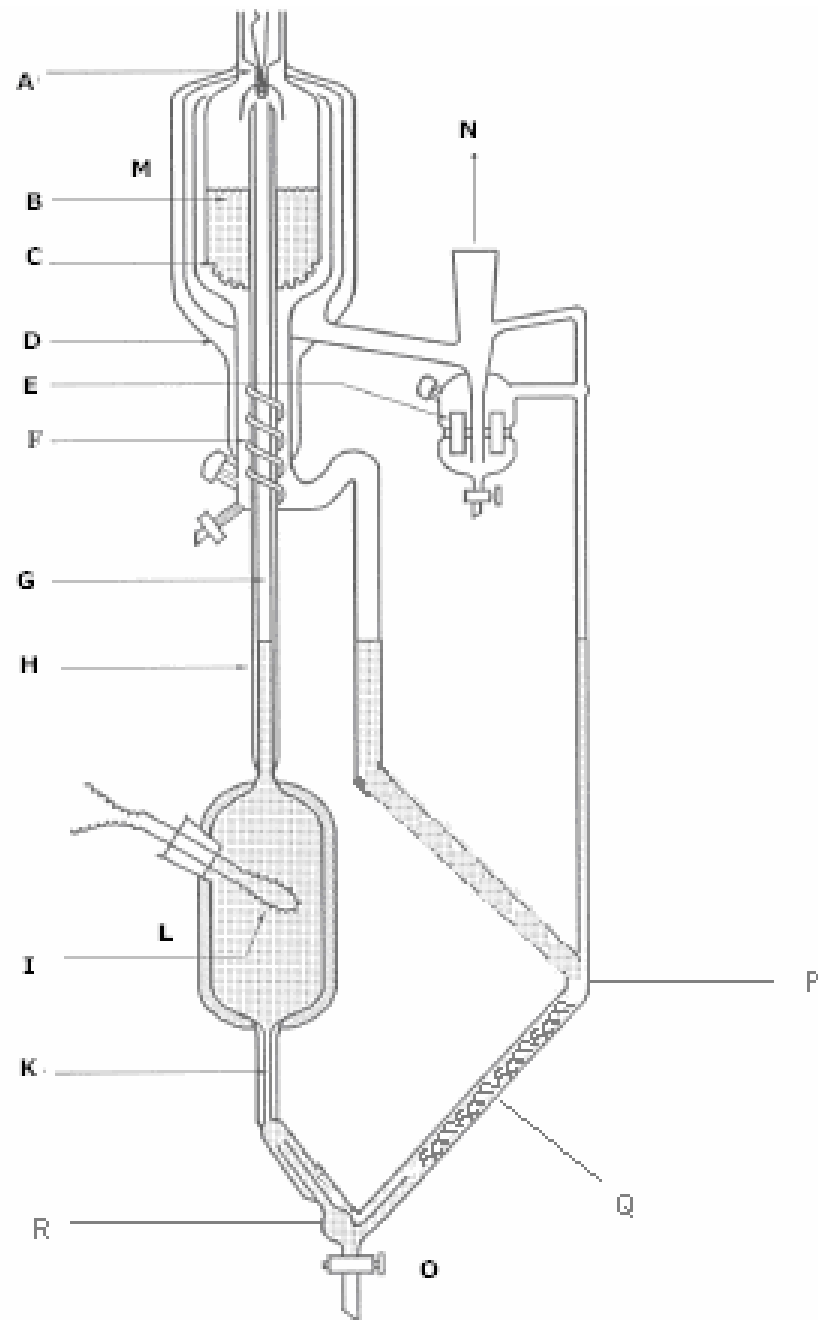


Figure 4.1: Schematic diagram of the VLE recirculating still (Bhownath, 2008)

A-temperature sensor, B-s/s wire mesh packing, C-equilibrium chamber, D-vacuum jacket, E-magnetic stirrer, F- s/s spiral, G-Cottrell tube, H-vacuum jacket, I-glass tube, K-capillary, L-reboiler, M-equilibrium chamber, N-inlet to condenser, O-drain valve, P-mixing tee, Q-glass spiral, R-mixing chamber.

For the recirculating method, a binary liquid solution of 75 ml is initially charged into the boiling chamber (L) and brought to boil via internal and external heaters. The internal heater consists of a heating cartridge placed in the glass tube (I) which facilitates the boiling process. The external heater contains nichrome wire that is wrapped around the boiling chamber and accounts for heat

losses to the environment. The boiling generates a vapour-liquid mixture that moves up through the vacuum insulated Cottrell tube (G) and then downward through the vacuum jacketed equilibrium chamber (M) where the phases disengage. The liquid phase channels down through holes at the bottom of the equilibrium chamber to the liquid sampling point, while the vapour flows upward around the equilibrium chamber and towards the condenser. The condensate is collected in the vapour sampling point. Both phases recirculate via the reboiler. Equilibrium is achieved when the plateau region (the region where the boiling temperature does not change for a slight increase in the internal heater setting (Kneisl, et al., 1989)), is reached, there is a good circulation rate in the still and a drop rate of approximately 60 drops per minute from the condenser is observed. At this point, the contents in the still were left to circulate for a further 15 – 20 minutes to ensure equilibrium was actually achieved. There-after, the liquid and vapour samples were withdrawn from the sampling points using a 1 $\mu$ l gas tight GC syringe through a chemically resistant septum. This ensured there was no effect on equilibrium temperature, pressure and composition in the still during the withdrawal process. The samples were then injected into a Shimadzu GC-2014 to obtain the equilibrium composition measurements.

A Pt-100 temperature sensor (A), class B with an uncertainty of 0.1 K, housed in a glass tube (I) shown in Figure 4.1 was used to measure the equilibrium temperature. The Pt-100 was connected to a Hewlett-Packard (model 34401A) multi-meter that displayed resistance. For isothermal measurements, temperature was maintained at fixed values by adjusting the pressure set point. Decreasing the pressure reduced the temperature and increasing the pressure increased the temperature. The pressure was controlled with a BUCHI model B-721 pressure controller that used a two-way solenoid valve connected to a KNF vacuum pump and a vent to the atmosphere. The vacuum pump was connected to a ballast tank to reduce pressure fluctuations. The allowable operating pressure range in the still was 0 – 100 kPa. The pressure was measured using a WIKA model P10 pressure transmitter with an uncertainty of 0.05 kPa.

The following modifications were made to the design of the VLE recirculating still of Raal and Mühlbauer (1998):

- Joseph et al. (2001) improved the isothermal operation of the still by implementing a design based on pulse-width modulation of two solenoid valves with the aid of computer control as opposed to manually changing the pressure controller setting to achieve the desired temperature.
- Ndlovu (2005) implemented an innovative design modification enabling the still to obtain low pressure VLE data for partially miscible systems.
- Bhowanath (2008) combined the vapour condensate and liquid return lines into a tee formation to increase the contact time and mixing time of the liquid mixture. A mixing chamber was also added for further agitation of the liquid mixture. Resistance wire was wrapped around the mixing tee and mixing chamber. These modifications allowed the

measurement of systems with a high relative volatility by reducing the channelling of the more volatile component into boiling chamber.

For a more detailed discussion on the equipment design and operation, the following texts are recommended: Raal & Muhlbaier (1998), Joseph, et al (2001), Ndlovu (2005) and Bhowanath (2008).

## **4.2 Experimental Method**

### **4.2.1 Preparation**

Before commencing with experiments, the following checks were required:

- Leak detection: accurate measurements and pressure control are only possible if the still is operated without any leaks. Therefore, the first step is the identification and elimination of any leaks. Since the apparatus could not withstand pressures above atmospheric pressure, the method to detect leaks involved setting the pressure control to a set-point below atmospheric pressure. The VLE still was then isolated by shutting of the necessary valves and any increase in pressure was recorded. Joint leaks were detected by adding liquid acetone on the outside of joints. If a small spike in pressure was detected then a leak was identified. The spike in pressure is caused by liquid acetone flashing in the still due to the low pressure in the VLE still. Leaks were eliminated by adding vacuum grease onto glass joints and vacuum seal to steel joints. The septa placed at the liquid and vapour sampling points could also produce leaks as they are easily worn and hence were changed regularly.
- Cleaning: The still required cleaning each time a new component or different binary system was to be measured. This was achieved by circulating pure acetone in the VLE still under isobaric conditions for approximately an hour. Thereafter, the acetone was drained and the process repeated with clean acetone. This acetone was then drained and the still was placed under vacuum (10 kPa) via a vacuum pump, for approximately 30 minutes, to allow the excess acetone to evaporate.

### **4.2.2 Temperature and Pressure Calibration**

The Pt-100 temperature sensor was calibrated against a standard temperature (WIKA) probe by placing both probes in a water bath, varying the temperature of the bath and manually recording temperature from the unit display. The standard temperature probe was calibrated directly with WIKA instruments and has an internal uncertainty of 0.05 K as stated by the manufacturer. The bath temperature was increased and there-after decreased incrementally over the temperature range of interest. At each stabilised temperature, measurements were taken every 5 minutes for 25 minutes and the values averaged. Figure 4.2 displays a plot of the resistance recorded from the

Pt-100 temperature probe against the temperature recorded from the standard temperature probe. The data collected was fitted to a second order polynomial and has a maximum correlation error of 0.03 K as shown in Figure 4.3.

The WIKA P10 pressure transmitter was calibrated against a standard pressure transmitter (Mensor CPC 3000) by connecting both transmitters to the VLE apparatus, varying the pressure in the still and manually recording the pressure on the display units connected to each transmitter. The standard pressure transmitter was calibrated directly by WIKA and has a standard uncertainty of 0.05 kPa as stated by the manufacturer. The pressure in the still was increased and there-after decreased incrementally over the allowable pressure range of the still (10 kPa to 100 kPa). Figure 4.4 displays a plot of the pressure recorded from the WIKA P10 pressure transmitter against the standard pressure transmitter. The data collected was fitted to a second order polynomial and has a maximum correlation error of 0.01 kPa as shown in Figure 4.5.

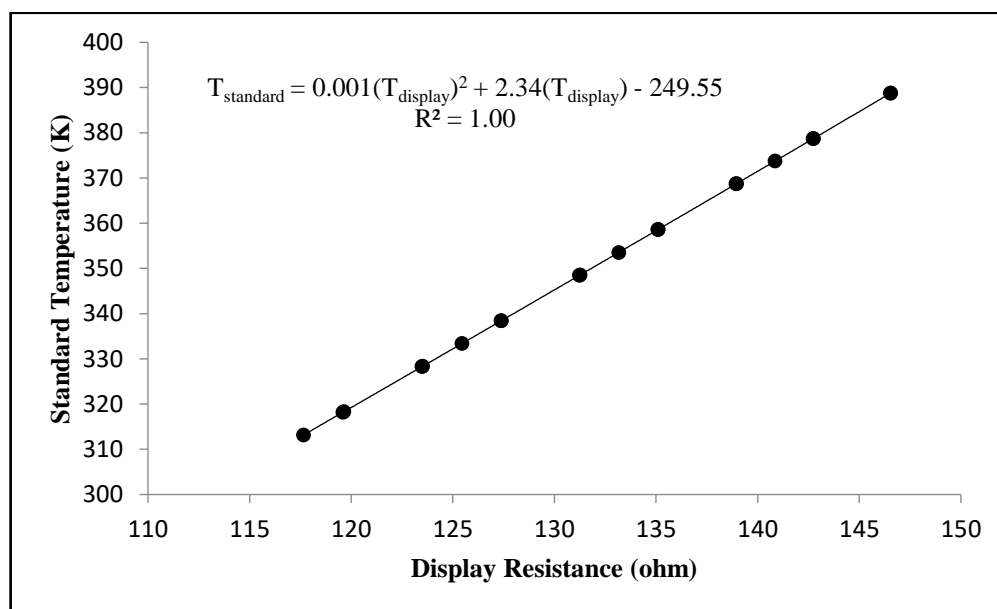


Figure 4.2: Temperature calibration for the VLE still



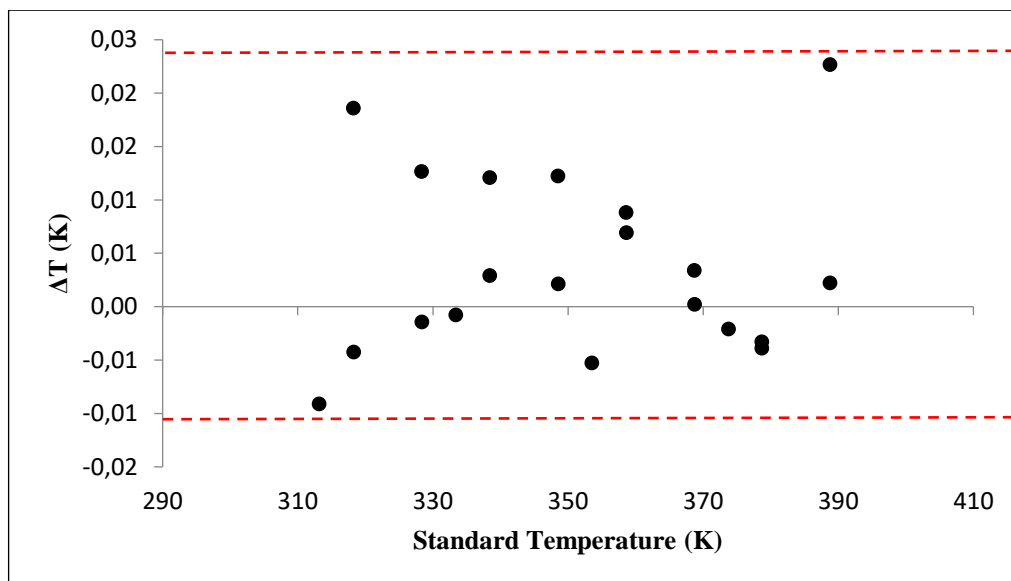


Figure 4.3: Uncertainty in temperature calibration for the VLE still

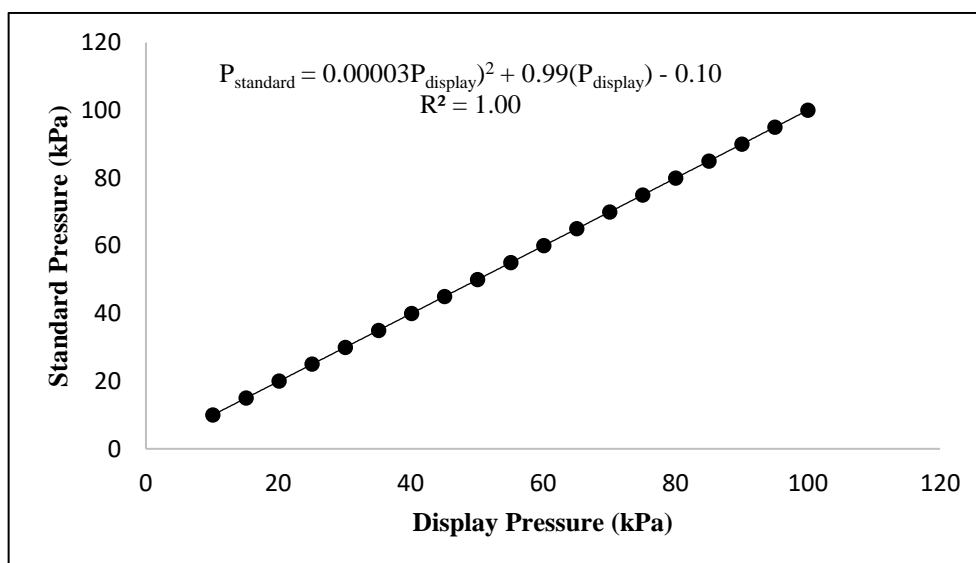


Figure 4.4: Pressure calibration for the VLE still

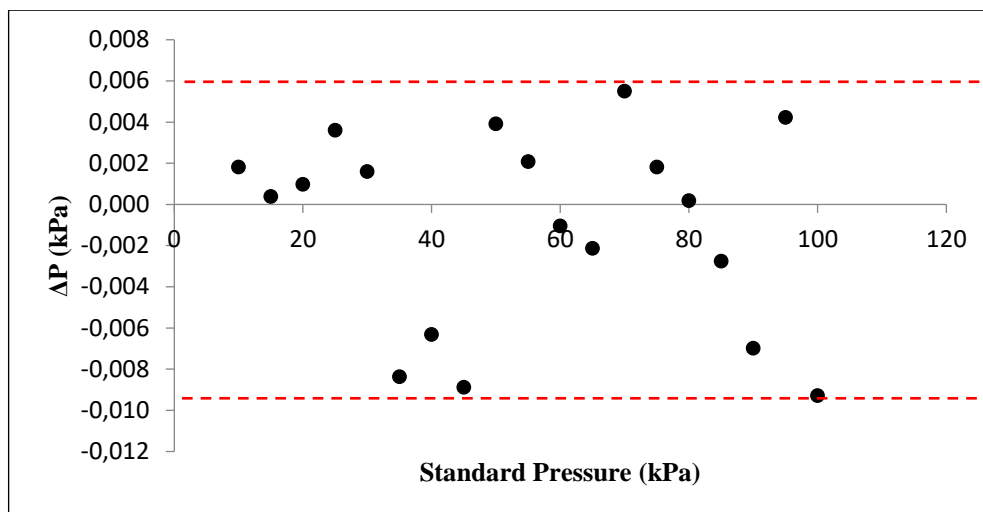


Figure 4.5: Uncertainty in pressure calibration for the VLE still

### 4.2.3 Gas Chromatograph Thermal Conductivity Detector Calibration

A Shimadzu GC - 2014 with a thermal conductivity detector (TCD), which used helium as the carrier gas was used to analyse compositions for the VLE systems studied in this project. A 2 m × 2.2 mm Porapack Q column was utilised for component separation in the GC. The operating conditions of the GC is presented in Table 4.1. The systems measured included: cyclohexane + ethanol test system, ethanol + pyridine and water + pyridine. The purpose of measuring the test system was to ensure the correct operation of the VLE apparatus and demonstrate the accuracy of the experimental procedures.

Table 4.1: Operating conditions for the Shimadzu GC- 2014

System	Cyclohexane + Ethanol (Test System)	Ethanol + Pyridine	Water + Pyridine
<b>Gas flow rate (ml/min)</b>	25	25	30
<b>Oven Temperature (K)</b>	453.15	483.15	493.15
<b>Detector Temperature (K)</b>	473.15	503.15	513.15
<b>Injector Temperature (K)</b>	473.15	503.15	513.15

The GC detector was calibrated following the method suggested by Raal & Muhlbaüer (1998) which involved gravimetrically preparing binary liquid mixtures of known composition, injecting the mixtures into the GC and plotting the ratio of the binary composition ( $x_1/x_2$ ) against the ratio of the peak area ( $A_1/A_2$ ) generated after injection of sample into the GC. The samples were prepared across the entire composition range in 4 ml vials. The volume of each sample injected into the GC was 0.5  $\mu$ l. The response of the detector is defined by:

$$n_i = A_i F_i \quad (4.1)$$

The symbols  $n_i$  is the number of moles of component  $i$ ,  $F_i$  is the response factor and  $A_i$  is the integrated peak area. For a binary system:

$$\frac{n_1}{n_2} = \frac{A_1 F_1}{A_2 F_2} = \frac{x_1}{x_2} \quad (4.2)$$

From equation (4.2), it can be seen that the response factor ratio,  $F_1/F_2$ , is the slope of the linear plot of  $A_1/A_2$  versus  $x_1/x_2$ . If this plot is in fact linear, the plot of  $A_2/A_1$  versus  $x_2/x_1$  should equal to  $F_2/F_1$  (i.e.  $F_1/F_2$  should equal the inverse of  $F_2/F_1$  and vice versa). However, the shape of the calibration plot depends on the detector type and the system under investigation. Therefore, non-linear plots are also possible. The calibration charts generated in this research project were fitted to a second order polynomial and are shown in Appendix C. The nonlinearity is usually due to a non-linear response of the detector. This is due to the instrument itself, the column utilised in the GC or the system studied, including the range of measurement.

#### 4.2.4 Isobaric Operation

For operation in the isobaric mode, pressure was held constant while the equilibrium temperature was determined, followed by sample analysis to obtain equilibrium compositions. The procedure is as follows:

- i. The cooling unit was first switched on to allow the ethylene glycol solution in the water bath to cool down to 276.15 K. Once this temperature was reached, 75 ml of the first component was charged into the still. The power supply, motors for the stirrers, temperature and pressure displays were then switched on.
- ii. The pressure controller was set to the operating pressure of interest and the vacuum pump turned on. Once the desired pressure set point was achieved, the internal and external heaters were switched on. The external heater is set to a constant value of 20 to 30 volts depending on the system of components (a heavier boiler requires a higher setting to achieve equilibrium). The internal heater was set to a value of 5 volts and increased incrementally until the equilibrium was achieved.
- iii. The liquid samples were first withdrawn from the still followed by the vapour samples using a gas-tight liquid GC syringe. The samples were injected into the GC to obtain the peak areas. Three samples were withdrawn and analysed from each sampling point (liquid and vapour) to measure its consistency. The temperature and pressure were recorded for each withdrawal and the values averaged.
- iv. To measure the next composition point, 3ml of liquid was removed from the still and an equal volume of the second component was added to the still. This allowed the system composition to be altered.

- v. Steps ii to iv were then repeated.
- vi. The procedure was repeated until half of the phase diagram was complete. The still was then cleaned with acetone and the procedure repeated starting with the second pure component.

#### **4.2.5 Isothermal Operation**

To attain isothermal data, it is easier to operate the still in the isobaric mode so that the pressure set point can be selected such that the equilibrium temperature is close to the desired operating temperature (as opposed to a trial and error method). Once equilibrium was achieved as followed by the steps in section 4.2.4, the isobaric operation was stopped and the temperature manually adjusted to reach the temperature of interest by increasing or decreasing the pressure set point. Once this temperature was reached and equilibrium was obtained, the liquid and vapour samples were withdrawn then analysed and the procedure repeated in the same manner as the isobaric operation.

## CHAPTER 5: RESULTS AND DISCUSSION: EXPERIMENTAL VLE DATA AND MODELLING

This chapter presents the results of the chemical characterisation of components, vapour pressure and phase equilibrium data of the test system and the systems measured at new conditions. Also included is a comparison of the measured data to literature data and modelled data obtained with the use of suitable thermodynamic models.

The indicators used to judge the agreement between the experimental data and either referenced or modelled data are the absolute average deviation (AAD) and absolute average relative deviation (AARD) as represented by equations 5.1 and 5.2 respectively:

$$AAD(\bar{\theta}) = \frac{1}{N_p} \sum |\bar{\theta}_{exp} - \bar{\theta}_{calc}| \quad (5.1)$$

$$AARD(\bar{\theta}) \% = \frac{1}{N_p} \sum \frac{|\bar{\theta}_{exp} - \bar{\theta}_{calc}|}{\bar{\theta}_{exp}} \times 100 \quad (5.2)$$

The symbols  $\bar{\theta}_{exp}$  and  $\bar{\theta}_{calc}$  are the experimental and calculated (or referenced) values of a measured  $\bar{\theta}$  and  $N_p$  is the total number of data points.

### 5.1 Chemical Characterisation

All the chemicals used in this work were analysed via the Shimadzu 2014 gas chromatograph, the Atago Co Ltd., RX-7000 $\alpha$  refractometer with a resolution of 0.0001 n<sub>D</sub> and the Anton Paar, DMA 5000 densitometer which has an accuracy to 0.0001 g/cm<sup>3</sup>. The experimental results and literature values are shown in Table 5.1. All chemicals were used without further purification as no significant impurities were observed.

Table 5.1: Chemical characterisation at 293.15 K

Component	Refractive Index (n <sub>D</sub> )		Density (g/cm <sup>3</sup> )		GC (peak area %)	Supplier and specified purity
	Exp	Lit	Exp	Lit	Exp	Volume (%)
Cyclohexane	1.4263	1.4262 <sup>e</sup>	0.7786	0.7785 <sup>f</sup>	99.94	Sigma Aldrich: 99.8
Ethanol	1.3613	1.3617 <sup>c</sup>	0.7912	0.7910 <sup>g</sup>	99.91	ACS: 99.9
Pyridine	1.5102	1.5102 <sup>h</sup>	0.9831	0.9832 <sup>d</sup>	99.94	Merck: 99.0
Water	1.333	1.333 <sup>a</sup>	0.9982	0.9982 <sup>b</sup>	99.78	Distilled water

<sup>a</sup> (Harris, 2011)

<sup>b</sup> (Allen, 2007)

<sup>c</sup> (Haynes, 2011)

<sup>d</sup> (PubChem, 2015)

<sup>e</sup> (PubChem, 2015)

<sup>f</sup> (ChemicalBook, 2016)

<sup>g</sup> (Khattab, et al., 2012)

<sup>h</sup> (Kyte, et al., 1960)

## 5.2 Vapour Pressure Measurement

The combined expanded uncertainty for both temperature and pressure is calculated by the method outlined by Taylor & Kuyatt (1994).

The combined standard uncertainty for temperature and pressure is calculated by:

$$u_c(T) = \pm \sqrt{u_{cali}(\theta)^2 + u_{rep}(\theta)^2 + u_{std}(\theta)^2 + u_{fluct}(\theta)^2} \quad (5.3)$$

$u_{cali}(\theta)$  is the uncertainty induced by the calibration,  $u_{rep}(\theta)$  is the uncertainty due to measurement repeatability,  $u_{std}(\theta)$  is the standard uncertainty of the temperature or pressure sensor as reported by the manufacturer and  $u_{fluct}(\theta)$  is the fluctuation observed from the temperature or pressure unit display. Refer to Table 5.7 for the numerical values of each term in equation 5.3.

The combined expanded uncertainty is then calculated by multiplying the combined standard uncertainty by a coverage factor of 2 and is displayed in Table 5.2. A more detailed description of this method is presented in Appendix D.

Table 5.2: Combined expanded uncertainties for temperature and pressure

Uc (Temperature) <sup>a</sup>	Uc (Pressure) <sup>a</sup>
0.3 K	0.10 kPa

<sup>a</sup>Expanded uncertainties calculated using a coverage factor of  $k = 2$

Figures 5.1 to 5.3 present the measured vapour pressure data for cyclohexane, ethanol and pyridine respectively, all plotted against literature sources. These measurements were performed to validate the calibrations for the temperature and pressure sensors. It can be seen that the vapour pressure curves are linear indicating the stability of the components during the vapour pressure measurements (no decomposition or polymerisation of the components were observed). Tables 5.3 to 5.5 contain the list of temperatures and pressures measured as well the deviation between experimental data and literature. From the Tables, it can be seen that the percentage errors are well below 1 % which indicates good agreement between the measured data and literature. Regarding the difference in experimental temperature and literature temperature, some of the values lie outside the calculated uncertainties. This is not unexpected since there is a deviation between the literature sources as discussed below.

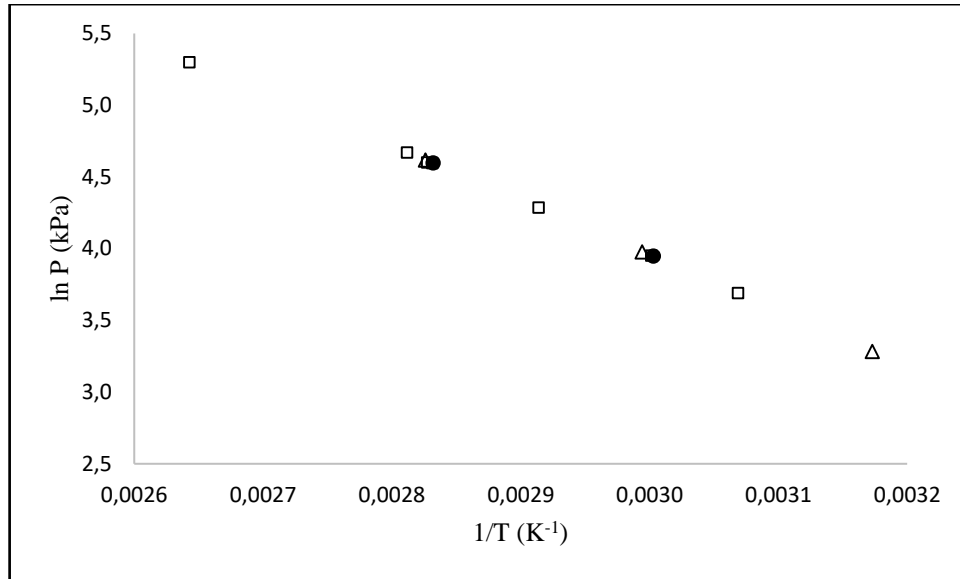


Figure 5.1: Vapour pressure data for cyclohexane. (●) Exp, This work; (□) (Scatchard, et al., 1939); (Δ) (Perry & Green, 1999).

Table 5.3: Comparison of experimental vapour pressure data for cyclohexane to literature sources

$P_{\text{exp}}$ (kPa)	$T_{\text{exp}}$ (K)	$\Delta T^a$ (K)	$\Delta T^b$ (K)	$\Delta T/T^a$ (%)	$\Delta T/T^b$ (%)
99.28	353.08	0.6	0.1	0.16	0.02
51.81	332.92	0.1	0.3	0.04	0.10

$$\Delta T = |T_{\text{exp}} - T_{\text{lit}}|$$

$$\Delta T/T = 100 \left| \frac{T_{\text{exp}} - T_{\text{lit}}}{T_{\text{exp}}} \right|$$

<sup>a</sup> (Dortmund Data Bank, 2015)

<sup>b</sup> (Perry & Green, 1999)

From Table 5.3, the deviation between literature sources a and b for the  $\Delta T$  values can clearly be seen. For a pressure of 99.28 kPa, literature source b (0.1 K) lies within the uncertainty in temperature (0.3 K) while literature source a (0.6 K) does not. Similar deviations between literature sources are observed in Tables 5.4 and 5.5 for the ethanol and pyridine vapour pressure data respectively. Of the three references listed, there is at least one referenced value for each point that is within the calculated uncertainty.

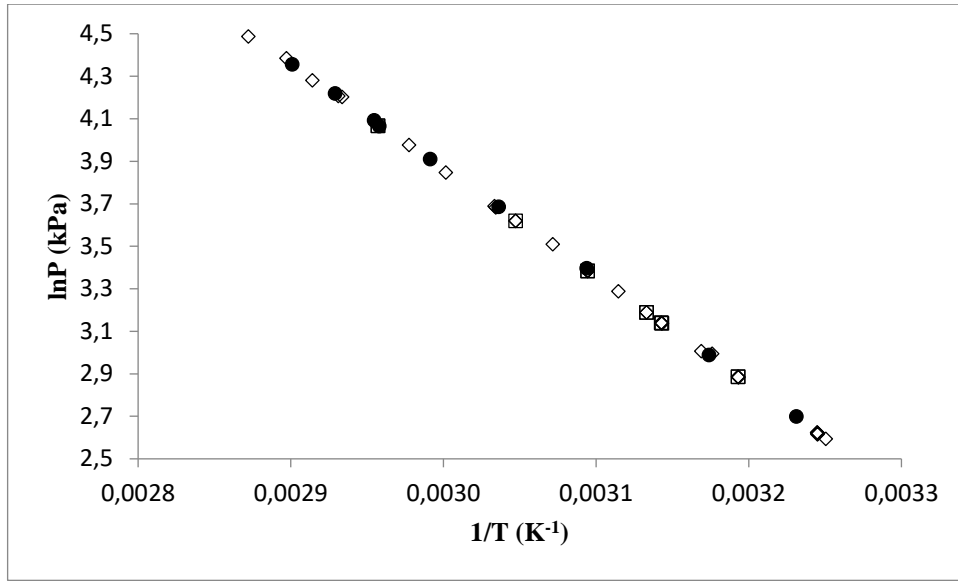


Figure 5.2: Vapour pressure data for ethanol. (●) Exp, This work; (□) (Satkiewicz, 1964); (△) (Perry & Green, 1999); (◇) (Von Wirkner , 1897).

Table 5.4: Comparison of the experimental vapour pressure data for ethanol to literature sources.

$T_{exp}$ (K)	$P_{exp}$ (kPa)	$\Delta T^a$ (K)	$\Delta T^b$ (K)	$\Delta T$ (K) <sup>c</sup>	$\Delta T/T^a$ (%)	$\Delta T/T^b$ (%)	$\Delta T/T^c$ (%)
351.23	99.95	0.2	0.1	0.4	0.06	0.03	0.11
344.71	77.93	0.5	0.4	0.1	0.15	0.12	0.04
341.41	67.92	0.3	0.2	0.0	0.09	0.07	0.01
338.45	59.91	0.2	0.2	0.2	0.05	0.07	0.05
338.06	58.30	0.1	0.1	0.1	0.03	0.04	0.03
334.29	49.90	0.2	0.4	0.1	0.05	0.12	0.04
329.35	39.88	0.0	0.3	0.2	0.01	0.09	0.08
323.22	29.87	0.2	0.2	0.2	0.05	0.05	0.05
315.06	19.86	0.0	0.4	0.3	0.00	0.12	0.10
309.48	14.86	0.0	0.1	0.0	0.00	0.04	0.00

$$\Delta T = |T_{exp} - T_{lit}|$$

$$\Delta T/T = 100 \left| \frac{T_{exp} - T_{lit}}{T_{exp}} \right|$$

<sup>a</sup> (Satkiewicz, 1964)

<sup>b</sup> (Perry & Green, 1999)

<sup>c</sup> (Von Wirkner, 1897)



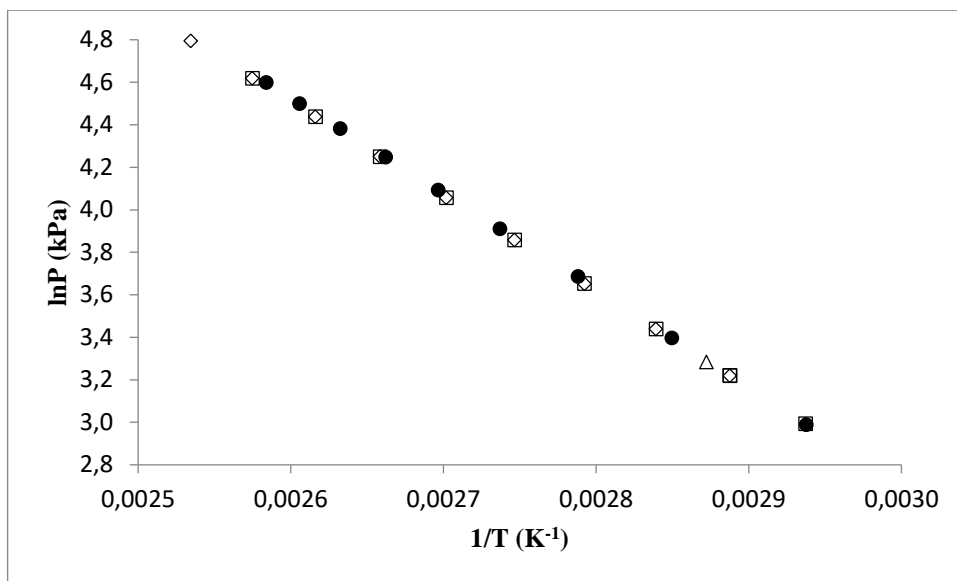


Figure 5.3: Vapour pressure data for pyridine. (●) Exp, This work; (□) (Chirico, et al., 1996); (Δ) (Perry & Green, 1999); (◇) (McCullough, et al., 1957).

Table 5.5: Comparison of the experimental vapour pressure data for pyridine to literature sources.

$T_{exp}$ (K)	$P_{exp}$ (kPa)	$\Delta T^a$ (K)	$\Delta T^b$ (K)	$\Delta T$ (K) <sup>c</sup>	$\Delta T/T^a$ (%)	$\Delta T/T^b$ (%)	$\Delta T/T^c$ (%)
383.76	89.94	0.4	0.1	0.5	0.12	0.03	0.12
379.86	79.93	0.4	0.1	0.5	0.11	0.04	0.12
375.62	69.92	0.4	0.0	0.4	0.11	0.01	0.11
370.83	59.91	0.3	0.6	0.3	0.08	0.17	0.09
365.36	49.90	0.2	0.7	0.2	0.05	0.20	0.06
358.79	39.88	0.2	0.4	0.2	0.06	0.12	0.07
350.91	29.87	0.0	0.3	0.1	0.01	0.08	0.02

$$\Delta T = |T_{exp} - T_{lit}|$$

$$\Delta T/T = 100 \left| \frac{T_{exp} - T_{lit}}{T_{exp}} \right|$$

<sup>a</sup> (Chirico, et al., 1996)

<sup>b</sup> (Perry & Green, 1999)

<sup>c</sup> (McCullough, et al., 1957)

The AADs and AARDs for the experimental vapour pressure as well as the literature sources are displayed in Table 5.6. The AARDs are well below 1 % and the AADs are below the experimental uncertainties for the temperature measurement thereby indicating a good agreement between the experimental and reference data.

Table 5.6: Average absolute deviation (AAD) and average absolute relative deviation (AARD) for the experimental vapour pressures using the reference sources.

Component	Reference	AAD [T] (K)	AARD [T] (%)
Cyclohexane	Scatchard, et al. (1939)	0.3	0.10
	Perry & Green (1999)	0.2	0.06
Ethanol	Satkiewicz (1964)	0.2	0.05
	Perry & Green (1999)	0.3	0.08
	Von Wirkner (1897)	0.2	0.05
Pyridine	Chirico, et al. (1996)	0.2	0.06
	Perry & Green (1999)	0.3	0.07
	McCullough, et al. (1957)	0.3	0.07

$AAD [T] = \frac{1}{N_p} \sum |T_{exp} - T_{lit}|$ , where  $N_p$  is the total number of points.

$$AARD [T] = \frac{100}{N_p} \sum \left| \frac{T_{exp} - T_{lit}}{T_{exp}} \right|$$

### 5.3 Phase Equilibrium Measurements and Modelling

The combined standard uncertainty for temperature and pressure is calculated by:

$$u_c(T) = \pm \sqrt{u_{cali}(\theta)^2 + u_{rep}(\theta)^2 + u_{std}(\theta)^2 + u_{fluct}(\theta)^2} \quad (5.4)$$

$u_{cali}(\theta)$  is the uncertainty induced by the calibration,  $u_{rep}(\theta)$  is the uncertainty due to measurement repeatability,  $u_{std}(\theta)$  is the standard uncertainty of the temperature or pressure sensor as reported by the manufacturer and  $u_{fluct}(\theta)$  is the fluctuation observed from the temperature or pressure unit display. Table 5.7 presents the numerical values for each of these terms.

Table 5.7: Uncertainties observed in temperature and pressure for the systems of interest

System	Variable	$U_{calibration}$	$U_{repeatability}$	$U_{standard}$	$U_{fluctuation}$
Vapour Pressure	Temperature	0.03	0.079	0.10	0.15
	Pressure	0.01	0.015	0.05	0.05
Ethanol/Cyclohexane	Temperature	0.03	0.117	0.10	0.36
	Pressure	0.01	0.030	0.05	0.10
Ethanol/Pyridine	Temperature	0.03	0.130	0.10	0.39
	Pressure	0.01	0.087	0.05	0.15
Water/Pyridine	Temperature	0.03	0.129	0.10	0.39
	Pressure	0.01	0.038	0.05	0.15

The combined standard uncertainty for composition is:

$$u_C(x_i) = \pm \sqrt{u_{cali}(x_i)^2 + u_{rep}(x_i)^2} \quad (5.5)$$

$u_{cali}(x_i)$  is the uncertainty induced by the mole composition calibration polynomial and  $u_{rep}(x_i)$  is the uncertainty due to measurement repeatability. Table 5.8 displays the numerical values for each of these terms.

Table 5.8: Uncertainties observed in composition for the systems of interest

System	Variable	$U_{calibration}$	$U_{repeatability}$
Ethanol/Cyclohexane	x	0.010	0.002
	y	0.010	0.002
Ethanol/Pyridine	x	0.006	0.006
	y	0.006	0.006
Water/Pyridine	x	0.015	0.003
	y	0.015	0.003

The combined expanded uncertainties were then calculated by multiplying the combined standard uncertainty by a coverage factor of 2 and are listed in Table 5.9. The values displayed for temperature, pressure and composition are averaged over all data points for each binary VLE system. A more detailed description of this method is presented in Appendix D.

Table 5.9: Combined expanded uncertainties for temperature, pressure and mole compositions for the VLE binary systems, averaged over all data points for each system

Component i	Component j	$U_C [T]^a$ (K)	$U_C (P)^a$ (kPa)	$U_C (x_i)^a$	$U_C (y_i)^a$
Ethanol	Cyclohexane	0.5	0.15	0.012	0.012
Ethanol	Pyridine	0.6	0.26	0.013	0.013
Pyridine	Water	0.6	0.20	0.018	0.018

<sup>a</sup> Expanded uncertainties calculated using a coverage factor of  $k = 2$

From Table 5.9, it can be seen that the uncertainties are large. This is due to the  $u_{fluct}(\theta)$  value incorporated in equation (5.4) to account for the high fluctuation in display pressure and resistance while operating the still at low pressures. The pressure control setup was unstable at pressures below 30 kPa. The value for  $u_{fluct}(\theta)$  consisted of the highest fluctuation observed as shown in Tables 5.7 and 5.8.

### 5.3.1 Test System: Ethanol (1) + Cyclohexane (4)

Figures 5.4 to 5.7 present the isobaric and isothermal VLE data for the ethanol (1) + cyclohexane (4) test system at 40 kPa and 313.15 K respectively. The purpose of measuring a test system is to validate the accuracy of the experimental procedure by comparing the measured experimental data to literature data.

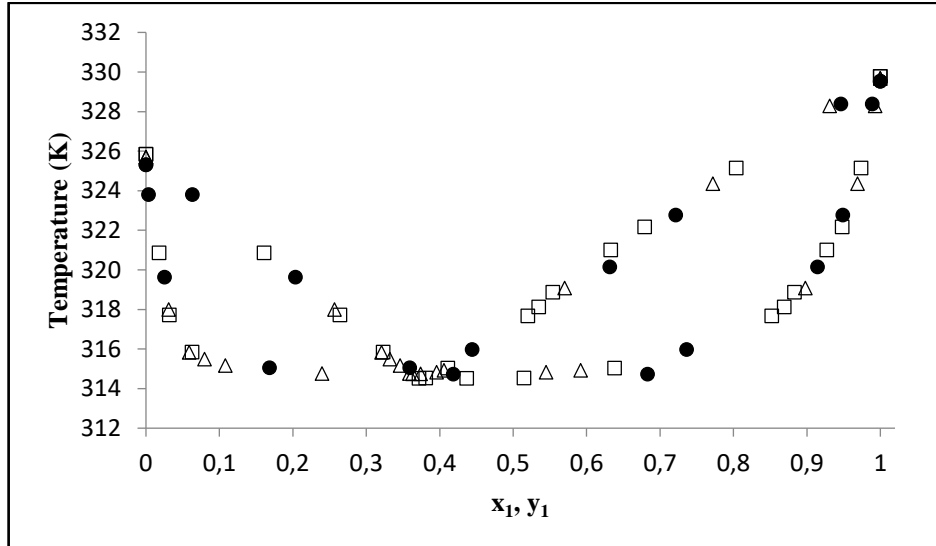


Figure 5.4: Isobaric VLE data for the ethanol (1) + cyclohexane (4) system at 40 kPa. (●) Exp, This work; (□) (Narasigadu, 2006); (Δ) (Bhowmath, 2008).

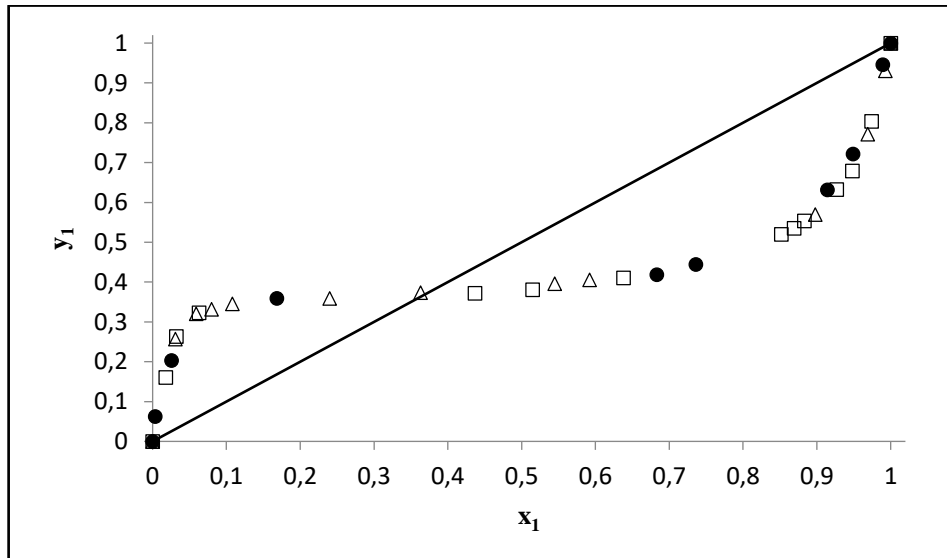


Figure 5.5: Isobaric x-y data for the ethanol (1) + cyclohexane (4) system at 40 kPa. (●) Exp, This work; (□) (Narasigadu, 2006); (Δ) (Bhowmath, 2008).

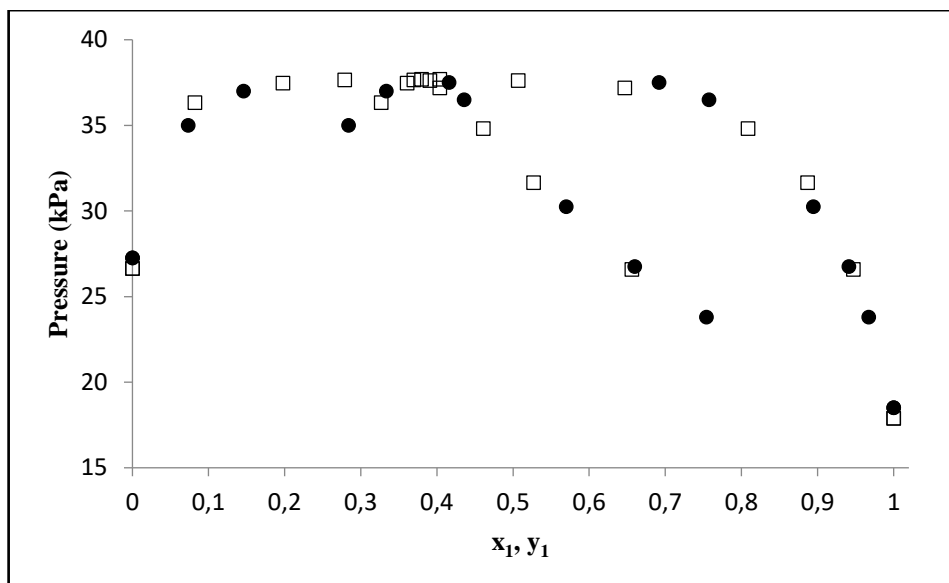


Figure 5.6: Isothermal VLE data for the ethanol (1) + cyclohexane (4) system at 313.15 K. (●) Exp, This work; (□) (Bhownath, 2008).

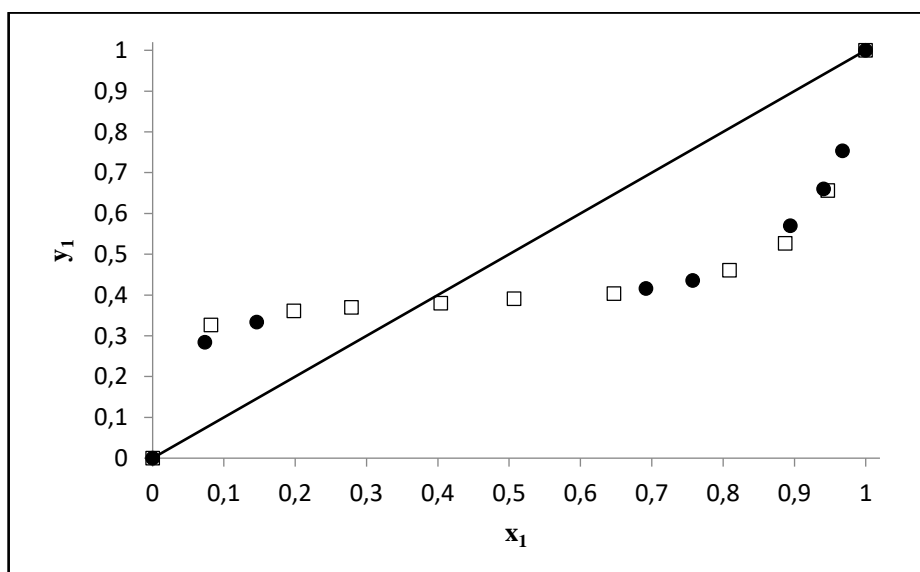


Figure 5.7: Isothermal x-y data for the ethanol (1) + cyclohexane (4) system at 313.15 K. (●) Exp, This work; (□) (Bhownath, 2008).

From the Figures, it can be seen that there is good correlation between the measured and literature data thereby indicating the correct operation of the VLE still with reproducible results. No regression and parameter fitting for this system was executed as these experiments were performed to validate the experimental method.

### 5.3.2 New Binary Phase Equilibrium Data

Phase equilibrium data for the binary systems ethanol (1) + pyridine (3) and water (2) + pyridine (3) systems were measured. The water/pyridine system was measured since the VLE data found in literature was inconsistent. The ethanol/pyridine system was measured since only three data sets exist in literature (isothermal data at 333.15 K, 338.15 K and 348.15 K) and there is no vapour composition data available for this system.

The isothermal and isobaric binary VLE data measurements were undertaken for ethanol (1) + pyridine (3) at 313.15 K, 100 kPa and 40 kPa respectively. The isothermal and isobaric VLE data measurements for water (2) + pyridine (3) were performed at 333.15 K and 40 kPa respectively. The operating conditions of each data system were influenced based on the process conditions, the characteristics of the systems and the limitations of the equipment.

The measured data were compared to predicted data using the PSRK and UNIFAC models from Aspen Plus®. The common thermodynamic models presented in literature for the regression of the VLE data for similar systems are the NRTL, Wilson and UNIQUAC. These models were selected for the regression along with combinations of these models with the Peng-Robinson equation of state (PR EoS) with the classical one - fluid mixing rule (PR-NRTL, PR-Wilson, PR-UNIQUAC) and the Peng-Robinson equation of state incorporating the Mathias Copeman alpha function (MC-alpha) and the Wong-Sandler mixing rules. (PR-MC-WS-NRTL, PR-MC-WS-Wilson, PR-MC-WS-UNIQUAC). Only the PR-MC-WS-activity coefficient models are presented since this model combination provided a better fit to the experimental data.

The regressed MC parameters are listed in Table 5.10. Table 5.11 presents the errors (AAD and AARD) in experimental vapour pressure data for each modelled data set. The AARDs are well below 1 % and the AADs are below the experimental uncertainties for the temperature and pressure measurements thereby indicating a good agreement between the experimental and modelled data.

Table 5.10: Regressed MC parameters (PR-MC-EoS)

Component	Model	C <sub>1,i</sub>	C <sub>2,i</sub>	C <sub>3,i</sub>	RMSE
Ethanol	PR-MC-WS	1.39	-1.16	2.57	0.43
Pyridine	PR-MC-WS	0.62	0.61	-0.55	0.15

RMSE: Residual mean square error:  $\sqrt{\frac{\sum_{t=1}^n (\theta_t - \hat{\theta}_t)^2}{n}}$ ;  $\theta_t$ : estimated data;  $\hat{\theta}_t$ : experimental data

Table 5.11: Deviations in the experimental vapour pressure data from modelled data using the PR EoS with the MC alpha function

Component	Model	AAD [P] (kPa)	AARD [P] (%)
Ethanol	PR-MC-WS	0.18	0.27
Pyridine	PR-MC-WS	0.06	0.09

$AAD [P] = \frac{1}{N_p} \sum |P_{exp} - P_{lit}|$ ,  $N_p$  is the total number of points.

$$AARD [P] = \frac{100}{N_p} \sum \left| \frac{P_{exp} - P_{lit}}{P_{exp}} \right|$$

In the sections to follow, the phase behaviour (P-x-y/T-x-y and x-y) for each binary system is presented comprising the comparison of the experimental, literature and predicted data as well as the comparison of the experimental and modelled data followed by the regressed model parameters for each data set, the AADs and AARDs of each data point and the total AAD and AARD for each system averaged over all data points.

#### Ethanol (1) + Pyridine (3) System: Comparison of Experimental Data to Predicted Data and Literature Data

Figures 5.8 to 5.11 displays the experimental isobaric VLE data for the binary system of ethanol (1) + pyridine (3) measured at 40 kPa and 100 kPa respectively while Figures 5.12 and 5.13 display the experimental isothermal VLE data measured at 313.15 K. The experimental measurements are compared to literature data where they are available and the predictive models from Aspen Plus®: PSRK and UNIFAC.

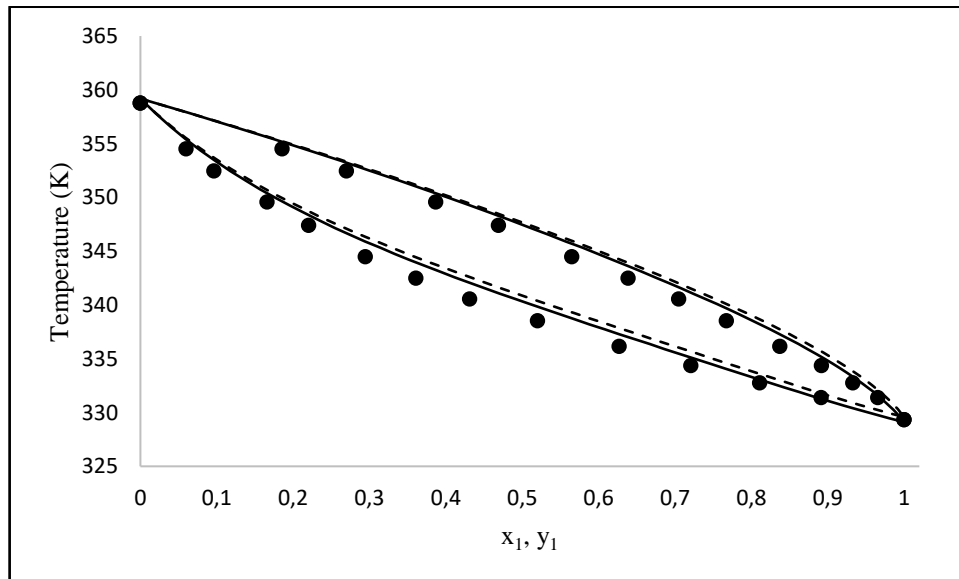


Figure 5.8: Isobaric VLE data for the ethanol (1) + pyridine (3) system at 40 kPa. (●) Exp, This work; (—) PSRK model; (----) UNIFAC model.

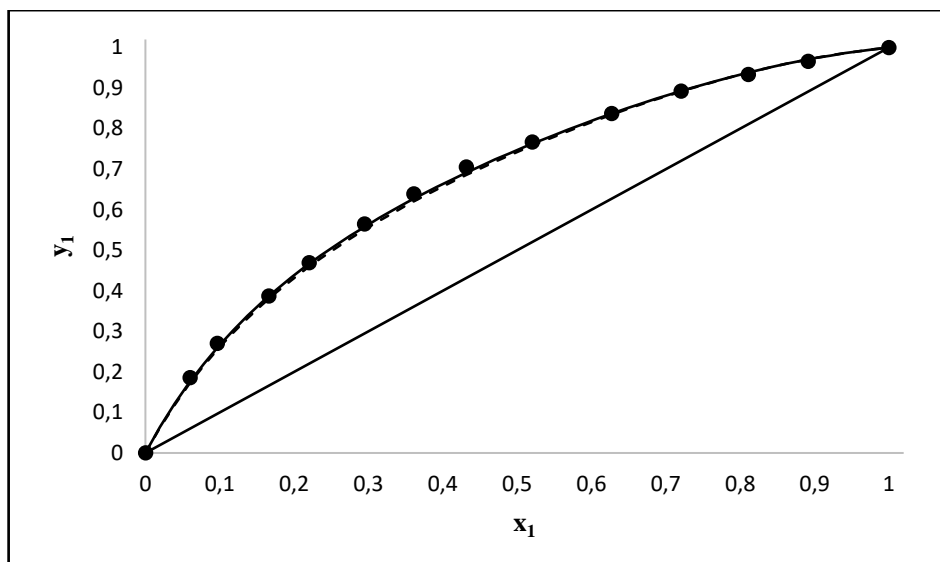


Figure 5.9: Isobaric x-y data for the ethanol (1) + pyridine (3) system at 40 kPa. (●) Exp, This work; (—) PSRK model; (----) UNIFAC model.

From Figures 5.8 and 5.9, it can be seen that the measured data correlate well with the predicted data from Aspen Plus® for the isobaric system at 40 kPa.

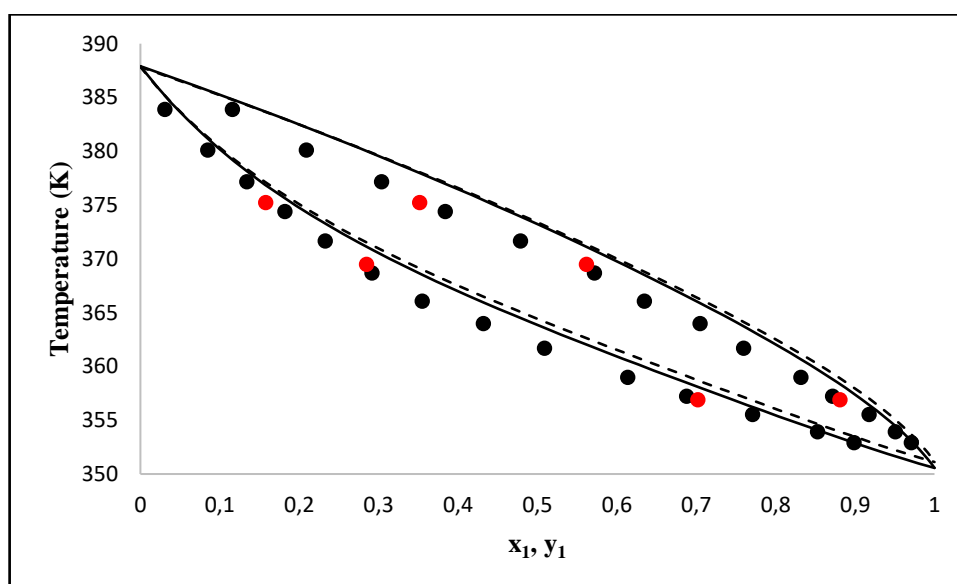


Figure 5.10: Isobaric VLE data for the ethanol (1) + pyridine (3) system at 100 kPa. (●) Exp, This work; (●) Exp, This work, Re-measured points; (—) PSRK model; (----) UNIFAC model.



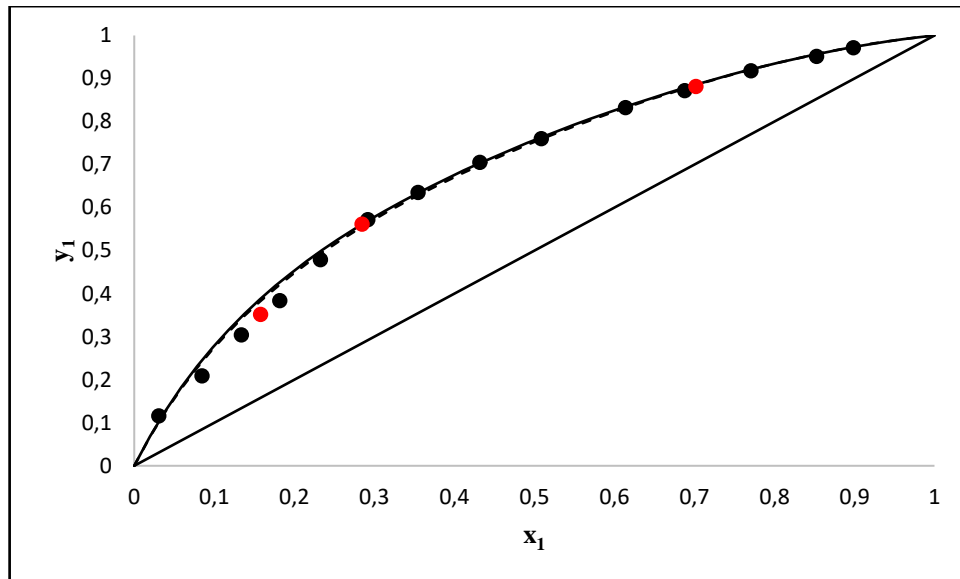


Figure 5.11: Isobaric x-y data for the ethanol (1) + pyridine (3) system at 100 kPa. (●) Exp, This work; (●) Exp, This work, Re-measured points; (—) PSRK model; (----) UNIFAC model.

In Figure 5.11 a good correlation between the measured and the predicted data is observed. However, the T-x-y diagram in Figure 5.10 show the measured temperatures are lower than the predicted temperatures at each data point. The data was re-measured (indicated by the red dots in the Figure) and the same trend observed. Although this measured data differs from the predicted data, the trend obtained is consistent. Since there exists no literature data for this system at the conditions measured, it can be concluded that either the models from Aspen Plus® does not represent the system at this condition well or there was an error with the equilibrium temperature reading from the VLE still used in this study due to the high fluctuations observed.

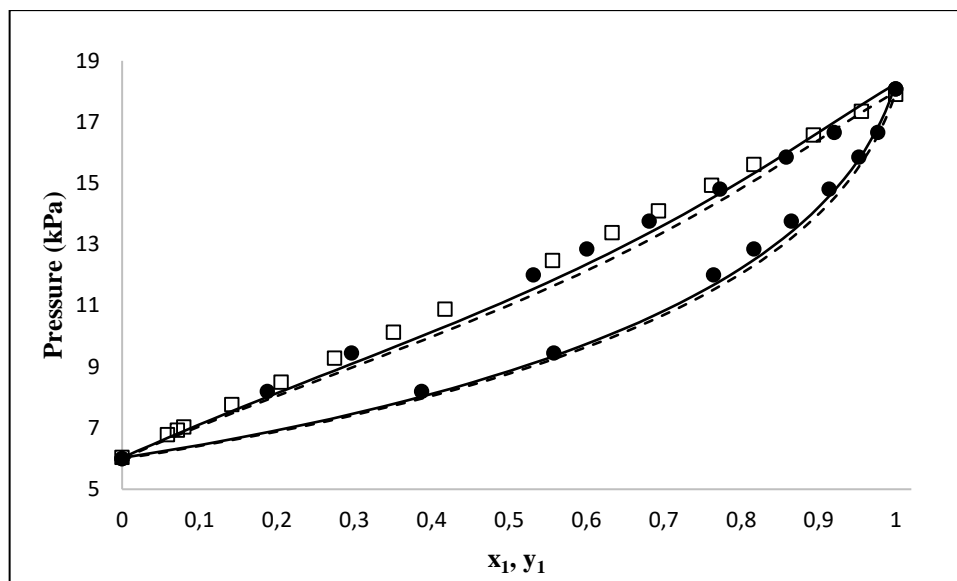


Figure 5.12: Isothermal VLE data for the ethanol (1) + pyridine (3) system at 313.15 K. (●) Exp, This work; (—) PSRK model; (---) UNIFAC model; (□) P-x data (Warycha, 1977).

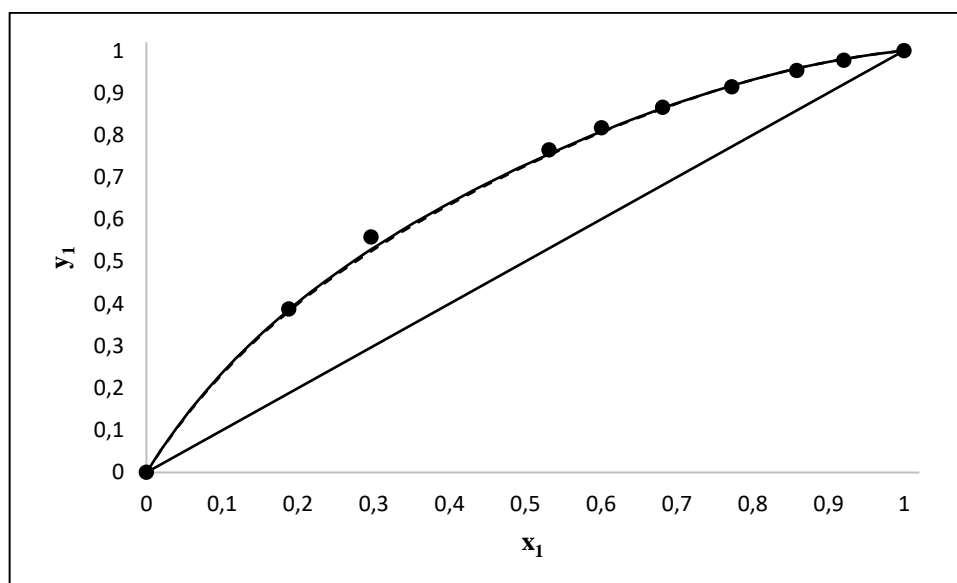


Figure 5.13: Isothermal x-y data for the ethanol (1) + pyridine (3) system at 313.15 K. (●) Exp, This work; (—) PSRK model; (---) UNIFAC model.

Figure 5.13 demonstrates a good correlation between the measured and the predicted data. The P-x-y diagram in Figure 5.12 shows the measured pressures for the liquid compositions are higher than the predicted pressures at each data point. However, the literature data measured by Warycha (1977) follows the same trend as the data measured in this study. Warycha (1977) used the static apparatus described by Janaszewski, et al (1982) for the determination of the P-x data for the ethanol/pyridine system. The data is measured by the following method: “A small amount of gas

is withdrawn from the apparatus to a reservoir; the equilibrium pressure in the apparatus and the pressure in the reservoir are then measured with the use of a manometer. The apparatus together with the reservoir form a closed system consisting of three parts: the gas volume in the reservoir, the gas volume in the apparatus, and the liquid volume in the apparatus. The increase in the number of moles of gas collected in the reservoir must be equal to the total decrease in the number of moles of both the gas and liquid phases in the apparatus. The temperatures and volumes of the gas phases in the reservoir and in the apparatus are known as well as their pressures before and after each measurement cycle. Hence both the increase in the amount of gas collected in the reservoir and the decrease in the amount of gas in the apparatus can be calculated using the equation of state for an ideal gas. Subtracting these two values from each other yields the amount of liquid evaporated” (Janaszewski, et al., 1982). Since the measured data in this work matches the literature data, it can be deduced that the predictive models from Aspen Plus® does not represent the system at this condition well.

### Ethanol (1) + Pyridine (3) System: Comparison of Experimental Data to Modelled Data

Figures 5.14 to 5.17 displays the isobaric VLE data for the binary system of ethanol (1) + pyridine (3) at 40 kPa and 100 kPa while Figures 5.18 and 5.19 display the isothermal VLE data at 313.15 K. The experimental measurements are compared to the modelled data from Aspen Plus®.

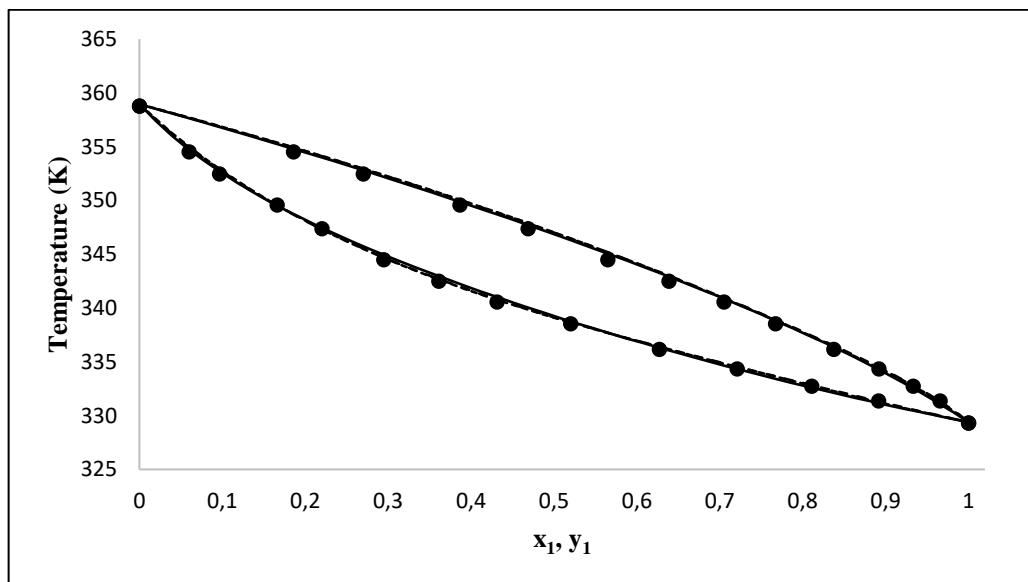


Figure 5.14: Isobaric VLE data for the ethanol (1) + pyridine (3) system at 40 kPa. (●) Exp, This work; (—) PR-MC-WS-NRTL model, (---) PR-MC-WS-Wilson model; (....) PR-MC-WS-UNIQUAC model.

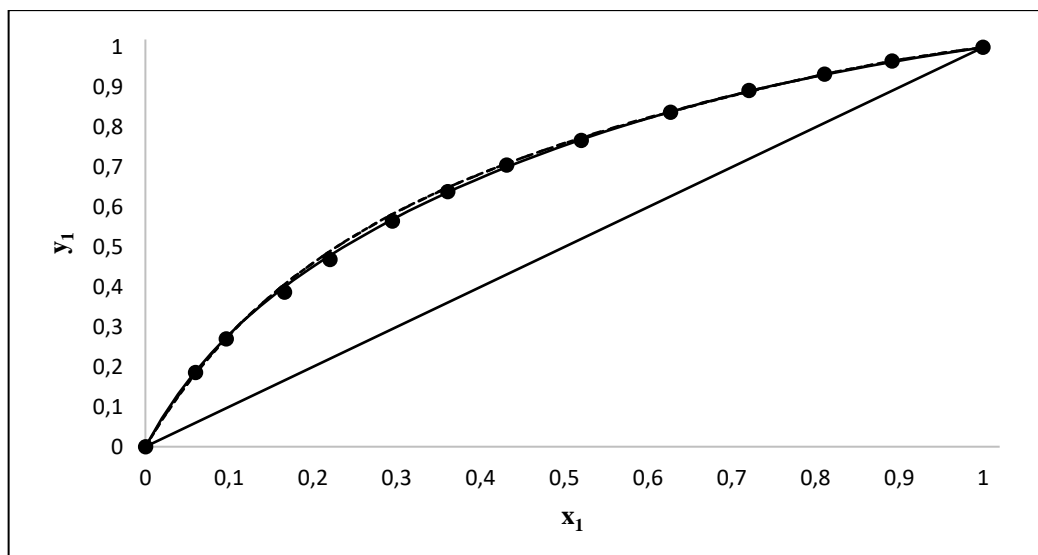


Figure 5.15: Isobaric x-y data for the ethanol (1) + pyridine (3) system at 40 kPa. (●) Exp, This work; (—) PR-MC-WS-NRTL model, (---) PR-MC-WS-Wilson model; (....) PR-MC-WS-UNIQUAC model.

From Figures 5.14 and 5.15, it can be seen that the measured data correlate well with the regressed data from Aspen Plus® for the 40 kPa isobaric system.

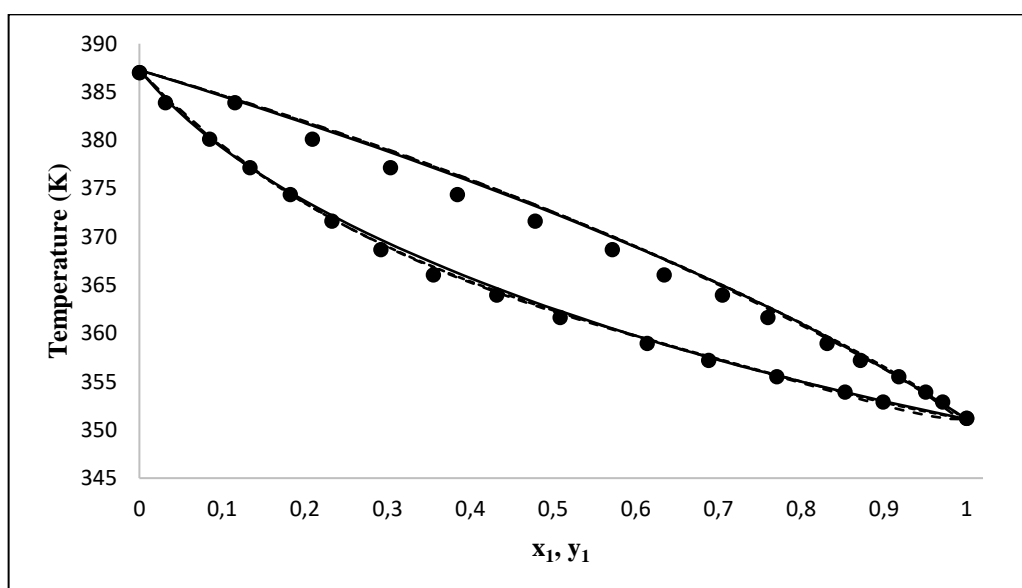


Figure 5.16: Isobaric VLE data for the ethanol (1) + pyridine (3) system at 100 kPa. (●) Exp, This work; (—) PR-MC-WS-NRTL model, (---) PR-MC-WS-Wilson model; (....) PR-MC-WS-UNIQUAC model.

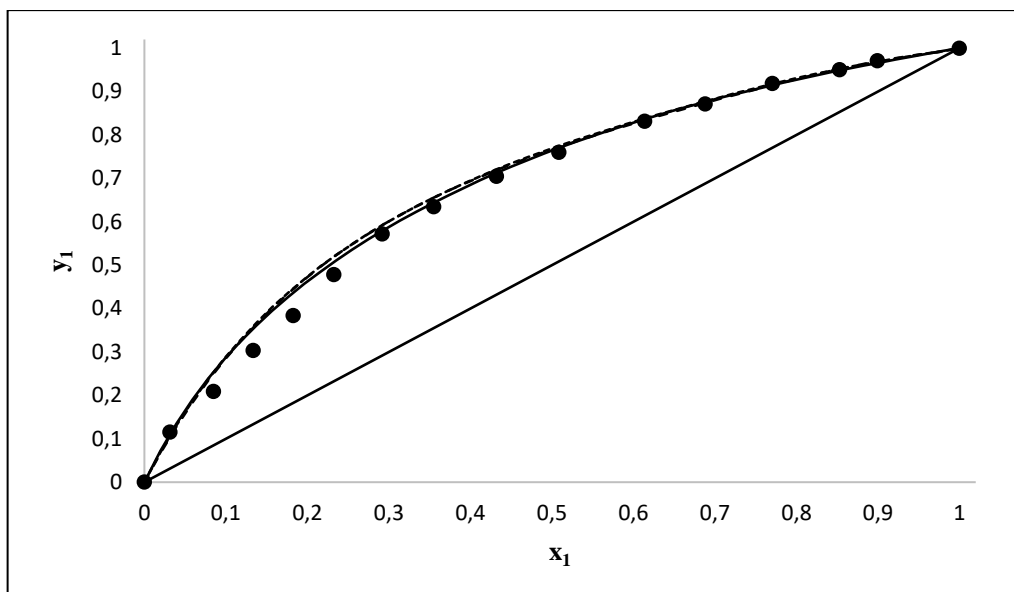


Figure 5.17: Isobaric x-y data for the ethanol (1) + pyridine (3) system at 100 kPa. (●) Exp, This work; (—) PR-MC-WS-NRTL model, (---) PR-MC-WS-Wilson model; (...) PR-MC-WS-UNIQUAC model.

In Figures 5.16 and 5.17, a fairly good correlation between the measured and the regressed data is observed with slight discrepancies. Figure 5.16 show the measured temperatures are lower than the regressed temperatures at each data point in the middle region while Figure 5.17 show the measured vapour compositions are lower than the regressed data in the ethanol rich region. However, as stated previously, the data was re-measured and the same trend observed. Furthermore, although this measured data differs from the regressed data, the trend obtained is consistent. Hence, it can be concluded that either the models from Aspen Plus® does not represent the system at this condition well or there was an error with the equilibrium temperature reading from the VLE still used in this study due to the high fluctuation observed.

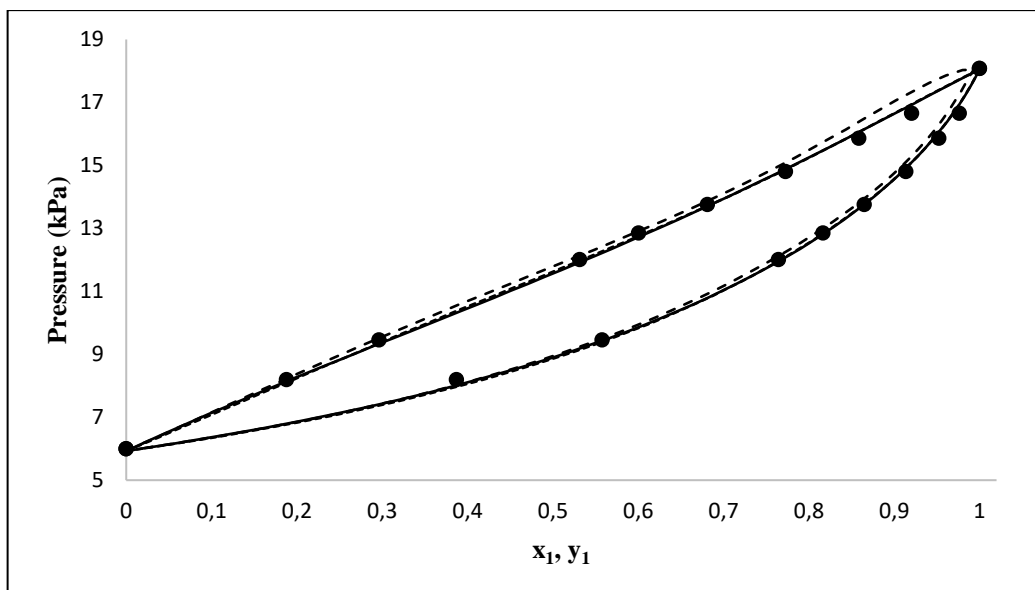


Figure 5.18: Isothermal VLE data for the ethanol (1) + pyridine (3) system at 313.15 K. (●) Exp, This work; (—) PR-MC-WS-NRTL model, (----) PR-MC-WS-Wilson model; (....) PR-MC-WS-UNIQUAC model.

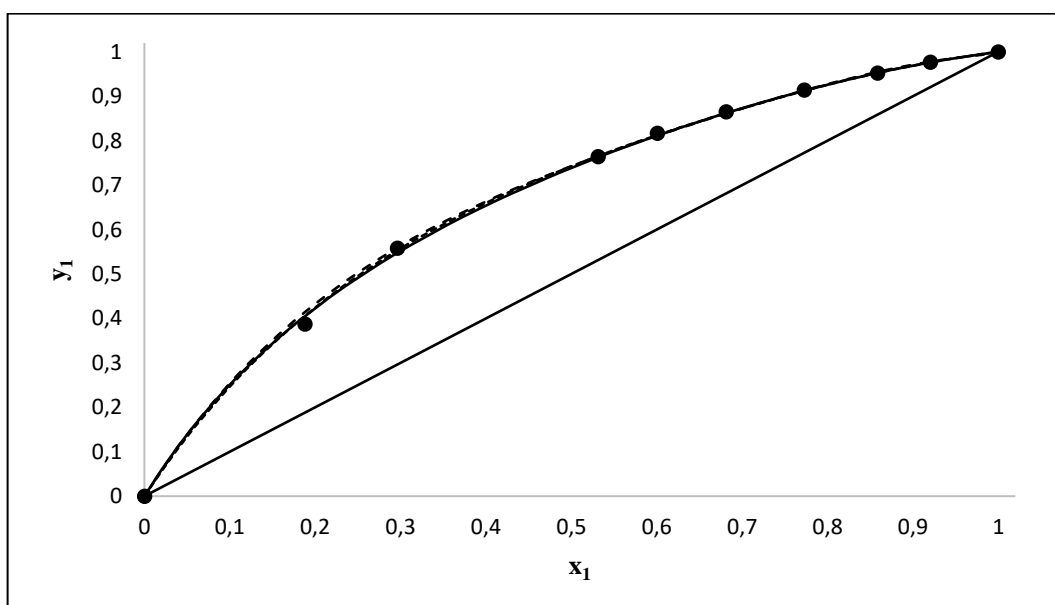


Figure 5.19: Isothermal x-y data for the ethanol (1) + pyridine (3) system at 313.15 K. (●) Exp, This work; (—) PR-MC-WS-NRTL model, (----) PR-MC-WS-Wilson model; (....) PR-MC-WS-UNIQUAC model.

From Figures 5.18 and 5.19, it can be seen that the regressed data closely follows the experimental data thereby demonstrating a good correlation between the measured and the regressed data. Tables 5.12 to 5.14 list the measured VLE data as well the deviation in temperature or pressure and vapour compositions between the experimental data and modelled data for each data point.

Tables 5.15 and 5.16 list the AADs and AARDs for each system averaged over all data points. The total AARD in each Table represents the combined AARDs for temperature or pressure and vapour compositions. Table 5.17 presents the regressed model parameters for each system.

Table 5.12: Comparison of the experimental VLE data to modelled data for the isobaric ethanol (1) + pyridine (3) system at 40 kPa

T (K)	x <sub>1</sub>	y <sub>1</sub>	ΔT <sup>a</sup> (K)	ΔT/T <sup>a</sup> (%)	Δy <sub>1</sub> <sup>a</sup>	Δy <sub>1</sub> /y <sub>1</sub> <sup>a</sup> (%)	ΔT <sup>b</sup> (K)	ΔT/T <sup>b</sup> (%)	Δy <sub>1</sub> <sup>b</sup>	Δy <sub>1</sub> /y <sub>1</sub> <sup>b</sup> (%)	ΔT <sup>c</sup> (K)	ΔT/T <sup>c</sup> (%)	Δy <sub>1</sub> <sup>c</sup>	Δy <sub>1</sub> /y <sub>1</sub> <sup>c</sup> (%)
354.52	0.060	0.186	0.1	0.03	0.003	1.83	0.3	0.09	0.001	0.42	0.4	0.11	0.003	1.52
352.48	0.096	0.270	0.2	0.05	0.003	1.01	0.3	0.09	0.002	0.65	0.4	0.11	0.000	0.03
349.60	0.166	0.387	0.1	0.04	0.013	3.45	0.2	0.04	<b>0.020</b>	5.12	0.1	0.03	<b>0.020</b>	5.05
347.40	0.220	0.469	0.0	0.00	0.009	1.99	0.2	0.04	<b>0.020</b>	4.23	0.2	0.04	<b>0.020</b>	4.35
344.50	0.295	0.565	0.4	0.11	0.004	0.74	0.1	0.04	<b>0.017</b>	2.96	0.1	0.03	<b>0.018</b>	3.12
342.51	0.361	0.639	0.4	0.11	0.002	0.27	0.1	0.04	0.010	1.56	0.1	0.02	0.011	1.64
340.57	0.431	0.705	0.4	0.11	0.005	0.73	0.2	0.05	0.004	0.55	0.1	0.04	0.004	0.53
338.56	0.520	0.767	0.2	0.04	0.002	0.24	0.1	0.02	0.007	0.88	0.1	0.01	0.006	0.73
336.18	0.627	0.837	0.1	0.02	0.001	0.18	0.2	0.05	0.003	0.31	0.2	0.05	0.001	0.12
334.37	0.721	0.892	0.1	0.03	0.002	0.20	0.1	0.03	0.002	0.20	0.1	0.03	0.003	0.31
332.77	0.811	0.933	0.2	0.07	0.001	0.13	0.0	0.00	0.000	0.04	0.1	0.02	0.001	0.05
331.41	0.892	0.966	0.3	0.10	0.002	0.19	0.2	0.05	0.000	0.00	0.2	0.07	0.000	0.01

$$\Delta T = |T_{exp} - T_{calc}|$$

$$\Delta y_1 = |y_{1exp} - y_{1calc}|$$

$$\Delta T/T = 100 \left| \frac{T_{exp} - T_{calc}}{T_{exp}} \right|$$

$$\Delta y_1/y_1 = 100 \left| \frac{y_{1exp} - y_{1calc}}{y_{1exp}} \right|$$

<sup>a</sup> PR-MC-WS-NRTL model

<sup>b</sup> PR-MC-WS-Wilson model

<sup>c</sup> PR-MC-WS-UNIQUAC model

From Table 5.12, the deviations are below the experimental uncertainties except for three points with slight deviations in vapour composition for the PR-MC-WS-Wilson and PR-MC-WS-UNIQUAC models ( $\Delta y = 0.017 - 0.020$  as opposed to the vapour composition uncertainty of 0.013).



Table 5.13: Comparison of the experimental VLE data to modelled data for the ethanol (1) + pyridine (3) system at 100 kPa

T (K)	x <sub>1</sub>	y <sub>1</sub>	ΔT <sup>a</sup> (K)	ΔT/T <sup>a</sup> (%)	Δy <sub>1</sub> <sup>a</sup>	Δy <sub>1</sub> /y <sub>1</sub> <sup>a</sup> (%)	ΔT <sup>b</sup> (K)	ΔT/T <sup>b</sup> (%)	Δy <sub>1</sub> <sup>b</sup>	Δy <sub>1</sub> /y <sub>1</sub> <sup>b</sup> (%)	ΔT <sup>c</sup> (K)	ΔT/T <sup>c</sup> (%)	Δy <sub>1</sub> <sup>c</sup>	Δy <sub>1</sub> /y <sub>1</sub> <sup>c</sup> (%)
383.89	0.031	0.116	0.3	0.07	0.006	5.18	0.5	0.13	0.013	10.92	0.4	0.11	0.010	8.52
380.09	0.085	0.209	0.1	0.03	<b>0.046</b>	21.86	0.4	0.10	<b>0.042</b>	19.98	0.2	0.06	<b>0.045</b>	21.69
377.16	0.134	0.304	0.0	0.00	<b>0.051</b>	16.94	0.1	0.03	<b>0.054</b>	17.84	0.0	0.00	<b>0.057</b>	18.70
374.39	0.182	0.384	0.2	0.05	<b>0.051</b>	13.36	0.1	0.03	<b>0.060</b>	15.55	0.0	0.01	<b>0.061</b>	15.93
371.64	0.233	0.479	0.5	0.14	<b>0.029</b>	6.09	0.2	0.06	<b>0.041</b>	8.62	0.2	0.06	<b>0.042</b>	8.73
368.68	0.292	0.572	<b>0.9</b>	0.25	0.007	1.28	0.5	0.14	<b>0.020</b>	3.58	0.6	0.16	<b>0.021</b>	3.60
366.06	0.355	0.635	<b>0.9</b>	0.28	0.010	1.52	0.6	0.16	<b>0.021</b>	3.30	<b>0.7</b>	0.19	<b>0.021</b>	3.35
363.97	0.432	0.705	0.6	0.18	0.008	1.08	0.3	0.07	<b>0.014</b>	2.04	0.4	0.10	<b>0.016</b>	2.24
361.67	0.509	0.760	0.6	0.16	0.010	1.37	0.3	0.09	0.012	1.61	0.4	0.12	<b>0.015</b>	1.95
358.97	0.614	0.832	0.4	0.11	0.005	0.61	0.3	0.10	0.003	0.32	0.4	0.12	0.006	0.78
357.22	0.688	0.872	0.3	0.08	0.004	0.51	0.3	0.09	0.002	0.23	0.4	0.11	0.006	0.66
355.52	0.771	0.918	0.1	0.03	0.003	0.35	0.1	0.01	0.003	0.33	0.2	0.04	0.001	0.06
353.92	0.853	0.951	0.0	0.00	0.002	0.21	0.3	0.08	0.001	0.14	0.1	0.03	0.002	0.17
352.90	0.899	0.971	0.1	0.02	0.005	0.55	0.3	0.09	0.002	0.17	0.0	0.01	0.002	0.24

$$\Delta T = |T_{exp} - T_{calc}|$$

$$\Delta y_1 = |y_{1exp} - y_{1calc}|$$

$$\Delta T/T = 100 \left| \frac{T_{exp} - T_{calc}}{T_{exp}} \right|$$

$$\Delta y_1/y_1 = 100 \left| \frac{y_{1exp} - y_{1calc}}{y_{1exp}} \right|$$

<sup>a</sup> PR-MC-WS-NRTL model

<sup>b</sup> PR-MC-WS-Wilson model

<sup>c</sup> PR-MC-WS-UNIQUAC model

From table 5.13, the deviations are below the experimental uncertainties for the temperature measurement ( $\Delta T$  [K] = 0.6) except for two points ( $\Delta T$  [K] = 0.9) for the PR-MC-WS-NRTL model and one point ( $\Delta T$  [K] = 0.7) for the PR-MC-WS-UNIQUAC model. There is a greater discrepancy in the vapour composition with an error in the range of  $\Delta y = 0.014 - 0.061$ . However, as stated previously, the data was re-measured and the same consistent trend

observed. Therefore, it can be concluded that either the models from Aspen Plus® does not represent the system at this condition well or there was an error with the equilibrium temperature reading from the VLE still used in this study due to the high fluctuation observed.

Table 5.14: Comparison of the experimental VLE data to modelled data for the ethanol (1) + pyridine (3) system at 313.15 K.

T (K)	x <sub>1</sub>	y <sub>1</sub>	ΔP <sup>a</sup> (K)	ΔP/P <sup>a</sup> (%)	Δy <sub>1</sub> <sup>a</sup>	Δy <sub>1</sub> /y <sub>1</sub> <sup>a</sup> (%)	ΔP <sup>b</sup> (K)	ΔP/P <sup>b</sup> (%)	Δy <sub>1</sub> <sup>b</sup>	Δy <sub>1</sub> /y <sub>1</sub> <sup>b</sup> (%)	ΔP <sup>c</sup> (K)	ΔP/P <sup>c</sup> (%)	Δy <sub>1</sub> <sup>c</sup>	Δy <sub>1</sub> /y <sub>1</sub> <sup>c</sup> (%)
8.20	0.188	0.387	0.01	0.08	<b>0.018</b>	4.63	0.00	0.04	<b>0.027</b>	7.04	0.01	0.09	<b>0.019</b>	4.98
9.45	0.296	0.558	0.01	0.08	0.011	1.93	0.00	0.00	0.001	0.21	0.01	0.06	0.005	0.87
12.00	0.532	0.764	0.01	0.07	0.001	0.17	0.00	0.00	0.001	0.16	0.01	0.05	0.001	0.19
12.85	0.601	0.817	0.01	0.08	0.005	0.59	0.00	0.02	0.005	0.60	0.01	0.07	0.004	0.48
13.76	0.681	0.865	0.00	0.00	0.003	0.33	0.01	0.05	0.004	0.46	0.00	0.00	0.003	0.38
14.81	0.773	0.914	0.01	0.03	0.001	0.11	0.01	0.08	0.001	0.08	0.00	0.03	0.002	0.17
15.86	0.859	0.952	0.01	0.05	0.000	0.02	0.02	0.12	0.002	0.25	0.01	0.05	0.000	0.04
16.66	0.920	0.977	0.01	0.04	0.001	0.06	0.02	0.12	0.001	0.10	0.01	0.04	0.000	0.03

$$\Delta P = |P_{exp} - P_{calc}|$$

$$\Delta y_1 = |y_{1exp} - y_{1calc}|$$

$$\Delta P/P = 100 \left| \frac{P_{exp} - P_{calc}}{P_{exp}} \right|$$

$$\Delta y_1/y_1 = 100 \left| \frac{y_{1exp} - y_{1calc}}{y_{1exp}} \right|$$

<sup>a</sup> PR-MC-WS-NRTL model

<sup>b</sup> PR-MC-WS-Wilson model

<sup>c</sup> PR-MC-WS-UNIQUAC model

From Table 5.14, the deviations are well below the experimental uncertainty for the pressure measurement. Regarding the deviations observed in vapour composition, there is only one point for each model that lies outside the experimental uncertainty.

Table 5.15: Data regression deviations for the isobaric ethanol (1) + pyridine (3) binary system.

System	Model	AAD [T] (K)	AARD [T] (%)	AAD y <sub>1</sub>	AARD [y <sub>1</sub> ] (%)	AAD y <sub>2</sub>	AARD [y <sub>2</sub> ] (%)	Total AARD (%)
40 kPa	PR-MC-WS-NRTL	0.2	0.05	0.004	0.90	0.003	1.44	2.39
	PR-MC-WS-Wilson	0.1	0.04	0.007	1.42	0.006	1.70	3.16
	PR-MC-WS-UNIQUAC	0.2	0.04	0.007	1.47	0.006	1.69	3.20
100 kPa	PR-MC-WS-NRTL	0.3	0.09	0.017	5.05	0.015	4.75	9.90
	PR-MC-WS-Wilson	0.3	0.08	0.020	6.03	0.018	4.37	10.47
	PR-MC-WS-UNIQUAC	0.3	0.07	0.022	6.17	0.019	4.88	11.12

$$\text{AAD [T]} = \frac{1}{N_p} \sum |T_{exp} - T_{calc}|, N_p \text{ is the total number of data points}$$

$$\text{AAD [y}_i] = \frac{1}{N_p} \sum |y_{1exp} - y_{1calc}|,$$

$$\text{AARD [T]} = \frac{100}{N_p} \sum \left| \frac{T_{exp} - T_{calc}}{T_{exp}} \right|$$

$$\text{AARD [y}_i] = \frac{100}{N_p} \sum \left| \frac{y_{1exp} - y_{1calc}}{y_{1exp}} \right|$$

In Tables 5.15 and 5.16, it can be seen that the thermodynamic model with the lowest deviation is the PR-MC-WS–NRTL for the 40 kPa system (AARD = 2.39 %), hence the model parameters calculated with the use of this combination (displayed in Table 5.17) were selected for the ethanol (1) + pyridine (3) system.

Table 5.16: Data regression deviations for the isothermal ethanol (1) + pyridine (3) binary system.

System	Model	AAD [P] (kPa)	AARD [P] (%)	AAD $y_1$	AARD [ $y_1$ ] (%)	AAD $y_2$	AARD [ $y_2$ ] (%)	Total AARD (%)
313.15 K	PR-MC-WS-NRTL	0.01	0.04	0.005	1.00	0.004	1.97	3.01
	PR-MC-WS-Wilson	0.01	0.05	0.005	1.13	0.004	2.27	3.45
	PR-MC-WS-UNIQUAC	0.00	0.04	0.005	0.92	0.004	1.83	2.80

$$\text{AAD [P]} = \frac{1}{N_p} \sum |P_{exp} - P_{calc}|, N_p \text{ is the total number of data points}$$

$$\text{AAD } [y_1] = \frac{1}{N_p} \sum |y_{1exp} - y_{1calc}|$$

$$\text{AARD [P]} = \frac{100}{N_p} \sum \left| \frac{P_{exp} - P_{calc}}{P_{exp}} \right|$$

$$\text{AARD } [y_1] = \frac{100}{N_p} \sum \left| \frac{y_{1exp} - y_{1calc}}{y_{1exp}} \right|$$

Table 5.17: Model parameters regressed for the ethanol (1) + pyridine (3) binary system

System	Model	$k_{ij}^a$	$a_{ij}^b$	$a_{ji}^b$	$b_{ij}^b$	$b_{ji}^b$	$\alpha_{ij}^b$	RMSE <sup>c</sup>
40 kPa	PR-MC-WS-NRTL	0.04			-383.65	607.83	0.3	3.43
	PR-MC-WS-Wilson	0.21	-0.69	-2.26	562.68	460.71		3.59
	PR-MC-WS-UNIQUAC	0.30			-518.79	357.35		3.41
100 kPa	PR-MC-WS-NRTL	0.11			-456.65	684.21	0.3	11.25
	PR-MC-WS-Wilson	0.36	1.52	-24.83	43.14	-4146.41		11.32
	PR-MC-WS-UNIQUAC	0			-714.05	415.79		10.82
313.15 K	PR-MC-WS-NRTL	-0.30			64.34	165.97	0.3	4.14
	PR-MC-WS-Wilson	0.35	2.91	-24.83	-388.22	-4146.41		11.32
	PR-MC-WS-UNIQUAC	0.31			-474.50	338.36		4.01

<sup>a</sup> WS mixing rule parameter incorporated into the PR EoS

<sup>b</sup> NRTL/Wilson/UNIQUAC model parameters

<sup>c</sup> RMSE: Residual mean square error

## Water (2) + Pyridine (3) System: Comparison of Experimental Data to Predicted Data and Literature Data

Figures 5.20 to 5.23 displays the isobaric and isothermal VLE data for the binary system of water (2) + pyridine (3) at 40 kPa and 333.15 K respectively. The experimental measurements are compared to literature data where they are available and the predictive models from Aspen Plus®: PSRK and UNIFAC.

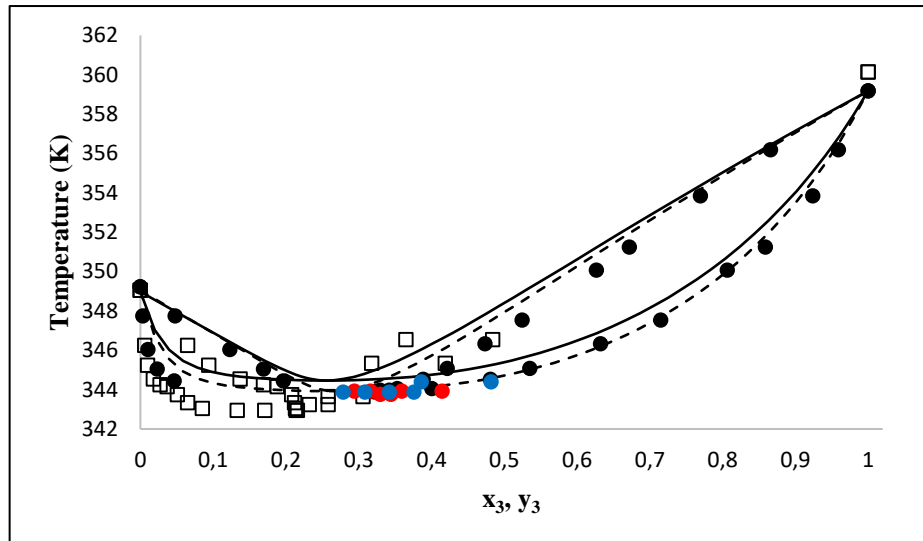


Figure 5.20: Isobaric VLE data for the water (2) + pyridine (3) system at 40 kPa. (●) Exp, This work; (●) Exp, This work, Re-measured points; (●) Exp, This work, Re-measured points; (—) PSRK model; (----) UNIFAC model; (□) (Fowler, 1952).

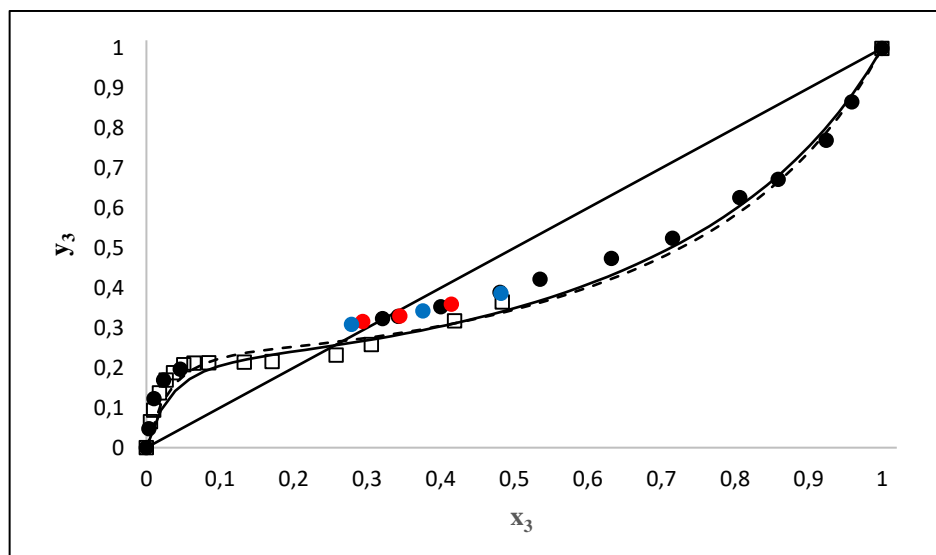


Figure 5.21: Isobaric x-y data for the water (2) + pyridine (3) system at 40 kPa. (●) Exp, This work; (●) Exp, This work, Re-measured points; (●) Exp, This work, Re-measured points; (—) PSRK model; (----) UNIFAC model; (□) (Fowler, 1952).

From Figures 5.20 and 5.21, it can be seen that the measured data fits the predictive models well at/near the pure component vapour pressures however, there is a discrepancy in the middle region, near and at the azeotropic point. In Figure 5.20, the literature data measured by Fowler (1952) does not fit the measured data in this study neither does it fit the predictive models from Aspen Plus®. Fowler (1949) used the equilibrium still proposed by Gillespie (1946) to acquire the binary VLE data for the water/pyridine system. In this still, the condensed vapour sample and the liquid sample were not in equilibrium. Hence, Fowler (1949) modified the still by introducing a liquid trap below the detachment chamber in order to obtain a sample of the liquid in equilibrium with the vapour. However, the setup of the still had further problems; “partial condensation was possible at the temperature well, sampling interrupted the operation, and the mass transfer in the Cottrell pump was not satisfactory because of the short contact time” (Pokki, 2004). These are possible reasons for the poor data produced. Detailed explanations of the equilibrium still design and drawbacks can be found in the following texts: Fowler (1949), Raal & Muhlbaüer (1998) and Pokki (2004). In Figure 5.21, the x-y plot shows that the literature data fairly fits the predictive models thereby suggesting a discrepancy in their temperature measurements.

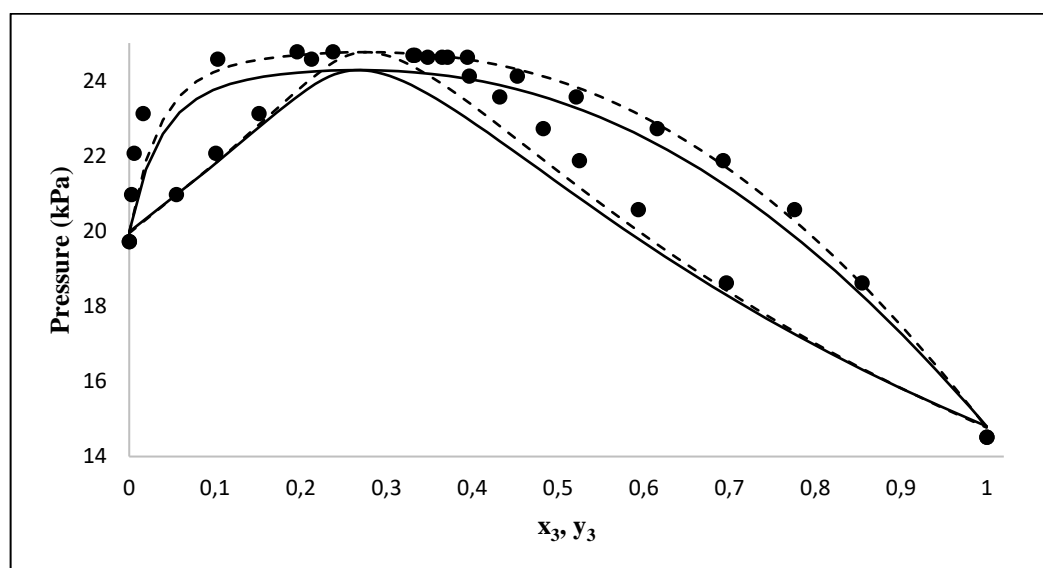


Figure 5.22: Isothermal VLE data for the water (2) + pyridine (3) system at 333.15 K. (●) Exp, This work; (—) PSRK model; (---) UNIFAC model.

A similar trend is observed in Figures 5.22 and 5.23. The measured data fits the predictive models well at and near the pure components vapour pressures however, there is a discrepancy in the middle region, near and at the azeotropic point. Possible reasons for this outcome will be discussed in the sections to follow.

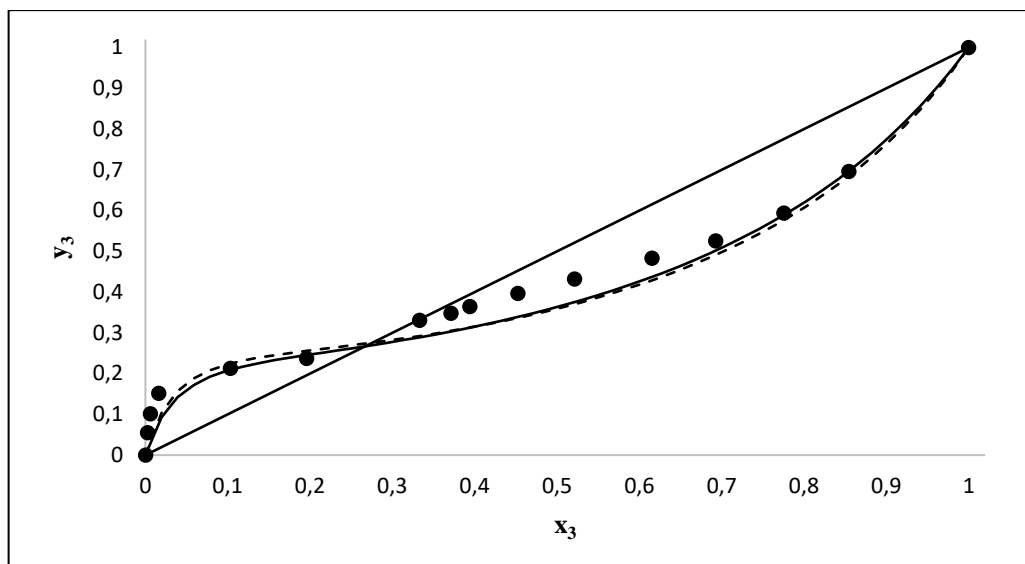


Figure 5.23: Isothermal x-y data for the water (2) + pyridine (3) system at 333.15 K. (●) Exp, This work; (—) PSRK model; (---) UNIFAC model.

#### Water (2) + Pyridine (3) System: Comparison of Experimental Data to Modelled Data

Figures 5.24 to 5.27 displays the isobaric and isothermal VLE data for the binary system of water (2) + pyridine (3) at 40 kPa and 333.15 K respectively. The experimental measurements are compared to the modelled data from Aspen Plus®.

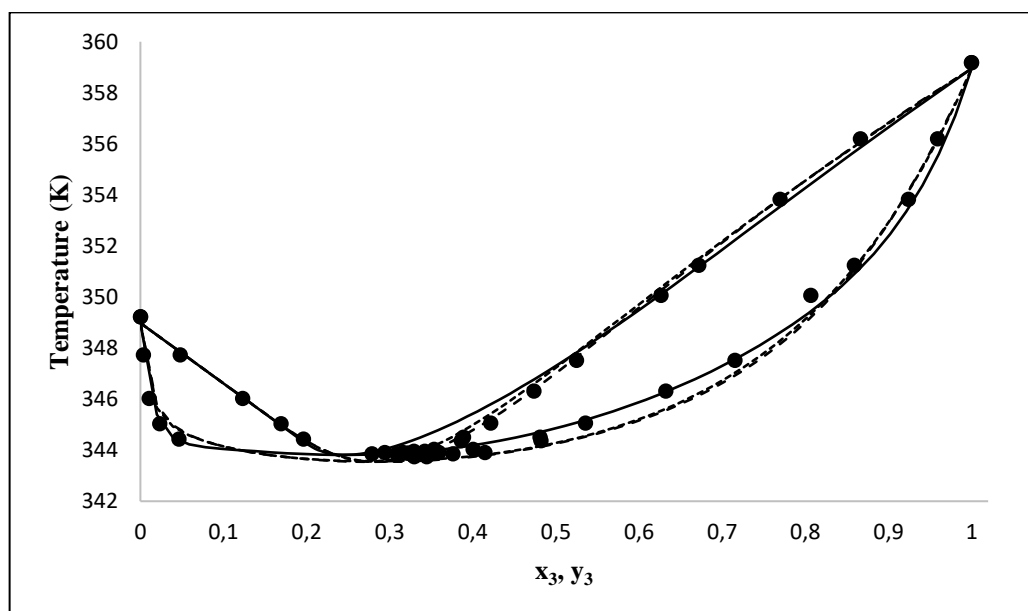


Figure 5.24: Isobaric VLE data for the water (2) + pyridine (3) system at 40 kPa. (●) Exp, This work; (—) PR-MC-WS-NRTL model, (---) PR-MC-WS-Wilson model; (...) PR-MC-WS-UNIQUAC model.

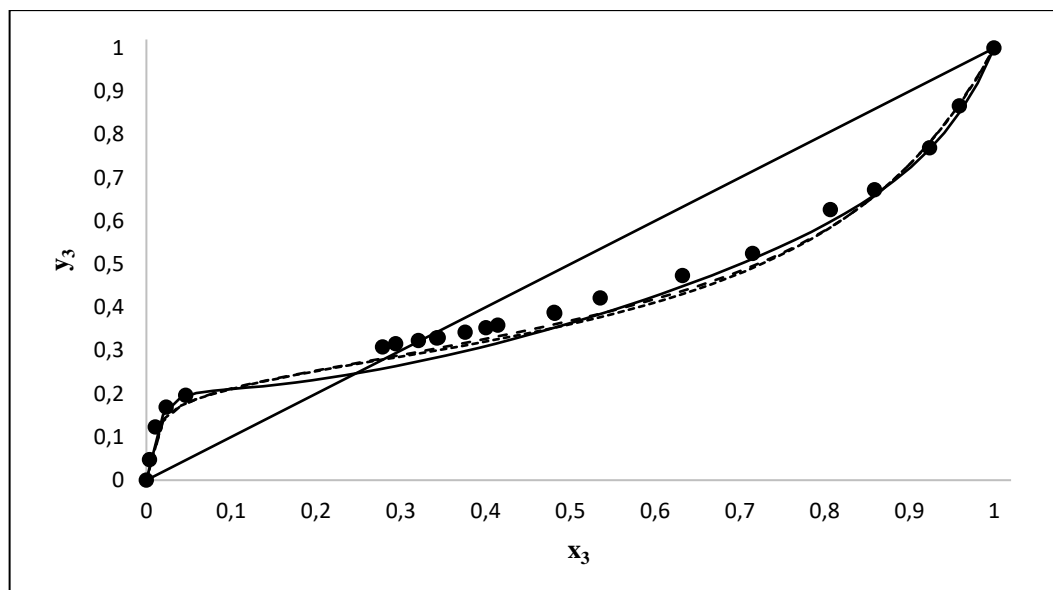


Figure 5.25: Isobaric x-y data for the water (2) + pyridine (3) system at 40 kPa. (●) Exp, This work; (—) PR-MC-WS-NRTL model, (----) PR-MC-WS-Wilson model; (....) PR-MC-WS-UNIQUAC model.

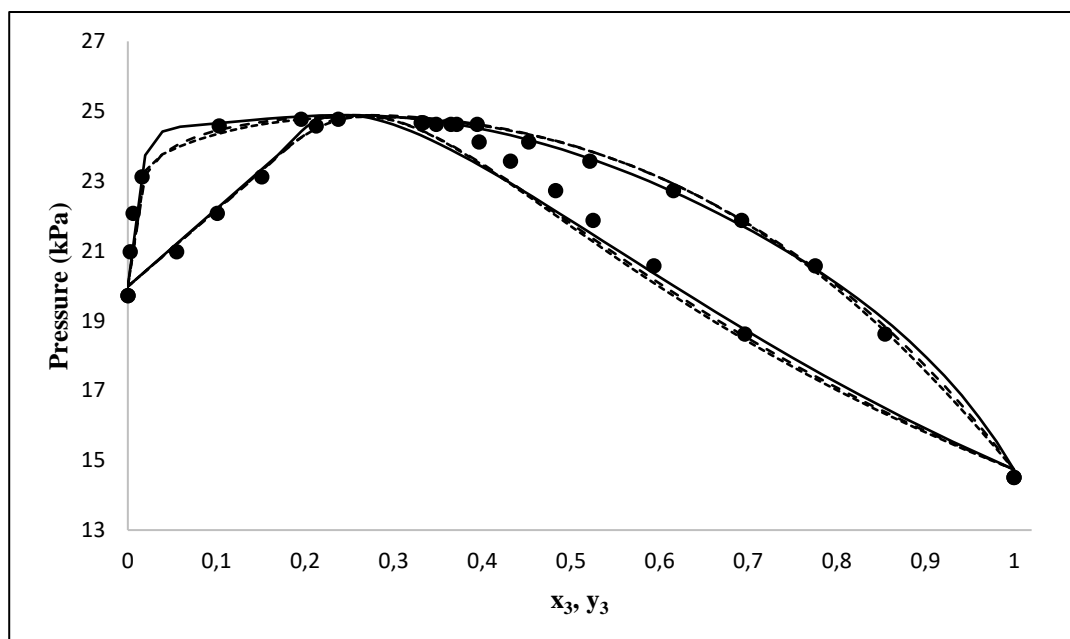


Figure 5.26: Isothermal VLE data for the water (2) + pyridine (3) system at 333.15 K. (●) Exp, This work; (—) PR-MC-WS-NRTL model, (----) PR-MC-WS-Wilson model; (....) PR-MC-WS-UNIQUAC model.



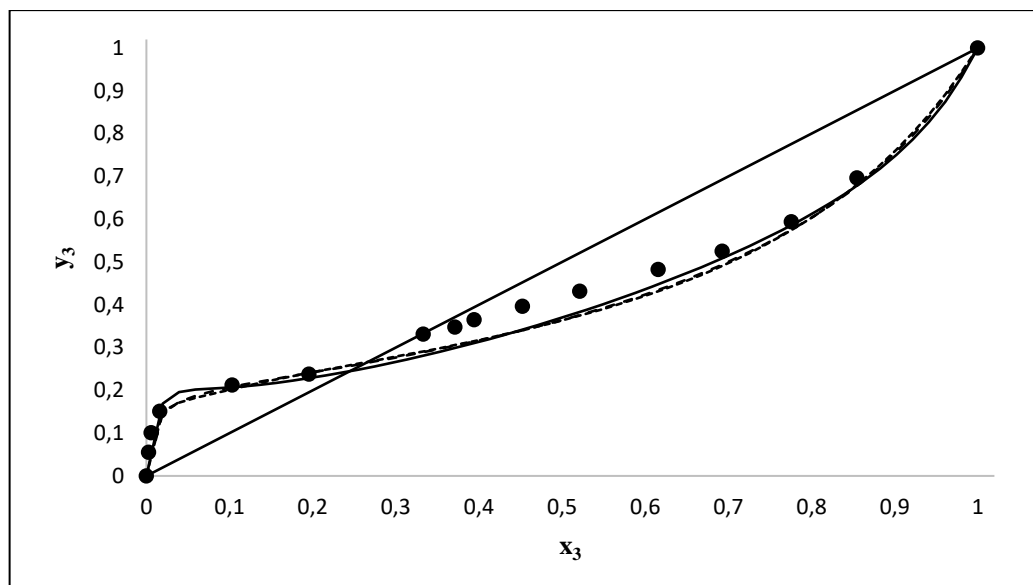


Figure 5.27: Isothermal x-y data for the water (2) + pyridine (3) system at 333.15 K (●) Exp, This work; (—) PR-MC-WS-NRTL model, (---) PR-MC-WS-Wilson model; (....) PR-MC-WS-UNIQUAC model.

In Figures 5.24 to 5.27, the correlated data for the PR-MC-WS-Wilson and the PR-MC-WS-UNIQUAC models are almost indistinguishable. The data calculated with the PR-MC-WS-NRTL model differs slightly from the other two models but closely follows the measured VLE data at and near the pure components vapour pressures however, as the azeotrope is approached, a departure from the model fits is observed. The divergence between measured data in this work and literature, predictive data and regressed data could have been due to experimental error. Therefore, the temperature, pressure and composition calibrations were repeated. All the data points were updated with the adjusted calibrations and the VLE measurements were repeated (represented by the red and blue dots in the Figures) in order to verify the accuracy of the data obtained. Although all the experimental methods were redone, the exact same trend was observed. Hence there was no error in the techniques used to acquire the data.

It is difficult to measure a system that contains water due to the phenomenon known as surface tension. “The water molecules at the surface do not have like molecules on all sides of them and consequently they cohere more strongly to those directly associated with them on the surface” (USGS, 2016). This means that the water tends to stick onto the sides of the VLE still thereby reducing its composition at the sampling point. This was observed during the experiments performed in this study. Furthermore, from the x-y plots shown in Figures 5.21, 5.23, 5.25 and 5.27, the measured vapour composition of pyridine is higher than the predicted composition thereby verifying the lower amount of water collected during sampling and composition analysis. This could be the reason for the disagreement between measured and predicted/regressed data.

However, in this work, the water/pyridine feed composition (in the separation process) lies in the water-rich region displayed on the graphs. It can be seen that a good correlation between the experimental and modelled data is observed in this region, hence, the phase behaviour predicted and separation process designed for the water/pyridine feed composition in this work will provide an accurate representation of the real system.

Table 5.18 presents the azeotropic data for the water (2) + pyridine (3) system. Reported are the azeotropic compositions observed in this work, literature, from predictive models and regressed models from Aspen Plus®. It can be seen that the azeotropic composition in this study has a greater pyridine composition than the sources to which it is compared. A possible reason for the discrepancy is the surface tension phenomenon.

Table 5.18: Azeotropic data for the water (2) + pyridine (3) system

System	Model	$x_3$	$y_3$	T (K)	P (kPa)
<b>40 kPa</b>	Experimental	0.321	0.323	344.5	
	Literature	0.258	0.232	343.3	
	PSRK	0.255	0.256	344.5	
	UNIFAC	0.255	0.264	343.9	
	PR-MC-WS-NRTL	0.255	0.250	343.8	
	PR-MC-WS-Wilson	0.275	0.280	343.5	
	PR-MC-WS-UNIQUAC	0.275	0.278	343.6	
<b>333.15 K</b>	Experimental	0.333	0.331		24.67
	PSRK	0.275	0.278		25.30
	UNIFAC	0.275	0.276		24.93
	PR-MC-WS-NRTL	0.255	0.249		24.88
	PR-MC-WS-Wilson	0.255	0.261		24.88
	PR-MC-WS-UNIQUAC	0.255	0.262		24.84

Tables 5.19 and 5.20 list the measured VLE data as well the deviation between temperature or pressure and vapour compositions between experimental data and modelled data for each data point, while Tables 5.21 and 5.22 list the AADs and AARDs for each system averaged over all data points. The total AARD in each table represents the combined AARDs for temperature or pressure and vapour compositions. Table 5.23 lists the regressed model parameters for each system.

Table 5.19: Comparison of the experimental VLE data to modelled data for the water (2) + pyridine (3) system at 40 kPa

T (K)	x <sub>3</sub>	y <sub>3</sub>	ΔT <sup>a</sup> (K)	ΔT/T <sup>a</sup> (%)	Δy <sub>3</sub> <sup>a</sup>	Δy <sub>3</sub> /y <sub>3</sub> <sup>a</sup> (%)	ΔT <sup>b</sup> (K)	ΔT/T <sup>b</sup> (%)	Δy <sub>3</sub> <sup>b</sup>	Δy <sub>3</sub> /y <sub>3</sub> <sup>b</sup> (%)	ΔT <sup>c</sup> (K)	ΔT/T <sup>c</sup> (%)	Δy <sub>3</sub> <sup>c</sup>	Δy <sub>3</sub> /y <sub>3</sub> <sup>c</sup> (%)
347.74	0.004	0.048	0.1	0.02	0.005	10.75	0.1	0.03	0.007	15.10	0.1	0.04	0.008	16.77
346.04	0.010	0.123	0.4	0.12	0.018	14.44	0.5	0.14	<b>0.022</b>	18.17	0.4	0.12	<b>0.020</b>	15.91
345.05	0.023	0.169	0.0	0.01	0.007	4.42	0.4	0.13	<b>0.025</b>	14.55	0.3	0.10	<b>0.021</b>	12.32
344.45	0.046	0.196	0.2	0.04	0.002	0.80	0.3	0.09	<b>0.019</b>	9.85	0.2	0.08	0.018	9.33
343.87	0.279	0.309	0.1	0.03	<b>0.050</b>	16.28	0.4	0.12	<b>0.026</b>	8.59	0.4	0.11	<b>0.029</b>	9.52
343.92	0.294	0.316	0.2	0.04	<b>0.052</b>	16.43	0.5	0.13	<b>0.028</b>	8.99	0.4	0.12	<b>0.032</b>	10.04
343.90	0.321	0.323	0.1	0.02	<b>0.049</b>	15.05	0.4	0.12	<b>0.026</b>	8.06	0.4	0.11	<b>0.030</b>	9.33
343.98	0.342	0.329	0.1	0.03	<b>0.046</b>	13.86	0.5	0.13	<b>0.024</b>	7.33	0.4	0.13	<b>0.029</b>	8.77
343.77	0.344	0.330	0.1	0.04	<b>0.045</b>	13.69	0.3	0.07	<b>0.024</b>	7.20	0.2	0.06	<b>0.029</b>	8.66
343.87	0.376	0.342	0.1	0.04	<b>0.043</b>	12.65	0.3	0.08	<b>0.024</b>	7.07	0.3	0.07	<b>0.030</b>	8.76
344.05	0.400	0.353	0.1	0.02	<b>0.043</b>	12.14	0.4	0.11	<b>0.026</b>	7.34	0.4	0.10	<b>0.032</b>	9.16
343.92	0.415	0.359	0.3	0.08	<b>0.041</b>	11.52	0.2	0.06	<b>0.026</b>	7.21	0.2	0.05	<b>0.033</b>	9.10
344.53	0.481	0.389	0.1	0.03	<b>0.036</b>	9.23	0.5	0.14	<b>0.028</b>	7.19	0.4	0.13	<b>0.036</b>	9.26
344.39	0.482	0.386	0.2	0.07	<b>0.033</b>	8.51	0.3	0.10	<b>0.025</b>	6.48	0.3	0.09	<b>0.033</b>	8.57
345.07	0.535	0.422	0.0	0.01	<b>0.037</b>	8.82	<b>0.7</b>	0.18	<b>0.036</b>	8.57	0.6	0.17	<b>0.045</b>	10.58
346.33	0.632	0.474	0.1	0.03	<b>0.025</b>	5.32	<b>0.9</b>	0.25	<b>0.036</b>	7.57	<b>0.8</b>	0.23	<b>0.043</b>	9.12
347.53	0.715	0.525	0.1	0.02	0.013	2.42	<b>0.7</b>	0.20	<b>0.029</b>	5.56	0.6	0.17	<b>0.034</b>	6.43
350.07	0.807	0.626	<b>0.7</b>	0.20	<b>0.028</b>	4.54	<b>0.9</b>	0.27	<b>0.041</b>	6.52	<b>0.8</b>	0.23	<b>0.042</b>	6.63
351.25	0.859	0.672	0.4	0.12	0.012	1.76	0.3	0.08	0.014	2.15	0.2	0.05	0.014	2.08
353.84	0.924	0.769	0.5	0.13	0.003	0.38	0.2	0.06	0.013	1.62	0.2	0.06	0.012	1.53
356.20	0.959	0.866	<b>0.8</b>	0.23	0.016	1.80	0.1	0.03	0.005	0.58	0.2	0.04	0.003	0.36

$$\Delta T = |T_{exp} - T_{calc}|$$

$$\Delta y_2 = |y_{2exp} - y_{2calc}|$$

$$\Delta T/T = 100 \left| \frac{T_{exp} - T_{calc}}{T_{exp}} \right|$$

$$\Delta y_2/y_2 = 100 \left| \frac{y_{2exp} - y_{2calc}}{y_{2exp}} \right|$$

<sup>a</sup>PR-MC-WS-NRTL model

<sup>b</sup>PR-MC-WS-Wilson model

<sup>c</sup>PR-MC-WS-UNIQUAC model

Table 5.20: Comparison of the experimental VLE data to modelled data for the water (2) + pyridine (3) system at 333.15 K

<b>P (K)</b>	<b>x<sub>3</sub></b>	<b>y<sub>3</sub></b>	<b>ΔP<sup>a</sup> (K)</b>	<b>ΔP/P<sup>a</sup> (%)</b>	<b>Δy<sub>3</sub><sup>a</sup></b>	<b>Δy<sub>3</sub>/y<sub>3</sub><sup>a</sup> (%)</b>	<b>ΔP<sup>b</sup> (K)</b>	<b>ΔP/P<sup>b</sup> (%)</b>	<b>Δy<sub>3</sub><sup>b</sup></b>	<b>Δy<sub>3</sub>/y<sub>3</sub><sup>b</sup> (%)</b>	<b>ΔP<sup>c</sup> (K)</b>	<b>ΔP/P<sup>c</sup> (%)</b>	<b>Δy<sub>3</sub><sup>c</sup></b>	<b>Δy<sub>3</sub>/y<sub>3</sub><sup>c</sup> (%)</b>
20.96	0.003	0.055	0.07	0.33	0.000	0.43	<b>0.22</b>	1.03	0.006	11.04	0.19	0.90	0.005	9.04
22.07	0.006	0.101	<b>0.21</b>	0.96	0.009	8.59	0.19	0.87	0.009	8.47	0.15	0.67	0.007	6.49
23.12	0.016	0.151	<b>0.27</b>	1.15	0.006	4.08	<b>0.22</b>	0.95	0.014	9.05	0.07	0.32	0.008	5.27
24.57	0.103	0.212	0.08	0.30	0.005	2.50	0.12	0.49	0.005	2.15	<b>0.22</b>	0.88	0.009	4.46
24.77	0.196	0.238	0.07	0.29	0.009	3.82	0.03	0.14	0.003	1.24	0.01	0.05	0.003	1.32
24.67	0.333	0.331	0.05	0.19	<b>0.050</b>	15.10	0.08	0.32	<b>0.042</b>	12.81	0.07	0.28	<b>0.040</b>	12.05
24.62	0.371	0.348	0.04	0.15	<b>0.049</b>	14.11	0.03	0.11	<b>0.044</b>	12.70	0.02	0.10	<b>0.042</b>	12.11
24.62	0.394	0.365	0.14	0.58	<b>0.054</b>	14.89	0.06	0.23	<b>0.051</b>	14.05	0.05	0.22	<b>0.050</b>	13.60
24.12	0.452	0.396	0.00	0.00	<b>0.055</b>	13.81	0.12	0.51	<b>0.057</b>	14.29	0.16	0.64	<b>0.056</b>	14.16
23.57	0.521	0.432	0.02	0.06	<b>0.049</b>	11.28	0.19	0.79	<b>0.056</b>	13.02	<b>0.24</b>	1.00	<b>0.057</b>	13.30
22.72	0.615	0.483	0.08	0.35	<b>0.035</b>	7.31	0.10	0.44	<b>0.048</b>	10.03	0.15	0.68	<b>0.052</b>	10.68
21.86	0.693	0.525	0.20	0.91	0.016	3.06	0.09	0.41	<b>0.030</b>	5.77	0.06	0.27	<b>0.034</b>	6.45
20.56	0.776	0.594	0.12	0.58	0.008	1.27	0.15	0.74	0.018	2.95	0.20	0.95	<b>0.019</b>	3.25
18.61	0.855	0.696	<b>0.35</b>	1.89	0.017	2.51	0.12	0.62	0.017	2.40	0.03	0.15	0.015	2.23

$$\Delta P = |P_{exp} - P_{calc}|$$

$$\Delta y_2 = |y_{2exp} - y_{2calc}|$$

$$\Delta P/P = 100 \left| \frac{P_{exp} - P_{calc}}{P_{exp}} \right|$$

$$\Delta y_2/y_2 = 100 \left| \frac{y_{2exp} - y_{2calc}}{y_{2exp}} \right|$$

<sup>a</sup> PR-MC-WS-NRTL model

<sup>b</sup> PR-MC-WS-Wilson model

<sup>c</sup> PR-MC-WS-UNIQUAC model

From Tables 5.19 and 5.20, it can be seen that the deviations are below the experimental uncertainties for the temperature ( $\Delta T = 0.6$ ) and pressure ( $\Delta P = 0.20$ ) measurements except for a few data points for each model ( $\Delta T = 0.7 - 0.9$ ;  $\Delta P = 0.21 - 0.35$ ). The deviations observed in vapour composition lie within the experimental uncertainty ( $\Delta y = 0.018$ ) for a few data points but are higher for the bulk of the data, ranging from  $\Delta y = 0.019 - 0.057$ . This is

not unexpected since the discrepancies in the data were shown in the graphical representations. As stated previously, the deviation in the measured experimental data is due to surface tension.

Table 5.21: Data regression deviations for the isobaric water (2) + pyridine (3) binary system

System	Model	AAD [T] (K)	AARD [T] (%)	AAD $y_2$	AARD [ $y_2$ ] (%)	AAD $y_3$	AARD [ $y_3$ ] (%)	Total AARD (%)
40 kPa	PR-MC-WS-NRTL	0.2	0.07	0.029	5.14	0.026	8.37	13.57
	PR-MC-WS-Wilson	0.4	0.12	0.024	4.38	0.022	7.51	12.01
	PR-MC-WS-UNIQUAC	0.4	0.11	0.027	4.85	0.025	8.26	13.21

$AAD [T] = \frac{1}{N_p} \sum |T_{exp} - T_{calc}|$ ,  $N_p$  is the total number of data points

$AAD [y_1] = \frac{1}{N_p} \sum |y_{2exp} - y_{2calc}|$

$AARD [T] = \frac{100}{N_p} \sum \left| \frac{T_{exp} - T_{calc}}{T_{exp}} \right|$

$AARD [y_1] = \frac{100}{N_p} \sum \left| \frac{y_{2exp} - y_{2calc}}{y_{2exp}} \right|$

Table 5.22: Data regression deviations for the isothermal water (2) + pyridine (3) binary system.

System	Model	AAD [P] (kPa)	AARD [P] (%)	AAD $y_2$	AARD [ $y_2$ ] (%)	AAD $y_3$	AARD [ $y_3$ ] (%)	Total AARD (%)
333.15 K	PR-MC-WS-NRTL	0.14	0.65	0.026	4.48	0.023	6.87	12.00
	PR-MC-WS-Wilson	0.14	0.65	0.028	5.01	0.025	7.96	13.62
	PR-MC-WS-UNIQUAC	0.13	0.62	0.028	5.02	0.025	7.59	13.23

$$\text{AAD [P]} = \frac{1}{N_p} \sum |P_{exp} - P_{calc}|, N_p \text{ is the total number of data points}$$

$$\text{AAD } [y_1] = \frac{1}{N_p} \sum |y_{2exp} - y_{2calc}|$$

$$\text{AARD [P]} = \frac{100}{N_p} \sum \left| \frac{P_{exp} - P_{calc}}{P_{exp}} \right|$$

$$\text{AARD } [y_1] = \frac{100}{N_p} \sum \left| \frac{y_{2exp} - y_{2calc}}{y_{2exp}} \right|$$

From Tables 5.21 and 5.22, it can be seen that the thermodynamic model with the lowest deviation is the PR-MC-WS–NRTL for the 333.15 K system (AARD = 12 %), hence the model parameters calculated with the use of this combination (presented in Table 5.23) were selected for the water (2) + pyridine (3) system.

Table 5.23: Model parameters regressed for the water (2) + pyridine (3) binary system

System	Model	$k_{ij}^a$	$a_{ij}^b$	$a_{ji}^b$	$b_{ij}^b$	$b_{ji}^b$	$\alpha_{ij}^b$	RMSE <sup>c</sup>
40 kPa	PR-MC-WS-NRTL	0.37			996.40	419.40	0.69	11.67
	PR-MC-WS-Wilson	0.22	8.40	13.49	-3178.64	-6044.71		11.32
	PR-MC-WS-UNIQUAC	-0.72			-853.65	-374.96		10.94
333.15 K	PR-MC-WS-NRTL	0.37			1052.13	345.52	0.69	13.46
	PR-MC-WS-Wilson	0.25	-75.60	148.35	25063.29	-50872.47		14.33
	PR-MC-WS-UNIQUAC	-0.75			-891.38	-300.07		12.70

<sup>a</sup> WS mixing rule parameter incorporated into the PR EoS<sup>b</sup> NRTL/Wilson/UNIQUAC model parameters<sup>c</sup> RMSE: Residual mean square error

### Ethanol (1) + Water (2) Binary System

The ethanol (1) + water (2) system was not measured since there is a wide range of consistent VLE data available for this system. Aspen Plus® stores physical property parameters for several components in numerous databanks which are developed from the thermodynamic models available and data from the Dortmund Databank. Hence the built-in parameters from Aspen Plus® for the ethanol (1) + water (2) system was used for the design.

## 5.4 Comparison of Model Parameters

The experimental data was regressed using both the Dortmund Data Bank (DDB) software and the Aspen Plus® simulation software. The model that provided the best fit on DDB was the Wilson activity coefficient model with the ideal gas law (Wilson DDB). The model with the lowest percentage error (AARD) on Aspen Plus® was the Peng-Robinson equation of state incorporating the Mathias Copeman alpha function with the Wong-Sandler mixing rules and the NRTL activity coefficient model (PR-MC-WS-NRTL). In theory, the outcome of each simulation software should be identical resulting in the same thermodynamic model that best represents the system. In this case however, the resulting models are different on each software. The information on the thermodynamic models and objective functions in DDB are proprietary. However, according to a source (Rarey, 2017), the objective functions in DDB are quite different from the objective functions in Aspen Plus®, this is the reason for the differing results. The parameters obtained from each model regression were inputted into Aspen Plus® and data was predicted at conditions available in literature so that a direct comparison was possible.

Figure 5.28 displays the isothermal P-x data for the ethanol (1) + pyridine (3) system at temperatures of 313.15 K, 338.15 K and 348.15 K. These three data sets are the only available data for this system in literature. The experimental data from literature is compared to the two model predictions from Aspen Plus®.

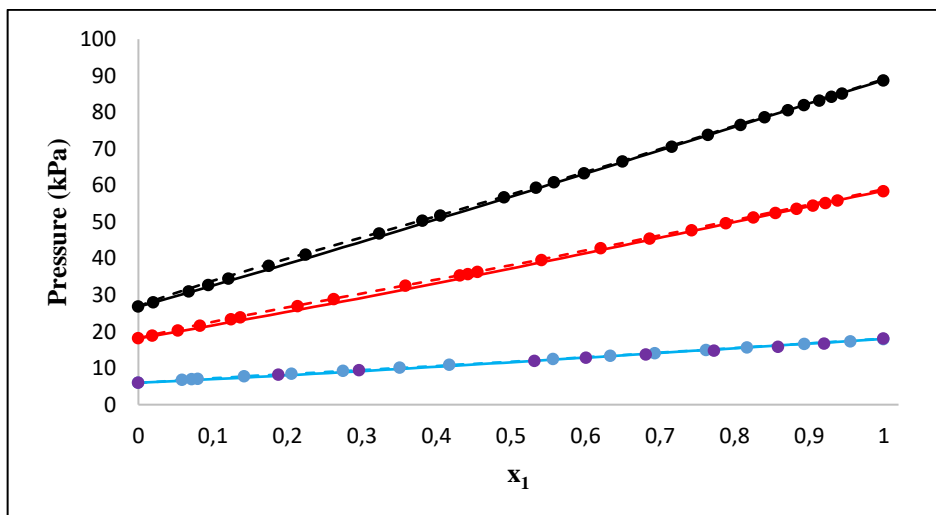


Figure 5.28: Isothermal VLE data for the ethanol (1) + pyridine (3) system. (●) Exp, This work at 313.15 K; (●) (Warycha, 1977) at 313.15 K, (●) (Findlay & Copp, 1969) at 338.15 K, (●) (Findlay & Copp, 1969) at 348.15 K. The solid lines represent predicted data using Wilson (DDB) parameters. The dotted lines represent predicted data using PR-MC-WS-NRTL (Aspen Plus®) parameters

From Figure 5.28, it can be seen that while both models fit the data fairly well, the PR-MC-WS-NRTL model provides a slightly better fit to the measured and literature data.



Figures 5.29 and 5.30 display isothermal P-x-y and x-y data for the water (2) + pyridine (3) system at 323.15 K, 333.15 K and 343.01 K. The data set at 333.15 K is measured data from this work. The data sets at 323.15 K and 343.01 K were selected from literature. There is a wide range of data available for the water (2) + pyridine (3) system however, only low-pressure data was selected since the distillation design in this work is operated low pressure. The experimental data from literature is compared to the two model predictions from Aspen Plus®.

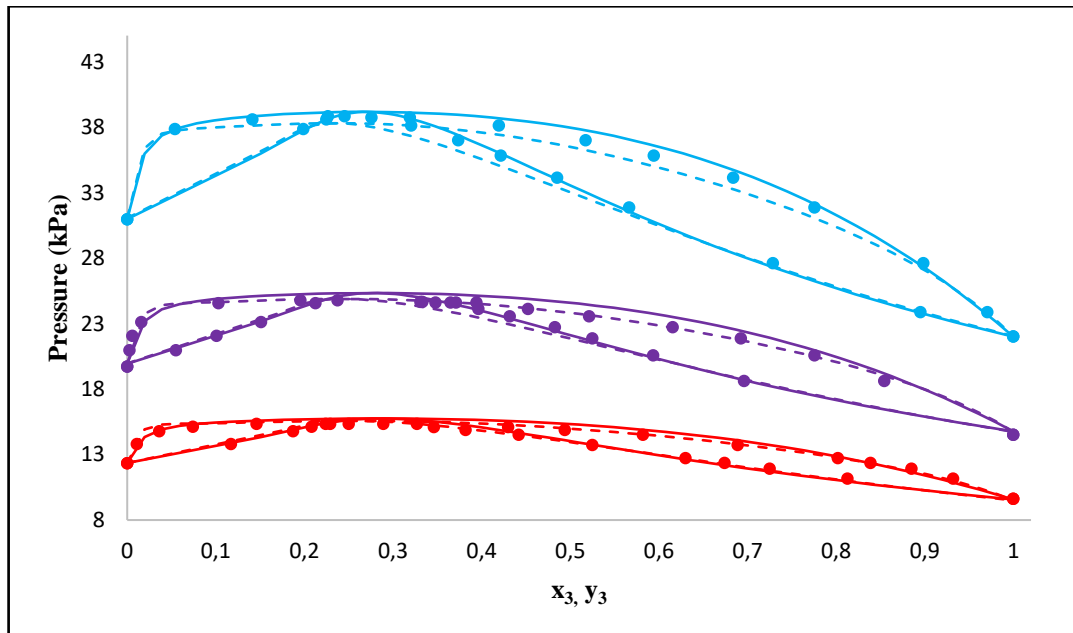


Figure 5.29: Isothermal VLE data for the water (2) + pyridine (3) system. (●) Exp, This work at 333.15 K; (●) (Ibl, et al., 1954) at 323.15 K, (●) (Andon, et al., 1957) at 343.01 K. The solid lines represent predicted data using Wilson (DDB) parameters. The dotted lines represent predicted data using PR-MC-WS-NRTL (Aspen Plus®) parameters.

From Figure 5.29, it can be seen that the difference in model fits at 323.15 K are almost indistinguishable. However, as the temperature is increased, a significant discrepancy is observed. The measured data fits both the predictive models well at the pure component vapour pressures however, as the azeotrope is approached, a departure from the model fits is observed.

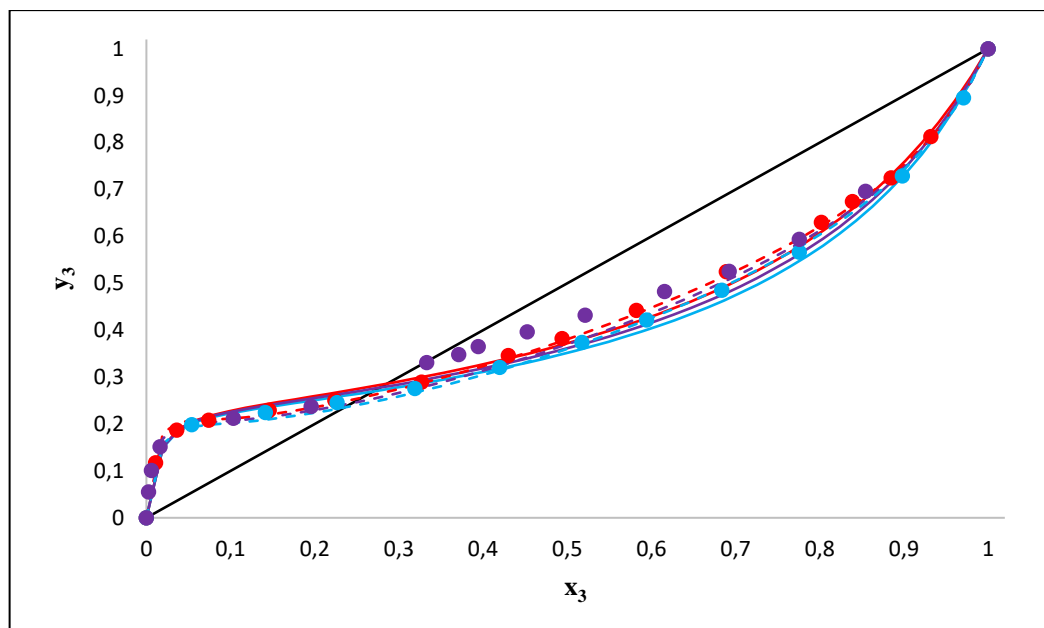


Figure 5.30: Isothermal x-y data for the water (2) + pyridine (3) system. (●) Exp, This work at 333.15 K; (●) (Ibl, et al., 1954) at 323.15 K, (●) (Andon, et al., 1957) at 343.01 K. The solid lines represent predicted data using Wilson (DDB) parameters. The dotted lines represent predicted data using PR-MC-WS-NRTL (Aspen Plus®) parameters.

Similarly, in Figure 5.30, there is a deviation between the measured data from this work and the trend predicted with the selected model parameters, as the azeotropic composition is approached. Additionally, it can be seen that the measured data in the middle region lies closer to the equilibrium line resulting in a relative volatility ( $\alpha$ ) closer to 1. For example, at  $x = 0.5$ , experimental  $\alpha = 1.38$ , Wilson DDB  $\alpha = 1.70$  and PR-MC-WS-NRTL  $\alpha = 1.77$ . The closer the relative volatility is to 1, the greater the number of theoretical stages required for the separation process. Since the thermodynamic models predict a relative volatility further away from 1, the theoretical stages calculated in the simulation will be lower than what is required for the real system. However, the efficiency introduced into the column design will account for this discrepancy. Nonetheless, as discussed in previous sections, the water/pyridine feed composition in this work lies in the water-rich region. As seen from the Figure, there is a good correlation between the experimental and modelled data in this region. Hence, the phase behaviour predicted and separation process designed in this region will provide an accurate representation of the real system.

Table 5.24 presents the AADs for each system averaged over all data points. From the Table, it can be seen that the AADs are lower for the PR-MC-WS-NRTL model. Hence, this model combination better represents the measured data.

Table 5.24: Data regression deviations for the systems studied averaged over all points.

<b>System</b>	<b>Model</b>	<b>AAD [T] (K)</b>	<b>AAD [P] (kPa)</b>	<b>AAD <math>y_1</math></b>	<b>AAD <math>y_3</math></b>
EP 40 kPa	Wilson DDB	0.4		0.005	
	PR-MC-WS-NRTL	0.2		0.004	
EP 100 kPa	Wilson DDB	0.3		0.026	
	PR-MC-WS-NRTL	0.3		0.017	
EP 313.15 K	Wilson DDB		0.24	0.008	
	PR-MC-WS-NRTL		0.01	0.005	
WP 40 kPa	Wilson DDB	0.3			0.027
	PR-MC-WS-NRTL	0.2			0.026
WP 333.15 K	Wilson DDB		0.28		0.031
	PR-MC-WS-NRTL		0.14		0.025

EP: Ethanol (1) + Pyridine (3)

WP: Water (2) + Pyridine (3)

## CHAPTER 6: PROCESS DESIGN AND COSTING

### 6.1 Design Methodology

In this study, process design via a simulative approach is used to represent the behaviour of a chemical process. This is based on the information and thermodynamic models in the design methods of the simulation software. The objective of process design in this study was to develop and simulate a process (with the use of the Aspen Plus® process simulator) to efficiently separate and recover the waste material comprising pyridine, ethanol, water and nitrogen with recovery rates and mole purities greater than 99.9 % so that the components could be recycled and reused in the LiPF<sub>6</sub> production process.

Two separation schemes were investigated. The first proposed process (process A) comprises a flash vessel to remove the nitrogen, a conventional distillation column to separate the pyridine from the mixture followed by an extractive distillation column to separate the ethanol from water. As discussed in section 2.3, the solvent chosen for extractive distillation was ethylene glycol. This was recovered in a solvent recovery distillation column and recycled to the extractive distillation column for reuse. This recycle loop was closed and the process converged with the use of a calculator block. In Aspen Plus®, a calculator is used to insert FORTRAN code into the simulation. FORTRAN is a programming language widely used for scientific calculations. Converging a process simulation that contains a recycle loop is not easy, hence the calculator was used to determine the amount of make-up solvent required to balance all component flow rates within the process.

The second process (process B) follows the same scheme as process A for the nitrogen and pyridine separation; however, it uses a pervaporation unit to separate ethanol from water as opposed to the extractive distillation column in process A. A polyvinylalcohol membrane in a spiral wound module configuration was selected as discussed in section 2.4. In this case, the retentate stream comprises the high purity ethanol product; the permeate stream comprises a mixture of ethanol and water. This permeate stream is recycled to the conventional distillation column to prevent the loss of ethanol.

A modification was made to each process where an additional flash vessel was used to further purify the nitrogen stream. However, the viability of this additional flash vessel had to be determined. Therefore, the processes were optimised and a cost evaluation performed to determine how the second flash would affect the total cost and final purities. In the sections to follow, process A will be referred to as process 1FE (1-flash extractive), process B will be referred to process 1FM (1-flash membrane), the modification to process A will be process 2FE (2-flash extractive) and the modification to process B will be process 2FM (2-flash membrane).

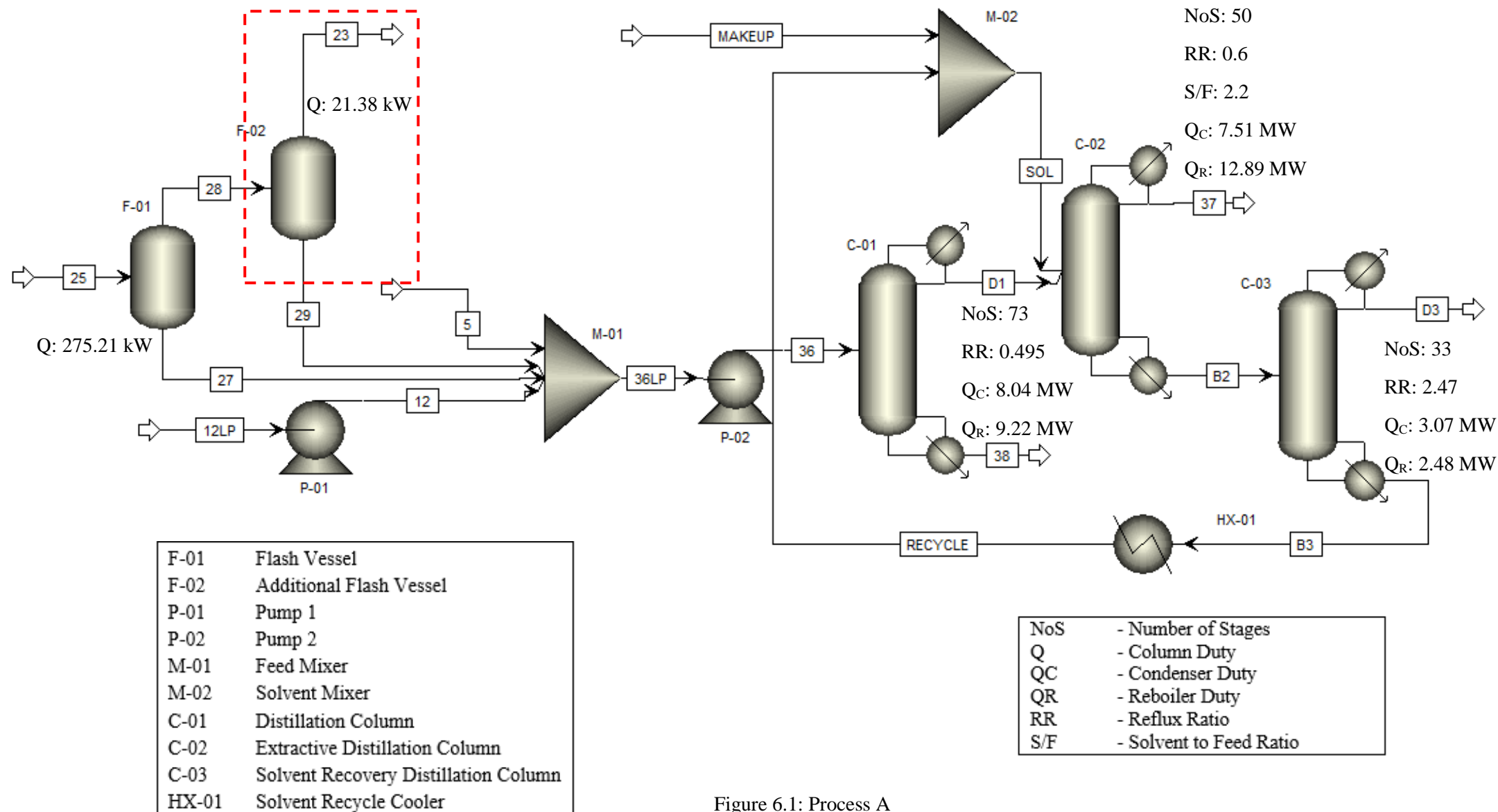


Figure 6.1: Process A

Table 6.1: Stream results for process 1FE (1-flash extractive)

Stream		5	12LP	12	25	27	28	36LP	36	37
Component	Unit									
Ethanol	kg/hr	16.32	19139.58	19139.58	309.57	298.20	<b>11.36</b>	19454.11	19454.11	<b>19450.1</b>
Water	kg/hr	886.75	467.50	467.50	7.61	7.36	0.2428	1361.61	1361.61	0.7445
Pyridine	kg/hr	785.71	1030.52	1030.52	16.70	16.51	0.1922	1832.74	1832.74	0
Nitrogen	kg/hr	0	0	0	9528.59	0.7505	<b>9527.84</b>	0.7505	0.7505	0.7505
Ethylene Glycol	kg/hr	0	0	0	0	0	0	0	0	1.08
Total	kg/hr	1688.79	20637.60	20637.60	9862.46	322.82	9539.63	22649.21	22649.21	19452.67
Temperature	K	303.15	298.15	298.20	313.15	243.15	243.15	297.49	297.57	345.87
Pressure	kPa	100	40	100	100	200	200	100	200	97
Vapour Fraction	-	0	0	0	1	0	1	0	0	0

Stream		38	B2	B3	D1	D3	MAKEUP	RECYCLE	SOL
Component	Unit								
Ethanol	kg/hr	0.0965	3.91	0	19454.01	3.91	0	0	0
Water	kg/hr	0.0040	1360.86	0.1899	1361.61	1360.67	0	0.1899	0
Pyridine	kg/hr	<b>1832.56</b>	0.1832	0.0329	0.1832	0.1503	0	0.0329	0
Nitrogen	kg/hr	0	0	0	0.7505	0	0	0	0
Ethylene Glycol	kg/hr	0	68025.93	68025.25	0	0.6802	<b>1.76</b>	68025.25	68027.01
Total	kg/hr	1832.66	69390.89	68025.47	20816.55	1365.42	1.76	68025.47	68027.01
Temperature	K	407.65	455.64	447.07	358.82	341.66	348.15	348.15	348.15
Pressure	kPa	179.48	127.32	48.96	150	30	100	100	100
Vapour Fraction	-	0	0	0	0	0	0	0	0

Table 6.2: Stream results for process 2FE (2-flash extractive)

Stream		5	12LP	12	23	25	27	28	29	36LP	36
Component	Unit										
Ethanol	kg/hr	16.32	19139.58	19139.58	<b>4.81</b>	309.57	291.83	17.74	12.92	19460.66	19460.66
Water	kg/hr	886.75	467.50	467.50	0.0580	7.61	7.23	0.3807	0.3227	1361.80	1361.80
Pyridine	kg/hr	785.71	1030.52	1030.52	0.0410	16.70	16.39	0.3050	0.2640	1832.89	1832.89
Nitrogen	kg/hr	0	0	0	<b>9527.60</b>	9528.59	0.6912	9527.90	0.2916	0.9828	0.9828
Ethylene Glycol	kg/hr	0	0	0	0	0	0	0	0	0	0
Total	kg/hr	1688.79	20637.60	20637.60	9532.51	9862.46	316.14	9546.32	13.80	22656.33	22656.33
Temperature	K	303.15	298.15	298.20	248.15	313.15	248.15	248.15	248.15	297.54	297.62
Pressure	kPa	100	40	100	1930	100	200	200	1930	100	200
Vapour Fraction	-	0	0	0	1	1	0	1	0	0	0

Stream		37	38	B2	B3	D1	D3	MAKEUP	RECYCLE	SOL
Component	Unit									
Ethanol	kg/hr	<b>19456.28</b>	0.0964	4.29	0	19460.56	4.29	0	0	0
Water	kg/hr	0.9352	0.0040	1361.05	0.1882	1361.79	1360.86	0	0.1882	0.1882
Pyridine	kg/hr	0.0008	<b>1832.71</b>	0.2231	0.0405	0.1833	0.1825	0	0.0405	0.0405
Nitrogen	kg/hr	0.9828	0	0	0	0.9828	0	0	0	0
Ethylene Glycol	kg/hr	0.3692	0	68026.64	68025.96	0	0.6803	<b>1.05</b>	68025.96	68027.01
Total	kg/hr	19458.56	1832.81	69392.19	68026.19	20823.52	1366.01	1.05	68026.19	68027.24
Temperature	K	343.38	407.65	454.45	447.36	358.15	341.61	348.15	348.15	348.15
Pressure	kPa	93	179.49	123.17	49.44	150	30	100	100	100
Vapour Fraction	-	0	0	0	0	0	0	0	0	0

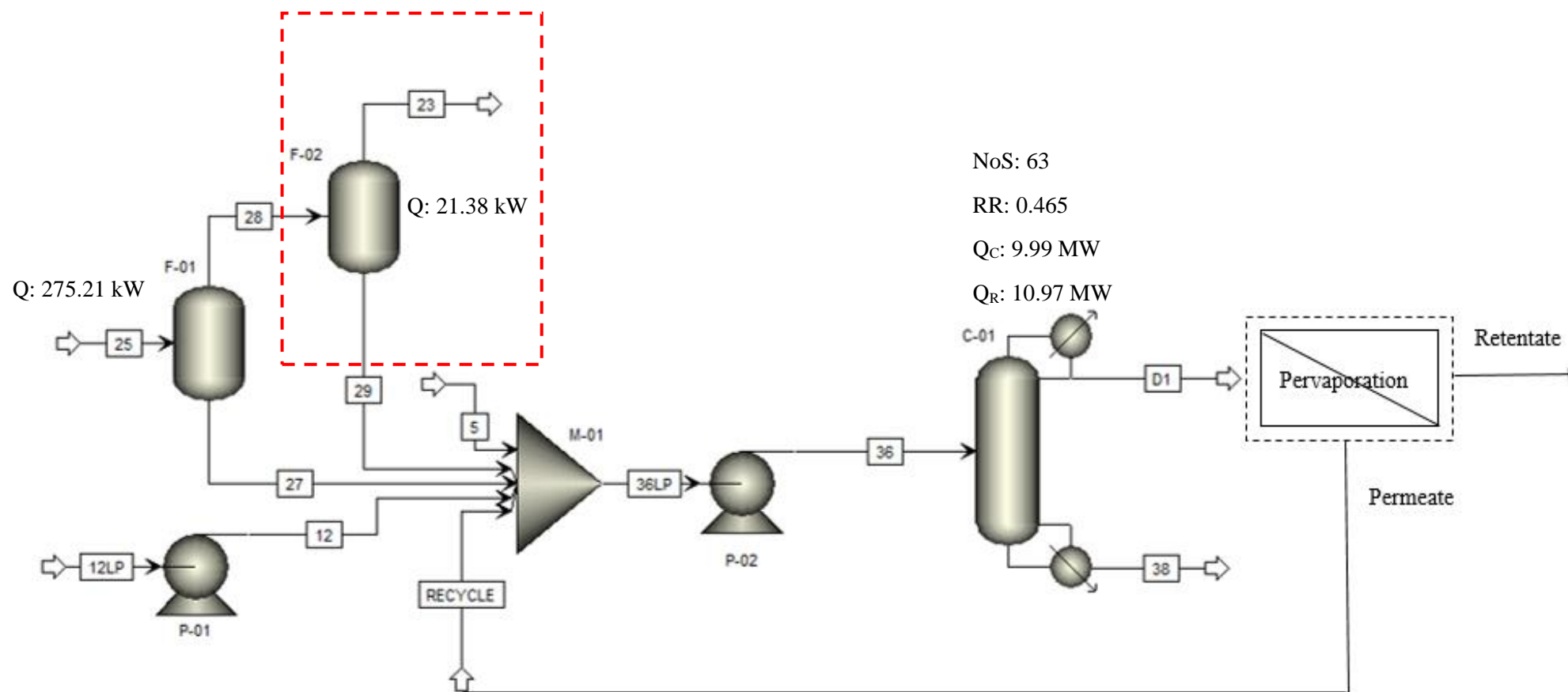
## Process A

Process A is presented in Figure 6.1 while the flow rates and operating conditions for each stream are shown in Table 6.1 for process 1FE (1-flash extractive) and 6.2 for process 2FE (2-flash extractive). The waste streams that require purification and recycling from the  $\text{LiPF}_6$  production process are stream 25 (comprising nitrogen, ethanol, water and pyridine at 313.15 K and 100 kPa), stream 5 (comprising ethanol, water and pyridine at 303.15 K and 100 kPa) and stream 12 (comprising ethanol, water and pyridine at 298.15 K and 40 kPa). Stream 25 is first fed into flash vessel F-01 which operates at a temperature and pressure of 243.15 K and 200 kPa respectively. Stream 28 exits the top of F-01 and is fed to flash vessel F-02 which is operated at a temperature and pressure of 248.15 K and 1930 kPa respectively. Nitrogen with a recovery of 99.99 mol % and a purity of 99.97 mol % exits the top of F-02 (stream 23). The bottoms of F-01 (stream 27) and F-02 (stream 29) is then combined with streams 5 and 12 and fed to a conventional distillation column (C-01) with an operating pressure of 150 kPa. Pyridine exits the bottom of the column (stream 38) with a recovery and purity of 99.99 mol %. The distillate (stream D1) comprising the ethanol/water azeotrope is then fed to an extractive distillation column (C-02) together with the ethylene glycol solvent (operating pressure of 97 kPa). Ethanol exits in the distillate (stream 37) with a recovery and purity of 99.98 mol %. The bottoms (stream B2) comprising water and ethylene glycol is then fed to a solvent recovery column (C-03) with an operating pressure of 30 kPa. Ethylene glycol exits the bottom of the column with a recovery and purity of 99.99 mol % and is recycled to the extractive distillation column (C-02) for reuse. The recycle loop was closed and the process converged with the use of a calculator block. The distillate (stream D3) comprises mainly water and trace amounts of ethylene glycol. Therefore, a solvent make-up of 0.02 kmol/hr (stream MAKEUP) is required to account for the loss of solvent to the water-rich stream D3. All the purities and recovery rates are greater than 99.9 mol % and hence meet the required specifications as proposed by NECSA.

The modification to process A is indicated by the additional flash vessel within the red dotted lines. As seen in Table 6.1, the nitrogen-rich stream (stream 28) exiting the top of flash vessel F-01 still contains 11.36 kg/hr of ethanol. The purpose of the additional flash vessel was to reduce this ethanol thereby further purifying the nitrogen stream. As seen in Table 6.2, the nitrogen rich stream (stream 23) exiting the top of flash vessel F-02 contains 4.81 kg/hr of ethanol. Therefore, the additional flash vessel recovered a further 6.55 kg/hr of ethanol. Furthermore, an additional 0.15 kg/hr of pyridine was recovered in stream 37 and the solvent make-up required decreased by 0.71 kg/hr.

The column specifications shown in Figure 6.1 (number of stages, reflux ratio, duties, etc) are discussed in section 6.2.





F-01	Flash Vessel
F-02	Additional Flash Vessel
P-01	Pump 1
P-02	Pump 2
M-01	Feed Mixer
C-01	Distillation Column

Figure 6.2: Process B

NoS	- Number of Stages
Q	- Column Duty
QC	- Condenser Duty
QR	- Reboiler Duty
RR	- Reflux Ratio

Table 6.3: Stream results for process 1FM (1-flash membrane)

Stream		5	12LP	12	25	27	28	36LP	36	38	D1	Retentate	Permeate
Component	Unit												
Ethanol	kg/hr	16.32	19139.6	19139.6	309.57	298.20	<b>11.36</b>	19454.1	19454.1	0.0965	19454.1	<b>17650.09</b>	1832.63
Water	kg/hr	886.75	467.50	467.50	7.61	7.36	0.2428	1361.61	1361.61	0.0040	1361.61	14.45	1346.19
Pyridine	kg/hr	785.71	1030.52	1030.52	16.70	16.51	0.1922	1832.74	1832.74	<b>1832.56</b>	0.1832	0	0
Nitrogen	kg/hr	0	0	0	9528.59	0.7505	<b>9527.84</b>	0.7505	0.7505	0	0.7505	0	0
Ethylene Glycol	kg/hr	0	0	0	0	0	0	0	0	0	0	0	0
Total	kg/hr	1688.79	20637.6	20637.6	9862.46	322.82	9539.63	22649.2	22649.2	1832.66	20816.6	17664.54	3169.82
Temperature	K	303.15	298.15	298.20	313.15	243.15	243.15	303.03	303.07	395.11	346.59	333.15	333.15
Pressure	kPa	100	40	100	100	200	200	100	150	129.98	100	100	2.03
Vapour Fraction	-	0	0	0	1	0	1	0	0	0	0	0	0

Table 6.4: Stream results for process 2FM (2-flash membrane)

Stream		5	12LP	12	23	25	27	28	29	36	38	D1	Retentate	Permeate
Component	Unit													
Ethanol	kg/hr	16.32	19139.6	19139.6	<b>4.81</b>	309.57	291.83	17.74	12.92	19460.7	0.0964	19460.6	<b>17650.09</b>	1823.63
Water	kg/hr	886.75	467.50	467.50	0.0580	7.61	7.23	0.3807	0.3227	1361.80	0.0040	1361.79	14.45	1346.19
Pyridine	kg/hr	785.71	1030.52	1030.52	0.0410	16.70	16.39	0.3050	0.2640	1832.89	<b>1832.71</b>	0.1833	0	0
Nitrogen	kg/hr	0	0	0	<b>9527.60</b>	9528.59	0.6912	9527.90	0.2916	0.9828	0	0.9828	0	0
Ethylene Glycol	kg/hr	0	0	0	0	0	0	0	0	0	0	0	0	0
Total	kg/hr	1688.79	20637.6	20637.6	9532.51	9862.46	316.14	9546.32	13.80	22656.3	1832.81	20823.5	17664.54	3169.82
Temperature	K	303.15	298.15	298.20	248.15	313.15	248.15	248.15	248.15	303.11	394.90	345.89	333.15	333.15
Pressure	kPa	100	40	100	1930	100	200	200	1930	150	129.21	100	100	2.03
Vapour Fraction	-	0	0	0	1	1	0	1	0	0	0	0	0	0

## Process B

Process B is presented in Figure 6.2 while the flow rates and operating conditions for each stream are shown in Table 6.3 for process 1FM (1-flash membrane) and 6.4 for process 2FM (2-flash membrane). Stream 25 is first fed into flash vessel F-01 which operates at a temperature and pressure of 243.15 K and 200 kPa respectively. Stream 28 exits the top of F-01 and is fed to flash vessel F-02 which is operated at a temperature and pressure of 248.15 K and 1930 kPa respectively. Nitrogen with a recovery of 99.99 mol % and a purity of 99.97 mol % exits the top of F-02 (stream 23). The bottoms of F-01 (stream 27) and F-02 (stream 29) is then combined with streams 5 and 12 and fed to a conventional distillation column (C-01) with an operating pressure of 100 kPa. Pyridine exits the bottom of the column (stream 38) with a recovery and purity of 99.99 mol %. The distillate (stream D1) comprising the ethanol/water azeotrope is then fed to a pervaporation unit where ethanol leaves in the retentate stream with a recovery and purity of 90.64 mol % and 99.79 % respectively. The permeate stream (comprising water and the remaining ethanol) is then recycled to the conventional distillation column (C-01) to prevent the loss of ethanol.

The modification to process B is indicated by the additional flash vessel within the red dotted lines. As seen from Tables 6.3 and 6.4, the use of the additional flash vessel results in the recovery increase for ethanol and pyridine by 6.55 kg/hr and 0.15 kg/hr respectively, similarly to process A.

The column specifications shown in Figure 6.2 (number of stages, reflux ratio, duties, etc) are discussed in section 6.2.

## 6.2 Process Optimisation

### 6.2.1 Flash Vessels

The first units to be optimised were the flash vessels. The purpose of these vessels were to separate nitrogen from pyridine, ethanol and water. The vessel temperature and pressure were both varied to maximise recovery of nitrogen in the vapour outlet and maximise recovery of ethanol, water and pyridine in the liquid outlet. Pyridine and water separates easily from nitrogen; however recovering the ethanol was more challenging. The results showed that as the temperature decreased, the separation improved; however to avoid the use of a more expensive refrigerant and higher cooling duty costs, the temperature selected was 243.15 K for processes 1FE & 1FM and 248.15 K for processes 2FE & 2FM. The material of construction selected was stainless steel due to the low vessel temperature required for separation.

Figure 6.3 displays a plot of the nitrogen mole fraction, nitrogen mole recovery and ethanol mass flow rate in the vapour outlet (stream 28) varied with the column pressure for flash vessel F-01 for processes 1FE & 1FM. It can be seen that as the nitrogen purity increases the ethanol flow rate and nitrogen recovery decreases. The pressure selected should achieve a high nitrogen purity and recovery whilst minimising the ethanol flow rate in the vapour outlet. A pressure of 200 kPa was chosen since this is the point at which the curvature is most sharply changing. This results in a nitrogen purity and recovery of 99.92 mol % and 99.99 mol % respectively, and 11.36 kg/hr of ethanol in the vapour stream.

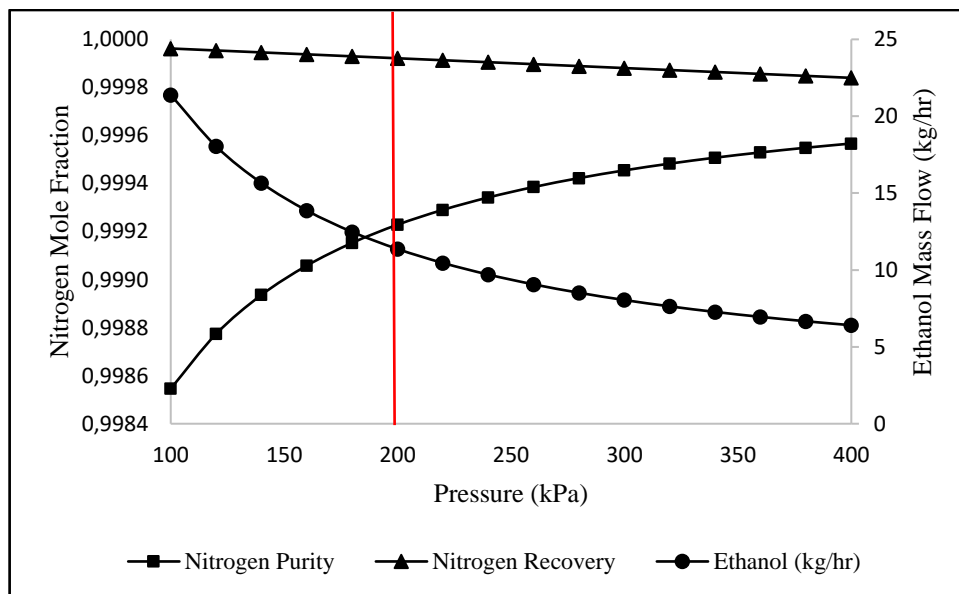


Figure 6.3: Influence of pressure on the nitrogen mole purity, nitrogen recovery and ethanol mass flow rate in the vapour outlet for F-01 (1-flash process)

Figures 6.4 and 6.5 present the sensitivity analysis plots for processes 2FE & 2FM. It can be seen that in Figure 6.4 the same trends are observed as in Figure 6.3. In Figure 6.5, the nitrogen purity and recovery are fairly constant whilst the ethanol flow rate decreases, reaches a minimum and there-after increases. A pressure of 200 kPa (point where the curvature is most sharply changing) and 1930 kPa (point of minimum ethanol flow rate) was selected for F-01 and F-02 respectively which resulted in a nitrogen purity of 99.97 mol %, a nitrogen recovery of 99.99 mol % and 4.81 kg/hr of ethanol in the vapour stream. Therefore, the use of the additional flash vessel improved the nitrogen purity by 0.05 % and reduced the loss of ethanol by 6.55 kg/hr.

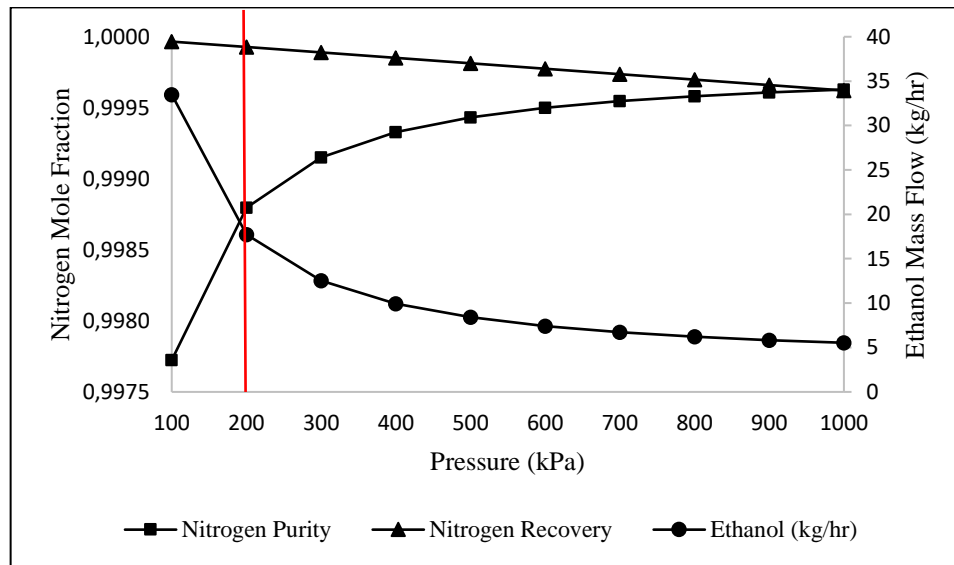


Figure 6.4: Influence of pressure on the nitrogen mole purity, nitrogen recovery and ethanol mass flow rate in the vapour outlet for F-01 (2-flash process)

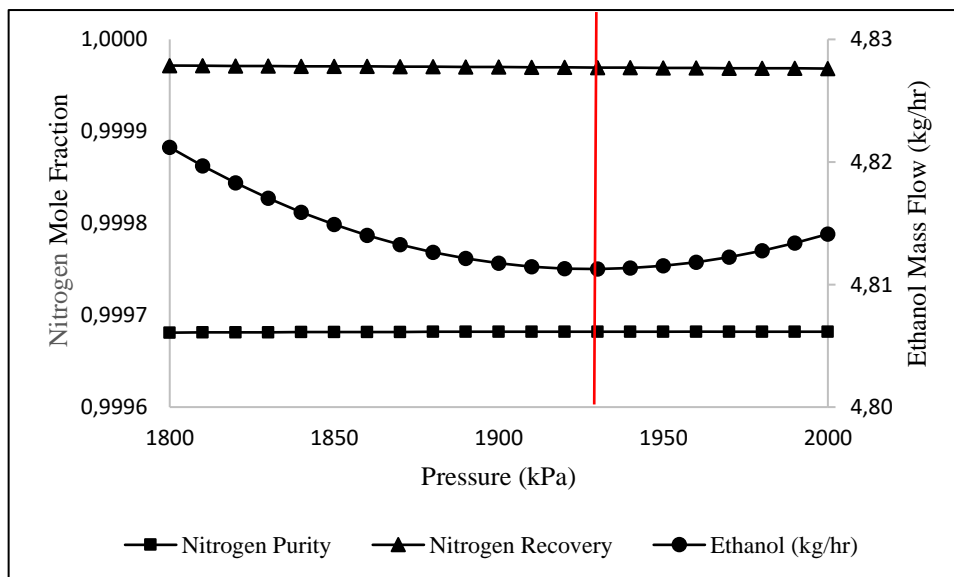


Figure 6.5: Influence of pressure on the nitrogen mole purity, nitrogen recovery and ethanol mass flow rate in the vapour outlet for F-02 (2-flash process)

### 6.3.2 Distillation Columns

The RadFrac model in Aspen Plus® was selected to simulate the distillation processes. RadFrac is a rigorous model for simulating multi-stage vapour-liquid fractioning operations. RadFrac may operate using either the traditional equilibrium-based approach (efficiency required to account for deviations from equilibrium) or the rate-based method (able to simulate real tray behaviour). It is more efficient to use the equilibrium-based method for column optimisation due to the longer calculation times and higher likelihood of convergence problems in the rate-based method. Hence, in this work, the total number of theoretical stages were calculated using an equilibrium-based method. The rate-based method was then incorporated to back-calculate the Murphree efficiencies of each component. These efficiencies were averaged over the entire column (Table 6.5) and were there-after used to resize the column using the equilibrium-based method. Sieve trays were specified due to their low cost, low pressure drop and high efficiency. The column material selected was carbon steel since the operating conditions were not extreme (too high or too low temperatures and pressures) and the components used in the process were not particularly corrosive.

Table 6.5: Component Murphree Efficiencies

Components	C-01	C-02	C-03
Ethanol	0.61	0.62	-
Water	0.65	0.67	0.65
Pyridine	0.63	0.67	-
Ethylene Glycol	-	-	0.65

#### Distillate or bottoms rate

For effective separation of species to occur in the distillation column, the distillate or bottoms flow rate is specified. If the light key component was to be removed, the distillate rate was specified. Similarly, if the heavy key component was to be removed, the bottoms rate was specified. For example, for a mixture of ethanol, water and pyridine; it was desired to achieve a separation with 99.8% mole composition of pyridine recovered as a product for reuse. Since pyridine has the highest boiling point, it is the heavy key component. Thus, the bottoms rate was selected, with a purity of 99.8% pyridine specified. The remaining 0.02% was sent to the distillate along with majority of the ethanol and water.

#### Column Pressure

The effect of the column pressure depends on the system of components to be separated. A change in the column pressure could possibly increase equipment or operating costs. However, in some cases this change may be necessary to reach desired purities, prevent thermal degradation and

avoid the use of refrigeration or high heating requirements. It is ideal to operate the distillation column at atmospheric pressure; however, it is not always possible. Table 6.6 present the critical temperatures and pressures for the components of interest. The reboiler temperature and pressure should not be close to or above these critical values so that vapour-liquid equilibrium is still possible.

The columns were operated at/near atmospheric pressure resulting in high condenser and reboiler temperatures of 341 – 359 K and 407 – 456 K respectively, due to the pyridine and ethylene glycol present in the system. However, this pressure is required to enable the use of cooling water as the condensing medium (reducing the pressure to vacuum operation requires chilled water). Furthermore, the resulting reboiler temperatures and pressures were well below the critical values and low enough such that thermal degradation did not occur at the specified column conditions. A pressure drop 0.0068 atm was specified per tray as advised by Luyben (2013).

Table 6.6: Critical properties of components

	<b>T<sub>c</sub> (K)</b>	<b>P<sub>c</sub> (MPa)</b>
Ethanol	516.25 <sup>a</sup>	6.39 <sup>a</sup>
Water	647.10 <sup>b</sup>	22.06 <sup>b</sup>
Pyridine	620 <sup>c</sup>	5.63 <sup>c</sup>
Ethylene Glycol	720 <sup>d</sup>	8.2 <sup>d</sup>

<sup>a</sup> (Vesovic, 2011)

<sup>c</sup> (PubChem, 2004)

<sup>b</sup> (Chaplin, 2017)

<sup>d</sup> (MEGlobal, 2017)

This section presents the optimisation procedure for process A (1FE & 1FM). The remaining processes followed a similar approach and are presented in Appendix E.

### Conventional Distillation Column (C-01)

This design involved optimising the following variables: number of stages, feed stage location, reflux ratio and the distillate or bottoms rate. Since the system of components are non-ideal and each with a significant difference in boiling temperature, the simple heuristic design approach (setting the total number of trays to twice the minimum or setting the reflux ratio to 1.3 times the minimum) could not be utilised. Instead the rigorous method was implemented. This involved varying the number of stages against the capital and operating costs and selecting the configuration that gave the minimum total annual cost (TAC).

The total annual cost (TAC) is represented by the following equation:

$$TAC \left( \frac{R \cdot 10^3}{year} \right) = C_v + C_f + (i_r + i_m) \times F_C \quad (6.1)$$

$C_v$  is the process variable cost comprising mainly of the annual utility costs (steam, cooling water, electricity, refrigerant, solvent make-up);  $C_f$  is the annual fixed cost such as wages and maintenance;  $F_C$  is the fixed capital investment;  $i_r$  is the fixed capital recovery rate applied to  $F_C$ ;  $i_m$  is the minimum acceptable rate of return of  $F_C$ .  $C_f$  is assumed to be 10 % of  $F_C$  and  $i_r + i_m$  is assumed to be 20 % of  $F_C$  hence the expression for TAC can be rewritten (Munoz, et al., 2006):

$$TAC \left( \frac{R \cdot 10^3}{year} \right) = C_v + (0.3) \times F_C \quad (6.2)$$

The capital investment cost of all units were evaluated using the Aspen Plus® computer software. The operating costs were determined by means of the utility prices obtained from literature. A detailed explanation of this procedure is shown in appendix B.2.

The first step was to determine the optimum ratio of the feed stage to the total number of stages. This was accomplished via the Design/Spec Vary (DSV) function incorporated in Aspen Plus®. The DSV function requires a control variable to be specified (in this case, distillate purity of pyridine). A column variable is then manipulated (in this case, the reflux ratio) to achieve the controlled variable. Therefore, an estimate is selected for the initial total number of stages, the feed stage is then varied while the DSV function calculates the reflux ratio required to meet the distillate purity specification. The optimal feed stage is located at the minimum reflux ratio as shown in Table 6.7. The DSV function was also utilised to calculate the distillate rate required to meet the specified distillate recovery of pyridine.

Table 6.7: Variation of feed stage (FS) location and reflux ratio (RR) to meet desired distillate specifications for column C-01 (process A: 1 flash extractive), and set Number of stages (NoS)

NoS	FS	RR
60	42	0.5607
<b>60</b>	<b>43</b>	<b>0.5578</b>
60	44	0.5582
60	45	0.5622

The total number of stages were then varied assuming that the ratio of the feed stage to the number of stages remained constant. The DSV function calculated the reflux ratio and the TAC was calculated by equation 6.2. A plot of the variation in TAC to the total number of stages in column C-01 for processes 1FE (1-flash extractive) is displayed in Figure 6.6.



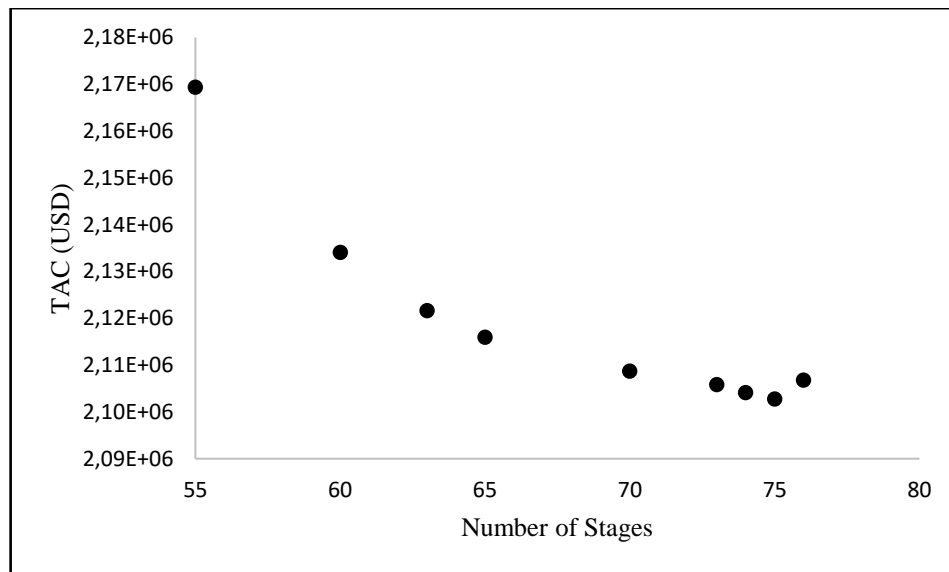


Figure 6.6: Influence of the number of stages on TAC for column C-01, process A: 1 flash extractive

As seen from the Figure, the minimum TAC is located at 75 stages hence this was selected as the optimal value. There-after, the feed stage was once again varied while the number of stages remained constant at 75. The DSV function calculated the reflux ratio for each case. The TAC was then calculated for each case and is displayed in Figure 6.7. The optimal feed stage is located at stage 58 (minimum TAC) with a reflux ratio of 0.490.

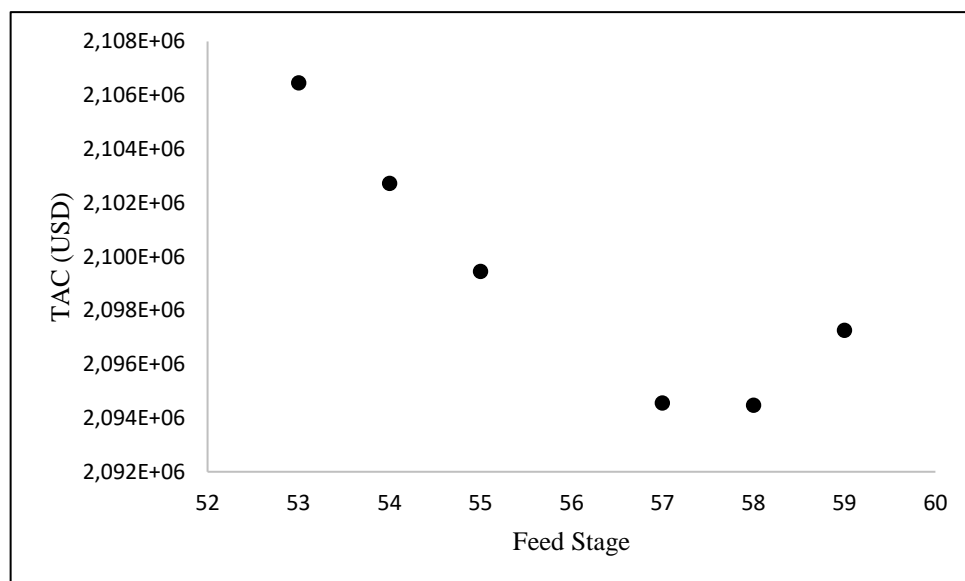


Figure 6.7: Influence of the feed stage on the total annual cost at 75 stages for column C-01, process A: 1 flash extractive

### Extractive Distillation Column (C-02)

The extractive distillation design is more complicated and a different approach is adopted as compared to the conventional distillation column. In this case, the distillate purity and recovery of ethanol was set to 99.98 mol %. The solvent to feed ratio was set to 2.0 initially (less than 2.0 does not meet the distillate specifications despite the number of stages). The number of stages were varied selecting in each case the optimal feed stage, solvent feed stage and reflux ratio. The reboiler heat duty (RHD) was recorded in each case and plotted against the number of stages as shown in Figure 6.8.

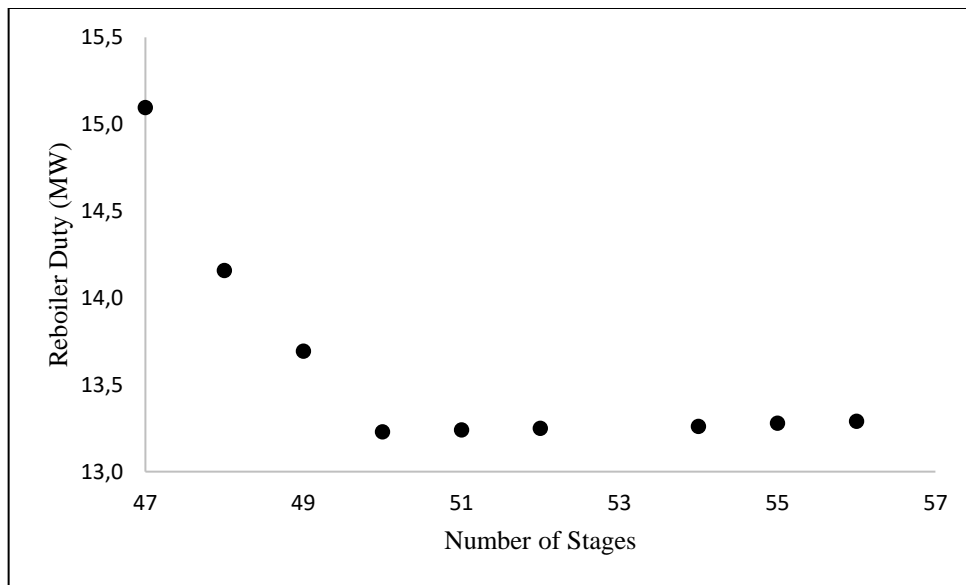


Figure 6.8: Influence of number of stages on reboiler heat duty for column C-02, process A: 1 flash extractive

The 6 cases with the lowest RHD were selected for further investigation. As seen from the Figure, this includes stages 50 (case 1), 51 (case 2), 52 (case 3), 54 (case 4), 55 (case 5) and 56 (case 6). The variables (number of stages, feed stage, solvent feed stage and reflux ratio) for each case were inputted into Aspen Plus® and there-after, the solvent to feed ratio was adjusted to minimise the RHD in each case. Figure 6.9 shows this effect for case 5.

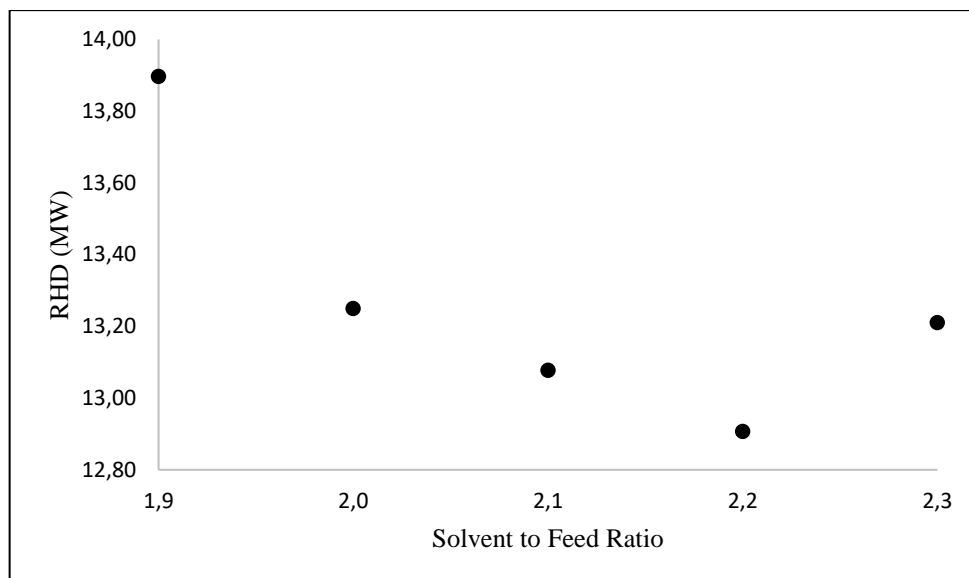


Figure 6.9: Effect of solvent to feed ratio on RHD for case 5 for column C-02, process A: 1 flash extractive

As seen in Figure 6.9, the optimal solvent to feed ratio was 2.2 as this is the value with the minimum RHD. The same procedure was followed for the remaining cases. The results are displayed in Table 6.8.

Table 6.8: Extractive distillation column specifications for each case for column C-02, process A: 1 flash extractive

Case	NoS	FS	SFS	RR	S/F Ratio	Purity	Recovery	RHD (MW)
1	47	37	8	0.6	2.4	0.9998	0.9998	13.47
2	48	38	8	0.6	2.3	0.9998	0.9998	13.18
3	49	39	8	0.7	2.1	0.9998	0.9998	13.06
<b>4</b>	<b>50</b>	<b>38</b>	<b>8</b>	<b>0.6</b>	<b>2.2</b>	<b>0.9998</b>	<b>0.9998</b>	<b>12.90</b>
5	51	37	8	0.6	2.2	0.9998	0.9998	12.91
6	52	37	8	0.6	2.2	0.9998	0.9998	12.92

NoS: Number of Stages  
 FS: Feed Stage  
 SFS: Solvent Feed Stage

RR: Reflux Ratio  
 S/F: Solvent to Feed  
 RHD: Reboiler Heat Duty

As seen in Table 6.8, the optimal was at case 4 as this combination resulted in the lowest RHD. The RHD is a major contributor to the process variable costs and is hence used as an indicator for optimal solutions. For a more thorough investigation, the TAC was calculated as this takes into account the capital investment cost as well as the process variable costs. Presented in Figure 6.10 is a plot of the TAC for each case. As seen from the Figure, the optimum was at case 4 since this resulted in the minimum TAC.

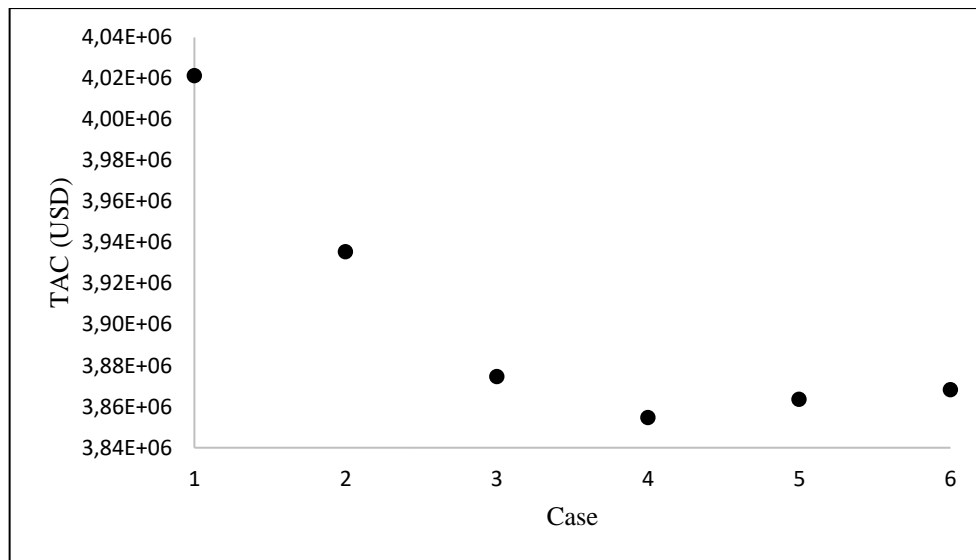


Figure 6.10: Total annual cost for the different cases in column C-02, process A, 1 flash extractive.

### Solvent Recovery Distillation Column (C-03)

The optimisation of the solvent recovery distillation column follows the same procedure as the first distillation column (C-01). This results in a 32 stage column with a feed stage of 12 and a reflux ratio of 2.56. The plots and tables of the detailed results can be found in appendix E.1.

### 6.3 Membrane Design

The membrane (pervaporation) was used as an alternative solution to the extractive distillation process. Hence, in process 1FM, the conventional distillation column (C-01) was followed by the pervaporation unit replacing columns C-02 and C-03. The membrane network was designed following the procedure by Wijmans & Baker (1993) as discussed in section 2.4 and Appendix A. A total flow rate of 20824 kg/hr was fed into the membrane configuration which consisted of 12 modules in parallel by 4 modules in series as shown in Figure 6.11. This configuration was selected as it proved to be practically possible and economically feasible according to Flemmer, et al. (1987) and Matteo (2015). Flemmer, et al. (1987) presents possible configurations for spiral wound modules. In each case an arrangement of 12 modules was considered with 12 modules in parallel demonstrating a clear superiority over other configurations. Matteo discusses and presents typical membrane and module specifications to successfully design the process. The aim is to produce a selective, high flux membrane and to assemble this membrane into compact, economical membrane modules. The total flow rate was divided by 12 (number of parallel modules) and fed in equal amounts to each parallel arrangement as shown in the Figure. The retentate exiting each module becomes the feed to the next module, this is represented by the black lines in the diagram. The permeate exits the bottom of each module and accumulates to a single stream, this is represented by the red lines in the diagram.

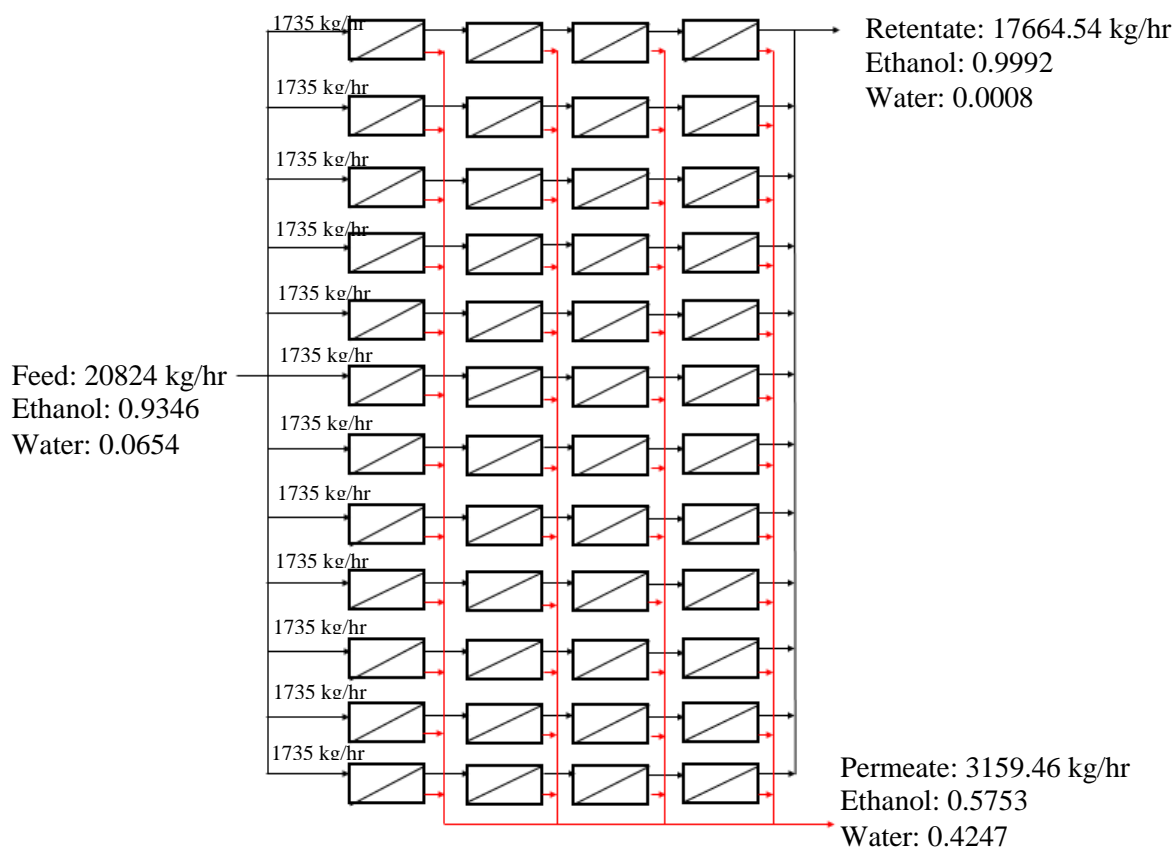


Figure 6.11: Membrane network configuration

Table 6.9 displays the membrane and module specifications. The membrane material, feed temperature and permeate pressure were specified by Wijmans & Baker (1993). The remaining specifications were selected for a spiral wound module as specified by Matteo (2015).

Table 6.9: Membrane and module specifications

<b>Membrane Material</b>	Poly(vinyl alcohol)
<b>Feed Temperature (°C)</b>	60
<b>Permeate Pressure (kPa)</b>	2.03
<b>Module</b>	Spiral wound
<b>Configuration</b>	Cross-flow
<b>Inside tube diameter (m)</b>	0.2
<b>Module diameter (m)</b>	0.2032
<b>Module length (m)</b>	1.016
<b>Number of envelopes</b>	15
<b>Membrane Area</b>	20

The first row of the membrane configuration is expanded and displayed in Figure 6.12 to enable a clear explanation of the process. Firstly, the total flow rate was divided by 12, resulting in a flow of approximately 1735 kg/hr (which is acceptable for the type of configuration utilised according to Cao & Henson (2002)) and fed into each parallel arrangement.

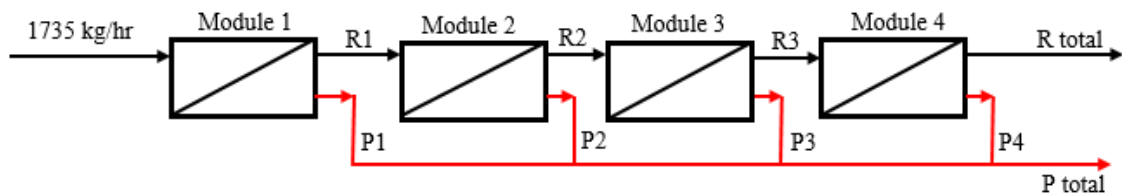


Figure 6.12: First row expansion of module configuration

Each module has an area of 20 m<sup>2</sup> and 15 envelopes. Therefore, the 4 modules connected in series in Figure 6.12 has a total area of 80 m<sup>2</sup>. The retentate exiting each module becomes the feed to the next module, this is represented by the black lines in the diagram. The permeate exits the bottom of each module and accumulates to a single stream, this is represented by the red lines in the diagram. Table 6.10 presents the stream flow rates and compositions for each module displayed in Figure 6.12.

Table 6.10: First row results of module configuration

<b>Stream</b>	<b>Flow rate (kmol/hr)</b>	<b>R<sub>ethanol</sub> Mole Fraction</b>	<b>P<sub>ethanol</sub> mass flow (kg/hr)</b>
R1	34.77	0.986	-
R2	33.71	0.993	-
R3	32.82	0.996	-
R total	31.99	0.998	-
P1	6.76	-	43.60
P2	1.05	-	37.00
P3	0.89	-	35.93
P4	0.83	-	35.43

P: Permeate and R: Retentate

As seen from the Table, an ethanol mole composition of 0.998 is achieved in the retentate stream exiting module 4. However, it is important to note the loss of ethanol to the permeate stream as the liquid passes through each module. This amounts to 43.6 kg/hr from module 1, 37 kg/hr from module 2, 35.93 kg/hr from module 3 and 35.43 kg/hr from module 4 resulting in a total of 151.96 kg/hr of ethanol lost to the permeate for the first row of the module configuration.

The remaining 11 rows follow the same procedure and contains the same exact values displayed in Table 6.10. Therefore, the total ethanol loss to the permeate stream is 151.96 kg/hr multiplied by 12 resulting in 1823.63 kg/hr. However, the accumulated permeate stream exiting the total membrane configuration is recycled to distillation column C-01 thus preventing the loss of ethanol. The final retentate stream exits the total membrane configuration with an ethanol mole purity of 99.79 %.

## 6.4 Simulation Results

Table 6.11: Distillation column specifications for process A (2FE & 1FE)

	Process 2FE			Process 1FE		
	C-01	C-02	C-03	C-01	C-02	C-03
<b>Number of Stages</b>	73	50	33	75	50	32
<b>Feed Stage</b>	56	39	13	58	38	12
<b>Solvent Feed Stage</b>	-	9	-	-	8	-
<b>Solvent Feed Temperature (K)</b>	-	348.15	-	-	348.15	-
<b>Solvent/Feed Ratio</b>	-	2.2	-	-	2.2	-
<b>Reflux Ratio</b>	0.495	0.6	2.47	0.490	0.6	2.56
<b>Diameter (m)</b>	3	3	2	3	3	2
<b>Length (m)</b>	51.94	35.11	22.68	53.40	35.11	21.95
<b>L/D Ratio</b>	17.31	11.70	11.34	17.80	11.70	10.97
<b>Pressure (kPa)</b>	150	93	30	150	97	30
<b>Condenser Temperature (K)</b>	358.15	343.38	341.61	358.82	345.87	341.66
<b>Reboiler Temperature (K)</b>	407.65	454.45	447.36	407.65	455.64	447.07
<b>Condenser Duty (MW)</b>	-8.04	-7.51	-3.07	-7.99	-7.45	-3.15
<b>Reboiler Duty (MW)</b>	9.22	12.89	2.48	9.19	12.93	2.47

2FE: process with 2 flash vessel and extractive distillation

1FE: process with 1 flash vessel and extractive distillation

Table 6.12: Distillation column specifications for process B (2FM & 1FM)

	Process 2FM	Process 1FM
	C-01	C-01
<b>Number of Stages</b>	63	65
<b>Feed Stage</b>	48	50
<b>Reflux Ratio</b>	0.465	0.462
<b>Diameter (m)</b>	3	3
<b>Length (m)</b>	44.62	46.09
<b>L/D Ratio</b>	14.87	15.36
<b>Pressure (kPa)</b>	100	100
<b>Condenser Temperature (K)</b>	345.89	346.59
<b>Reboiler Temperature (K)</b>	394.90	395.11
<b>Condenser Duty (MW)</b>	-9.99	-9.95
<b>Reboiler Duty (MW)</b>	10.97	10.94

2FM: process with 2 flash vessels and membrane unit

1FM: process with 1 flash vessel and membrane unit

Tables 6.11 and 6.12 display the distillation column specifications for processes A and B respectively. The number of stages, feed stage, reflux ratio, solvent feed stage, solvent feed



temperature and solvent/feed ratio were determined via the optimisation procedures described in section 6.2. The values were selected based on either the minimum total annual cost, the minimum reboiler heat duty or the purity/recovery requirement.

The diameter was calculated using the Aspen Plus® tray sizing function while the length was calculated by equation 6.3 (typical distance between trays is 0.61 m according to Luyben (2013)).

$$L = 1.2 \times (\text{Tray spacing}) \times (\text{Number of Stages} - 2) \quad 6.3$$

According to KLM Technology Group (2011), the length/diameter (L/D) ratio of a tower should be no more than 30 and preferably below 20. As seen from Tables 6.11 and 6.12, the L/D ratios are well below 20 and hence are acceptable.

The pressures for each column were selected to enable the use of cooling water as the cooling medium and to prevent the occurrence of thermal degradation. It can be seen that the resulting condenser and reboiler temperatures of 341 – 359 K and 394 – 456 K respectively are high. This however is due to the high boiling pyridine and ethylene glycol present in the system. The condenser and reboiler duties were minimised during the optimisation procedure and are also displayed in the Tables.

Table 6.13 presents the flash vessel specifications for each process. The pressures and temperatures were selected via the optimisation procedures described in section 6.2. Also displayed are the column duties.

Table 6.13: Flash vessel specifications

	<b>Processes 2FE &amp; 2FM</b>		<b>Processes 1FE &amp; 1FM</b>
	<b>F-01</b>	<b>F-02</b>	<b>F-01</b>
<b>Pressure (kPa)</b>	200	1930	200
<b>Temperature (K)</b>	248.15	248.15	243.15
<b>Duty (kW)</b>	-275.21	-21.38	-291.95

2FE: process with 2 flash vessels extractive distillation

2FM: process with 2 flash vessels and membrane unit

1FE: process with 1 flash vessel and extractive distillation

1FM: process with 1 flash vessel and membrane unit

Table 6.14 presents the final flow rates and compositions for the relevant streams in process A. It can be seen that the mole purities and recoveries of key components ethanol, pyridine and nitrogen are all greater than 99.9 mol % and hence meet the required specifications as proposed by NECSA.

Process 1FE utilises one flash vessel and process 2FE utilises two flashes for the nitrogen separation. As seen from Table 6.14, the nitrogen rich stream for process 1FE still contained 11.36 kg/hr of ethanol. Therefore, this stream was sent to another flash vessel for further purification.

As seen from Table 6.14, the additional flash vessel in process 2FE increased the nitrogen purity by 0.05 % and recovered a further 6.55 kg/hr of ethanol and 0.16 kg/hr of pyridine. Though the additional flash vessel improved the separation, a cost comparison was required to determine the its feasibility. This is discussed further in section 6.6.

Table 6.14: Final stream compositions and purities for process A:

	Process 2FE				Process 1FE			
Stream	23	38	37	Recovery	28	38	37	Recovery
<b>Mole Flow (kmol/hr)</b>								
Ethanol	0.1044	0.0021	422.33	<b>0.9998</b>	0.2467	0.0021	422.19	<b>0.9998</b>
Water	0.0032	0	0.0519		0.0135	0	0.0413	
Pyridine	0.0005	23.17	0	<b>0.9999</b>	0.0024	23.17	0	<b>0.9999</b>
Nitrogen	340.11	0	0.0351	<b>0.9999</b>	340.12	0	0.0268	<b>0.9999</b>
Ethylene Glycol	0	0	0.0059		0	0	0.0174	
<b>Mole Fraction</b>								
Ethanol	0.0003	0.0001	<b>0.9998</b>		0.0008	0.0001	<b>0.9998</b>	
Water	0	0	0.0001		0	0	0.0001	
Pyridine	0	<b>0.9999</b>	0		0	<b>0.9999</b>	0	
Nitrogen	<b>0.9997</b>	0	0.0001		<b>0.9992</b>	0	0.0001	
Ethylene Glycol	0	0	0		0	0	0	
<b>Mass Flow (kg/hr)</b>								
Ethanol	<b>4.81</b>	0.0964	<b>19456.28</b>		<b>11.36</b>	0.0965	<b>19450.10</b>	
Water	0.0580	0.0040	0.9352		0.2428	0.0040	0.7445	
Pyridine	0.0410	<b>1832.71</b>	0.0008		0.1922	<b>1832.55</b>	0	
Nitrogen	9527.60	0	0.9828		9527.84	0	0.7505	
Ethylene Glycol	0	0	0.3692		0	0	1.08	
<b>Mass Fraction</b>								
Ethanol	0.0005	0.0001	0.9999		0.0012	0.0001	0.9999	
Water	0	0	0		0	0	0	
Pyridine	0	0.9999	0		0	0.9999	0	
Nitrogen	0.9995	0	0.0001		0.9988	0	0	
Ethylene Glycol	0	0	0		0	0	0.0001	
<b>Total Flow (kg/hr)</b>	9532.51	1832.81	19458.56		9539.63	1832.66	19452.67	
<b>Temperature (K)</b>	248.15	407.65	343.38		243.15	407.65	345.87	
<b>Pressure (kPa)</b>	1930	179.49	93		200	179.48	97	

2FE: process with 2 flash vessels and extractive distillation

1FE: process with 1 flash vessel and extractive distillation

Table 6.15 presents the final flow rates and compositions for the relevant streams in process B. Process 1FM utilises one flash vessel and process 2FM utilises two flashes for the nitrogen separation. As seen from Table 6.15, the use of the additional flash vessel increased the nitrogen

purity by 0.05 % and recovered a further 6.55 kg/hr of ethanol and 0.15 kg/hr of pyridine similarly to process A.

It is also observed that an ethanol mole recovery of 90.64 % was obtained in the retentate stream resulting in an ethanol loss of 1823.63 kg/hr (9.36 %) to the permeate stream. However, this stream was recycled to the distillation column preventing any loss of chemical. The addition of this stream to the distillation column shifts the feed composition such that the separation of pyridine becomes more difficult. As seen in Table 6.15, the maximum allowable recovery and purity of pyridine is 99.5 mol % (as opposed to the 99.99 mol % achieved with extractive distillation).

An ethanol mole purity of 99.79 % was obtained in the retentate stream. The total membrane area discussed in section 6.3 could have been increased to improve the ethanol purity however, the separation became extremely slow as the amount of water decreased. The retentate stream contains a water content of 0.21 mol %; had this stream been dehydrated to a water content of 0.01 mol % (like the purity obtained in extractive distillation), the total membrane area would have increased to a value of 2000 m<sup>2</sup> resulting in a cost of 8 million euros (Wolf, 2017). The area required for the membrane then becomes practically and economically unfeasible. Furthermore, increasing the membrane area, increases the flow rate of the recycle stream (permeate) thereby decreasing the allowable recovery and purity of the core component, pyridine. A cost evaluation was performed and is discussed further in section 6.6.

Table 6.15: Final stream compositions and purities for process B

	Process 2FM				Process 1FM			
Stream	23	38	Retentate	Recovery	28	38	Retentate	Recovery
<b>Mole Flow (kmol/hr)</b>								
Ethanol	0.1044	0.0132	382.87	<b>0.9064</b>	0.2467	0.0132	382.87	<b>0.9064</b>
Water	0.0032	0.1027	0.80		0.0135	0.1026	0.80	
Pyridine	0.0005	23.06	0	<b>0.9950</b>	0.0024	23.06	0	<b>0.9950</b>
Nitrogen	340.11	0	0	<b>0.9999</b>	340.12	0	0	<b>0.9999</b>
Ethylene Glycol	0	0	0		0	0	0	
<b>Mole Fraction</b>								
Ethanol	0.0003	0.0006	<b>0.9979</b>		0.0008	0.0006	<b>0.9979</b>	
Water	0	0.0044	0.0021		0	0.0044	0.0021	
Pyridine	0	<b>0.9950</b>	0		0	<b>0.9950</b>	0	
Nitrogen	<b>0.9997</b>	0	0		<b>0.9992</b>	0	0	
Ethylene Glycol	0	0	0		0	0	0	
<b>Mass Flow (kg/hr)</b>								
Ethanol	<b>4.81</b>	0.6072	17650.09		<b>11.36</b>	0.6092	17650.09	
Water	0.0580	1.85	14.45		0.2428	1.85	14.45	
Pyridine	0.0410	<b>1823.88</b>	0		0.1922	<b>1823.73</b>	0	
Nitrogen	9527.60	0	0		9527.84	0	0	
Ethylene Glycol	0	0	0		0	0	1	
<b>Mass Fraction</b>								
Ethanol	0.0005	0.0003	0.9992		0.0012	0.0003	0.9992	
Water	0	0.0010	0.0008		0	0.0010	0.0008	
Pyridine	0	0.9987	0		0	0.9987	0	
Nitrogen	0.9995	0	0		0.9988	0	0	
Ethylene Glycol	0	0	0		0	0	0	
<b>Total Flow (kg/hr)</b>	9532.51	1826.34	17664.54		9539.63	1826.19	17664.54	
<b>Temperature (K)</b>	248.15	394.90	333.15		243.15	395.11	333.15	
<b>Pressure (kPa)</b>	1930	129.21	100		200	129.98	100	

2FM: process with 2 flash vessels and membrane unit

1FM: process with 1 flash vessel and membrane unit

## 6.5 Comparison of the Design Proposed by NECSA and this study

Two separation schemes were developed to recover pyridine, ethanol and nitrogen for reuse in the LiPF<sub>6</sub> production process. NECSA also proposed a process to recover these components. However, this process was not designed, but merely suggested based on assumptions. The final mole purities and recovery rates estimated from NECSA's proposal were used as a basis for the separation schemes developed in this work. The recovery rates achieved in this study for process A (99.99 mol % nitrogen, 99.98 mol % ethanol, 99.99 mol % pyridine) are greater than the values

reported by NECSA (95.00 mol % nitrogen, 99.80 mol % ethanol, 99.99 mol % pyridine) for all three components whilst the recovery rates achieved in process B (99.99 mol % nitrogen, 100 mol % ethanol, 99.50 mol % pyridine) are greater than NECSA's proposal for nitrogen and ethanol but 0.49 mol % lower for pyridine. The mole purities obtained in process A for ethanol (99.98 %) and pyridine (99.99 %) were also greater than the mole purities stated by NECSA (99.98 % ethanol, 97.76 % pyridine) whilst the mole purities obtained in process B was greater for pyridine (99.5 %) and slightly lower for ethanol (99.79%). The nitrogen mole purity in both processes A & B (99.97 %) was slightly lower than NECSA's proposal (99.99 %). However, it is important to note that in NECSA's recycle process proposal, some of the assumptions made were inaccurate. For example, it is assumed that 100 % of the nitrogen entering a gas permeation unit is removed in the permeate. This is unlikely. Furthermore, NECSA's separation scheme could not be designed and verified since an extensive search showed that there is currently no permeation flux data for the systems of interest in the open literature. Without this data, the membranes could not be designed. Therefore, in terms of the overall mole purities and recovery rates, the processes developed in this work achieves a better separation.

## 6.6 Cost Evaluation

Table 6.16 is a summary of the capital and operating costs for processes developed in this study. The capital investment cost of the membrane and modules were calculated manually on Microsoft Excel. This involved multiplying the membrane/module area by the typical costs obtained in literature. The total membrane/module area required was calculated using the methodology by Wijmans & Baker (1993) shown in appendix A. The capital investment cost of all other units were evaluated using the Aspen Plus® computer software. The operating costs were determined by means of the utility correlations and prices obtained in literature. A detailed explanation is provided in Appendix B. In Table 6.16, the total capital investment costs, operating costs and total annual costs are highlighted in bold.

Table 6.16: Capital and operating cost summary

<b>Equipment Cost (R 10<sup>3</sup>/hr)</b>	<b>Process A (2FE)</b>	<b>Process A (1FE)</b>	<b>Process B (2FM)</b>	<b>Process B (1FM)</b>
F-01-flash vessel	394.95	394.95	394.95	394.95
F-02-flash vessel	541.85		541.85	
P-01-pump	60.21	60.21	60.21	60.21
P-02-pump	61.41	61.41	62.61	62.61
C-01-condenser	462.38	459.97	622.53	618.92
C-01-reflux drum	180.62	149.31	181.82	181.82
C-01-reboiler	1201.71	1199.31	1080.10	1080.10
C-01-reflux pump	60.21	60.21	61.41	61.41
C-01-tower	7687.11	7887.00	6666.02	6939.35
C-02-condenser	511.75	496.10		
C-02-reflux drum	181.82	181.82		
C-02-reboiler	1326.94	1334.17		
C-02-reflux pump	60.21	60.21		
C-02-tower	5439.02	5439.02		
C-03-condenser	233.60	236.01		
C-03-reflux drum	181.82	181.82		
C-03-reboiler	385.32	385.32		
C-03-reflux pump	51.78	51.78		
C-03-tower	2591.27	2449.18		
HX-01-cooler	396.16	396.16		
Membrane Module				
<b>Total Capital (R 10<sup>3</sup>)</b>	<b>22010.14</b>	<b>21483.94</b>	<b>13120.43</b>	<b>12848.30</b>

<b>Operating Costs (R 10<sup>3</sup>/year)</b>	<b>Process A (2FE)</b>	<b>Process A (1FE)</b>	<b>Process B (2FM)</b>	<b>Process B (1FM)</b>
P-01	5.94	5.94	5.94	5.94
P-01	10.50	10.50	5.82	5.82
F-01	2079.95	2206.41	2079.95	2206.41
F-02	161.59		161.59	
C-01 condenser	980.72	974.47	1218.44	1213.41
C-01 reboiler	10164.18	10122.91	16710.19	12058.44
C-02 condenser	915.41	908.56		
C-02 reboiler	19712.51	19778.24		
C-03 condenser	374.54	383.92		
C-03 reboiler	3793.76	3778.93		
HX-01	620.88	618.92		
Solvent make up	68.00	113.94		
Refrigeration				
Feed Cooler				
Vacuum Pump				
Inter-stage Heaters				
Total	38887.97	38902.75	30515.36	25823.46
Solvent	550.90	500.90		
Replacement			1842.99	1842.99
<b>Total Operating Costs (R 10<sup>3</sup>/year)</b>	<b>39438.87</b>	<b>39453.65</b>	<b>32358.35</b>	<b>27666.45</b>
<b>TAC (R 10<sup>3</sup>)</b>	<b>46041.91</b>	<b>45898.83</b>	<b>36294.48</b>	<b>31520.94</b>

---

The total annual cost of the processes including extractive distillation are much larger than the processes with the membranes. However, the total membrane area required (960 m<sup>2</sup>) is large and the membrane process allows a recovery and purity of only 99.5 mol % pyridine as opposed to the 99.99 mol % achieved with extractive distillation. Furthermore, the capital investment cost of the membrane was calculated based on estimates (such as membrane and module cost, structural arrangement and flow rate allowance) from one research paper and the total area calculated was restricted to 960 m<sup>2</sup> due to the reduction in pyridine recovery and purity. The retentate stream contains a water content of 0.21 mol %; had this stream been dehydrated to a water content of 0.01 mol % (similar to the purity obtained in extractive distillation), the pyridine loss, total membrane area and capital costs would have increased significantly.

The processes with two flash vessels have higher capital and operating costs than the processes with one flash vessel. The higher capital cost is due to the costs associated with purchasing and installing an additional unit. The higher operating cost is due to the additional liquid flow rate recovered of 7.12 kg/hr (comprising pyridine, ethanol and water) which is sent to the distillation columns resulting in higher flow rates and hence higher operating costs (for example, more steam or cooling water will be required to heat/cool process streams). The cost difference between processes 1FE and 2FE is minimal (R0.14 million). The cost difference between processes 1FM and 2FM is significant (R5 million).

Table 6.17 includes the final mole purity, mole flow and mass flow for each component after separation. It can be seen that processes 1FM and 2FM show little to no change and the only significant change between processes 1FE and 2FE is the additional 6.18 kg/hr of ethanol recovered with two flash vessels.



Table 6.17: Purity and flow rate of relevant streams

<b>Mole Purity</b>	<b>Process 2FE</b>	<b>Process 1FE</b>	<b>Process 2FM</b>	<b>Process 1FM</b>
Nitrogen	0.9997	0.9992	0.9997	0.9992
Pyridine	0.9999	0.9999	0.9950	0.9950
Ethanol	0.9998	0.9998	0.9979	0.9979
Ethylene Glycol Recycle	0.9999	0.9999		
<b>Mole Flow (kmol/hr)</b>				
Nitrogen	340.11	340.12	340.11	340.12
Pyridine	23.17	23.17	23.06	23.06
Ethanol	422.33	422.19	382.87	382.87
Ethylene Glycol Recycle	1095.98	1095.97		
<b>Mass (kg/hr)</b>				
Nitrogen	9527.60	9527.84	9527.60	9527.84
Pyridine	1832.71	1832.56	1823.88	1823.73
Ethanol	<b>19456.28</b>	<b>19450.10</b>	17650.09	17650.09
Ethylene Glycol Recycle	68025.96	68025.25		

2FE: process with 2 flash vessels and extractive distillation

1FE: process with 1 flash vessel and extractive distillation

2FM: process with 2 flash vessels and membrane unit

1FM: process with 1 flash vessel and membrane unit

Therefore, the use of the additional flash vessel in process B is infeasible due to the significant increase in cost and little to no improvement in component flows. The use of the additional flash vessel in process A however recovers more ethanol and contains a purer nitrogen stream whilst increasing the total annual cost by only R0.14 million thereby proving its feasibility.

Figures 6.13 and 6.14 display an operating cost summary of the two processes developed, showing the major utility costs. It can be seen that the highest contributors are the steam requirement for the reboilers and the refrigerant required for permeate condensing.

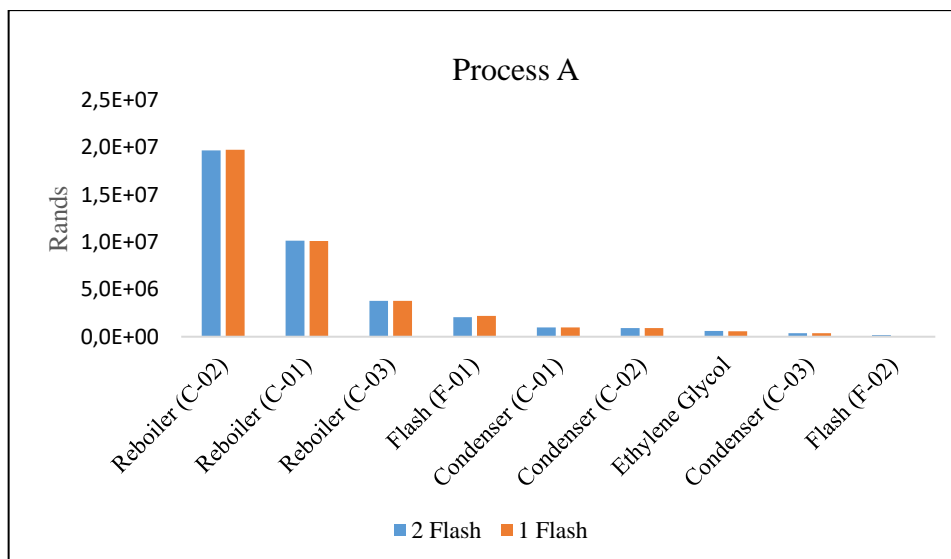


Figure 6.13: Operating cost summary for process A (process with extractive distillation)

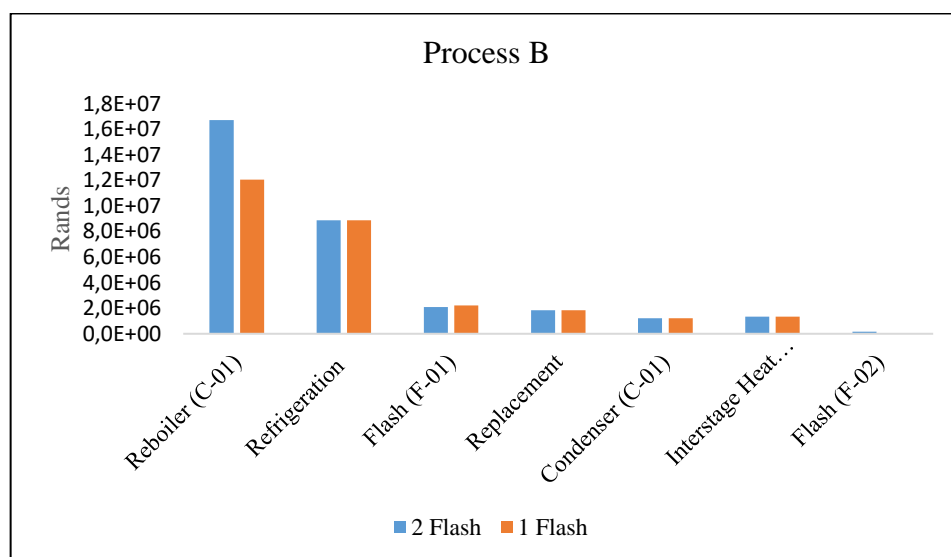


Figure 6.14: Operating cost summary for process B (process with membranes)

## CHAPTER 7: CONCLUSION

A novel process for the production of lithium hexafluorophosphate ( $\text{LiPF}_6$ ) was developed by NECSA. The purpose of this study was the design and economic evaluation of a process to treat the waste streams (comprising pyridine, ethanol, water and nitrogen) leaving the  $\text{LiPF}_6$  production process. The objective was to separate and recover these components such that they could be recycled and reused in the  $\text{LiPF}_6$  production.

The design and development of separation processes rely on accurate vapour liquid equilibrium (VLE) data. The ethanol/pyridine (40 kPa, 100 kPa, 313.15 K) and water/pyridine (40 kPa, 333.15 K) phase data were measured since the VLE data found in literature for these systems were inconsistent. A modified recirculating VLE still was used to measure the phase equilibrium data with sample analysis performed using a Shimadzu GC-2014.

The measured data was regressed using various thermodynamic models in Aspen Plus®. The model that best suited the components of interest was the Peng-Robinson equation of state incorporating the Mathias Copeman alpha function with the Wong-Sandler mixing rules and the NRTL activity coefficient model (PR-MC-WS-NRTL). The binary parameters obtained with the use of this model was then incorporated into the Aspen Plus® computer software where it was used to simulate proposed process schemes.

The ethanol/water system was not measured since there is a wide range of consistent VLE data available for this system. Aspen Plus® stores physical property parameters for numerous components in several databanks which are developed from the thermodynamic models available and data from the Dortmund Databank. Hence the built-in parameters from Aspen Plus® for the ethanol/water system was used for the design.

A mixture of four components (nitrogen, ethanol, water and pyridine) required separation and recovery. Nitrogen could easily be removed with the use of a flash vessel. The behaviour of the remaining components (ethanol, water and pyridine) was studied and residue curve maps drawn to determine the type of separation expected. It was observed from these diagrams that pyridine could be separated via conventional distillation. The separation of ethanol and water however, required the use of an enhanced separation technique due to the azeotrope formed. Extractive distillation and pervaporation were selected to separate ethanol from water since these are common and simple processes, less energy intensive than the alternatives and can handle the feed capacity.

Two separation schemes were investigated. Process A treats the waste stream firstly via a flash vessel to remove the nitrogen, then a conventional distillation column to separate the pyridine from the mixture followed by an extractive distillation column to separate the ethanol from water.

The solvent chosen for extractive distillation was ethylene glycol since it is less energy intensive than its alternative liquid solvents and ionic liquids and contains no unwanted entrainment (solid salt) into the product or equipment. Process B follows the same scheme as process A for the nitrogen and pyridine separation; however it uses a pervaporation membrane modular setup, incorporating a polyvinylalcohol (PVA) membrane in a spiral wound configuration, to break the ethanol/water azeotrope as opposed to the use of the extractive distillation column use in process A. PVA was selected as the membrane material since an extensive search showed that the only permeation flux data available in the open literature was one which used a PVA membrane. The spiral wound module was selected since it is simpler and less expensive than its alternatives. Modifications were made to each process where an additional flash vessel was used to further purify the nitrogen stream. Pyridine and water separated from nitrogen easily; however, separating the ethanol was more challenging. Therefore, this additional flash vessel was utilised to separate the remaining ethanol from nitrogen.

The membranes were designed on Microsoft Excel, while all other units were designed on Aspen Plus®. The flash vessels and distillation columns were optimised using sensitivity analysis plots. These are graphs that vary variables such as temperature, pressure, number of stages, feed stage location, reflux ratio, etc. against mole purities, column duties and total costs. The membranes were designed following a procedure from a research paper.

The final mole purity and recovery rate of nitrogen was >99.9 mol % for all processes. The ethanol and pyridine mole purities and recovery rates for the extractive distillation processes were also >99.9 mol %. Regarding the membrane processes, the pyridine purity and recovery was 99.5 mol % while the ethanol purity was 99.79 mol % with a recovery of 100 mol % (since the permeate was recycled).

The economic analysis showed that while process A met the specified purity and recovery of 99.9 mol %, it had a high total annual cost (approximately R46 million) due to the large amount of solvent required for extractive distillation. Process B using the modular membrane setup, had a significantly lower total annual cost (approximately R32 million). However, this is due to the area restriction imposed on the membrane (960 m<sup>2</sup>) due to the pyridine loss and slow separation process as the water composition decreased. The ethanol-rich stream (retentate) leaving the membrane unit contained a water content of 0.21 mol %; had this stream been dehydrated to a water content of 0.01 mol % (similar to the purity obtained with extractive distillation), the total membrane area would have increased to a value of 2000 m<sup>2</sup> resulting in a cost of 8 million euros. The area required for the membrane then becomes practically and economically unfeasible. Furthermore, increasing the membrane area, increases the flow rate of the recycle stream (permeate) thereby decreasing the allowable recovery and purity of the core component, pyridine.

The use of the additional flash vessel in process B was not economically feasible due to the significant increase in cost (R4 million) and little to no improvement in final component purities. However, the additional flash vessel in process A recovered a further 6.18 kg/hr of ethanol producing a purer nitrogen stream whilst slightly increasing the total annual cost by R0.14 million.

To conclude, process B does not meet the purity and recovery specifications for pyridine and ethanol. If it is attempted to achieve the ethanol purity specification, the membrane process becomes impractical due to the large membrane area required and the recovery and purity of the core component pyridine decreases. Furthermore, the additional flash vessel used in this process significantly increases the total annual cost and does not improve the product purities. Process A meets the required purity and recovery specifications for all components and is practically feasible. The additional flash vessel used in this process recovers a further 6.18 kg/hr of ethanol whilst slightly increasing the total annual cost and hence is the optimal solution.

## CHAPTER 8: RECOMMENDATIONS

The extractive distillation processes have a large total annual cost. This is due to the high solvent to feed ratio, high liquid phase load and great amount of solvent recycling resulting in a high consumption of energy. A combination of ethylene glycol and calcium chloride salt should be investigated. The addition of the salt increases the relative volatility of the ethanol-water system thereby reducing the number of theoretical stages, the amount of solvent required and hence the energy consumption. Furthermore, mixing the solid salt with ethylene glycol allows utilising the advantages of both components and reduces the shortcomings such as corrosion caused by the salt and high energy consumption by the liquid solvent.

Experiments on the ethanol/water/pyridine, ethanol/water and pyridine/water systems should be performed to determine the permeation fluxes for a membrane design. This will allow the selection of a more suitable membrane material and numerous possibilities for the design procedure.

Different membrane modules should be investigated. Other modules could possibly produce a simpler configuration with lower area and cost requirements.

Heat integration is a technique utilised to minimise energy consumption and maximise heat recovery in a chemical process. This is done by recovering heat that was previously cooled off and reusing it in another unit operation. This task minimises the operating costs as it reduces the utility requirements such as steam and cooling water. This however was not performed in this research project as the process designed is not the entire plant but just a sector. Heat integration should be performed on the entire process (this study along with  $\text{LiPF}_6$  production process), this would give a better representation of the total costs.

## REFERENCES

- Abbott, M., 1979. *Cubic Equations of State: An Interpretive Review*. Troy, New York: Department of Chemical and Environmental Engineering, Rensselaer Polytechnic Institute.
- Abe, J., Nakanishi, K. & Touhara, H., 1978. Thermodynamic properties of aqueous solutions of hydrophilic compounds 1. pyridine and methylpyridines. *Journal of Chemical Thermodynamics*, Issue 10, pp. 483 - 494.
- Abrams, D. & Prausnitz, J., 1975. Statistical thermodynamics of liquid mixtures: A new expression for the excess Gibbs energy of partly or completely miscible systems. *AIChE Journal*, 21(1), pp. 116-128.
- Abu Al-Rub, F. & Datta, R., 2001. *Chemical Engineering Journal*, pp. 81 - 83.
- Allen, M., 2007. *The Physics Factbook*. [Online]  
Available at: <http://hypertextbook.com/facts/2007/AllenMa.shtml>  
[Accessed 20 July 2015].
- Andon, R., Cox, J. & Herington, E., 1957. Phase relationships in the pyridine series. Part 6. The thermodynamic properties of mixtures of pyridine, and of the three of its homologues, with water. *Transactions of the Faraday Society*, I(53), pp. 410-426.
- AspenTech, 2015. *Aspen Plus Help*. Bedford, Massachusetts: Aspen Technology Inc.
- Bastidas, P., Gil, I. & Rodríguez, G., 2010. *Comparison of the main ethanol dehydration technologies through process simulation*, Colombia: Elsevier.
- Beebe, A., Coulter, K., Lindsay, R. & Baker, E., 1942. Equilibria in Ethanol-Water System at Pressures less than atmospheric. *Journal of Industrial and Engineering Chemistry*, Issue 34, pp. 1501 - 1504.
- Bhownath, R., 2008. *The Use of n-Dodecane as a Solvent in the Extraction of Light Alcohols from Water*, Master of Science in Engineering (Chemical Engineering) Thesis: University of KwaZulu-Natal, South Africa.
- Cao, B. & Henson, M., 2002. Modeling of spiral wound pervaporation module with application to the separation of styrene/ethylbenzene mixtures. *Journal of Membrane Science*, I(197), pp. 117-146.
- Chaplin, M., 2017. *Water Structure and Science*. [Online]  
Available at: [http://www1.lsbu.ac.uk/water/water\\_properties.html](http://www1.lsbu.ac.uk/water/water_properties.html)  
[Accessed 26 May 2017].
- Chemical Engineering Online, 2008. *Chemical Engineering Cost Indices*. [Online]  
Available at:  
<http://www.engr.uconn.edu/~ewanders/Design/Chemical%20Engineering%20Cost%20Indices%20Jan%202008.pdf>  
[Accessed 15 September 2016].
- Chemical Engineering Online, 2016. *Economic Indicators*. [Online]  
Available at: [tekim.undip.ac.id/v1/wp-content/uploads/CEPCI\\_2008\\_2015.pdf](http://tekim.undip.ac.id/v1/wp-content/uploads/CEPCI_2008_2015.pdf)  
[Accessed 15 September 2016].

- ChemicalBook, 2016. *Cyclohexane*. [Online]  
Available at: [http://www.chemicalbook.com/ChemicalProductProperty\\_EN\\_CB4193601.htm](http://www.chemicalbook.com/ChemicalProductProperty_EN_CB4193601.htm)  
[Accessed 30 January 2016].
- Cheng, R., Cho, C. H., Kirby, S. & Lim, B., 2010. *Economic recovery of pyridine and 3-methylpyridine*, Pennsylvania: Scholarly Commons.
- Chirico, R. et al., 1996. Thermodynamic properties of pyridine I. Vapor pressures, high-temperature heat capacities, densities, critical properties, derived thermodynamic functions, vibrational assignment, and derivation of recommended values. *J.Chem*, 28(8), pp. 797-818.
- Crew, C. & Schafer, T., 1993. *Recovery of Pyridine Saves \$1.5 Million Per. s.l.:Pharmaceutical Engineering*.
- Daniel, C., 2008. Materials and Processing for Lithium-ion Batteries. *The Member Journal of the Minerals, Metals & Minerals Society*, 60(9), pp. 43-48.
- D'Avila, S. & Silva, R., 1970. Isothermal vapor-liquid equilibrium data by total pressure method. *Journal of Chemical Engineering Data*, 3(15), pp. 421-424.
- Dharmendra Kumar, M. & Rajendran, M., 1998. Effect of dissolved salts on the vapor-liquid equilibrium relationships of three miscible binary systems at the pressure of 101.3 kPa. *Journal of Chemical Engineering*, Issue 31.
- Dortmund Data Bank, 2015. *Vapour Pressure of Ethanol*. [Online]  
Available at: [www.ddbst.com/ddb.html](http://www.ddbst.com/ddb.html)  
[Accessed 28 August 2015].
- Ewert, M., 1936. Theory of concentrated solutions. XII Aq. soln. of organic compounds. *Bulletin des Societes Chimiques Belges*, Issue 45, p. 493.
- Findlay, T. & Copp, J., 1969. Thermodynamics of binary systems containing amines. Part 5 - Alcohols and Pyridine. *Transactions of the Faraday Society*, 65(558), pp. 1463-1469.
- Flemmer, R., Buckley, C. & Groves, G., 1987. The Arrangement of Spiral-Wound Ultrafiltration Modules. *Desalination*, 1(61), pp. 159-168.
- Fowler, R., 1949. A modified vapour liquid equilibrium still. *J.S.C.I*, Volume 68, pp. 131-132.
- Fowler, R., 1952. Azeotropism in binary solutions at reduced pressures: III pyridine + water solution. *Journal of Applied Chemistry*, Issue 2, p. 246.
- Gierycz, P., 1996. Vapor pressures and activity coefficients at infinite dilution of (water + pyridine, or 2-methylpyridine, or 3-ethylpyridine, or 2,4,6- trimethylpyridine) at T = 353.15 K. *Journal of Chemical Thermodynamics*, Issue 28, pp. 343 - 347.
- Gil, I., Garcia, L. & Rodriguez, G., 2014. Simulation of Ethanol Extractive Distillation with Mixed Glycols as Separating Agent. *Brazilian Journal of Chemical Engineering*, 31(1), pp. 259-270.
- Gil, I. et al., 2008. Separation of Ethanol and Water by Extractive Distillation with Salt and Solvent as Entrainer: Process Simulation. *Brazilian Journal of Chemical Engineering*, 25(1), pp. 207-215.
- Gutierrez H, J., 2013. *Extractive Distillation with Ionic Liquids as Solvents: A Conceptual Process Design*, Netherlands: Eindhoven University of Technology.



- Harris, D., 2011. *refractometer.pl*. [Online]  
Available at: <http://www.refractometer.pl/refraction-datasheet-ethanol>  
[Accessed 20 July 2015].
- Haynes, W., 2011. *CRC Handbook of Chemistry and Physics*. 91st ed. Boca Raton: CRC Press Inc.
- Heertjies, P., 1060. Determination of Vapour-Liquid Equilibrium of Binary Mixtures. *Chemical and Process Engineering*, Volume 41, pp. 385-386.
- Holderbaum, B. & Gmehling, J., 1991. PSRK: A Group Contribution Equation of State based on UNIFAC. *Fluid Phase Equilibria*, Volume 70, pp. 251-265.
- Ibl, N., Daendliker, G. & Truempler, G., 1954. Über das Verdampfungsgleichgewicht des systems wasser - pyridin. *Helvetica Chimica Acta*, I(37), pp. 1661-1672.
- Ibl, N., Dandliker, G. & Trumpler, G., 1956. The Vapour-Liquid Equilibrium of the System Water-Pyridine. *Chemical Engineering Science*, Issue 5, p. 193.
- Janaszewski, P., Oracz, P., Goral, M. & Warycha, S., 1982. Vapour-Liquid Equilibria. I. An Apparatus for Isothermal Total Vapour Pressure Measurements: Binary Mixtures of Ethanol and t-Butanol with n-Hexane, n-Heptane and n-Octane at 313.15 K. *Fluid Phase Equilibria*, Issue 9, pp. 295-310.
- Jobson, M., 2014. Energy Considerations in Distillation. In: *Distillation: Fundamentals and Principles*. Manchester: Elsevier, pp. 225-270.
- Joseph, M., Raal, J. & Ramjugernath, D., 2001. Phase Equilibrium Properties of Binary Systems with Diacetyl from a Computer Controlled Vapour-Liquid Equilibrium Still. *Fluid Phase Equilibria*, Volume 182, pp. 157-176.
- Kaewkannetra, P. et al., 2012. Experimental study and cost evaluation for ethanol separation from fermentation broth using pervaporation. *Desalination and Water Treatment*, I(41), pp. 88-94.
- Khattab, I. S., Bandarkar, F., Fahkree, M. A. A. & Jouyban, A., 2012. Density, viscosity, and surface tension of water+ethanol mixtures from 293 to 323K. *Korean Journal of Chemical Engineering*, 29(6), pp. 812-817.
- KLM Technology Group, 2011. *Distillation Column Selection and Sizing (Engineering Design Guidelines)*. [Online]  
Available at:  
<http://kolmetz.com/pdf/EDG/ENGINEERING%20DESIGN%20GUIDELINES%20-%20distillation%20column%20-%20Rev%2003%20web.pdf>  
[Accessed 10 July 2017].
- Kneisl, P., Zondlo, J. & Wallace, B., 1989. The Effect of Fluid Properties on Ebulliometer Operation. *Fluid Phase Equilibria*, Volume 46, pp. 85-94.
- Kontogeorgis, G. & Folas, G., 2009. *Thermodynamic Models for Industrial Applications: From Classical and Advanced Mixing Rules to Association Theories*. s.l.:Wiley.
- Kujawski, W., 2000. Application of Pervaporation and Vapor Permeation in Environmental Protection. *Polish Journal of Environmental Studies*, 9(1), pp. 13-26.
- Kumar, M., Dixit, S. K., Singh, S. K. & Agarwal, A., 2010. *Eco-friendly process for recovery of pyridine and/or its derivatives*. United States, Patent No. US 20100041894 A1.

- Kumar, M., Dixit, S., Singh, S. & Agarwal, A., 2011. *Eco-friendly Process for Recovery of Pyridine*. United States, Patent No. US8057643 B2.
- Kyte, C. T., Jeffery, G. H. & Vogel, A. I., 1960. Physical Properties and Chemical Constitution. Part XXVIII.\* Pyridine Derivatives. *Journal of the Chemical Society*, pp. 4454-4472.
- Lekgoathi, M., Crouse, P. & Kock, L., 2015. *High purity LiPF<sub>6</sub>: its physical properties and the synthesis of PF<sub>5</sub> gas as a precursor for LiPF<sub>6</sub> production*, Pretoria: University of Pretoria.
- Lie, Z., Li, C. & Chen, B., 2003. Extractive Distillation: A Review. *Separation and Purification Reviews*, 32(2), pp. 121-213.
- Lladosa, E., Monton, J. & Burguet, M., 2011. Chemical Engineering and Processing. *Separation of di-n-propyl ether and n-propyl alcohol by extractive distillation and pressure-swing distillation: Computer simulation and economic optimisation*, I(50), pp. 1266-1274.
- Luyben, W., 2013. *Distillation Design and Control Using Aspen Simulation*. 2nd ed. Canada: John Wiley & Sons, Inc..
- Matteo, G., 2015. *Membrane modules and configurations*. Zurich: Separation Process Laboratory.
- MEGlobal, 2017. *Physical Properties of Ethylene Glycol*. [Online] Available at: <http://www.meglobal.biz/monoethylene-glycol/physical-properties> [Accessed 26 May 2017].
- Munoz, R., Monton, J., Burguet, M. & de la Torre, J., 2006. Separation and Purification Technology. *Separation of isobutyl alcohol and isobutyl acetate by extractive distillation and pressure-swing distillation: Simulation and Optimisation*, I(50), pp. 175-183.
- Naidoo, M., 2014. *Thermodynamic properties of mixtures containing ethanol, water and pyridine*, University of KwaZulu-Natal, South Africa: Chemical Engineering Vacation Work Project .
- Narasigadu, C., 2006. *Phase Equilibrium Investigation of the Water and Acetonitrile Solvent with Heavy Hydrocarbons*, Master of Science in Engineering (Chemical Engineering) Thesis: University of KwaZulu-Natal, South Africa.
- Ndlovu, M., 2005. *Development of a Dynamic Still for Measuring Low Pressure Vapour-Liquid-Liquid Equilibria (Systems of Partial Liquid Miscibility)*, Master of Science in Engineering (Chemical Engineering) Thesis: University of KwaZulu-Natal, South Africa.
- NECSA, 2017. *Personal Communication*. Pretoria: NECSA.
- Nelson, W., 2012. *Separation of Trichlorosilane: Measurement, Modelling and Simulation*, Doctor of Philosophy in Engineering (Chemical Engineering) Thesis: University of KwaZulu-Natal, South Africa.
- Ocie, O., 2012. *Energy Efficiency in Oil Processing Industry*. Europe: European Commission.
- Orbey, H. & Sandler, S., 1998. *Modeling vapor-liquid equilibria: cubic equations of state and their mixing rules*, s.l.: Cambridge University Press.
- Perry, R. & Green, D., 1999. *Perry's Chemical Engineers' Handbook*. 7th ed. New York: McGraw-Hill.
- Pickering, S., 1893. A study of the properties of some strong solutions. *Journal of Chemical Society*, Issue 63, pp. 998-1027.

- Pokki, J., 2004. *Development of Vapour Liquid Equilibrium*, Doctor of Science in Technology Thesis: Helsinki University of Technology, Finland, Espoo.
- Prausnitz, J. M. & Targovnik, J., 1958. Salt effects in aqueous vapor-liquid equilibria. *Chemical Engineering Data Series*, Issue 3, p. 124.
- PubChem, 2004. *Pyridine*. [Online]  
Available at: <http://pubchem.ncbi.nlm.nih.gov/compound/pyridine#section=Top>  
[Accessed 26 May 2017].
- PubChem, 2015. *Cyclohexane*. [Online]  
Available at: <http://pubchem.ncbi.nlm.nih.gov/compound/cyclohexane>  
[Accessed 22 July 2015].
- PubChem, 2015. *Pyridine*. [Online]  
Available at: <http://pubchem.ncbi.nlm.nih.gov/compound/pyridine#section=Information-Sources>  
[Accessed 22 July 2015].
- Raal, J. & Muhlbaüer, A., 1998. *Phase Equilibria: Measurement and Computation*. Washington, D.C: Taylor and Francis.
- Rarey, J., 2017. *Personal Communication*. University of Oldenburg: Germany.
- Renewable Energy, 2017. *Renewable Energy South Africa*. [Online]  
Available at: <https://renewableenergy.co.za>  
[Accessed 03 01 2017].
- Renon, H. & Prausnitz, J., 1968. Local compositions in thermodynamic excess functions for liquid mixtures. *AIChE Journal*, Issue 14, pp. 135-144.
- Sadus, R., 2012. *High Pressure Phase Behaviour of Multicomponent Fluid Mixtures*, s.l.: Elsevier Science.
- Safobein, S., 2011. *Plant for Separation of Styrene, Ethyl Benzene, Ammonia and Hydrogen Sulfide*, New York: s.n.
- Sandler, S., 1994. *Models for thermodynamic and phase equilibria calculations*, s.l.: Dekker.
- Satkiewicz, F., 1964. The System Ethanol-Cyclohexane from 50 to 65°. *J.Am.Chem.Soc.*, Volume 86, pp. 130-133.
- Scatchard, G., Wood, S. & Mochel, J., 1939. III. Benzene - Cyclohexane Mixtures. *Journal of Physical Chemistry*, Volume 43, pp. 119-130.
- Schiffmann, P., 2014. *Three step modelling approach for the simulation of industrial scale pervaporation modules*, Freiberg: Technische Universität Bergakademie Freiberg.
- Seader, J., Henley, E. & Roper, D., 2011. *Separation Process Principles: Chemical and Biochemical Operations*. 3rd ed. United States of America: John Wiley & Sons.
- Taylor, B. & Kuyatt, C., 1994. *Guidelines for evaluating and expressing the uncertainty of NIST measurement results: NIST Technical Note 1297*, Gaithersburg: National Institute of Standards and Technology.
- The Money Converter, 2016. *The Money Converter*. [Online]  
Available at: <https://themoneyconverter.com/EUR/ZAR.aspx>  
[Accessed 10 December 2016].

- TradeKey, 2016. *AJL Chemical Trading*. [Online]  
Available at: [http://www.tradekey.com/product\\_view/Mono-Ethylene-Glycol-meg--7696007.html](http://www.tradekey.com/product_view/Mono-Ethylene-Glycol-meg--7696007.html)  
[Accessed 20 January 2017].
- Twu, C., Sim, W. & Tassone, V., 2002. Getting a handle on advanced cubic equations of state.. *Chemical Engineering Progress*, Issue 98, pp. 58-65.
- USGS, 2016. *Surface Tension and Water*. [Online]  
Available at: <http://water.usgs.gov>  
[Accessed 5 January 2018].
- Van Hoof, V. et al., 2004. Separation and Purification Technology. *Economic comparison between azeotropic distillation and different hybrid systems combining distillation with pervaporation for the dehydration of isopropanol*, I(37), pp. 33-49.
- Vesovic, V., 2011. *Thermopedia*. [Online]  
Available at: <http://www.thermopedia.com/content/739/>  
[Accessed 26 May 2017].
- Vriens, G. N. & Medcalf, E. C., 1953. Correlation of ternary liquid-liquid equilibria an explanation of solutropy. *Journal of Industrial and Engineering Chemistry*, Issue 45, p. 1098.
- Warycha, S., 1977. Vapour-liquid equilibria and excess gibbs free energy in binary systems of pyridine bases with aliphatic alcohols at 313.15 k (40.00 c): II alcohols with pyridine and 2-picoline. *Phys.Chem.(Leipzig)*, 258(5), pp. 873-878.
- Wijmans, J. & Baker, R., 1993. A simple predictive treatment of the permeation process in pervaporation. *Journal of Membrane Science*, I(79), pp. 101-113.
- Willmann, P., Naejus, R., Coudert, R. & D, L., 1999. *Solvate of Lithium Hexafluorophosphate and Pyridine, It's Preparation and Preparation Process for Lithium Hexafluorophosphate Using Said Solvate*. United States of America, Patent No. 5,993,767.
- Wilson, G., 1964. Vapor-liquid equilibria, correlation by means of a modified Redlick-Kwong equation of state. *Advances in Cryogenic Engineering*.
- Wolf, M., 2017. *Personal Communication*. Netherlands: Pervatech.
- Woycicka, M. K. & Kurtyka, Z., 1965. *Bulletin of the Polish Academy of Sciences*, Issue 13, p. 469.
- Wu, T. C. & Chien, I. L., 2009. Design and Control of Heterogeneous Azeotropic Column System for the Separation of Pyridine and Water. 48(23), pp. 10564-10576.
- Xu, W., 2001. *Design and development of a pervaporation membrane sepration module*, Toronto: Univeraity of Toronto.
- Yerazunis, S., Plowright, J. & Smola, F., 1964. Vapour-Liquid Equilibrium Determination by a New Apparatus. *Determination by a New Apparatus*, Volume 10, pp. 660-665.
- Zawidzki, J., 1900. Vapour pressures of binary liquid mixtures. *Journal of Physical Chemistry*, Issue 35, p. 129.

## APPENDIX A: MEMBRANE DESIGN

The performance of the pervaporation system was calculated using equation (A.1). This required the normalized permeation fluxes ( $J_i$ ) of the membrane and the operating conditions of the pervaporation process, such as, the feed composition ( $c_i$ ), the feed temperature and the permeate pressure ( $p''$ ) to be known. The normalized permeation flux of ethanol and water is read from Figures A.1 and A.2 or calculated from equations (A.10) and (A.11) respectively, the saturated vapour pressure is calculated from the Antoine equation as shown in Table A.1 and the activity coefficients are calculated using the Van Laar equations shown in Table A.2. Only the partial permeation flux  $Q_i$  and the partial vapour pressure on the permeate side  $p_i''$  are then unknown. The relationship between  $Q_i$  and  $p_i''$  is shown in equation (A.2). The result of combining equations (A.1) and (A.2) and solving for the ratio of the partial permeate pressure to the total permeate pressure is shown in equation (A.3). It is then known that the sum of all partial vapour pressures on the permeate side is equal to the total permeate pressure as shown in equation (A.4). Therefore, we obtain equation (A.5) where the total permeation flux can be calculated. Thereafter, the partial permeate pressure and partial permeation fluxes of all components can be calculated and the separation can be evaluated for one fixed feed composition using equations (A.6) and (A.7). However, it is important to note that the composition of the feed changes if a substantial fraction of the liquid was permeated. Hence, the total membrane area was divided into N differential elements and the new parameters calculated for each sector using equations (A.8) and (A.9) (Wijmans & Baker, 1993).

$$Q_i = J_i (c_i' \gamma_i' p_i^o - p_i'') \quad (\text{A.1})$$

$$Q_i = Q_{tot} \frac{p_i''}{p''} \quad (\text{A.2})$$

$$\frac{p_i''}{p''} = \frac{J_i c_i' \gamma_i' p_i^o}{Q_{tot} + J_i p''} \quad (\text{A.3})$$

$$\sum \frac{p_i''}{p''} = 1 \quad (\text{A.4})$$

$$\sum \frac{J_i c_i' \gamma_i' p_i^o}{Q_{tot} + J_i p''} = 1 \quad (\text{A.5})$$

$$F_P = \sum (Q_{tot,k} dA_k) \quad (\text{A.6})$$

$$c_i'' = \frac{\sum (Q_{i,k} dA_k)}{F_P} \quad (\text{A.7})$$

$$F_{F,k+1} = F_{F,k} - Q_{tot,k} dA_k \quad (A.8)$$

$$F_{F,k+1} c'_{i,k+1} = F_{F,k} c'_{i,k} - Q_{i,k} dA_k \quad (A.9)$$

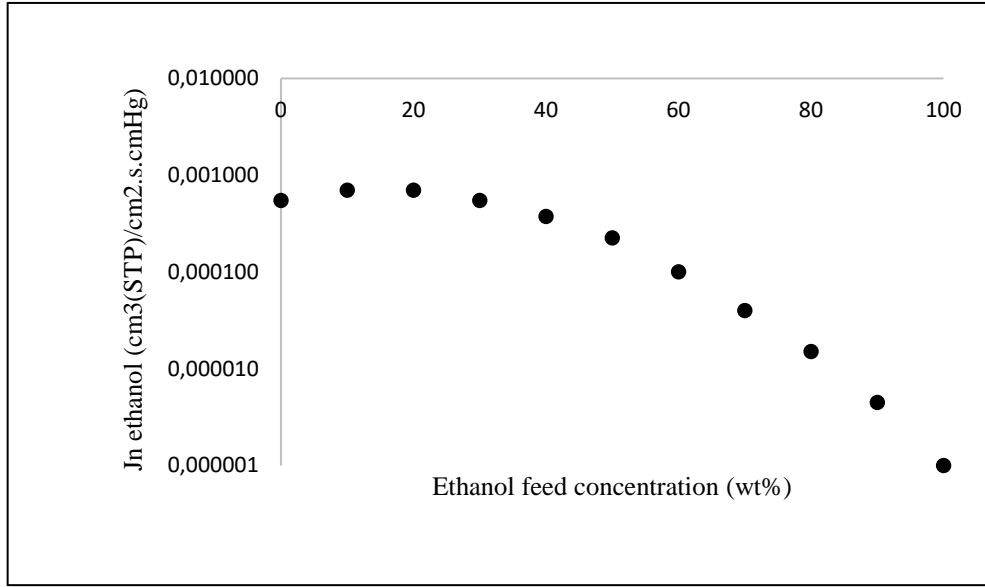


Figure A.1: Permeation flux of ethanol as a function of ethanol feed concentration (Wijmans & Baker, 1993)

$$\log(J_{ethanol}) = -3.26 + 1.19w_{ethanol} - 3.99w_{ethanol}^2 \quad (A.10)$$

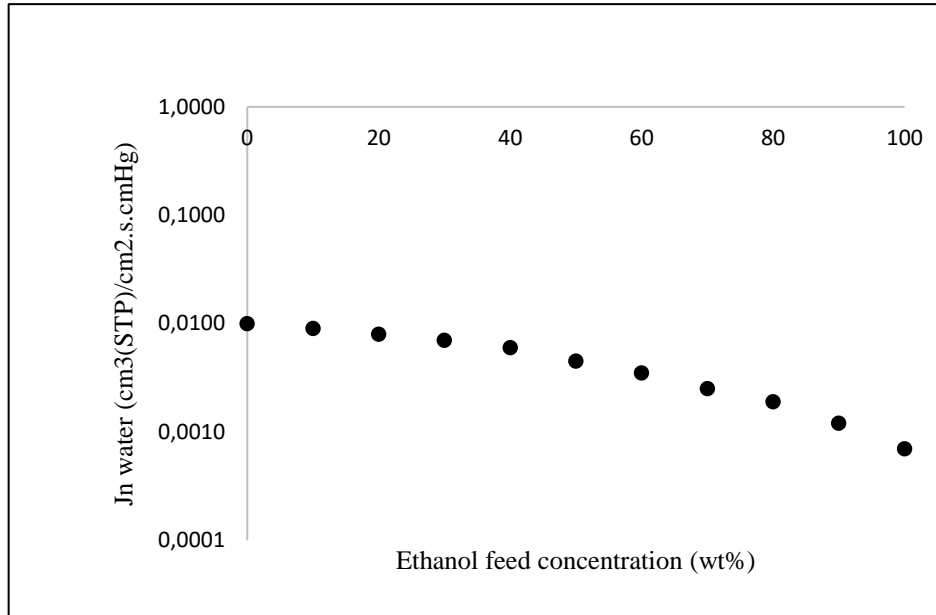


Figure A.2: Permeation flux of water as a function of ethanol feed concentration (Wijmans & Baker, 1993)

$$\log(J_{\text{water}}) = -2.03 - 0.071w_{\text{ethanol}} - 1.03w_{\text{ethanol}}^2 \quad (\text{A.11})$$

Table A.1: Coefficients for the Antoine equation:

$\log(p^\circ) = A - B/(t + C)$ ,  $p^\circ$  in mmHg and  $t$  in  $^\circ\text{C}$

	A	B	C
Water	8.07131	1730.63	233.426
Ethanol	8.1122	1592.86	226.184

Table A.2: Coefficients for the Van Laar equation:

$$\ln(\gamma_1) = A_{12} [A_{21}C_2/(A_{12}C_1 + A_{21}C_2)]^2$$

$$\ln(\gamma_2) = A_{21} [A_{12}C_1/(A_{12}C_1 + A_{21}C_2)]^2$$

	$A_{12}$	$A_{21}$
Ethanol/Water at 60 $^\circ\text{C}$	1.6276	0.9232

## APPENDIX B: DETAILED COSTING PROCEDURE

### B.1: Capital Investment Cost of Membrane and Module

The capital investment cost of the membrane and modules were calculated manually on Microsoft Excel. This involved multiplying the membrane/module area by the literature costs shown in Table B.1. The total membrane/module area required was calculated using the methodology by Wijmans & Baker (1993) shown in appendix A. The capital investment cost of all other units were evaluated using the Aspen Plus® computer software.

Table B.1: Literature cost of membrane and module

Polyvinyl alcohol Membrane	200 US Dollar/m <sup>2</sup> (Kaewkannetra, et al., 2012)
Spiral Wound Module	100 US Dollar/m <sup>2</sup> (Safobeen, 2011)

### B.2: Operating Costs

The operating costs were determined by means of the utility prices displayed in Table B.2.

Table B.2: Utility costs

Utility Description	Unit	Price
Electricity (Jobson, 2014)	Pound/kW.hr	0.08
Cooling water (Lladosa, et al., 2011)	Euro/m <sup>3</sup>	0.04
Low pressure steam (Safobeen, 2011)	USD/1000 kg steam	7
Medium pressure steam (Ocic, 2012)	USD/1000 kg steam	9.66
High pressure steam (Ocic, 2012)	USD/1000 kg steam	10.83
Liquid nitrogen (Safobeen, 2011)	USD/litre	0.1
Ethylene glycol (TradeKey, 2016)	USD/1000 kg steam	650
Membrane replacement (Van Hoof, et al., 2004)	Euro/m <sup>2</sup>	550

As can be seen from Table B.2, the utility prices obtained from literature are in different currencies and from different years. In order to present the final costs in a consistent form, the currencies were converted into the South African rand via Table B.3 below. The prices were then updated with the CEPCI (chemical engineering plant cost index) as shown in Table B.4 and equation B.1.



Table B.3: Conversion of currencies to rands

<b>Currency</b>	
South African Rand	1
Euro (The Money Converter, 2016)	14.45
US Dollar (The Money Converter, 2016)	12.93
British Pound (The Money Converter, 2016)	16.45

Table B.4: Chemical Engineering Plant Cost Index

<b>Year</b>	<b>CEPCI (Chemical Engineering Plant Cost Index)</b>
2004 (Chemical Engineering Online, 2008)	444.2
2011 (Chemical Engineering Online, 2016)	585.7
2012 (Chemical Engineering Online, 2016)	584.6
2014 (Chemical Engineering Online, 2016)	576.1
2016 (Chemical Engineering Online, 2016)	536.5

$$R(2016) = R(\text{year}) \times \frac{CEPCI(2016)}{CEPCI(\text{year})} \quad (\text{B.1})$$

The process utilities such as steam, cooling water and refrigerant were determined via equations B.2 and B.3 below.

$$\text{For Steam/Refrigerant} \quad : Q = m\Delta h_{\text{vap}} \quad (\text{B.2})$$

$$\text{For Cooling water} \quad : Q = mC_p\Delta T \quad (\text{B.3})$$

$Q$  : column duty (kW)

$m$  : mass flow rate (kg/hr)

$\Delta h_{\text{vap}}$ : enthalpy of vaporisation (kJ/kg)

$C_p$  : Heat capacity (kJ/kg.K)

$\Delta T$  : temperature (K)

The duties are acquired from Aspen Plus®, the change in enthalpy of vaporisation and heat capacities are obtained from the literature sources shown in Table B.5, the temperature change is assumed to be 30 K. With this information, the mass flow rate of each utility can be calculated and multiplied by the literature cost.

Table B.5: Enthalpy of vaporisation and heat capacities

Component	$\Delta h_{\text{vap}}$ (kJ/kg)	$C_p$ (kJ/kg.K)
Low Pressure Steam	2167.00 (Jobson, 2014)	-
Medium Pressure Steam	2158.00 (Jobson, 2014)	-
Cooling Water	-	4.18 (Jobson, 2014)
Refrigerant (Nitrogen)	5592.80 (Safobeen, 2011)	-

The duties of the pumps (feed and vacuum) are acquired from Aspen Plus®. The cost is obtained by simply multiplying this value by the electricity cost from literature. The membrane replacement is assumed to take place every five years. Hence this cost is divided by 5 and added to the yearly process utility costs.

### B.3: Inter-stage Heat Exchangers

For the inter-stage heat exchangers, the first step was to calculate the temperature drop between each module. This was determined via equation B.4 (Schiffmann, 2014) and the values obtained from Aspen Plus® shown in Table B.6.

$$\Delta T = \frac{F_p}{F_f} \times \frac{\Delta h_{\text{vap},\text{wat}}}{x_{f,\text{eth}} C_{p,f,\text{eth}} + x_{f,\text{wat}} C_{p,f,\text{wat}}} \quad (\text{B.4})$$

$F_p$ : Permeate flow rate

$F_f$ : Feed flow rate

$x_f$ : mole fraction

Table B.6: Enthalpy of vaporisation and heat capacities from Aspen Plus®

Component	$\Delta h_{\text{vap}}$ (kJ/kmol)	$C_p$ (kJ/kmol.K)
Ethanol		136.58
Water	42515.7	77.11

This temperature change along with the retentate stream conditions from each module is then used to calculate the heat duty. The process utility cost is there-after evaluated.

## APPENDIX C: GAS CHROMATOGRAPH CALIBRATION CHARTS

### C.1 Test System: Ethanol (1) + Cyclohexane (4) System

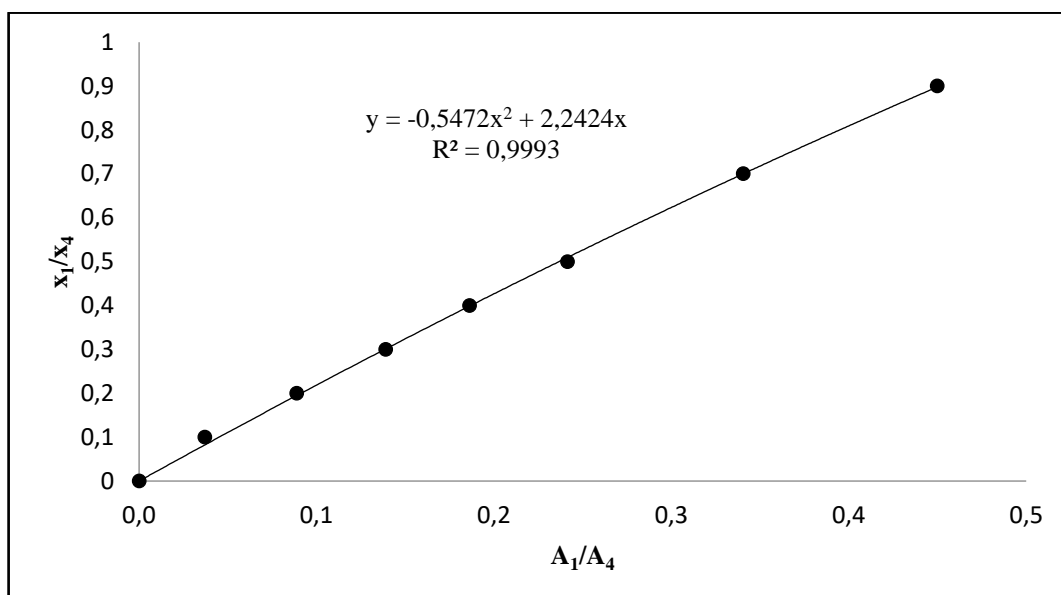


Figure C.1: GC calibration for the ethanol (1) + cyclohexane (4) system in the more dilute regions of ethanol. Representation of the relationship between the number of moles vs the peak area.

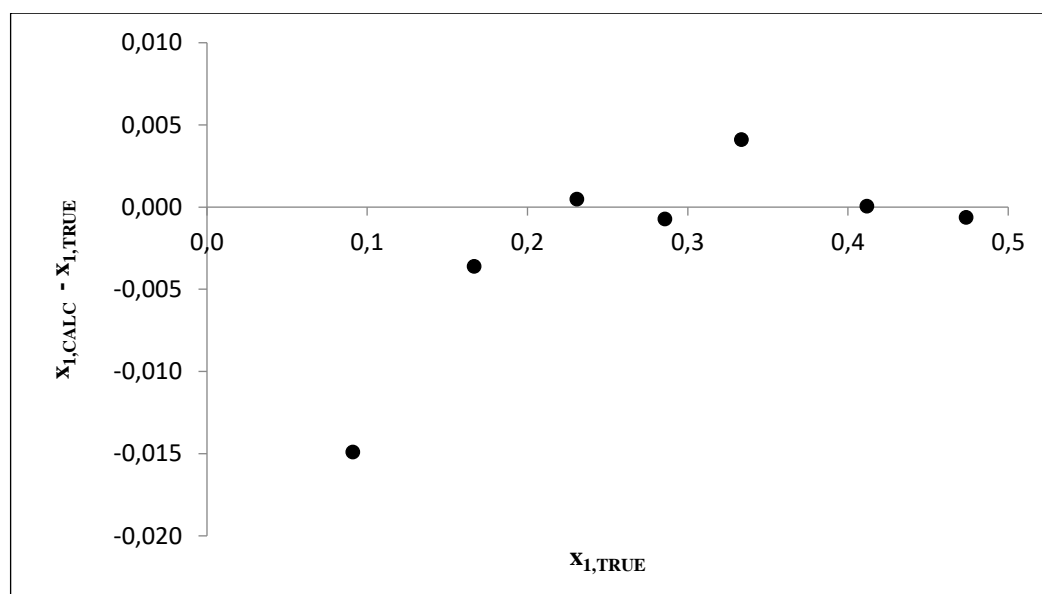


Figure C.2: GC calibration for ethanol (1) + cyclohexane (4) system in the more dilute regions of ethanol. Deviations in composition using a second order polynomial; where  $x_{1,TRUE}$  is the actual composition from the GC, and  $x_{1,CALC}$  is the composition calculated from the calibration polynomial.

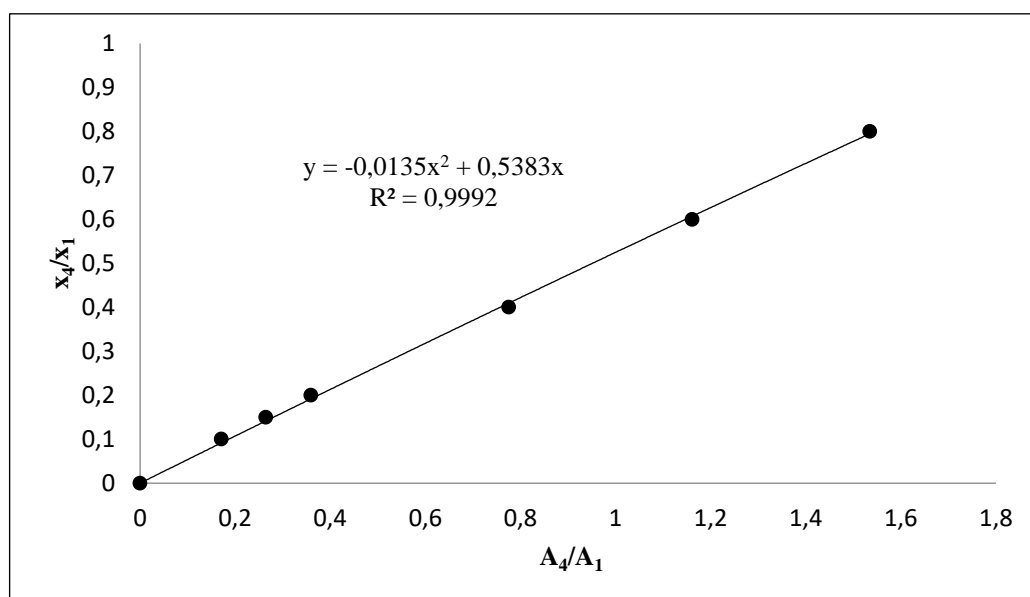


Figure C.3: GC calibration for the ethanol (1) + cyclohexane (4) system in the more concentrated regions of ethanol. Representation of the relationship between the number of moles vs the peak area.

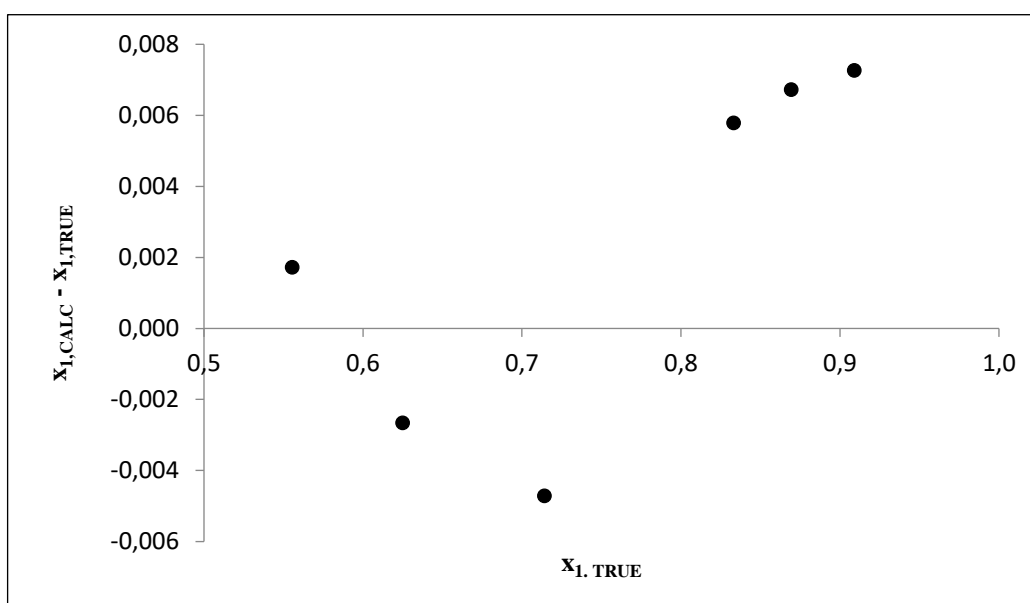


Figure C.4: GC calibration for the ethanol (1) + cyclohexane (4) system in the more concentrated regions of ethanol. Deviations in composition using a second order polynomial; where  $x_{1,TRUE}$  is the actual composition from the GC, and  $x_{1,CALC}$  is the composition calculated from the calibration polynomial.

## C.2 Ethanol (1) + Pyridine (3) System

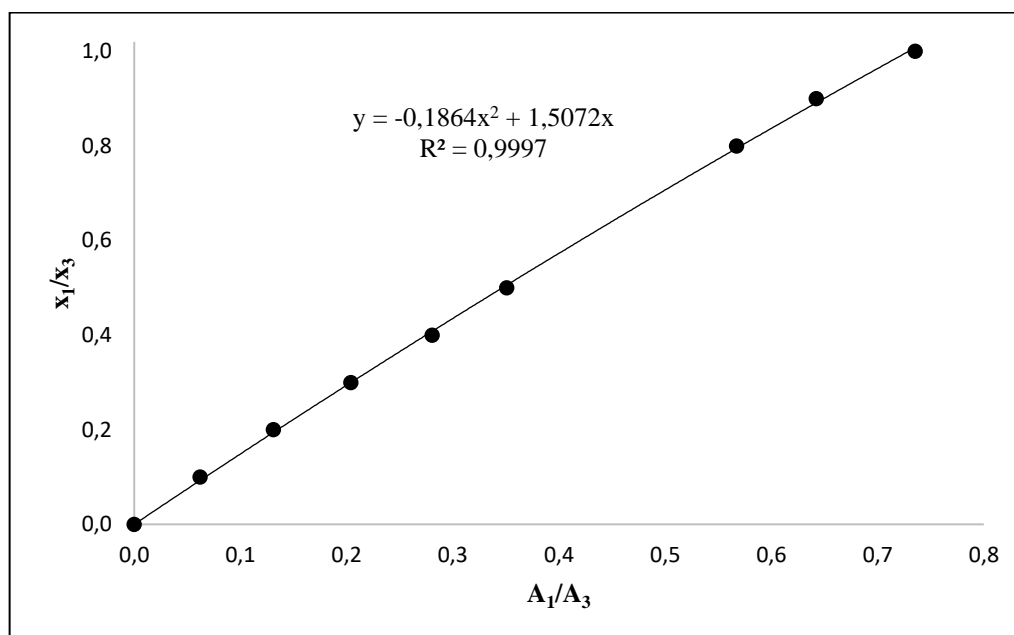


Figure C.5: GC calibration for the ethanol (1) + pyridine (3) system in the more dilute regions of ethanol. Representation of the relationship between the number of moles vs the peak area.

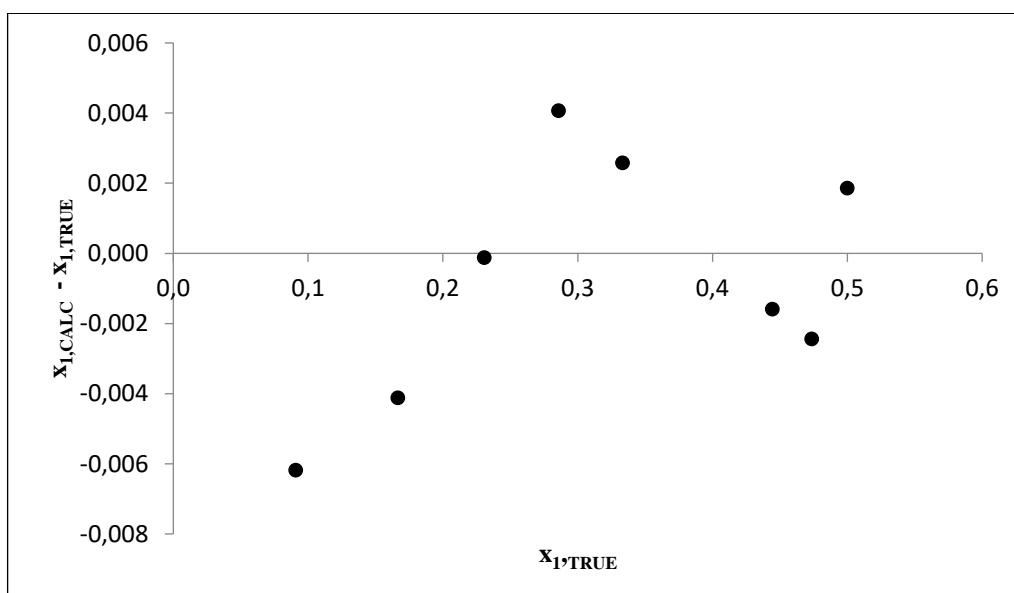


Figure C.6: GC calibration for the ethanol (1) + pyridine (3) system in the more dilute regions of ethanol. Deviations in composition using a second order polynomial; where  $x_{1,TRUE}$  is the actual composition from the GC, and  $x_{1,CALC}$  is the composition calculated from the calibration polynomial.

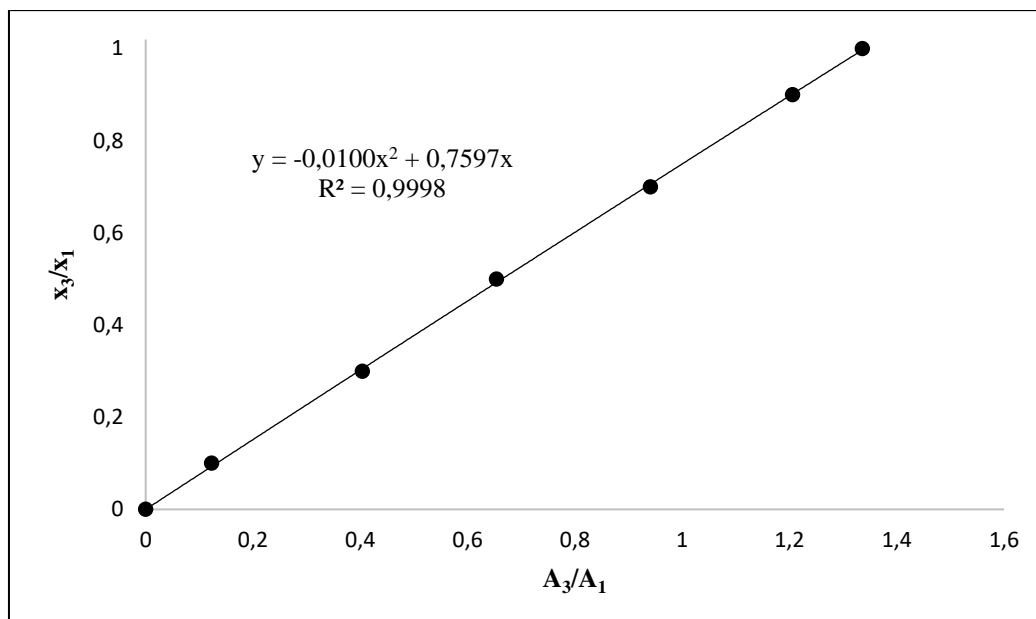


Figure C.7: GC calibration for the ethanol (1) + pyridine (3) system in the more concentrated regions of ethanol. Representation of the relationship between the number of moles vs the peak area.

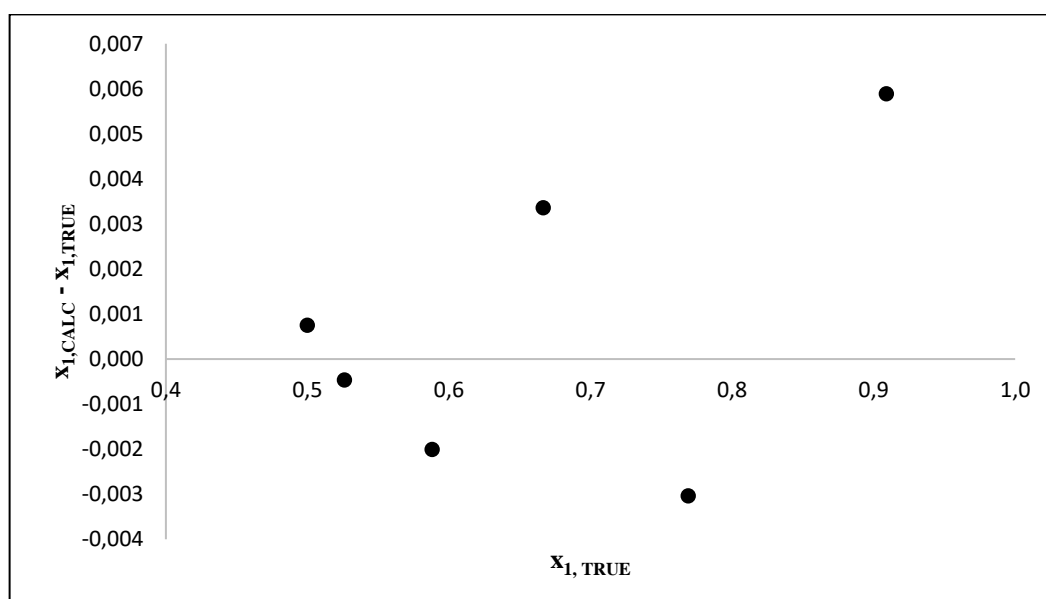


Figure C.8: GC calibration for the ethanol (1) + pyridine (3) system in the more concentrated regions of ethanol. Deviations in composition using a second order polynomial; where  $x_{1,TRUE}$  is the actual composition from the GC, and  $x_{1,CALC}$  is the composition calculated from the calibration polynomial.

### C.3 Water (2) + Pyridine (3) System

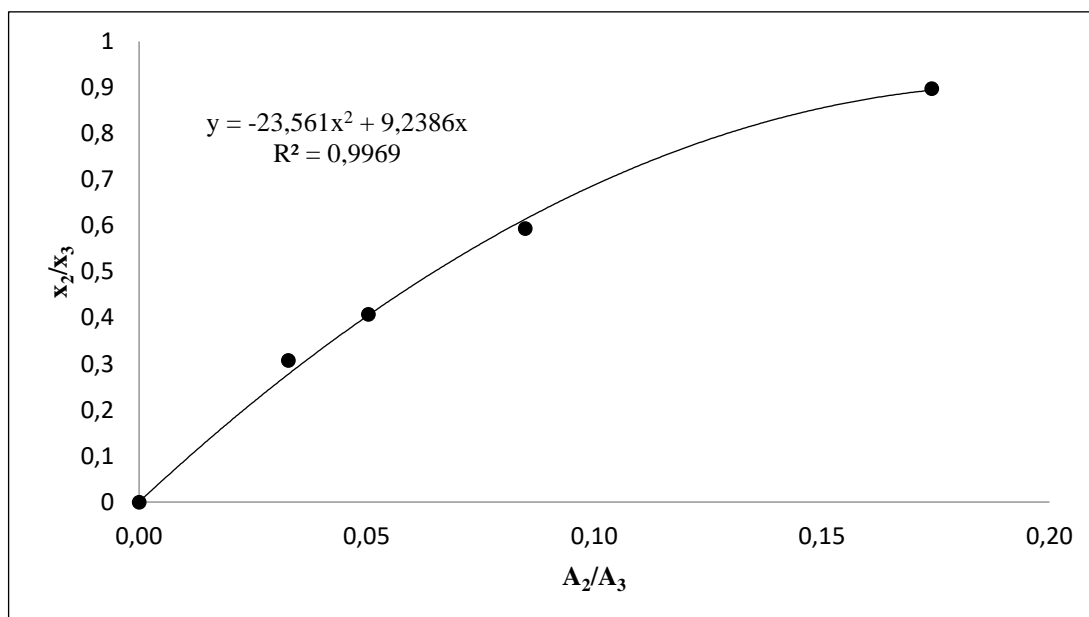


Figure C.9: GC calibration for the water (2) + pyridine (3) system in the more dilute regions of water. Representation of the relationship between the number of moles vs the peak area.

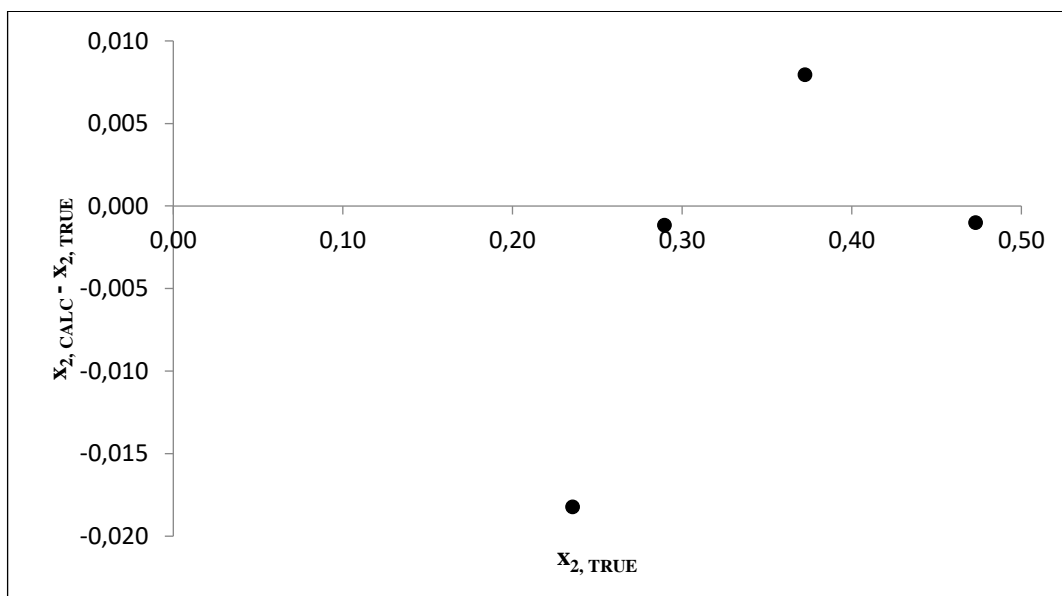


Figure C.10: GC calibration for the water (2) + pyridine (3) system in the more dilute regions of water. Deviations in composition using a second order polynomial; where  $x_{2,TRUE}$  is the actual composition from the GC, and  $x_{2,CALC}$  is the composition calculated from the calibration polynomial.

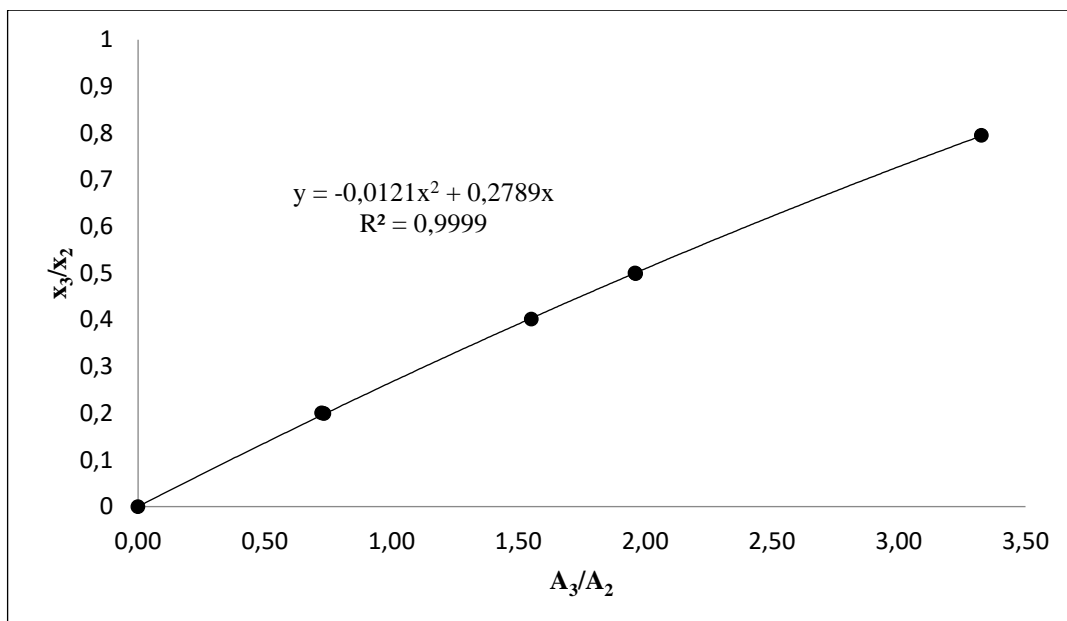


Figure C.11: GC calibration for the water (2) + pyridine (3) system in the more concentrated regions of water. Representation of the relationship between the number of moles vs the peak area.

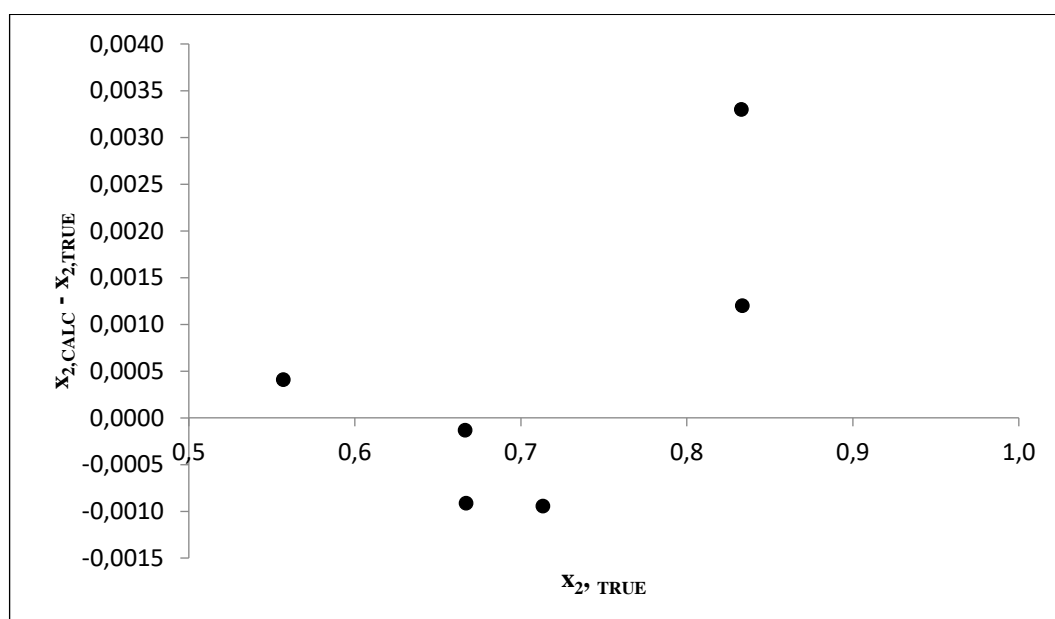


Figure C.12: GC calibration for the water (2) + pyridine (3) system in the more concentrated regions of water. Deviations in composition using a second order polynomial; where  $x_{2, \text{TRUE}}$  is the actual composition from the GC, and  $x_{2, \text{CALC}}$  is the composition calculated from the calibration polynomial.



## APPENDIX D: EXPERIMENTAL UNCERTAINTY CALCULATION

The uncertainty is defined as the interval within which the true value of the measured variable has a high probability of residing. The uncertainty does not account for errors that may occur during experiments but rather for errors resulting from the use of a calibration polynomial or repeatability of measurements, etc. The calculation of the experimental uncertainty follows the method by NIST (National Institute of Standards and Technology). The combined standard uncertainty of a value  $\theta$  is determined from equation D.1:

$$u_c(\theta) = \pm \sqrt{\sum_i^n u_i(\theta)^2} \quad (D.1)$$

where  $u_i(\theta)$  is the standard uncertainty for a value  $\theta$  and is calculated by either Type A or Type B below.

$$\text{Type A: } u_i(\theta) = \frac{\sigma}{\sqrt{n}} \quad (D.2)$$

$$u_i(\theta) = \sqrt{\frac{1}{n(n-1)} \sum_{i=1}^n (\theta_i - \bar{\theta})^2} \quad (D.3)$$

This uncertainty is calculated by statistical methods and has a larger tendency to lie around the mean.  $\sigma$  is the standard deviation of the data and  $n$  is the number of repeated data points.

$$\text{Type B: } u_i(\theta) = \frac{b}{\sqrt{3}} \quad (D.4)$$

The symbol  $b$  is half the width of the interval. This method is used when the variable could lie anywhere within the distribution and is known as a rectangular distribution. The uncertainty in temperature, pressure and composition calibrations were calculated from Type A where  $b$  is set to the maximum deviation observed from the calibration polynomial.

$u_i(\theta)$  is calculated by combining the standard uncertainties of all the measured quantities  $u(\bar{\alpha}_i)$  and evaluating the root sum squares (RSS):

$$u_c(\theta) = \sqrt{\left[ \left( \frac{\partial \theta}{\partial \bar{\alpha}_1} \right)_{\bar{\alpha}_i \neq 1} u(\bar{\alpha}_1) \right]^2 + \left[ \left( \frac{\partial \theta}{\partial \bar{\alpha}_2} \right)_{\bar{\alpha}_i \neq 2} u(\bar{\alpha}_2) \right]^2 + \dots + \left[ \left( \frac{\partial \theta}{\partial \bar{\alpha}_n} \right)_{\bar{\alpha}_i \neq n} u(\bar{\alpha}_n) \right]^2} \quad (D.5)$$

The combined expanded uncertainty is then calculated by:

$$U_c(\theta) = k u_c(\theta) \quad (D.6)$$

The symbol  $k$  is the coverage factor and is usually set to 2. The coverage factor creates an interval within which it is confidently believed that  $\theta$  will lie, the interval being  $\theta_{measured} - U_c(\theta) \leq \theta_{final} \leq \theta_{measured} + U_c(\theta)$ . Typically, a coverage factor of 2 is used to define an interval having

a level of confidence of approximately 95 percent and a coverage factor of 3 is used to define an interval having a level of confidence greater than 99 percent.

### D.1 Temperature and Pressure Uncertainty

The combined standard uncertainty for temperature is:

$$u_C(T) = \pm \sqrt{u_{cali}(T)^2 + u_{rep}(T)^2 + u_{std}(T)^2 + u_{fluct}(T)^2} \quad (D.7)$$

The symbols  $u_{cali}(T)$  is the uncertainty induced by the temperature calibration (Type B),  $u_{rep}(T)$  is the uncertainty due to measurement repeatability (Type A),  $u_{std}(T)$  is the standard uncertainty of the temperature probe (Type B) and  $u_{fluct}(T)$  is the fluctuation observed from the temperature unit display (Type B).

The combined standard uncertainty for pressure is:

$$u_C(P) = \pm \sqrt{u_{cali}(P)^2 + u_{rep}(P)^2 + u_{std}(P)^2 + u_{fluct}(P)^2} \quad (D.8)$$

The symbols  $u_{cali}(P)$  is the uncertainty induced by the pressure calibration (Type B),  $u_{rep}(P)$  is the uncertainty due to measurement repeatability (Type A),  $u_{std}(P)$  is the standard uncertainty of the pressure transducer (Type B) and  $u_{fluct}(P)$  is the fluctuation observed from the pressure unit display (Type B).

The combined expanded uncertainty of both temperature and pressure is then calculated by multiplying the combined standard uncertainty by a coverage factor of 2.

### D.2 Phase Composition Uncertainty

The combined standard uncertainty for composition is:

$$u_C(x_i) = \pm \sqrt{u_{cali}(x_i)^2 + u_{rep}(x_i)^2} \quad (D.9)$$

$$u_{cali}(x_i) = \pm \sqrt{u_{corr}(x_i)^2 + u_{bal}(x_i)^2} \quad (D.10)$$

The symbols  $u_{corr}(x_i)$  is the uncertainty induced by the mole composition calibration polynomial (Type B),  $u_{rep}(x_i)$  is the standard deviation from averaging the repeated samples withdrawn at equilibrium (Type A) and  $u_{bal}(x_i)$  is the uncertainty in the measured mass.

Since  $x_i$  is dependent on the measurement of the masses  $m_i$  and  $m_j$ :

$$u_{bal}(x_i) = \sqrt{\left[\left(\frac{\partial x_i}{\partial m_i}\right)_{m_j} u(m_i)\right]^2 + \left[\left(\frac{\partial x_i}{\partial m_j}\right)_{m_i} u(m_j)\right]^2} \quad (\text{D.11})$$

using the definition  $x_i = n_i/(n_i + n_j)$  and  $n_i = m_i/MM_i$  where  $MM$  is the molecular mass, equation B.11 can be simplified to:

$$u_{bal}(x_i) = x_i x_j \sqrt{\left(\frac{u(m_i)}{m_i}\right)^2 + \left(\frac{u(m_j)}{m_j}\right)^2} \quad (\text{D.12})$$

however  $u_{bal}(x_i)$  is neglected since  $u_{corr}(x_i) \gg u_{bal}(x_i)$ .

## APPENDIX E: SENSITIVITY ANALYSIS PLOTS

### E.1 Process 1FE (1 flash, extractive distillation):

#### Solvent Recovery Column (C-03)

Table E.1: Variation of feed stage location with reflux ratio

NoS	FS	RR
30	11	2.72
<b>30</b>	<b>12</b>	<b>2.63</b>
30	13	2.65

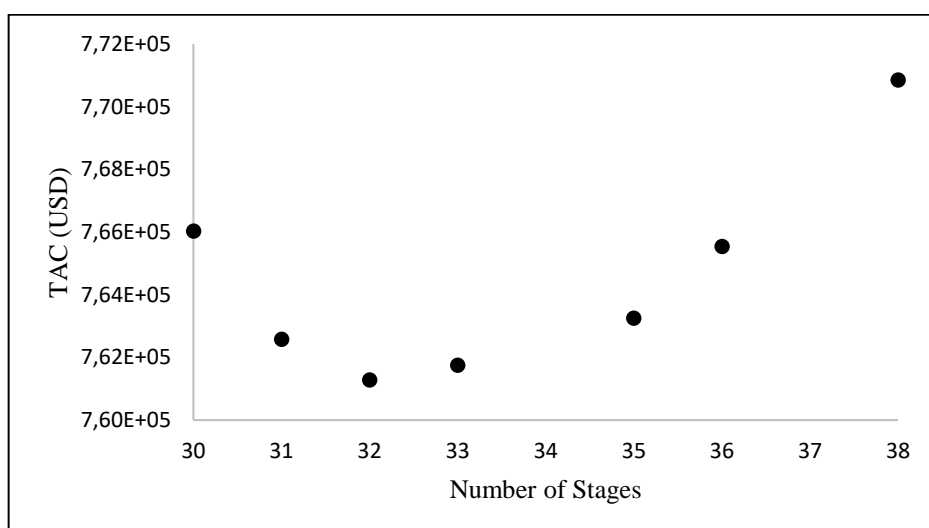


Figure E.1: Influence of number of stages on the total annual cost

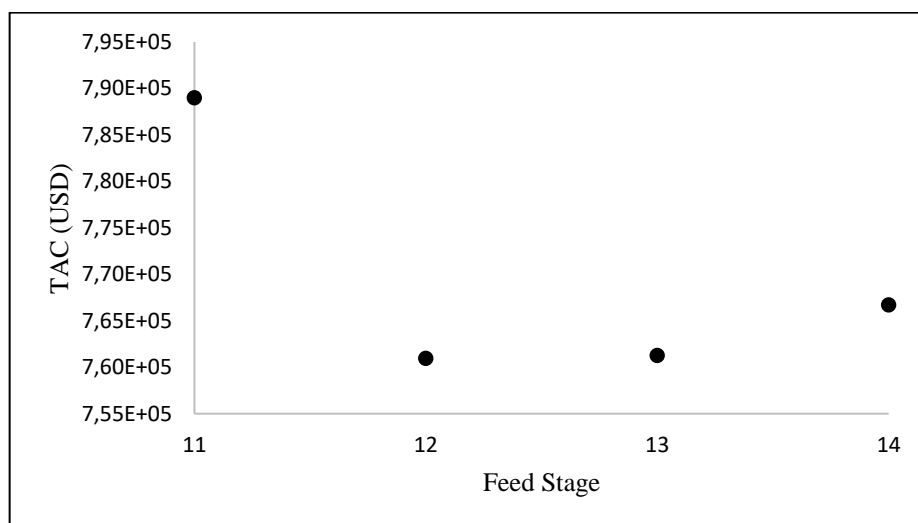


Figure E.2: Influence of feed entry stage on the total annual cost at 32 stages

## E.2 Process 2FE (2 flash, extractive distillation):

### Conventional Distillation Column (C-01)

Table E.2: Variation of feed stage location with reflux ratio

NoS	FS	RR
57	39	0.5832
57	40	0.5792
<b>57</b>	<b>41</b>	<b>0.5789</b>
57	42	0.5831
57	45	0.6315

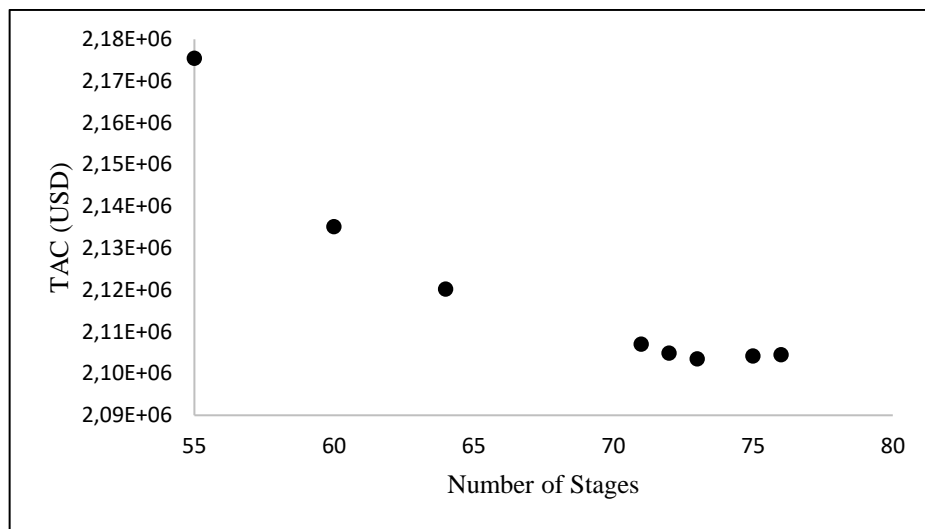


Figure E.3: Influence of number of stages on the total annual cost

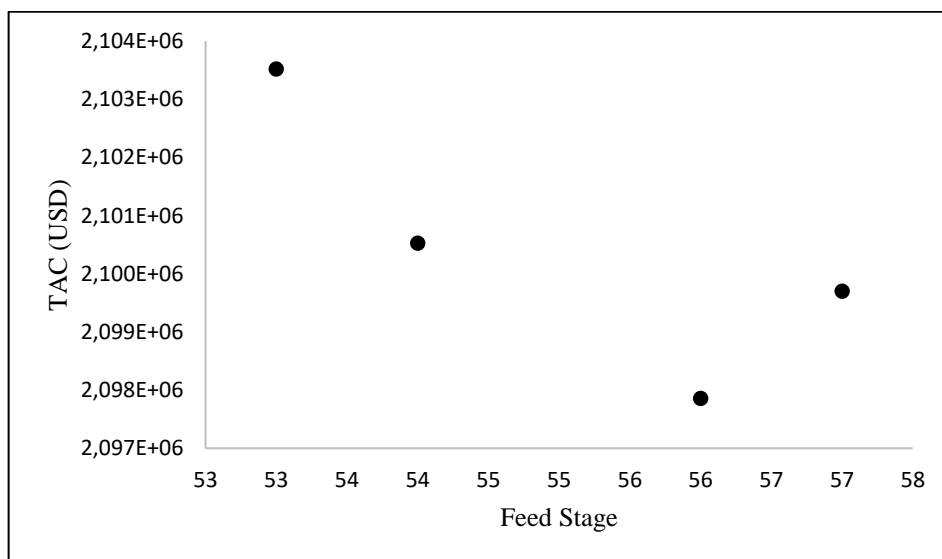


Figure E.4: Influence of feed entry stage on total annual cost at 73 stages

## Extractive Distillation Column (C-02)

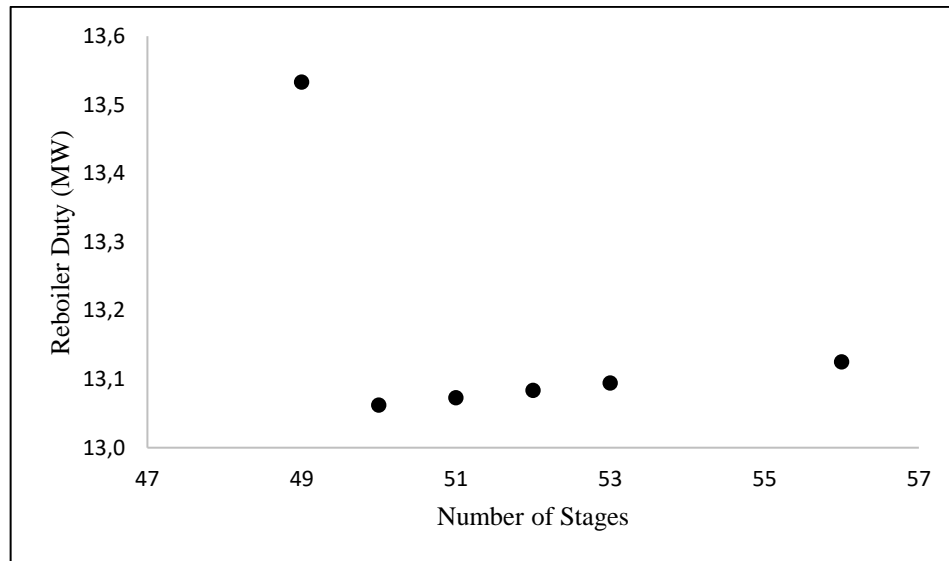


Figure E.5: Influence of number of stages on reboiler heat duty

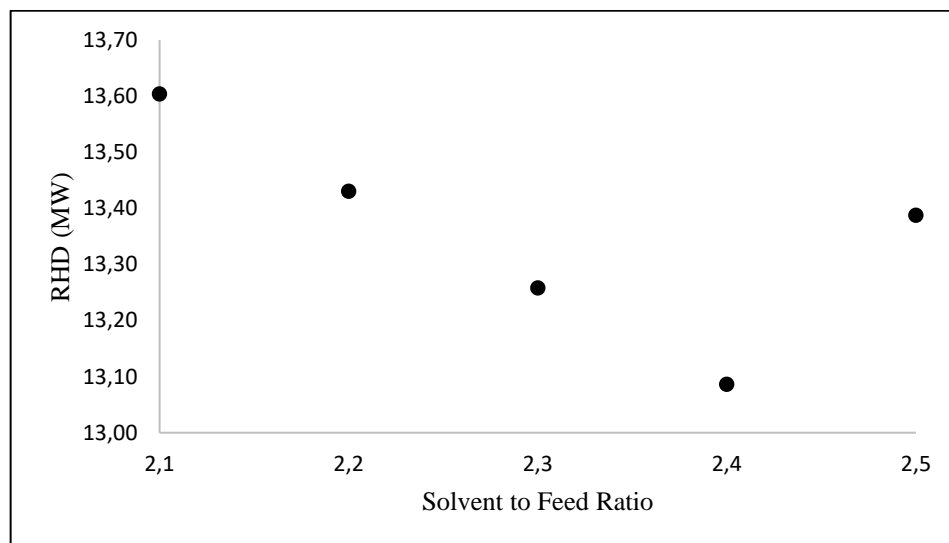


Figure E.6: Influence of solvent to feed ratio on reboiler heat duty for case 6

Table E.3: Extractive distillation column specifications for each case

Case	NoS	FS	SFS	RR	S/F Ratio	Purity	Recovery	RHD (MW)
1	49	39	8	0.6	2.3	0.9998	0.9998	13.18
<b>2</b>	<b>50</b>	<b>39</b>	<b>9</b>	<b>0.6</b>	<b>2.2</b>	<b>0.9998</b>	<b>0.9998</b>	<b>12.89</b>
3	51	38	9	0.6	2.2	0.9998	0.9998	12.90
4	52	38	9	0.6	2.2	0.9998	0.9998	12.91
5	53	37	9	0.5	2.4	0.9998	0.9998	13.05
6	56	37	9	0.5	2.4	0.9998	0.9998	13.09

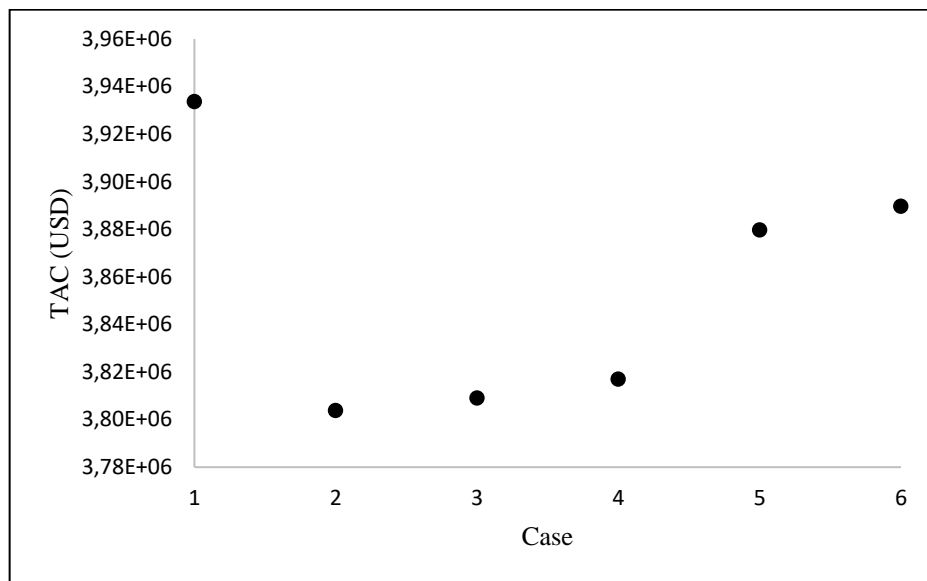


Figure E.7: Total annual cost for the different cases in the extractive distillation column

## Solvent Recovery Column (C-03)

Table E.4: Variation of feed stage location with reflux ratio

NoS	FS	RR
28	10	3.75
<b>28</b>	<b>12</b>	<b>2.67</b>
28	13	2.73

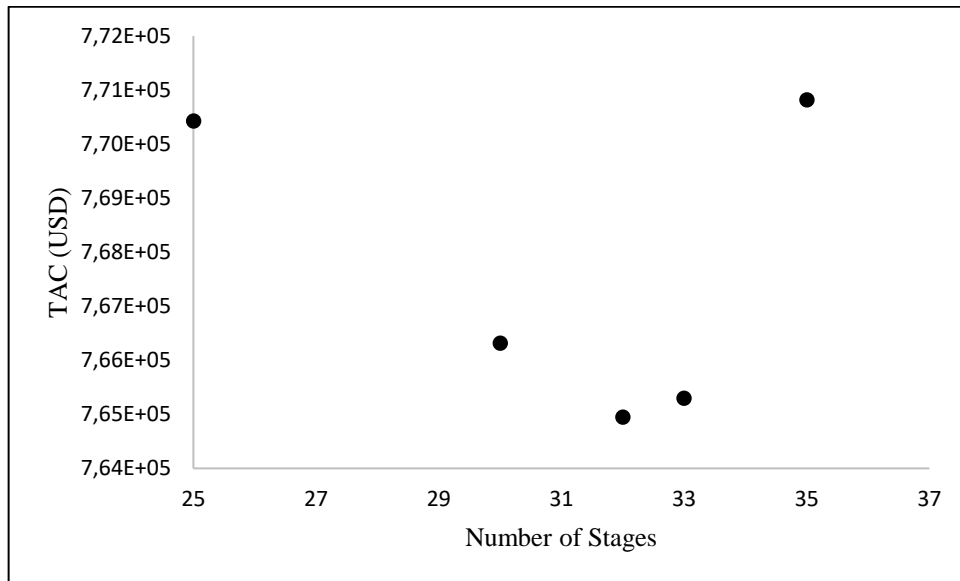


Figure E.8: Influence of number of stages on the total annual cost

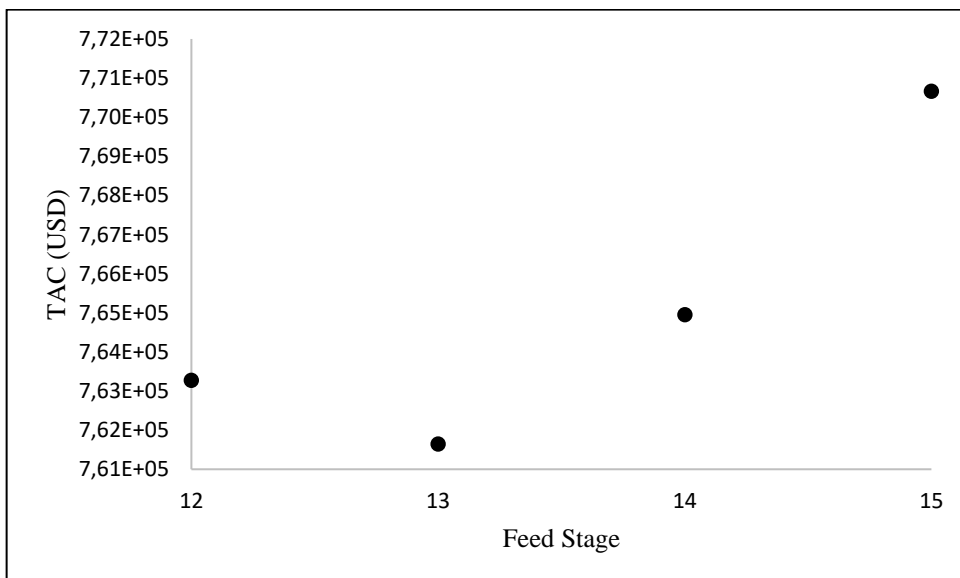


Figure E.9: Influence of feed entry stage on total annual cost at 33 stages



### E.3 Process 1FM (1 flash, membranes)

#### Conventional Distillation Column (C-01)

Table E.5: Variation of feed stage location with reflux ratio

NoS	FS	RR
40	25	0.649
40	26	0.626
40	27	0.611
<b>40</b>	<b>28</b>	<b>0.606</b>
40	29	0.609

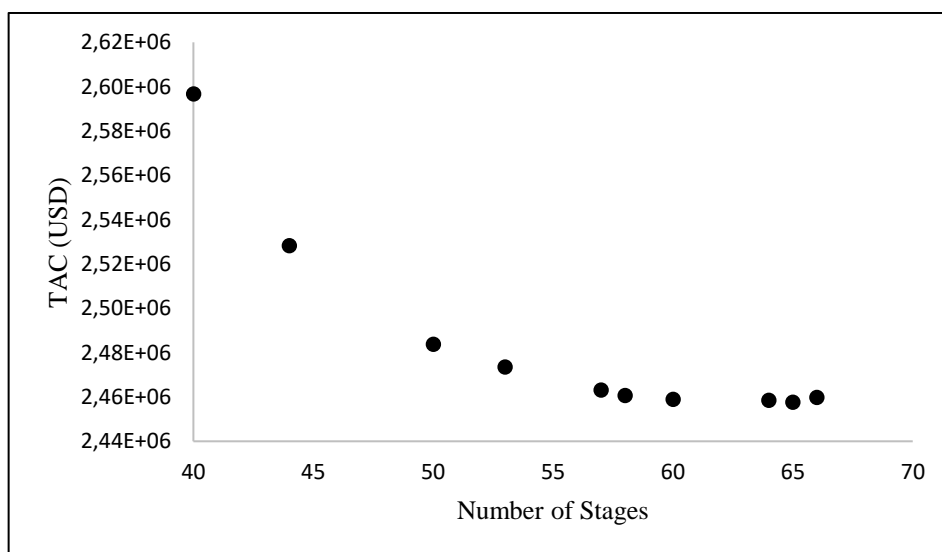


Figure E.10: Influence of number of stages on the total annual cost

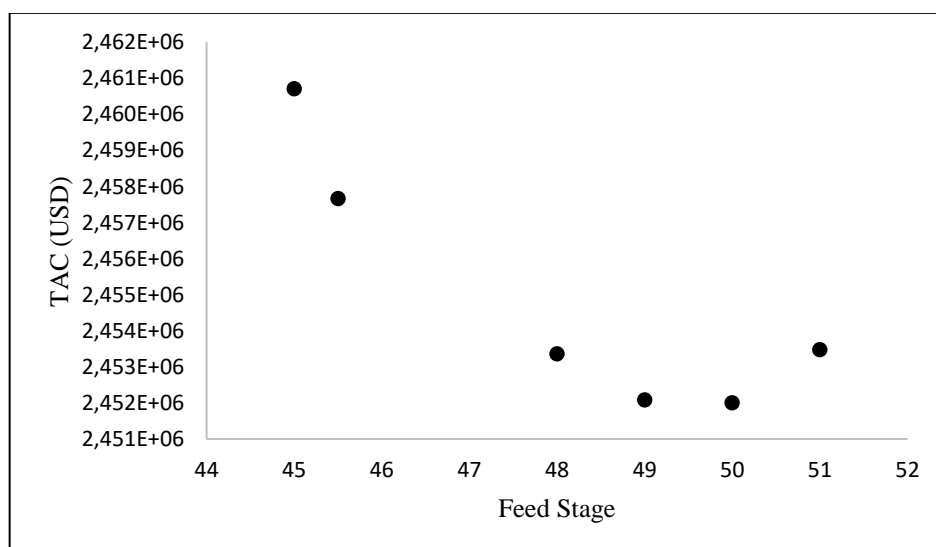


Figure E.11: Influence of feed entry stage on the total annual cost at 65 stages

## E.4 Process 2FM (2 flash, membranes)

### Conventional Distillation Column (C-01)

Table E.6: Variation of feed stage location with reflux ratio

NoS	FS	RR
40	25	0.654
40	26	0.624
40	27	0.609
<b>40</b>	<b>28</b>	<b>0.604</b>
40	29	0.608

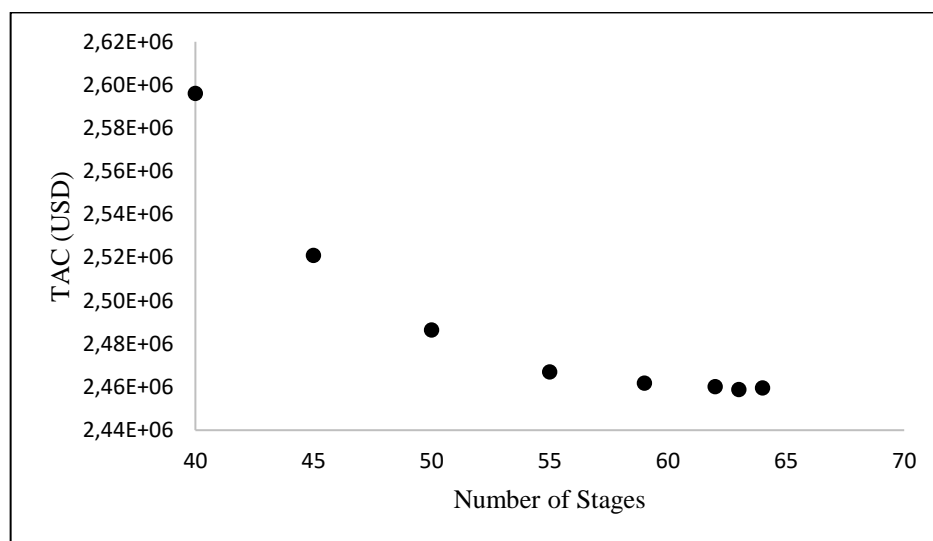


Figure E.12: Influence of number of stages on the total annual cost

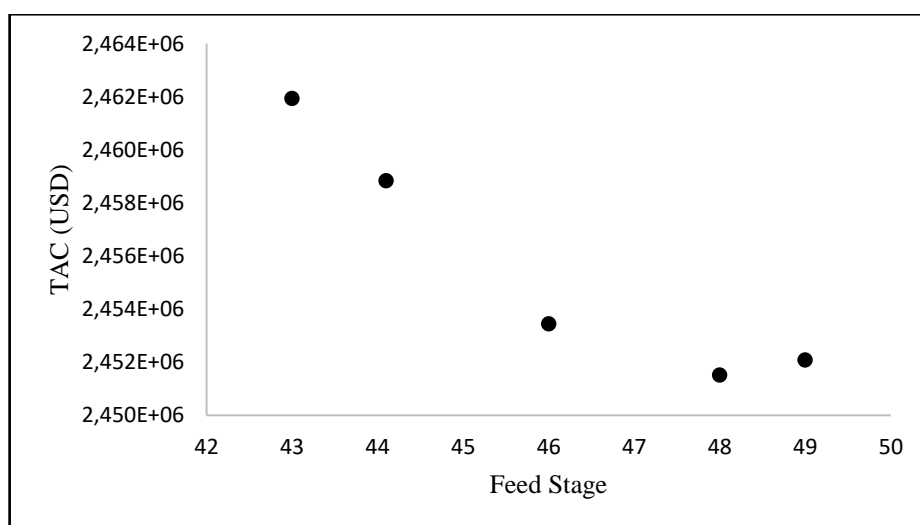


Figure E.13: Influence on feed entry stage on the total annual cost at 63 stages